UNIVERSITY OF CALIFORNIA, SAN DIEGO

Nonlinear Simulation, Validation Study, and Uncertainty Quantification of Drift-turbulence in CSDX Linear Plasma Device

A dissertation submitted in partial satisfaction of the
requirements for the degree
Doctor of Philosophy

in

Engineering Sciences (Engineering Physics)

by

Payam Vaezi

Committee in charge:

George R. Tynan, Chair
Farhat N. Beg
Juan Carlos del Alamo
Patrick H. Diamond
Christopher Holland
Kevin B. Quest

2017

The dissertation of Payam Vaezi is approved, and it is acceptable in quality and form for publication on microfilm and electronically:

_____

_____

_____

_____

_____

_____

Chair

University of California, San Diego

2017

DEDICATION

This dissertation is lovingly dedicated to my mother, for her endless love, support and encouragement.

EPIGRAPH

A wise man will make more opportunities than he finds.

—Sir Francis Bacon

TABLE OF CONTENTS

LIST OF FIGURES

LIST OF TABLES

ACKNOWLEDGEMENTS

This is a great opportunity to express my gratitude to all those people who have given me the possibility to complete this dissertation.

My deep gratitude is to my advisor, Prof. George R. Tynan. I have been very fortunate to have him as my advisor. He has given me this opportunity to study and explore a completely new field of science to me, and he let me to grow as an independent thinker. I also owe a great deal of gratitude to Dr. Christopher Holland, who has advised me every step of the way, with his patience and support all along helped me overcome many hard situations and finish this dissertation. I learned a lot from him and have a great deal of respect for him. Also, I would to like to thank Prof. Patrick H. Diamond who taught me a lot about physics, and science.

At UC San Diego, I would like to thank my colleagues S. C. Takhur, R. Hong, and R. Hajjar. I have also benefited greatly from discussions with many members of the research community, including B. D. Dudson, B. Friedman, X. Q. Xu, J. Loizu, A. Ashourvan, P. Manz, M. Xu, I. Cziegler, J. Feinberg, N. Howard, O. Meneghini, B. Asadi, and A. F. Chaghooshi, and I thank them for their useful comments. I especially thank B. D. Dudson for the development of BOUT++ framework which this thesis simulations are performed with.

My sincere gratitudes are also owed to the rest of Ph.D committee, Prof. Farhat N. Beg, Prof. Juan Carlos del Alamo, Prof. Kevin B. Quest. I thank them for reviewing my thesis and for their valuable comments.

Finally, I would like to thank my mother, and my sister to their on going love and support. I can not describe how much I owe them helping me navigate the ups and downs of life over the years.

The text and data in Chapter 3, is a reprint of the material as it appears in Vaezi, P., Holland, C., Thakur, S. C., & Tynan, G. R. (2017). *Understanding the impact of*

insulating and conducting endplate boundary conditions on turbulence in CSDX through nonlocal simulations. Physics of Plasmas, 24(4), 042306. Copyright 2017 American Institute of Physics. The dissertation author was the primary investigator and author of this paper.

The text and data in Chapter 4, is a reprint of the material as it appears in Vaezi, P., Holland, C., Thakur, S. C., & Tynan, G. R. (2017). *Validation Study of a Drift-Wave Turbulence Model for CSDX Linear Plasma Device*. Physics of Plasmas 24 (9), 092310. Copyright 2017 American Institute of Physics. The dissertation author was the primary investigator and author of this paper.

The text and data in Chapter 5, in full, is accepted for publication at Journal of Fusion Science and Technology under Vaezi, P. & Holland, C. (2017). *An Improved Approach to Uncertainty Quantification for Plasma Turbulence Validation Studies*. The dissertation author was the primary investigator and author of this paper.

This thesis was supported by the U.S. Department of Energy Grant No. DE-FG02-06ER54871.

VITA

2011	B. S. in Aerospace Engineering, Khajeh Nasir Toosi University of Technology, Tehran
2013	M. S. in Engineering Sciences (Engineering Physics), University of California, San Diego
2012-2017	Graduate Research Assistant, University of California, San Diego
2017	Ph. D. in Engineering Sciences (Engineering Physics), University of California, San Diego

PUBLICATIONS

P. Vaezi, C. Holland, S. C. Thakur, and G. R. Tynan, "Understanding the impact of insulating and conducting endplate boundary conditions on turbulence in CSDX through nonlocal simulations", *Phys. of Plasmas*, 24.4 (2017): 042306.

P. Vaezi, C. Holland, S. C. Thakur, and G. R. Tynan, "Validation Study of a Drift-Wave Turbulence Model for CSDX Linear Plasma Device", *Physics of Plasmas 24 (9), 092310*.

P. Vaezi, C. Holland, "An Improved Approach to Uncertainty Quantification for Plasma Turbulence Validation Studies", *accepted for publication at Journal of Fusion Science and Technology*.

ABSTRACT OF THE DISSERTATION

Nonlinear Simulation, Validation Study, and Uncertainty Quantification of Drift-turbulence in CSDX Linear Plasma Device

by

Payam Vaezi

Doctor of Philosophy in Engineering Sciences (Engineering Physics)

University of California, San Diego, 2017

George R. Tynan, Chair

The Controlled Shear Decorrelation Experiment (CSDX) linear plasma device provides a unique platform for investigating the underlying physics of self-regulating drift-wave turbulence/zonal flow dynamics. A 3D drift-reduced nonlocal cold ion fluid model which evolves density, vorticity, and electron temperature fluctuations, with proper sheath boundary conditions, is used to simulate dynamics of the turbulence in CSDX. The simulations show density gradient-driven drift-waves are the dominant instability in CSDX. However, the choice of insulating or conducting end plate boundary conditions affects the linear growth rates and energy balance of the system due to the absence or

addition of Kelvin-Helmholtz modes generated by the sheath-driven equilibrium $E \times B$ shear and sheath-driven temperature gradient instability.

The physics study is then followed by an extensive quantitative validation study. For the direct comparison of nonlinear simulation results to experiment, a synthetic Langmuir probe diagnostic is used to generate a set of synthetic observables which are in turn used to construct the validation metrics. A significant improvement of model-experiment agreement relative to the previous 2D simulations is observed. An essential component of this improved agreement is found to be the effect of electron temperature fluctuations on floating potential measurements, which introduces clear amplitude and phase shifts relative to the plasma potential fluctuations in synthetically measured quantities. Moreover, systematic simulation scans show that the self-generated $E \times B$ zonal flows profile is very sensitive to the steepening of density equilibrium profile. To minimize the number of simulations required for uncertainty quantification, a more advanced seed sampling methods for efficient sampling of the input parameter space, and a rapidly converging non-intrusive Probabilistic Collocation method to map out a probabilistic model response is implemented. This approach is shown to yield significantly better constrained uncertainty estimates than conventional uniform sampling methods for practical numbers of nonlinear simulations.

Chapter 1

Introduction

With rapid growth of energy demand, our modern society is more than ever in need of powerful yet environmentally friendly energy production solutions. Among current options for long term energy needs, controlled thermonuclear fusion is an attractive, safe and clean solution, with abundant fuel sources to power our infrastructure for a long period of time. Due to its great potential, scientists have been working on controlling fusion for over half a century. The typical fusion reactions include[Fre08]:

$$D + D \rightarrow He^3(0.82MeV) + n(4.25MeV) \tag{1.1}$$

$$D + D \rightarrow T(1.01MeV) + p(3.02MeV) \tag{1.2}$$

$$D + T \rightarrow He(3.5MeV) + p(14.1MeV) \tag{1.3}$$

The main obstacle to achieving net energy gain from fusion reactions is the confinement of the reaction fuel for a long enough time at sufficiently high temperatures and densities to achieve a self-sustaining reaction[Law57]. One of the best ways to contain the fuel is to maintain it in a plasma state and restrict the motion of the plasma using magnetic fields. Different magnetic configurations for magnetically confinement of burn-

ing plasma have been proposed; among them the tokamak and stellarator configurations are the most studied. Currently, tokamaks have achieved the temperatures and pressure necessary to produce fusion, however for plasma confinement times (τ_E) that are below that needed for energy production.

The plasma confinement time, for a given sized tokamak, is inversely proportional to the rate of cross-field transport in the tokamak[HH12], so it is of a great importance to understand how to minimize that transport. However, neoclassical transport theory (transport solely due to Coulomb collisions in toroidal magnetic fields) generally underpredicts the experimental transport. The experimental data show that actual ion thermal conductivity is anomalously large by a factor on the $\mathcal{O}(1-10)$ with respect to the neoclassical χ_{neo}, while the electron heat conduction and particle diffusion coefficients are each anomalous (non-collisional) by about two orders of magnitude larger than expected from neoclassical theory[HBB$^+$98].

It has been suggested the excess cross-field particle and energy transport is primarily driven by microturbulence, which is driven by instabilities due to the presence of free energy sources. These free energy sources are due to density gradient, temperature gradients, and/or non-equilibrium distribution function[CS84]. These free energy sources always exist in the normal operating conditions of a tokamak, such that turbulence transport is commonly expected. Recent studies show that the saturation of plasma microturbulence and transport can be mediated through self-generated zonal flow[DIIH05]. Understanding these turbulence induced effects on the plasma in the complex geometry setting of tokamaks (especially in the high fluctuation amplitude of edge region) and in the presence of multi-scale instabilities is a challenging task.

Numerical simulations have helped improve understanding of physical processes and spatial and temporal structures in all kinds of turbulent settings. Validation studies of numerical models which assess the accuracy and fidelity of these models in prediction

(or *postdiction* in many cases) of experimental observations represent one of the clearest and most direct means of quantifying our progress in developing a true understanding of fusion-relevant systems. In some instances, e.g. in the core of tokamaks, the simulations have uncovered new unexpected physics such as the Dimits shift of ITG turbulence[DBB$^+$00]. But in other instances, like in the edge of tokamaks, nonlinear turbulent simulations do not yet agree enough with experiment to provide good physical insight, let alone the ability for predictive analysis[Hol16]. At the same time, due to the strong nonlinear dependence of turbulence statistics, the experimental input uncertainties in the simulation can results in a wide variation in model response. Thus, to be able to use numerical simulations effectively one needs to quantify the uncertainties associated with the turbulence, and then systematically study the model response.

A possible path to making progress on this complex problem is to reduce the problem to a simpler one, by first validating models in a simple plasma device, and then slowly move up to more and more complex situations. Linear plasma devices such as Controlled Shear Decorrelation Experiment (CSDX) [BTA$^+$05, YTH$^+$10, XTH$^+$10, CTXM$^+$13] due to their rather simplistic geometry are useful in studying source of the basic underlying physics in detail. CSDX is inherently operates at low temperatures and is highly collisional, similar to the scrape-off layer (SOL) of tokamak. It excludes some of the toroidal-specific complexities such as ballooning instabilities while retaining turbulence-shear flow interactions. The insight gained from validation studies and uncertainty quantification of plasma turbulence in generalization the CSDX may therefore apply to tokamak edge turbulence as well, or at least provide methods of analysis that may be applied for simulations of larger magnetically confined devices.

1.1 Instabilities and Turbulence

Turbulence is a ubiquitous phenomenon in fluids that has been recognized and studied for a long time. It is often called the last unsolved problem in classical physics, mainly because we cannot predict in detail how or why turbulence occurs or fully predict its behavior. However, it is extremely important to gain an understanding of it in laboratory plasmas and magnetically confined fusion devices because it largely governs the particle and energy transport. Thus, a better understanding of plasma turbulence can be expected to lead to a better prediction of future device performance. As Richard Feynman remarks in his Lectures on Physics, "Turbulence is the most important unsolved problem of classical physics."

Early studies on turbulence suggested that turbulence was a random process that could only be described via statistical tools. Statistical descriptions of turbulence are still widely accepted, of which perhaps the most important is work of [Kol62]. Nevertheless, modern studies of turbulence show that deterministic set of equations can be used to model turbulence. [Lor63] showed that a deterministic equation derived from the Navier-Stokes equation could exhibit random-like behavior which is sensitive to the small changes of initial conditions. This deterministic approach shows that even though the turbulence is not random, it still can be stochastic (stochastic refers to a variable whose autocorrelation decays exponentially to zero), hinting that statistical studies will be useful. Deterministic systems are stochastic when they are controlled by large number of effective degrees of freedom[Fri13].

The turbulence state responsible for the anomalous transport in the magnetically confined fusion devices is often called micro-turbulence, which is characterized by density, potential, and temperature fluctuations of a few percent of background values, and can be destabilized by density or shear layer or temperature gradients or inhomogeneities

of the magnetic field[FBC+16]. In the core of tokamak where the temperatures are high, $\mathscr{O}\left(10^4 - 10^5\right) eV$, and plasma collisionality is low, intrinsically kinetic phenomena such as Landau damping or finite Larmor radii effects calls for the more complicated multi-species kinetic model (such as general Vlasov equation or gyrokinetic theory needed to solve the species distributions $f_s(\mathbf{x}, \mathbf{v}, t)$ in the phase space), and the fluid model cannot describe the turbulence. On the other hand, in the tokamak SOL, where the temperatures and densities are much lower, $\mathscr{O}\left(1 - 10^2\right) eV$, the plasma becomes highly collisional, and the fluid models can be used to predict the turbulence fluctuations and transport. Other major differences in SOL turbulence includes the open field line configuration, non-Maxwellian distribution, exponential decay of density, and high turbulence fluctuations with very strong intermittency.

Understanding the vast range of instabilities at different operating regimes of a magnetically confined fusion device has proved to be one of the biggest challenges in feasibility studies of fusion energy production. Nevertheless, at this point, many aspects of turbulence and transport in the tokamak core are fairly well understood, largely due to the success of gyrokinetic simulations[GIVW10]. However, the edge transport in tokamak SOL at this point is still not very well understood[FBC+16]. The challenge of understanding edge turbulence is mainly due to the complex geometry of open field lines configuration, the large number of possible instabilities, and large range of spatial and temporal scales of perturbations in plasmas from the Debye length and plasma frequency ($\mathscr{O}\left(10^{-3}\right) cm$ and $\mathscr{O}\left(10^{11}\right) s^{-1}$, respectively) to the machine size and turbulence frequencies ($\mathscr{O}\left(10^2\right) cm$ and $\mathscr{O}\left(10^3\right) s^{-1}$, respectively).

The focus of this thesis is on the specific turbulent processes in the CSDX cylindrical linear plasma device, which has an open field line configuration with a modest radial density gradient profile, resembling a simplified SOL setting without magnetic shear. The overall length of CSDX device is $\sim 3m$, and the vacuum vessel diameter

is 20cm, and Argon gas is used for plasma generation operated with typical $\sim 4mTorr$ Argon gas pressure. The power deposition into plasma is through $m = 0$ or $m = 1$ RF helicon source, and disk-shaped electromagnet coils provides a solenoidal magnetic field that can be varied up to 2.4kG. In Fig. 1.1, the schematic of CSDX linear device is shown.

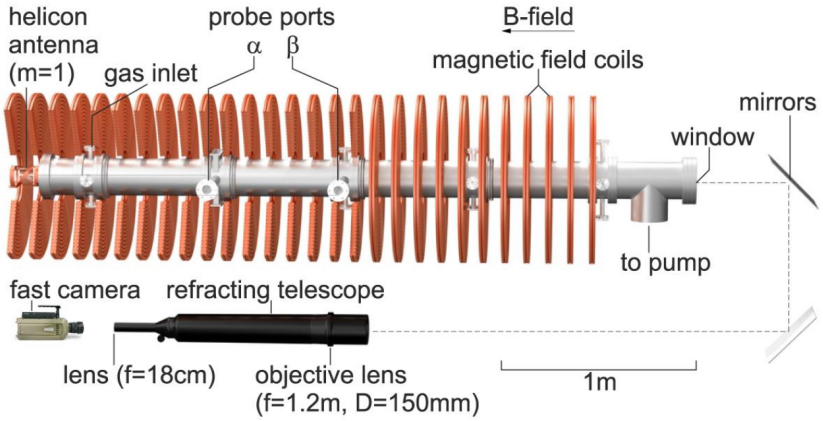

Figure 1.1: (a) Schematic of the CSDX linear plasma device, including the setup of the measurement diagnostics.

In a brief look at the CSDX device, the typical plasma density range is in $\mathcal{O}\left(10^{11}-10^{13}\right) cm^{-3}$, electron temperature $\mathcal{O}\left(1\right) eV$, and ion temperature $\mathcal{O}\left(10^{-1}\right) eV$, where the drift-waves are the dominant drive instability in the turbulence drive[BTA^{+}05]. In addition, the choice of end plate where the open field lines meet the material surface, may trigger additional instabilities, such as the sheath-driven Kelvin-Helmholtz (KH) and sheath-driven electron temperature gradient instabilities[XRD93, FRR^{+}15]. Moreover, the transfer of energy to low frequency flows, acts as a self-regulating system of drift-wave/zonal flow turbulence[XTH^{+}09]. The basic physics principles of the relevant instabilities and turbulence suppression occurring in the CSDX experiments are explained below.

1.1.1 Drift-wave Instability

The collisional drift-wave instability exists in a plasmas with density inhomogeneity and finite resistivity, and occurs due to the interaction between the dynamics perpendicular and parallel to the magnetic field arising from the combined effects of spatial gradients, ion inertia, and adiabaticity (rapid transfer of energy) of the electrons in parallel direction. The physics of drift-wave instability can be explained through a decreasing density gradient profile perpendicular to the magnetic field, shown in Fig. 1.2.

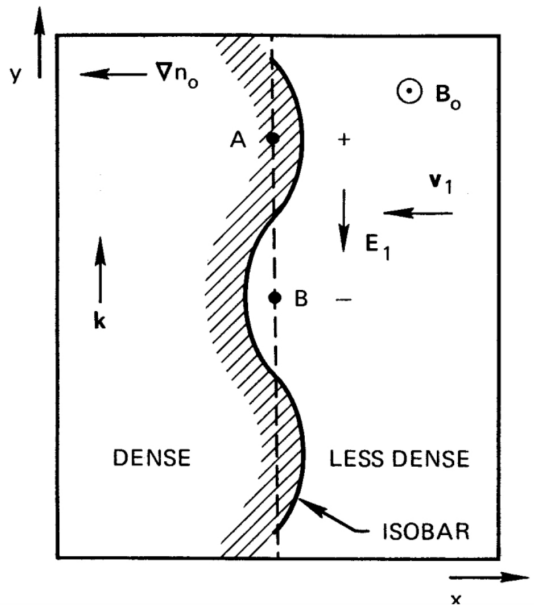

Figure 1.2: Physical mechanism of drift-wave instability[CS84].

Here, the only driving force of the instability is the pressure gradient $T\nabla n_0$ (in this introduction section to the drift-waves, we have assumed constant temperatures T). In this case, zeroth-order electron diamagnetic drift is

$$\mathbf{v}_{*_e} = \frac{\nabla p_e \times \hat{z}}{enB} = -\frac{T_e}{eB}\frac{\nabla n_0}{n_0}\hat{y}. \tag{1.4}$$

Since drift-waves have finite parallel wavelength $k_{\|}$, electrons can flow along the magnetic field to establish a thermodynamic equilibrium among themselves. When there

is no resistivity, electrons will obey the linearized Boltzmann relation,

$$\frac{\tilde{n}}{n_0} = \frac{e\tilde{\phi}}{T_{e_0}}. \tag{1.5}$$

At point A in Fig. 1.2 where the density is larger than the equilibrium, $\tilde{n}$ and as a result $\tilde{\phi}$ is positive. Similarly at point B, $\tilde{n}$ and $\tilde{\phi}$ are negative. This difference will create a first-order electrical field perturbation $\tilde{E}$ between A and B, and The resulting electric field perturbation will cause a $E \times B$ drift in the x direction, $\tilde{v}_x = \tilde{E}_y/B = -ik_y\tilde{\phi}/B$. Since there is a gradient ∇n_0 in the x direction, the $E \times B$ drift will bring plasma of different density to a fixed point. Assuming quasi-neutrality, one can find dispersion relation as,

$$\frac{\omega}{k_y} = -\frac{T}{eB}\frac{\nabla n_0}{n0} = v_{*_e} \tag{1.6}$$

Thus, the waves travel with the electron diamagnetic drift velocity in y direction and are called the drift-waves, and satisfy the $k_\parallel \ll k_y$ and $v_{th_i} \ll \omega/k_\parallel \ll v_{th_e}$ conditions. Since ω is non-imaginary, there is no growth rate associated with this drift. Dispersion relation of Eqn. 1.6 can be obtained through linearized the Hasegawa-Mima equation for adiabatic electrons[HM78].

However, the drift-waves can become unstable, when the parallel resistivity ($\eta_\parallel$) modifies the the adiabatic response. In this case, the modified Boltzmann relation reads as

$$\frac{\tilde{n}}{n_0} = \frac{e\tilde{\phi}}{T_{e_0}}\frac{\omega_* + ib\sigma_\parallel}{\omega + ib\sigma_\parallel}. \tag{1.7}$$

where $b = \frac{T_e k_y^2}{m_i \omega_{c_i}}$, $\omega_* = k_y v_{*_e}$, and $\sigma_\parallel = \frac{k_\parallel \omega_{c_e} \omega_{c_i}}{k_y^2 \nu_{ei}} = \frac{1}{\eta_\parallel}$. The parallel resistivity then causes the potential distribution $\tilde{\phi}$ to lag behind the density distribution $\tilde{n}$, This phase shift causes $\tilde{v}_x$ to be outward where the plasma has already been shifted outward, and

vice versa; hence the perturbation grows. In the presence of resistivity and polarization drifts, the dispersion relation shown in Eqn. 1.6 will be modified to

$$\omega^2 + i\sigma_{\|}(\omega - \omega_*) = 0. \tag{1.8}$$

When $\sigma_{\|}$ is non-zero, ω is always complex, creating one branch of unstable modes. We should note that the drift-wave instability is a type of dissipative instability, and growth rates of the instability is proportional to the parallel resistivity of plasma. The drift-wave instability dispersion relation can be obtained from Hasegawa-Wakatani equations[HW83].

1.1.2 Transition to Turbulence

The concept of transition to turbulence was implicitly introduced by [Lan44] and later revised by [RT71]. According to [Lan44], turbulence is reached at the end of an indefinite superposition of successive oscillatory bifurcations, each bringing its unknown phase into the dynamics of the system. In contrast, [RT71] mathematically showed that quasi-periodicity is not generic when nonlinearities are acting. They identified turbulence with the stochastic regime of deterministic chaos characterized by long term unpredictability due to sensitivity to initial conditions and reached only after a finite and small number of bifurcations.

From the theory of nonlinear phenomena, two major types of transition exist. In a *supercritical* transition, a continuous evolution of states is observed as the control parameter is increased. In contrast, the *subcritical* transition is characterized by the coexistence of several possible locally stable states at a given value of the control parameter, and an hysteresis behavior as the control parameter is varied.

A simple explanation of subcritical and supercritical nonlinear phenomena can be

discussed by the evolution of the amplitude $|A|$ coupling with itself for the most unstable mode in the Landau equation[Lan44],

$$\frac{d|A|^2}{dt} = 2\gamma_1|A|^2 - \alpha|A|^4,$$

where γ_1 is the linear growth rate of the instability, α is the Landau parameter, and $\alpha|A|^4$ is the nonlinearity.

In a case where $\gamma_1 > 0$, and $\alpha > 0$, the analytical solution of the Landau equation as $t \to \infty$, $|A| \to (2\sigma/l)^{1/2}$ for any initial amplitude of A_0. This value of $A_e = (2\sigma/l)^{1/2}$ is called a fixed point attractor with a basin of attraction consisting of all values of A_0, since any initial state asymptotically evolves to it. Attractors are important objects in the field of dissipative dynamical equations. Note that the linear problem is unstable, but the nonlinear problem solution asymptotes to a fixed value. This is called supercritical stability, where the linear stability analysis governs the evolution of mathematically infinitesimal perturbations.

In the other case of Landau equation, if $\alpha < 0$, $\gamma_1 < 0$, and $A_0 > A_e$, the solution is unstable and breaks down at finite time. Note that if $A_e < A_0$ the solution decays to zero at $t \to \infty$, however for large enough initial amplitude of A_0 the solution is unstable and breaks down at finite time, which is known as subcritical instability. In reality, the is unphysical, and the simple Landau equation is not sufficient to find the attractor solution with only one degree of freedom. Perhaps the most known study of subcritical instability, is the transition from laminar flow to turbulent flow at a critical Reynolds number in neutral fluid pipe flow experiments[Pop01].

1.1.3 Zonal Flow Generation

Fluid turbulence is generally a 3D phenomena, but under certain conditions, plasma turbulence can be described as a 2D phenomena. Whenever vortex tube stretching is week or non-existent ($\nabla_{\|} v_{\|} = 0$), the turbulence exhibits a dual cascade of energy and enstrophy (mean squared vorticity) in which both are conserved. The instability energy is injected at some integral length-scale, in which the enstrophy transfers to smallest scales while energy is being transferred to largest scales[DIIH05]. The process of forward cascade can be described through breaking of eddies and viscous damping of the broken eddies. On the other hand, the process of inverse cascade can be illustrated by merging of vortecies and construction of larger spatial structures. Eventually, spatially large (respect to eddy size) coherent structures will be formed. Schematic of dual cascade energy spectrum in a typical 2D turbulence setting is shown in Fig. 1.3.

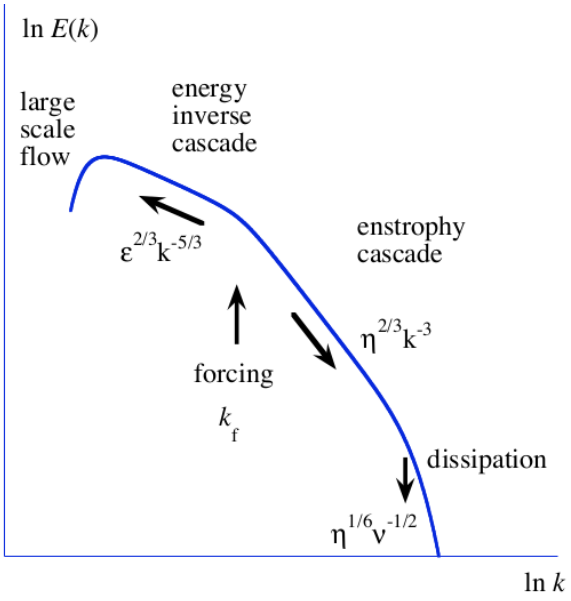

Figure 1.3: Dual cascade energy spectrum[DII10].

Note that the dual cascade shown in Fig. 1.3 is for the simple case of Euler 2D incompressible fluid equations. Note that depneding on the 2D turbulence model, the

cascade slopes changes. Moreover, it worths mentioning that in the CSDX, the scales are compromised, meaning the energy injection scale (L_n^{-1}) is close to dissipation scale (ρ_s^{-1}).

In the context of tokamak plasmas, the term zonal flow refers to the large scale toroidally and poloidally symmetric but radially localized band-like flow structures, i.e., it is an $m = n = 0$ electrostatic fluctuation with finite radial wavenumber. Here, m denotes the poloidal (azimuthal) mode number and n denotes the toroidal (axial) mode number. The zonal flow concept in plasma physics is similar to the quasi-two-dimensional atmospheric and oceanic flows along the latitude line in geophysics. Another feature of zonal flows is that in a large aspect ratio torus it has zero real frequency. Figure 1.4 shows a schematic of the typical structures of zonal flows.

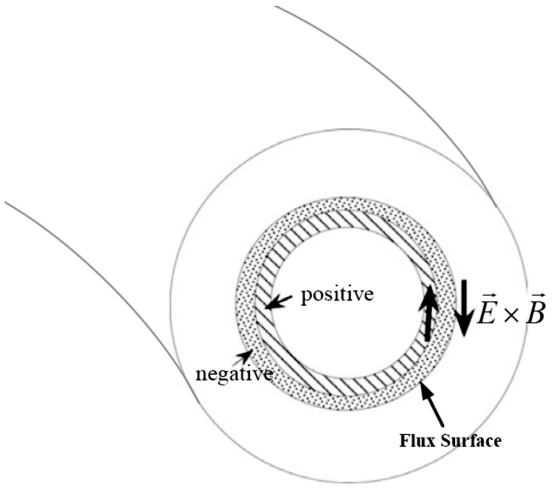

Figure 1.4: Schematic of zonal electric field and zonal flow in a poloidal cross-section. The hatched region and dotted region denote the positive and negative charges respectively[DIIH05].

Because zonal flows occur within a magnetic flux surface where plasma pressure is constant, they cannot tap expansion free energy stored in the equilibrium gradients, etc. that are normal to the surface, and as a result they can only be driven by nonlinear interactions that transfer energy from other instabilities, e.g. drift-wave, into this $m =$

$n = 0$ mode. That is why the zonal flow can essentially act as a regulatory process to reduce the turbulence intensity and transport. Also because of the zonal flow symmetry, they do not generate additional energy or particle transport, and are not subject to Landau damping and primarily damped by collisional processes. Finally, field line bending stabilizes Kelvin Helmholtz instability of zonal flow. All the above features are thought to make zonal flows a benign reservoir of free energy in the system[DIIH05]. Thus, the zonal flow can be saturated by the drift-turbulence, and thus acts to regulate the turbulence amplitude.

To illustrate the process, consider a simplified azimuthal momentum balance for an incompressible inviscid 2D plasma fluid in cylindrical plasma as

$$\frac{\partial u_\theta}{\partial t} + \frac{\partial u_\theta u_r}{\partial r} = \mu u_\theta, \tag{1.9}$$

where $u_\theta u_r$ is the Reynolds stress, and μ is dissipative damping rate. Therefore, kinetic energy evolution of such equation in spectral space reads as

$$\frac{\partial |u_\theta(\mathbf{k})|^2}{\partial t} - 2k_r \sum_{\mathbf{k}_1,\mathbf{k}_2,\mathbf{k}} \Im \left(u_\theta^*(\mathbf{k}) u_\theta(\mathbf{k}_1) u_r(\mathbf{k}_2) \right) = -\mu |u_\theta(\mathbf{k})|^2, \tag{1.10}$$

where $u_\theta(\mathbf{k})$ is transformed azimuthal velocity at wavenumber $\mathbf{k}$. The second term in above equation, shows nonlinear kinetic energy transfer in $\mathbf{k}$ space across spatial scale via three-wave coupling.

Considering zonal flow to have $\mathbf{k}_{ZF} = k_{ZF}\hat{r}$, and generally assuming $|\mathbf{k}_1|, |\mathbf{k}_2| \gg |k_r^{ZF}|$, triplet bracket $\{\mathbf{k}_{ZF}, \mathbf{k}_1, \mathbf{k}_2\}$ shows energy transfer between two big drift wavevectors to zonal wavevector. Assuming $k\rho_s \ll 1$ and electrostatic $\mathbf{E} \times \mathbf{B}$ drift velocity, i.e. $\mathbf{u}(\mathbf{k}) = -(i\mathbf{k}\phi(\mathbf{k}) \times \hat{z}/B_0)$, we can rewrite Eq.1.11 in form of $\phi(\mathbf{k}_{ZF})$,

$$\frac{\partial|\phi(\mathbf{k}_{ZF})|^2}{\partial t} - \Re \sum_{\mathbf{k}_1,\mathbf{k}_2} T_u(\mathbf{k}_1,\mathbf{k}_2)\langle(\phi^*(\mathbf{k}_{ZF})\phi(\mathbf{k}_1)\phi(\mathbf{k}_2)\rangle = \gamma|\phi(\mathbf{k}_{ZF})|^2, \tag{1.11}$$

where T_u is wave-wave coupling coefficient. The equation is showing that k_{ZF} is formed by linear growth rate/damping of the mode with energy transferred into this mode.

It is important to note that zonal flow has been widely accepted as a component to regulate turbulence and transport. Mean shear flow tilts turbulence eddies, and elongates them while narrowing radial extend of eddies. The increase of k_r, reduces effective step size (Δl) in turbulence diffusivity $\chi_{turb} \approx \Delta l^2/\tau_{corr}$, thus reducing turbulence transport. This zonal flow creation comes at the cost of drift-wave energy reduction, thus DW-ZF turbulence is a self-organizing system, where the scale of the drift wave intensity envelope sets the scale of the zonal flow.

1.1.4 Sheath-driven Instabilities

In the SOL region of different tokamaks e.g. limiter or divertor tokamak configuration (see Fig. 1.5), magnetic fields outside of last closed flux surface or separatrix, meet the material surface at an arbitrary angle. Since the end plates are cutting through the field lines, depending on the type of the end plate material, they can provide a free source of energy into the plasma, driving instabilities.

Where the open field lines meet the conducting material surface, a transition region between the end plate and plasma will be formed. In the special case where the magnetic field is perpendicular with respect to an absorbing wall e.g. in CSDX, the plasma-wall transition consists of two subregions (see Fig. 1.6): the Debye sheath, and a collisional pre-sheath[Sta00]. The Debye sheath is a small region adjacent to the wall, generally several Debye lengths long, and has a net positive charge ($n_i > n_e$) that shields

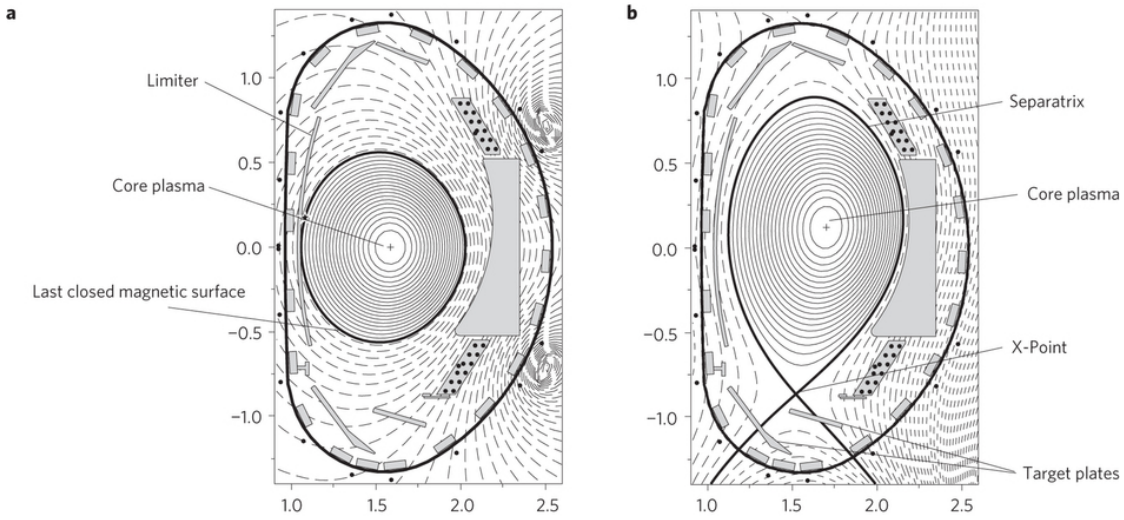

Figure 1.5: Schematic of (a) limiter, and (b) divertor tokamak configuration[OKWZ16].

the negative charge on the wall. The sheath does not completely shield the negative wall, however, and a small electric field penetrates into the main plasma (the ambipolar field), which mostly serves to accelerate the cold ions toward the wall, and slightly retard the electrons before entering the sheath. In the main plasma the quasi-neutrality ($n_e = n_i$) holds.

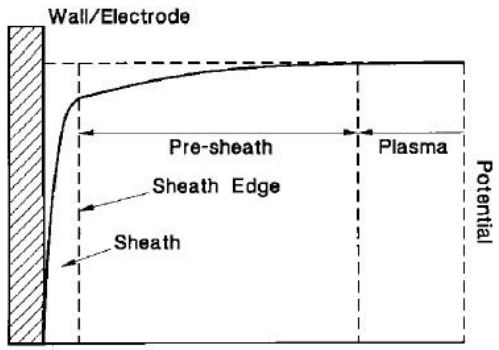

Figure 1.6: Schematics of Debye sheath and collisional pre-sheath of typical plasma near the end plate.

The ions gets accelerated through the Debye sheath, reaching about the ion sound speed (c_s) at the sheath entrance[Sta00]. This potential difference across the sheath

reflects slow electrons that enter the sheath. The electrons approximately maintain a cutoff Maxwellian velocity distribution throughout the sheath, and at the wall, their velocity is retarded by a Boltzmann factor due to the potential difference[LRT11]. In that setting, the total parallel current toward the end plate in the absence of secondary electron emissions from ion and electron bombardment is,

$$j_{\parallel_{sh}} = \pm e n_0 c_s \left[1 - \exp\left(\Lambda - \frac{e(\phi - \phi_w)}{T_e} \right) \right], \tag{1.12}$$

where ϕ_w is the wall potential, $\Lambda = \log \sqrt{m_e/2\pi m_i}$ is the sheath factor, and the $\pm$ sign indicates the different directions of plasma current to the wall for the different end plates.

The finite parallel current and potential at the sheath entrance could essentially tap in free sources of energy into the bulk of plasma. The typical sheath-driven instabilities due to the presence of conducting end plate configuration includes sheath-driven electron temperature gradient instability (also known as conducting wall modes), and KH modes generated by sheath-driven equilibrium $E \times B$. We briefly discuss them in the following sections.

Sheath-driven Electron Temperature Gradient Instability

In an unbiased grounded and conducting endplate $\phi_w = 0$, and when there is no equilibrium current drive along the magnetic field, the perturbation of parallel current can be written as

$$\tilde{j}_{\parallel_{sh}} = \pm e n_0 c_s \left(\frac{e\tilde{\phi}}{T_{e_0}} - \Lambda \frac{\tilde{T}_e}{T_{e_0}} \right). \tag{1.13}$$

Conductive walls trigger a linear instability in presence of electron temperature gradient. The physics of this instability is actually of the drift wave variety, but unlike the drift-waves, the pressure-potential coupling mechanism is through the sheath boundary

rather than adiabatic response. A very simple dispersion relation[BCR$^+$93] can be found by axially integrating the current conservation equation,

$$\frac{en}{\Omega_{c_i}B}\frac{\partial\nabla_\perp^2\tilde{\phi}}{\partial t}L_z = 2\tilde{j}_{\parallel_{sh}}, \tag{1.14}$$

and using it in an electron temperature fluctuations equation (neglecting direct axial net loss),

$$\frac{\partial\tilde{T}_e}{\partial t}L_z + \tilde{\mathbf{v}}_{\perp_e}\cdot\nabla T_{e_0} = 0. \tag{1.15}$$

resulting in dispersion relation,

$$\omega^2 + i\frac{b}{a^2}\omega + i\frac{c}{a} = 0, \tag{1.16}$$

where $a = k_y L_{T_e}$, $b = \frac{\Omega_{c_i} m_i L_z}{c_s T_{e_0} L_{T_e}^2}$, $c = \frac{\Omega_{c_i}\Lambda L_z}{c_s}$, and $L_{T_e} = \frac{d\ln T_{e_0}}{dr}$. Like the drift-wave dispersion relation, ω is complex where a branch of ω is always positive imaginary and unstable.

Sheath-driven Kelvin Helmholtz Instability

Moreover, since the equilibrium parallel current is vanishing, for a grounded conducting end plate ($\phi_w = 0$), the zeroth order approximation of Eqn. 1.12 for the sheath entrance reads as

$$\phi_0 = \Lambda T_0. \tag{1.17}$$

If there is zeroth order electron temperature gradient, the addition of a potential gradient (resulting in a corresponding $\mathbf{E}_0\times\mathbf{B} = -\nabla\phi_0\times\mathbf{B}$ flow profile) cause another linear instability at the sheath entrance. The Kelvin Helmholtz (KH) instability, which is a fluid instability, as opposed to a plasma-specific instability, is a 2D instability and is

caused by the radial gradient of the $E \times B$ velocity.

The KH instability is a convective vorticity instability[HTK87], meaning it can be described by the simple vorticity equation,

$$\frac{\partial \Omega}{\partial t} = -\mathbf{v} \cdot \nabla \Omega. \tag{1.18}$$

The physical process can be explained as follow. Imagine a boundary layer separating two flows that have equal speeds but velocities going in different directions. Since the vorticity is just the curl of the velocity, this boundary layer is a vortex sheet. Now a sinusoidal vorticity perturbation on this sheet causes a sinusoidal ripple in the elevation of the sheet. This ripple brings parts of the sheet into regions where the background flow is positive and other parts of the sheet into regions where the flow is negative. The vorticity on the sheet is then advected by this background flow in such a way that it reinforces the initial sinusoidal vorticity perturbation, thus causing instability[Fri13].

Usually, KH modes are damped in a system with strong magnetic shear[Bur97]. However, in weak magnetic shear SOL, or in CSDX where the magnetic shear is absent, this instability can be an important source of turbulence drive.

1.2 Dissertation Outline

This dissertation presents the results of numerical plasma turbulence studies of the CSDX linear plasma device. This thesis is structured by first deriving the equations, numerical implementation, and verification of a minimal fluid model of the CSDX experimental conditions. Most previous CSDX experiments are studied with anodized insulating end plates, however, a few dedicated CSDX experiments incorporated grounded conducting end plate conditions. Hence, in Chapter 2 a set of suitable reduced equations

from general two-fluid Braginskii formula with proper boundary conditions is derived to describe the instabilities and turbulence observed in the experiment. The model then implemented numerically, and the solutions are verified with analytical expectations. In Chapter 3, the linear and nonlinear physics of end plate boundary conditions on the turbulence is studied, and compared with the previous experimental and simulation results. The turbulence in tokamak SOL can be influenced because of the end plate configurations. Hence, the puzzling question of the impact of boundary conditions on the turbulence is pursued as the first avenue of this thesis in Chapter 3.

The initial results of verification and physics study performed in Chapters 2-3, yet lead to another question of goodness of model in capturing the experimental measurements. Hence, as the second focus of this thesis, the validity of this model in reproducing the experimental results for the insulating boundary case are studied in Chapter 4. The quantitative validation study of turbulence models have always been an important and challenging task in both fluid and plasma turbulence communities. Linear sensitivity of model to the input uncertainties is discussed, followed by extensive validation study of nonlinear simulation results. In the validation process, the impact of synthetic diagnostics on the simulation results is investigated. The validation study of conducting boundary condition simulation is discussed in Appendix A.

Another important question in the validation study of turbulence simulation is the uncertainty quantification due to the presence of experimental measurement uncertainties. Thus, the third focus in this thesis is a study of advanced uncertainty quantification and seed sampling methods presented in Chpater 5, with application to plasma turbulence simulations.

In the end, the findings of this work is summarized, and possible future avenues of study for continuation of this work is proposed in Chapter 6.

Furthermore, previous experimental studies in CSDX had indicated a transition

from the coherent modes at low magnetic fields to a state of broadband turbulence at higher magnetic fields. At the same time, by increasing the magnetic field further, the turbulence in the CSDX goes through changes that lead to steepening of mean density and ion pressure profiles, onset of strong $E \times B$ sheared flows, reduction of turbulence, and reduction in turbulent radial particle transport. Thus, the preliminary simulations of this magnetic field scan is reported in Appendix B of this dissertation to assess how much of these physics can be captured by the minimal collisional drift-wave model, as basis for future investigations. The code setup and its details is discussed in Appendix C, to enable and facilitate the reproduction of results in future works.

Chapter 2

Model Derivation and Verification Studies

In a general description, the plasma can be described by the distribution function $f_s(\mathbf{x},\mathbf{v},t)$ of each species in the phase space. The plasma behavior can be described by kinetic equations, which evolves the distribution function of species,

$$\frac{\partial f_s}{\partial t}+\mathbf{v}\cdot\nabla f_s+\frac{e_s}{m_s}(\mathbf{E}+\mathbf{v}\times\mathbf{B})\cdot\frac{\partial f_s}{\partial \mathbf{v}}=\left(\frac{\partial f_s}{\partial t}\right)_C. \tag{2.1}$$

where $\left(\frac{\partial f_s}{\partial t}\right)_C$ is the collisional operator. In the hot plasma, where the plasma is nearly collisionless, the collisional operator can be dropped, resulting in Vlasov equation. However, the dominant collisions in a plasma are Coulomb collisions, and the collision term takes the form of the Fokker-Planck operator. Solving the Fokker-Planck equation numerically for problems that require time intervals too much larger than the electron-cyclotron time is computationally expensive[FBC+16].

Therefore, model reduction up to some certain approximation is necessary for the feasibility of computational time. In the CSDX highly collisional regimes where

the electron mean free path is much smaller than the parallel lengthscale $\lambda_{mfp,e}/L_z \sim \mathcal{O}(10^{-2})$, the kinetic effects are negligible and plasma can be approximated through fluid equations by integrating the distribution moments in the velocity space. The fluid equations are derived by taking moments of the Fokker-Planck equation to create coupled equations of the independent variables, density n_s, velocity $\mathbf{v}_s$, and temperature T_s[Bra65]. Braginskii two-fluid equations[Bra65] for plasma species can describe the general plasma fluid behavior:

$$\frac{\partial n_e}{\partial t} + \mathbf{v}\cdot\nabla n_e + \nabla\cdot(n_e\mathbf{v}) = 0 \tag{2.2}$$

$$m_e n_e \frac{\partial \mathbf{v}}{\partial t} + m_e n_e \mathbf{v}\cdot\nabla\mathbf{v} + \nabla p_e + \nabla\cdot\Pi_e + e n_e(\mathbf{E}+\mathbf{v}\times\mathbf{B}) = \mathbf{R_e} \tag{2.3}$$

$$\frac{3}{2}\frac{\partial p_e}{\partial t} + \frac{3}{2}\mathbf{v}\cdot\nabla p_e + \frac{5}{2}p_e\nabla\cdot\mathbf{v} + \Pi_e : \nabla\mathbf{v} + \nabla\cdot\mathbf{q_e} = W_e \tag{2.4}$$

$$\frac{\partial n_i}{\partial t} + \mathbf{u}\cdot\nabla n_i + \nabla\cdot(n_i\mathbf{u}) = 0 \tag{2.5}$$

$$m_i n_i \frac{\partial \mathbf{u}}{\partial t} + m_i n_i \mathbf{u}\cdot\nabla\mathbf{u} + \nabla p_i + \nabla\cdot\Pi_i - e n_i(\mathbf{E}+\mathbf{u}\times\mathbf{B}) = \mathbf{R_i} \tag{2.6}$$

$$\frac{3}{2}\frac{\partial p_i}{\partial t} + \frac{3}{2}\mathbf{u}\cdot\nabla p_i + \frac{5}{2}p_i\nabla\cdot\mathbf{u} + \Pi_i : \nabla\mathbf{u} + \nabla\cdot\mathbf{q_i} = W_i \tag{2.7}$$

in which, $\mathbf{u}$ is ion velocity, $\mathbf{v}$ is electron velocity, Π is the viscosity tensor, $\mathbf{R}$ is momentum exchange between species (ion-electrons, ion-neutrals, etc.) and W is the energy transfer between different species.

2.1 Derivation of Nonlocal Drift-Reduced Cold-Ion Fluid Model

To simplify the Braginskii equations further to an even more reduced model, several ordering assumptions motivated by the CSDX experimental conditions are used.

Since $\Omega_{c_i}\tau_i \sim \mathscr{O}(10^{-1})$ in the CSDX ($\Omega_{c_i} = eB/m_i c$ is the ion cyclotron frequency and $\tau_i = 1/\nu_{ii}$ is the ion-ion collision frequency), a standard two-Laguerre-polynomial Chapman-Enskog closure scheme[Bra65] is used,

$$\mathbf{R_e} = \frac{ne\mathbf{j}}{\sigma_\parallel} - 0.71n\nabla T_e \tag{2.8}$$

$$\mathbf{R_i} = -\mathbf{R_e} - n_i m_i \nu_{in}\mathbf{u} \tag{2.9}$$

$$W_i = \frac{3m_e}{m_i}\frac{n(T_e - T_i)}{\tau_e} \tag{2.10}$$

$$W_e = -W_i + \frac{\mathbf{j}\cdot\mathbf{R}}{ne} = -\frac{3m_e}{m_i}\frac{n(T_e - T_i)}{\tau_e} + \frac{j^2}{\sigma_\parallel} - 0.71\frac{\mathbf{j}\cdot\nabla Te}{e} \tag{2.11}$$

where, $\mathbf{j} = ne(\mathbf{u} - \mathbf{v})$ is net plasma current, and $\sigma_\parallel = 1.96ne^2\tau_e/m_e$ is electrical conductivity.

Assuming plasma quasi-neutrality ($n_e \approx n_i \approx n$) valid for $k\lambda_D \ll 1$ and having cold ions in CSDX $T_i/T_e \sim \mathscr{O}(10^{-1})$, the ion temperature equation and ion density equation can be dropped. Moreover, in this thesis the parallel component of ion momentum equation is neglected, and its effects on the turbulence deferred to a future study.

For electron density equation, defining $E \times B$ drift velocity as $\mathbf{v_E} = -\frac{1}{B_0}\nabla\phi \times \hat{z}$, the electron density (Eqn. 2.2) as,

$$\frac{\partial n}{\partial t} + \mathbf{v_E}\cdot\nabla_\perp n + \mathbf{v}_\parallel\cdot\nabla_\parallel n + n\nabla\cdot\mathbf{v_E} + n\nabla_\parallel v_\parallel = 0. \tag{2.12}$$

Assuming density homogeneity along magnetic field, and replacing $v_\parallel = u_\parallel - j_\parallel/ne$, and neglecting ion parallel velocity, and adding a perpendicular density diffusion sink as $D_n\nabla_\perp^2 n$ where $D_n \propto \rho_s^2/\tau_e$ (ρ_s is the electron gyroradius and τ_e is electron collision

frequency), the above equation reads as,

$$\frac{\partial n}{\partial t} + \mathbf{v_E} \cdot \nabla_\perp n + n\nabla \cdot \mathbf{v_E} = \frac{\nabla_\parallel j_\parallel}{e} + D_n \nabla_\perp^2 n. \tag{2.13}$$

The next step is to obtain a relation for parallel current density from electron momentum (parallel component of Eqn. 2.3). Assuming electron inertia and electron-electron viscosity terms are negligible compared to other terms, the equation reads as

$$0 + \nabla p_e + 0 + en\left(-\nabla\phi + \mathbf{v} \times \mathbf{B}\right) = en\frac{\mathbf{j}}{\sigma_\parallel} - 0.71n\nabla_\parallel T_e. \tag{2.14}$$

Applying $p_e = nT_e$, along the magnetic field, the equation can be rewritten as

$$j_\parallel = \sigma_\parallel \left(\frac{1.71}{e}\nabla_\parallel T_e + \frac{T_e}{en}\nabla_\parallel n - \nabla_\parallel \phi\right). \tag{2.15}$$

From the perpendicular momentum equations and current density equation ($\nabla \cdot \mathbf{j} = 0$), one can derive the vorticity equation, where the current is $\mathbf{j} = j_\parallel \hat{z} + en(\mathbf{u}_\perp - \mathbf{v}_\perp)$. In collisional drift-wave, the parallel current is primarily carried by the light electrons, while the perpendicular current is primarily carried by the ions, because electron inertia is much smaller than ions $\omega/\Omega_{c_e} \ll \omega/\Omega_{c_i}$ (dropping electron polarization effect respect to ion polarization). Thus, the equation simplifies to,

$$-\nabla_\perp \cdot (en\mathbf{u}_\perp) = \nabla_\parallel j_\parallel. \tag{2.16}$$

The perpendicular ion component of above equation can be obtained from Eqn. 2.6. By solving for the ion velocity in the Lorentz force term, the perpendicular ions

velocity has four terms,

$$\mathbf{u}_\perp = \mathbf{u}_{\mathbf{E}\times\mathbf{B}} + \mathbf{u}_{\mathbf{pol}} + \mathbf{u}_{\mathbf{vis}} + \mathbf{u}_{\mathbf{in}}$$
$$= -\frac{\nabla\phi\times\hat{z}}{B_0} - \frac{m_i}{eB_0^2}\frac{\partial\nabla_\perp\phi}{\partial t} - \frac{m_i}{eB_0^2}\mathbf{v}_\mathbf{E}\cdot\nabla\left(\nabla_\perp\phi\right) + \mu_\perp\frac{m_i}{eB_0^2}\nabla_\perp^2\left(\nabla_\perp\phi\right) - \nu_{in}\frac{m_i}{eB_0^2}\left(\nabla_\perp\phi\right). \tag{2.17}$$

in which since the magnetization factor $X = \Omega_{c_i}\tau_i \approx 1$ in CSDX, the $\mu_\perp$ ion-ion viscosity needs to be approximated with generalized viscosity formula[Bra65],

$$\mu_\perp = v_{th_i}^2\tau_i\frac{2.23 + 1.2(2X)^2}{2.33 + 4.03(2X)^2 + (2X)^4} \tag{2.18}$$

Thus, by combining the Eqns. 2.16-2.17, we can obtain the plasma potential vorticity equation. Since $\nabla_\perp\cdot\hat{z}\times\nabla_\perp$ operator vanishes, and the plasma potential vorticity equation reads as,

$$\frac{m_i}{B_0^2}\frac{\partial\Omega}{\partial t} + \frac{m_i}{B_0^2}\nabla_\perp\cdot\left(n\mathbf{v}_\mathbf{E}\cdot\nabla_\perp(\nabla_\perp\phi)\right) = \nabla_\parallel j_\parallel + \mu_\perp\frac{m_i}{B_0^2}\nabla_\perp\cdot\left(n\nabla_\perp^2(\nabla_\perp\phi)\right) - \nu_{in}\frac{m_i}{B_0^2}\Omega. \tag{2.19}$$

At this point, we make two additional approximations to make solving the equation easier numerically: One in the advection term where we are taking density into the divergence (called Boussinesq approximation) and other is the viscosity term which we are simply approximating with the laplacian of generalized vorticity,

$$\frac{m_i}{B_0^2}\frac{\partial\Omega}{\partial t} + \frac{m_i}{B_0^2}\mathbf{v}_\mathbf{E}\cdot\nabla\Omega = \nabla_\parallel j_\parallel + \mu_\perp\frac{m_i}{B_0^2}\nabla_\perp^2\Omega - \nu_{in}\frac{m_i}{B_0^2}\Omega, \tag{2.20}$$

where $\Omega = \nabla_\perp\cdot(n\nabla_\perp\phi)$ is the generalized potential vorticity. Note that the density is radially varying on a scale comparable to the gyroradius $\rho_s/L_n \leq \mathcal{O}(1)$, hence the nonlocality effects must be preserved and density cannot be taken out of the divergence.

Here, nonlocality refers to the effects of keeping the density term inside the perpendicular divergence and retaining the radial variation of profiles across the radii.

For the electron energy equation, in the limit of $\Omega_{c_i}\tau_i < 1$ we have $\mathbf{q_e} = -\kappa_\parallel^e \nabla T_e - 0.71 Te\mathbf{j}/e$ where $\kappa_\parallel^e = 3.16 n T_e \tau_e / m_e$ is parallel heat conductivity, and hence the electron energy equation reads as,

$$\frac{3}{2}\frac{n\partial T_e}{\partial t} + \frac{3}{2} n\mathbf{v_E}\cdot\nabla T_e + \frac{5}{2} nT_e \nabla\cdot\mathbf{v} - \nabla\cdot\left(0.71\frac{T_e\mathbf{j}_\parallel}{e} + \kappa_\parallel^e \nabla_\parallel^2 T_e\right) = -3\frac{m_e}{m_i}\frac{nT_e}{\tau_e} + \frac{j^2}{\sigma_\parallel} - 0.71\frac{\mathbf{j}_\parallel\cdot\nabla T_e}{e} \tag{2.21}$$

Having $\chi_\parallel^e = \kappa_\parallel^e / n$ and assuming $j_\parallel = -env_{\parallel_e}$ (neglecting parallel ion velocity), dividing the equation by $3n/2$, and simplifying Eqn. 2.21, we will obtain,

$$\frac{\partial T_e}{\partial t} + \mathbf{v_E}\cdot\nabla T_e + T_e\nabla\cdot\mathbf{v} = \frac{2}{3}1.71\frac{T_e}{n}\frac{\nabla_\parallel j_\parallel}{e} + \chi_\parallel^e \nabla_\parallel^2 T_e - 2\frac{m_e}{m_i}\frac{T_e}{\tau_e} + \frac{2}{3}\frac{j^2}{n\sigma_\parallel} \tag{2.22}$$

For better usage of derived equations, the equations are normalized to the typical range of plasma parameters in the CSDX experiments. Considering $\bar{n}$ as maximum density, $\bar{T}_e$ as maximum electron temperature, B_0 as axial magnetic field, and a as plasma column radius, we can define reference values as $\Omega_{ci} = e_0 B_0/m_i$, $c_s = \sqrt{e_0\bar{T}_e/m_i}$, $\rho_s = c_s/\Omega_{ci}$. With can write as $\hat{n} = n/\bar{n}$, $\hat{\phi} = e\phi/\bar{T}_e$, $\hat{T}_e = T_e/\bar{T}_e$, $\hat{t} = c_s t/a$, $\hat{r} = r/\rho_s$, $\hat{\partial}_r = \rho_s\partial_r$, $\hat{z} = z/a$, $\hat{\nabla}_\parallel = a\nabla_\parallel$, $\hat{\nabla}_\perp = \rho_s\nabla_\perp$, $\hat{\mu}_\perp = \mu_\perp/(\rho_s^2 c_s/a)$, $\hat{D}_n = D_n/(\rho_s^2 c_s/a)$, $\hat{\chi}_\perp^e = \chi_\perp^e/(\rho_s^2 c_s/a)$, $\hat{\chi}_\parallel^e = \chi_\parallel^e/(ac_s)$, $\hat{j}_\parallel = j_\parallel/e\bar{n}c_s$, $\hat{\tau}_e = c_s\tau_e/a$, and $\hat{\Omega} = \Omega/(\bar{n}\bar{T}_e/e\rho_s^2)$. By definition $\bar{n} = n(r=0)$, and $\bar{T}_e = T_e(r=0)$ are the reference values of on-axis density and electron temperature respectively.

Therefore, normalized equations will take form of,

$$\frac{\partial\hat{n}}{\partial\hat{t}} - \frac{a}{\rho_s}\left(\nabla\hat{\phi}\times\hat{z}\right)\cdot\hat{\nabla}_\perp\hat{n} - \frac{a}{\rho_s}\hat{n}\hat{\nabla}\cdot\left(\nabla\hat{\phi}\times\hat{z}\right) = \hat{\nabla}_\parallel\hat{j}_\parallel + \hat{D}_n\hat{\nabla}_\perp^2\hat{n}, \tag{2.23}$$

$$\frac{\partial \hat{\Omega}}{\partial \hat{t}} - \frac{a}{\rho_s}\left(\nabla\hat{\phi}\times\hat{z}\right)\cdot\hat{\nabla}_\perp\hat{\Omega} = \hat{\nabla}_\parallel\hat{j}_\parallel + \hat{\mu}_\perp\hat{\nabla}_\perp^2\hat{\Omega} - \hat{\nu}_{in}\hat{\Omega}; \qquad \hat{\Omega} = \hat{\nabla}_\perp\cdot\left(\hat{n}\hat{\nabla}_\perp\hat{\phi}\right), \quad (2.24)$$

$$\frac{\partial \hat{T}_e}{\partial \hat{t}} - \frac{a}{\rho_s}\left(\nabla\hat{\phi}\times\hat{z}\right)\cdot\hat{\nabla}_\perp\hat{T}_e - \frac{a}{\rho_s}\hat{T}_e\hat{\nabla}\cdot\left(\nabla\hat{\phi}\times\hat{z}\right) = \frac{2}{3}1.71\frac{\hat{T}_e}{\hat{n}}\hat{\nabla}_\parallel\hat{j}_\parallel + \hat{\chi}_\parallel^e\hat{\nabla}_\parallel^2\hat{T}_e - \frac{2}{0.51}\hat{\eta}\hat{T}_e + \frac{2}{3}\hat{\eta}\hat{j}_\parallel^2, \quad (2.25)$$

$$\hat{j}_\parallel = \frac{1}{\hat{\eta}}\left(1.71\hat{n}\hat{\nabla}_\parallel\hat{T}_e + \hat{T}_e\hat{\nabla}_\parallel\hat{n} - \hat{n}\hat{\nabla}_\parallel\hat{\phi}\right), \quad (2.26)$$

where $\hat{\eta} = m_e a/1.96 m_i c_s \tau_e$ is the normalized resistivity. For the rest of the thesis, $\hat{(..)}$ notations will be dropped, and all equations are assumed in normalized units, unless otherwise noted.

To solve the equations, two different approaches can be taken. One approach is to solve the full equations with self-consistent profiles, with no experimental profile input, and solve the equations by specifying realistic sources, sinks, and boundary conditions, which are difficult (or impossible) to measure. At the time of writing this thesis, there is no experimental measurement of helicon source power deposition into the plasma. An alternative approach, is to implement a small fluctuations assumption[Pop01] to separate all variables into time-independent equilibrium parts and time-dependent fluctuating parts so that experimental time-independent profiles can be used as the driving force of instabilities. Moreover, the small fluctuations assumption considers the amplitude of first order fluctuations is much smaller than zeroth order equilibriums. The second approach is equivalent to the so-called δf approach used in gyrokinetic simulations of the core plasma[CW03].

Decomposing the total evolving variables into zeroth order radial dependent equilibrium and first order fluctuations, we can approximate total density as $n = n_0 + \tilde{n}$, total potential as $\phi = \phi_0 + \tilde{\phi}$, and total electron electron temperature as $T_e = T_{e_0} + \tilde{T}_{e_0}$. In which, 0 subscript denotes zeroth order equilibrium, and tilde superscript denotes

first-order fluctuation. Thus, the purturbation of Eqns. 2.23-2.26 can be rewritten as

$$\frac{\partial \tilde{n}}{\partial t} - \frac{a}{\rho_s}\frac{\partial n_0}{\partial r}\frac{\partial \tilde{\phi}}{\partial \theta} + \frac{a}{\rho_s}\frac{\partial \phi_0}{\partial r}\frac{\partial \tilde{n}}{\partial \theta} = \nabla_{\parallel}\tilde{j}_{\parallel} + D_n\nabla_{\perp}^2\tilde{n} + \frac{a}{\rho_s}\{\tilde{\phi},\tilde{n}\} + S_n, \tag{2.27}$$

$$\begin{aligned}\frac{\partial \tilde{\Omega}}{\partial t} - \frac{a}{\rho_s}\frac{\partial \Omega_0}{\partial r}\frac{\partial \tilde{\phi}}{\partial \theta} + \frac{a}{\rho_s}\frac{\partial \phi_0}{\partial r}\frac{\partial \tilde{\Omega}}{\partial \theta} + \frac{a}{\rho_s}\frac{1}{r}\frac{\partial \phi_0}{\partial r}\left(\frac{\partial n_0}{\partial r}\frac{\partial^2\tilde{\phi}}{\partial r\partial\theta} - \frac{\partial^2\phi_0}{\partial r^2}\frac{\partial \tilde{n}}{\partial \theta}\right) \\ = \nabla_{\parallel}\tilde{j}_{\parallel} + \mu_{\perp}\nabla_{\perp}^2\tilde{\Omega} - \nu_{in}\tilde{\Omega} + \frac{a}{\rho_s}\{\tilde{\phi},\tilde{\Omega}\}; \qquad \tilde{\Omega} = \nabla_{\perp}\cdot\left(n_0\nabla_{\perp}\tilde{\phi}\right),\end{aligned} \tag{2.28}$$

$$\frac{\partial \tilde{T}_e}{\partial t} - \frac{a}{\rho_s}\frac{\partial T_{e_0}}{\partial r}\frac{\partial \tilde{\phi}}{\partial \theta} + \frac{a}{\rho_s}\frac{\partial \phi_0}{\partial r}\frac{\partial \tilde{T}_e}{\partial \theta} = \frac{2}{3}1.71\frac{T_{e_0}}{n_0}\nabla_{\parallel}\tilde{j}_{\parallel} + \chi_{\parallel}^e\nabla_{\parallel}^2\tilde{T}_e + \frac{a}{\rho_s}\{\tilde{\phi},\tilde{T}_e\} + S_{T_e}, \tag{2.29}$$

$$\tilde{j}_{\parallel} = \frac{1}{\eta}\left(1.71 n_0\nabla_{\parallel}\tilde{T}_e + T_{e_0}\nabla_{\parallel}\tilde{n} - n_0\nabla_{\parallel}\tilde{\phi}\right) \tag{2.30}$$

where $\{\tilde{f},\tilde{g}\} = \frac{1}{r}(\partial_r\tilde{f}\partial_\theta\tilde{g} - \partial_\theta\tilde{g}\partial_r\tilde{f})$ is the Poisson bracket term, containing second order advective nonlinearity. For the vorticity bracket a Bouusinesq approximation has been applied for simplicity of numerical implementation. Moreover, second order Ohmic heating $\frac{2}{3}\eta\tilde{j}_{\parallel}^2$ is neglected, and the $-\frac{2}{0.51}\eta\tilde{T}_e$ term is dropped since it is obtained to be an order of magnitude smaller than the other terms for the CSDX parameters. Note that in a small perturbation approach, to sustain the turbulence saturation, sources need to be added to the equations (shown in the equations as S_n and S_{T_e}), otherwise the steady zonal density and electron temperature will suppress equilibriums, causing the relaxation in the turbulence.

Because we do not know the exact deposition profiles of these sources, or other processes such as ionization and recombination rates, we prescribed the equilibrium density and temperature profiles in our simulation to match experimental equilibrium measurements, and then damp out the zonal density and temperature components to prevent quasilinear relaxation or flattening of the profiles. This is a typical approach in both fluid plasma simulation[CW03, Hol16].

Since the CSDX helicon source acts as a particle (via ionization) and heat source to the plasma without any apparent momentum source, the particle source $S_n = -\nu_s \tilde{n}_Z$ and heat source $S_{T_e} = -\nu_s \tilde{T}_{e_Z}$ are added to Eqn. 2.27 and Eqn. 2.30, respectively. Here the Z subscript denotes the axially and azimuthally averaged zonal component of a fluctuating field or quantity, e.g. $\tilde{f}_Z = \iint \tilde{f} d\theta dz / \iint d\theta dz$, and ν_s denotes the damping rate of zonal component. In this setting, the mean profiles are then the sum of the equilibrium and time averaged zonal profiles, e.g. $f_{mean} = f_0 + \langle \tilde{f}_Z \rangle$. Hence, in the fixed-gradient approach, simulations use ad-hoc density and temperature sources ($S_n = -\nu_s \tilde{n}_Z$ and $S_{T_e} = -\nu_s \tilde{T}_{e_Z}$ terms) in order to keep the equilibrium profiles from relaxing away from their experimental shapes. These terms damp zonal average of density and electron temperature at each time step. The verification and convergence check of the source terms in the model is discussed in Chapter 2.4.4.

2.2 Boundary Conditions

The experimental studies of plasma turbulence in CSDX device has been done with both insulating and conducting end plates. Experimentally in the CSDX, it has been observed the choice of boundary condition affects the turbulence[CTXM$^+$13]. Hence, it is important to choose the right boundary conditions for the initial value solver.

The simulation is performed in cylindrical coordinates, using an annular domain with infinitesimal inner radius (1% of outer radius) to avoid the numerical singularity at the axis. Dirichlet boundary conditions ($\tilde{f} = 0$) have been used for evolving fluctuation properties at the outer radial boundary, while Neumann boundary conditions ($\partial \tilde{f} / \partial r = 0$) have been applied to evolve fluctuations at the inner radial boundary. Here for simplicity, at outer radii it is assumed the fluctuations vanish at the edge of plasma column, and for the inner radii even symmetry of cylindrical geometry is considered. The axial boundary

condition for insulating or conducting endplate is non-trivial. For a perfect insulating endplate, the fluctuations of potential, electron temperature and the parallel current at the sheath vanish. However, in a conducting plate the current as electron heat flux is allowed to escape the system through out the end plates. In this section, derivation of plasma sheath entrance boundary conditions in the presence of the insulating and conducting end plates are derived and discussed.

When the magnetic field is perpendicular to an absorbing wall, there is no magnetic presheath and the plasma-wall transition will consist of two regions between main bulk plasma and the wall: first a Debye sheath which is in contact with the wall, and a collisional presheath in between Debye sheath and unaffected plasma[Sta00]. The Debye sheath is where the recombination with the wall occurs, and has a size proportional to the Debye Length (λ_D) and both the quasi-neutrality and the ion-drift approximations break down in this region. The collisional presheath size usually scales with λ_{mfp} and is quasi-neutral, and in it the ions are magnetized and accelerated towards the wall, reaching approximately the plasma sound speed c_s at the sheath entrance.

Since our fluid model is quasi-neutral and uses the ion-drift approximation, the boundary values at the sheath entrance must be found. In order to describe steady-state dynamics of collisional presheath, the procedure used by [LRHJ12] is followed, to derive a rigorous system of equations including ion continuity, ion and electron parallel momentum, and electron temperature equations valid in the collisional presheath region.

2.2.1 Conducting Endplate Boundary Condition

We start by deriving the boundary condition for a conducting endplate, where the electrical and heat conductivity of sheath is very large.

The steady-state continuity equation for ions is

$$\nabla \cdot (n\mathbf{v}_i) = S_{p_i}, \tag{2.31}$$

where S_{p_i} contains other ionization and recombination processes. We can rewrite the dimensionless equation as

$$v_{\|_i}\partial_\| n + n\partial_\| v_{\|_i} + \left(-\frac{1}{r}\partial_\theta\phi\right)\partial_r n + n\frac{1}{r}\partial_r\left(r\left(-\frac{1}{r}\partial_\theta\phi\right)\right) + n\frac{1}{r}\partial_\theta\partial_r\phi + \partial_r\phi\frac{1}{r}\partial_\theta n = S_{p_i}. \tag{2.32}$$

The fourth and fifth terms cancel out each other in above equation. Since equilibrium gradients at the radial boundaries are vanishing in our experiment (See. Fig. 1d), we can omit the third and sixth terms in above equation up to first order expansion, therefore we can further simplify the equation,

$$v_{\|_i}\partial_\| n + n\partial_\| v_{\|_i} = S_{p_i}. \tag{2.33}$$

Now let us consider parallel component of ion momentum equation,

$$n\frac{d}{dt}v_{\|_i} - enE = S_{m_{\|_i}}. \tag{2.34}$$

Thus, in the electrostatic limit the equation reduces to

$$nv_{\|_i}\partial_\| v_{\|_i} + n\partial_\|\phi = S_{m_{\|_i}}. \tag{2.35}$$

Turning to the parallel component of electron momentum,

$$n\frac{d}{dt}v_{\parallel_e} + enE + \nabla_\parallel P_e = \frac{j_\parallel}{\sigma_\parallel} - 0.71n\nabla_\parallel T_e + S_{m_{\parallel_e}},$$

by assuming negligible electron inertia and high conductivity, the equation reduces to

$$-n\partial_\parallel \phi + 1.71n\partial_\parallel T_e + T_e\partial_\parallel n = S_{m_{\parallel_e}}. \tag{2.36}$$

Inclusion of non-isothermal electrons requires use of the electron heat equation. By assuming very large electron heat conductivity at sheath entrance, and neglecting inertia and diffusion, and omitting the transverse terms, the electron heat equation reads as,

$$\frac{2}{3}1.71T_e n\nabla_\parallel v_{\parallel_e} - \frac{2}{3}0.71T_e n\nabla_\parallel v_{\parallel_i} - \frac{2}{3}0.71T_e\left(v_{\parallel_i} - v_{\parallel_e}\right)\nabla_\parallel n = S_{T_e}.$$

Thus,

$$\frac{2}{3}0.71T_e\left(v_{\parallel_i} - v_{\parallel_e}\right)\partial_\parallel n + \frac{2}{3}0.71T_e n\partial_\parallel v_{\parallel_i} - \frac{2}{3}1.71T_e n\left(\partial_\phi v_{\parallel_e}\right)\partial_\parallel \phi - \frac{2}{3}1.71T_e n\left(\partial_{T_e} v_{\parallel_e}\right)\partial_\parallel T_e = S_{T_e}. \tag{2.37}$$

We can rewrite the system of equations (Eqns. 2.33, 2.35, 2.36 and 2.37) in vector

form $\mathbb{M}\mathbf{X} = \mathbf{S}$,

$$\begin{bmatrix} v_{\parallel_i} & n & 0 & 0 \\ 0 & nv_{\parallel_i} & n & 0 \\ T_e & 0 & -n & 1.71n \\ \frac{2}{3}0.71T_e\left(v_{\parallel_i} - v_{\parallel_e}\right) & \frac{2}{3}0.71T_e n & -\frac{2}{3}1.71T_e n\left(\partial_\phi v_{\parallel_e}\right) & -\frac{2}{3}1.71T_e n\left(\partial_{T_e} v_{\parallel_e}\right) \end{bmatrix} \times \begin{bmatrix} \partial_\parallel n \\ \partial_\parallel v_{\parallel_i} \\ \partial_\parallel \phi \\ \partial_\parallel T_e \end{bmatrix} = \begin{bmatrix} S_{p_i} \\ S_{m_{\parallel_i}} \\ S_{m_{\parallel_e}} \\ S_{T_e} \end{bmatrix}. \quad (2.38)$$

Note that all variables are total values (zeroth order plus fluctuations). Assuming source/sink terms do not affect axial gradients in the presheath region (i.e. assuming $|\mathbb{M}_{ij}\mathbf{X}_j| \gg |\mathbf{S}_j|$), we can solve for $\det(\mathbb{M}) = 0$, obtaining the value of ion parallel velocity at sheath entrance as

$$v_{\parallel_i} = c_s \sqrt{\frac{1 + \frac{2}{3}1.71(\frac{v_{\parallel_e}}{T_e}\partial_{T_e} v_{\parallel_e} - 0.71)}{1 + \frac{2}{3}1.71(\frac{v_{\parallel_e}}{T_e}\partial_{T_e} v_{\parallel_e} + 1.71\frac{v_{\parallel_e}}{T_e}\partial_\phi v_{\parallel_e})}}. \quad (2.39)$$

To obtain the parallel electron velocity at the sheath entrance, we use the Boltzmann relation and ambipolarity of electron flux between sheath entrance and the wall, and we assume $\lambda_D \gg \rho_e$ such that electrons stay magnetized all the way to the wall. This relation is not strictly true for the CSDX parameters, but for simplicity we will use this assumption.

Assuming Maxwellian electrons in the sheath, we can write Boltzmann relation for electrons between sheath entrance and wall,

$$n_e = n_{e_w} \exp\left(\frac{e(\phi_w - \phi)}{T_e}\right)$$

Where n_e and ϕ are the electron density and potential at the sheath entrance, and n_{e_w} and ϕ_w are the electron density and potential at the wall respectively. By assuming grounded wall ($\phi_w = 0$) and also assuming electrons hit the wall with their thermal velocity, the parallel electron velocity can be obtained through flux ambipolarity between sheath entrance and wall as

$$v_{\|_e} = \frac{n_{e_w} v_{th_e}}{n_e} = v_{th_e} \exp\left(\frac{-e\phi}{T_e}\right) = c_s \exp\left(\Lambda - \frac{e\phi}{T_e}\right), \tag{2.40}$$

in which $\Lambda = \log\sqrt{m_e/2\pi m_i}$ is the sheath factor, and for Argon gas $\Lambda_{Ar} = 5.1$[Sta00]. Therefore, we can obtain closure terms needed in Eqn. 2.39 as,

$$\partial_{T_e} v_{\|_e} = \frac{T_e}{v_{\|_e}}(0.5+\Lambda); \qquad \partial_\phi v_{\|_e} = -\frac{T_e}{v_{\|_e}}.$$

Using these closures for Argon gas, the ion parallel velocity (Eqn. 2.39) reduces to,

$$v_{\|_i} \approx 1.1 c_s.$$

The possibility $v_{\|_i} > c_s$ at the sheath entrance is discussed by [LRT11]. Hence, the axial electron temperature gradient and potential gradient at the sheath edge are given as

$$\partial_\| T_e = \frac{1 + 0.71\left(1 - c_s^2/v_{\|_i}^2\right)}{\frac{3}{2} + 1.71(0.5+\Lambda)} \partial_\| \phi \approx 0.11 \partial_\| \phi \approx 0.$$

We can see that the ion parallel velocity is near the sound speed, and $\partial_\| T_e$ is about an order of magnitude is smaller than $\partial_\| \phi$. Therefore, we can neglect electron temperature gradient with respect to other axial gradients at the sheath entrance. This assumption simplifies the set of equations further and we can solve for 3×3 set of

equations instead,

$$\begin{bmatrix} v_{\|_i} & n & 0 \\ 0 & nv_{\|_i} & n \\ T_e & 0 & -n \end{bmatrix} \begin{bmatrix} \partial_\| n \\ \partial_\| v_{\|_i} \\ \partial_\| \phi \end{bmatrix} = 0. \tag{2.41}$$

As a result, one can find axial boundary values of conducting sheath matrix by solving for the determinant and individual equations of Eqn. 2.66, and obtain

$$-n^2 v_{\|_i}^2 + nT_e = 0 \rightarrow v_{\|_i}^2 = T_e \rightarrow v_{\|_i} = \pm\sqrt{T_e} = \pm c_s, \tag{2.42}$$

$$v_{\|_i}\partial_\| n + n\partial_\| v_{\|_i} = 0 \rightarrow \partial_\| n = \mp\frac{n}{c_s}\partial_\| v_{\|_i}, \tag{2.43}$$

$$v_{\|_i}\partial_\| v_{\|_i} + \partial_\| \phi = 0 \rightarrow \partial_\| \phi = \mp c_s \partial_\| v_{\|_i}, \tag{2.44}$$

$$\partial_\| T_e \approx 0, \tag{2.45}$$

$$\Omega = \nabla \times \left(\nabla_\| \phi \times \mathbf{b}\right) \cdot \mathbf{b} = 0, \tag{2.46}$$

$$j_\| = ne\left(v_{\|_i} - v_{\|_e}\right) = \pm nec_s \left[1 - \exp\left(\Lambda - \frac{e\phi}{T_e}\right)\right]. \tag{2.47}$$

To set these axial boundary values with our three-field small perturbation model, we need to break down the total values into equilibrium and fluctuations. From Eqn. 2.47, for the equilibrium part, $j_{\|_0} = 0$ leads to a produce positive equilibrium plasma potentials $\phi_0 = \Lambda T_{e_0}$ in the absence of external biasing or edge flows. Since in our formulation of the model we assumes no axial variation of equilibrium profiles, we need to enforce the equilibrium potential profile throughout domain, which can then drive KH and rotational instability generated by the sheath-driven equilibrium $E \times B$ shear associated with the a $\phi_0 = \Lambda T_{e_0}$ profile. Also, in our 3-field model we assumed negligible fluctuation of ion parallel velocity everywhere ($\tilde{v}_{\|_i} = 0$). Hence, the axial boundary conditions of

fluctuations in normalized units reduce to Bohm-like condition,

$$\partial_{\parallel}\tilde{n} = \partial_{\parallel}\tilde{\phi} = \partial_{\parallel}\tilde{T}_e = 0; \tilde{\Omega} = 0; \tilde{j}_{\parallel} = \pm\left(\tilde{\phi} - \Lambda\tilde{T}_e\right). \tag{2.48}$$

We will use Eqn. 2.48 for axial boundary condition of conducting sheath in our simulations.

2.2.2 Perfect Insulating Endplate Boundary Condition

In general, solving for the boundary condition with finite wall resistivity requires the knowledge of the potential drop in the sheath region which implies the use of general kinetic description of the plasma[Loi13]. However, in the case of perfect insulating endplate, we can approximate some boundary values for drift-reduced fluid models, without the need for solving plasma distribution in each time-step. The perfect heat insulator assumption also may not be strictly true for CSDX experimental condition, but for the simplicity will consider the perfect insulating endplate in anodized experiments of CSDX. In a perfect electrical and heat insulator endplate, the time averaged parallel current ($\tilde{j}_{\parallel}$) and parallel electron heat flux ($\tilde{q}_e$) to the wall must vanish.

Unlike an unbiased grounded conducting endplate, an insulator can develop an arbitrary wall potential,

$$nec_s\left[1 - \exp\left(\Lambda - \frac{e(\phi_w - \phi)}{T_e}\right)\right] = 0.$$

The insulating wall potential (ϕ_w) self-consistently develops over time to set the equilibrium parallel current to zero. In addition, for zero parallel current fluctuations,

$$\tilde{j}_{\parallel} = \tilde{\phi} - \Lambda\tilde{T}_e = 0. \tag{2.49}$$

On the other hand, a general parallel electron heat flux equation is described by many such as [XRD93]. The heat flux fluctuations with no secondary emission, normalized to our reference values, can be written as

$$\tilde{q}_e = \tilde{T}_e + \tilde{\phi} = 0. \tag{2.50}$$

As a result, from Eqns. 2.49-2.50, one can approximate both fluctuations of $\tilde{\phi}$ and $\tilde{T}_e$ are negligible at the boundary. Therefore, we set the boundary condition for perfect insulating simulation as follow,

$$\partial_{\|}\tilde{n} = 0; \tilde{\phi} = \tilde{T}_e = \tilde{\Omega} = \tilde{j}_{\|} = 0. \tag{2.51}$$

We should note that the above derivation of boundary conditions is for a perfect conductor or perfect insulator, while neglecting equilibrium ion parallel velocity effects. For an endplate with finite resistivity, obtaining boundary conditions is much more complicated, and is not developed in this thesis.

2.3 Numerical Implementation

The model's equations are solved in the BOUT++ Boundary Turbulence plasma fluid framework, which is an object-oriented finite difference framework for fluid and plasma simulations in curvilinear geometry written in C++[DUX$^+$09]. The code has been developed at LNLL and University of York, and is parallelized to utilize up to thousands of coses. BOUT++ is an initial value solver, with boundary conditions applied at each time step. For our model, the code evolves three fluctuations $\tilde{n}$, $\tilde{\Omega}$, and $\tilde{T}_e$, by calculating the right hand side of the equations using prescribed equilibrium profiles and transport coefficients, and then applies a time integration scheme to find the next

time-step values of the evolving variables.

The derivatives, except for Poisson bracket terms, in the radial and axial directions are performed with a standard fourth order central finite-difference scheme, and in the azimuthal direction, a Fast Fourier Transform is used. In this setting, for instance first and second order derivatives of radial direction are calculated as

$$\frac{\partial f_i}{\partial x} = \frac{-f_{i+2} + 8f_{i+1} - 8j_{i-1} + f_{i-2}}{12\Delta x} + \mathscr{O}(\Delta x^4), \tag{2.52}$$

$$\frac{\partial^2 f_i}{\partial x^2} = \frac{-f_{i+2} + 16f_{i+1} - 30f_i + 16j_{i-1} - f_{i-2}}{12\Delta x} + \mathscr{O}(\Delta x^4). \tag{2.53}$$

For the parallel gradient operators, a quasi-staggered method has been used to prevent grid-sized oscillations on top of the solution that are called grid modes. These spurious modes are the cause of "red-black" numerical instability in neutral fluid simulations[Bew08]. In such cases, at the Nyquist parallel wavenumber ($k_\parallel = \pi/\Delta z$ where Δz is parallel grid spacing), the second parallel derivative may become zero which is unphysical. To remedy such an numerical instability, use of staggered grid has been suggested[PUCF10a]. However, since implementation of staggered grids with parallel computation can become cumbersome, therefore to avoid such unphysical behavior, we can calculate evolving variables $\tilde{n}$, $\tilde{\phi}$, $\tilde{\Omega}$, $\tilde{T}_e$ at grid points, while calculating $\tilde{j}_\parallel$ values at grid points shifted by $\Delta z/2$. The parallel current derivative and potential derivative are discretized similar to the approach by [PUCF10a],

$$\frac{\partial \tilde{j}_\parallel}{\partial z} = \frac{\tilde{j}_{\parallel,k} - \tilde{j}_{\parallel,k-1}}{\Delta z}, \qquad \frac{\partial \tilde{\phi}}{\partial z} = \frac{\tilde{\phi}_{k+1} - \tilde{\phi}_k}{\Delta z}. \tag{2.54}$$

where $k_\parallel^2$ does not become zero for any supported mode by the grid $-\pi/\Delta z \leq k \leq \pi/\Delta z$.

Moreover, for nonlinear advection terms in the Poisson brackets, the Arakawa discretization[AL81] is implemented. The Arakawa scheme has the advantage of conserving energy and vorticity, as expected from advection terms, and since the scheme

is completely explicit, it is easy to implement and code. Thus, Poisson brackets can be calculated as

$$\begin{aligned}\{f,g\} = -\frac{1}{12h^2}[&(g_{i,j-1}+g_{i+1,j-1}-g_{i,j+1}-g_{i+1,j+1})(f_{i+1,j}-f_{i,j})\\ &-(g_{i-1,j-1}+g_{i,j-1}-g_{i-1,j+1}-g_{i,j+1})(f_{i-1,j}-f_{i,j})\\ &+(g_{i+1,j}+g_{i+1,j+1}-g_{i-1,j}-g_{i-1,j+1})(f_{i,j+1}-f_{i,j})\\ &-(g_{i+1,j}+g_{i+1,j+1}-g_{i-1,j}-g_{i-1,j})(f_{i,j-1}-f_{i,j})\\ &+(g_{i+1,j}-g_{i,j+1})(f_{i+1,j+1}+f_{i,j})\\ &-(g_{i,j-1}-g_{i-1,j})(f_{i-1,j-1}+f_{i,j})\\ &+(g_{i,j+1}-g_{i-1,j})(f_{i-1,j+1}+f_{i,j})\\ &-(g_{i+1,j}-g_{i,j-1})(f_{i+1,j-1}+f_{i,j})].\end{aligned} \tag{2.55}$$

Note that the Arakawa scheme does not necessarily conserve positivity, which is required from simple advection equation ($\partial_t A + \mathbf{v}\cdot\nabla A = 0$). The deficiency of this finite difference advection scheme can be explained in a simple setting. When A becomes very small it produces a local minima where its zero gradient prevents a further decrease of the variable. However, in the finite difference this gradient may not exactly represent the the zero gradient at local minima. Nevertheless, in our case of nonlocal simulations, we have conserved positivity using Arakawa scheme by using sufficient radial and azimuthal resolution, as the fluctuations amplitudes fairly remain small compare to the mean profile in CSDX experiments. The sensitivity analysis on the convergence of simulation results with respect to grid resolution is performed as a part of the code verification studies and is discussed in detail in Chapter 2.4.3. Other higher order schemes such as Third order WENO (WENO3) or Fifth order Suresh-Huynh Limiters (SuHu) scheme maybe needed for simulating high fluctuation amplitude experiments e.g. as found in tokamak

SOL[PH13].

Last but not least, the PVODE (Parallel Variable Ordinary Differential Equation solver) solver[BH99] is used for time integration, which combines a Backward Difference Formula with a preconditioned Generalized Minimal Residual (GMRES) method. PVODE is a parallel solver that can solve stiff and non-stiff ODE initial value problems. For stiff problems, where explicit schemes such as Rounge-Kutta can be inefficient to use, PVODE implements implicit Backward Difference Formula (BDF). This approach approximates u at time n as

$$u_n = \sum_{i=1}^{q} \alpha_{n-i} u_{n-i} + h_n \beta_0 f_n. \tag{2.56}$$

where $f_n \equiv f(u_n, t_n)$, h_n is the time step at time n, q is the order of BDF formula, and α_{n-i} and β_0 are coefficients determined by the order of the BDF using a Taylor series assumption. Since f_n is unknown, PVODE uses a Newton formula to approximate it as

$$f_n = f_{n-1} + \frac{\partial f}{\partial u}(u_n - u_{n-1}). \tag{2.57}$$

where $\frac{\partial f}{\partial u} \equiv J$ is the Jacobian of f. Therefore, Eqn. can be written as

$$(1 - h_n \beta_0 J) u_n = \sum_{i=1}^{q} \alpha_{n-i} u_{n-i} + h_n \beta_0 f_{n-1} - h_n \beta_0 J u_{n-1}. \tag{2.58}$$

PVODE in addition implements adaptive time step adjustment to met its designated error tolerance. A detailed description of the procedure of PVODE solver can be found in [BH99].

2.4 Code Verification

Before studying the physics of a model implemented in the code, or compare any simulations with the experiment, it is important to verify the code. Usually the question "Does a code solve the model equations correctly?", which refers to the verification process, comes before the question "Does a model have the right equations?" which refers to the validation process. These concerns in any computational simulation of a physical phenomena, give rise to the Verification and Validation (V&V) process[Hol16]. Many of the differential operators used in BOUT++ framework have been verified[DMO$^+$16] through method of manufactured solutions (MMS). Additional linear and nonlinear verification tests of the specific model implementation described above are detailed in the rest of this Chapter, with model validation studies are explored in Chapter 4.

2.4.1 Linear Growth Rates Verification

The growth rates of the collisional drift-wave instability, and the sheath-imposed electron temperature gradient instability, in the linear local limit can be obtained analytically by solving their dispersion relations. In the local limit, the equilibrium density and temperature are taken to be radially constant and equal to their on-axis values, and the equilibrium density and temperature gradients taken to be independent parameters which are also radially uniform, and solving for Eqns. 2.27-2.30 in the linear limit. In the local linear limit, the simplest collisonal drift-wave instability equations (including diffusion and ion-neutral drag terms) can be written as

$$\frac{\partial \tilde{n}}{\partial t} - \frac{a}{\rho_s}\left(\nabla\tilde{\phi}\times\hat{z}\right)\cdot\nabla_\perp \ln n_0 = \frac{1}{\eta}\nabla_\parallel^2\left(\tilde{n}-\tilde{\phi}\right) + D_n\nabla_\perp^2\tilde{n}, \tag{2.59}$$

$$\frac{\partial \tilde{\Omega}}{\partial t} = \frac{1}{\eta}\nabla_\parallel^2\left(\tilde{n}-\tilde{\phi}\right) + \mu_\perp\nabla_\perp^2\tilde{\Omega} - \nu_{in}\tilde{\Omega}; \qquad \tilde{\Omega} = \nabla_\perp^2\tilde{\phi}. \tag{2.60}$$

For constant coefficients acting on the perturbation terms, an analytical linear dispersion relation assuming solution in form of $n(r,\theta,z,t) = n(r)\exp(ik_\theta\theta + ik_\parallel z - i\omega t)$ can be driven easily for an azimuthally and axially periodic system, by solving the eigenvalues equation of the matrix,

$$\begin{bmatrix} -i\omega + k_\parallel^2/\eta + D_n k_\perp^2 & i(a/\rho_s)\partial_r \ln n_0/rk_\theta + k_\parallel^2/\eta \\ -k_\parallel^2/\eta & -i\omega k_\perp^2 + k_\parallel^2/\eta + \mu_\perp k_\perp^4 - \nu_{in}k_\perp^2 \end{bmatrix} \begin{bmatrix} \tilde{n} \\ \tilde{\phi} \end{bmatrix} = 0.$$

where in this special case $k_\perp$s correspond to zeros of the Bessel functions for cylinder geometry. Thus, the dispersion relation in this case can be written as,

$$\begin{aligned} &\omega^2 + i\omega\left(\frac{k_\parallel}{\eta k_\perp^2} + k_\perp^2(\mu_\perp - D_n) - \nu_{in}\right) \\ &+D_n k_\perp^2\left(\frac{k_\parallel^2}{\eta} + \mu_\perp k_\perp^4 - \nu_{in}k_\perp^2\right) + \frac{k_\parallel^2}{\eta}\left(\frac{k_\parallel^2}{\eta} + i\left(\frac{a}{\rho_s}\right)\partial_r \ln n_0 k_\theta\right) = 0 \end{aligned} \tag{2.61}$$

After solving the second order dispersion relation, the imaginary part of ω corresponds to linear growth rates, and real part of ω is the real frequency of the mode. Now, we can cross check and verify the validity of our linear initial value code against analytical growth rates and real frequency from the dispersion relation. The linear growth rates (frequencies) of the eigenmodes in the code have been obtained by calculating imaginary (real) part of $\partial \ln \tilde{\phi}_m/\partial t$ after convergence in BOUT++ initial value solver, where m denotes the azimuthal mode number.

In Fig. 2.1, they linear growth rates and frequencies of the local linear run from BOUT++ is compared against the dispersion relation solution. We observe that the numerical solution agrees with the analytical growth rates and linear frequencies of the unstable modes. Note that the initial value solvers are not capable of capturing the stable linear modes, as the numerical values of fluctuations hit the magnitude of truncation

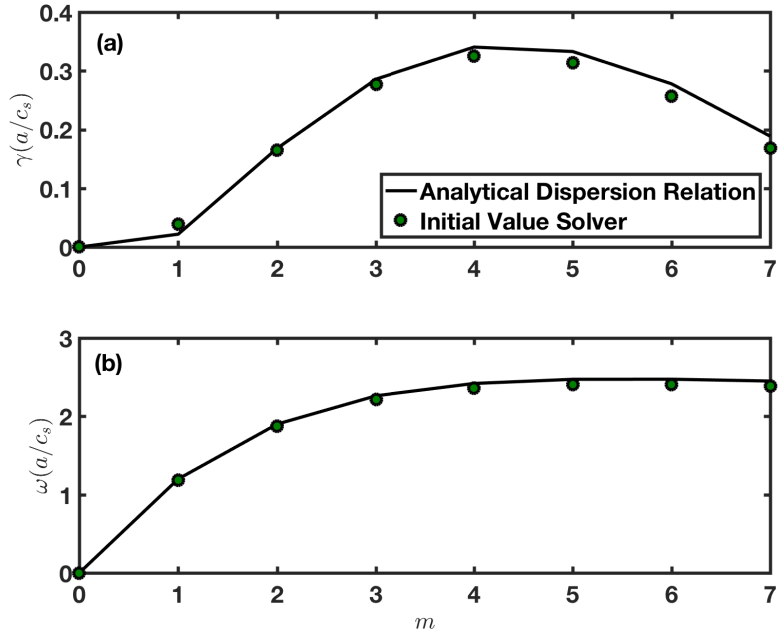

Figure 2.1: Linear (a) growth rate and (b) frequency of drift-wave instability for both analytical dispersion relation (black line) and initial value solver (green dots).

errors in computers after multiple time steps.

The dispersion relation of sheath-imposed electron temperature gradient instability in a field-line integrated setting can also be obtained analytically, and can be driven by isolating effects of density gradient drift-waves,

$$\frac{\partial \nabla_{\perp}^2 \tilde{\phi}}{\partial t} = \nabla_{\parallel} \tilde{j}_{\parallel} \tag{2.62}$$

$$\frac{\partial \tilde{T}_e}{\partial t} = \frac{a}{\rho_s}\frac{1}{r}\frac{\partial \ln T_{e_0}}{\partial r}\frac{\partial \tilde{\phi}}{\partial \theta} + \frac{2}{3}1.71\nabla_{\parallel}\tilde{j}_{\parallel} \tag{2.63}$$

Having $L_{T_e} = (d\ln T_0/dr)^{-1}$, $\tilde{j}_{\parallel}(z=L) = +\left(\tilde{\phi} - \Lambda\tilde{T}_e\right)$ and $\tilde{j}_{\parallel}(z=0) = -\left(\tilde{\phi} - \Lambda\tilde{T}_e\right)$ for the axial boundary of conducting end plate sheath entrance, and integrating the equa-

tions along the magnetic field, one can obtain

$$\frac{\partial \nabla_\perp^2 \tilde{\phi}}{\partial t}\frac{L_z}{a} = \tilde{j}_\parallel(z=L) - \tilde{j}_\parallel(z=0) = 2\left(\tilde{\phi} - \Lambda\tilde{T}_e\right), \tag{2.64}$$

$$\frac{\partial \tilde{T}_e}{\partial t}\frac{L_z}{a} = \frac{a}{\rho_s L_{T_e}}\frac{\partial \tilde{\phi}}{\partial \theta}\frac{L_z}{a} + \frac{2}{3}1.71 \times 2\left(\tilde{\phi} - \Lambda\tilde{T}_e\right). \tag{2.65}$$

Hence, the dispersion relation reads as,

$$\begin{bmatrix} i\omega k_\perp^2 - \frac{2a}{L_z} & \Lambda\frac{2a}{L_z} \\ -\frac{a}{\rho_s L_{T_e}} ik_\theta - \frac{2}{3}1.71\frac{2a}{L_z} & -i\omega + \frac{2}{3}1.71\Lambda\frac{2a}{L_z} \end{bmatrix} \begin{bmatrix} \tilde{\phi} \\ \tilde{T}_e \end{bmatrix} = 0 \tag{2.66}$$

Thus, the dispersion relation in this case reads as,

$$\omega^2 + i\frac{\omega}{k_\perp^2}\left(1 - \frac{2}{3}1.71\Lambda\left(\frac{2a}{L_z}\right)\right) - i\frac{k_\theta}{k_\perp^2}\frac{1}{L_{T_e}}\frac{a}{\rho_s}\left(\frac{2a}{L_z}\right) = 0 \tag{2.67}$$

Like the drift-wave dispersion relation, ω values can be compared against the initial value solver results. In the initial value solver, 3D equations are being solved. However, to find the growth rate, the $\tilde{\phi}$ is axially integrated, before finding temporal variations of its modes. The analytical dispersion relation solution and BOUT++ linear growth rates and frequencies are compared in Fig. 2.2, and again a very good accuracy for the unstable modes are obtained in the initial value solver.

2.4.2 Linear and Nonlinear Energy Balance Verification

The energy balance of the code in both the case of linear growing modes and nonlinearly saturating mode can be investigated by formulating the energy balance of model equations. The energy balance equation can be obtained by multiplying Eqn. 2.27-2.29 by $T_{e_0}\tilde{n}/n_0$, $-\tilde{\phi}$, and $3n_0\tilde{T}_e/2T_{e_0}$ respectively, so that sum of energy equations

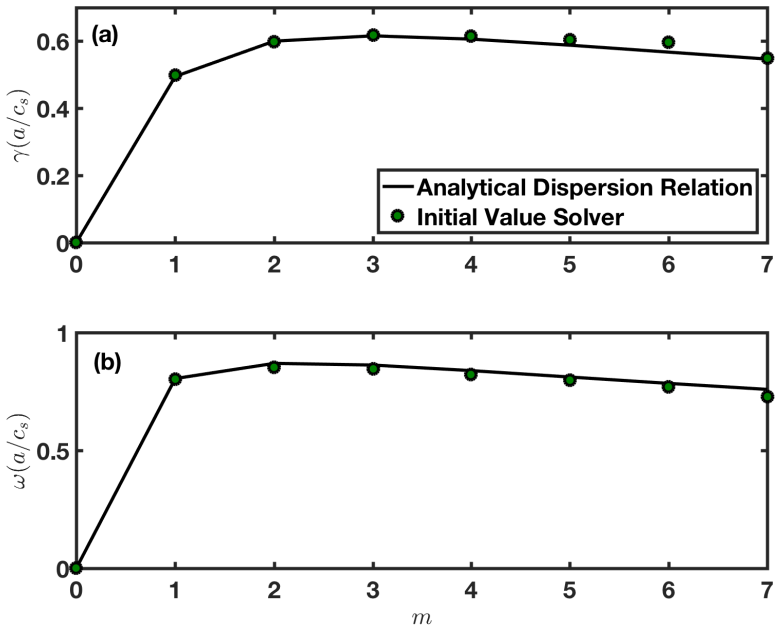

Figure 2.2: Linear (a) growth rate and (b) frequency of sheath-imposed electron temperature gradient instability for both analytical dispersion relation (black line) and initial value solver (green dots).

conserve the adiabatic response. The total energy balance equation, reads as

$$\frac{\partial \ln(E_{tot})}{\partial t} = S_n + S_{T_e} + S_{KH} + S_{rot} + S_{j_\parallel} + S_\perp + S_{drag} + S_{\chi_\parallel^e} + S_{source} + S_{adv}. \quad (2.68)$$

The equation is normalized to the instantaneous total energy of system $E_{tot} = \frac{1}{2}(\langle \frac{T_{e_0}}{n_0}\tilde{n}^2\rangle + \langle n_0(\nabla_\perp\tilde{\phi})^2\rangle + \frac{3}{2}\langle \frac{n_0}{T_{e_0}}\tilde{T}_e^2\rangle)$, where $S_n = -\frac{a}{\rho_s}\langle T_{e_0}\partial_r \ln(n_0)\tilde{n}\tilde{v}_r\rangle/E_{tot}$ is the extraction of energy from the equilibrium density gradient, $S_{T_e} = -\frac{a}{\rho_s}\langle \frac{3}{2}n_0\partial_r \ln(T_{e_0})\tilde{T}_e\tilde{v}_r\rangle/E_{tot}$ is the linear energy extraction from the equilibrium electron temperature gradient, $S_{KH} = \frac{a}{\rho_s}\langle \frac{1}{r}\partial_r\phi_0\tilde{\phi}\partial_\theta\tilde{\Omega}\rangle/E_{tot}$ is the KH energy extraction, and $S_{rot} = \frac{a}{\rho_s}\langle \frac{1}{r}\tilde{\phi}\partial_r\phi_0(\partial_r n_0\partial_{r\theta}^2\tilde{\phi} - \partial_{rr}^2\phi_0\partial_\theta\tilde{n})\rangle/E_{tot}$ is the energy extraction through rotational (centrifugal) modes. $S_{j_\parallel} = -\langle \frac{\eta_\parallel}{n_0}\tilde{j}_\parallel^2\rangle + \langle \nabla_\parallel(\frac{T_{e_0}}{n_0}\tilde{n}\tilde{j}_\parallel + 1.71\tilde{T}_e\tilde{j}_\parallel - \tilde{\phi}\tilde{j}_\parallel)\rangle/E_{tot}$ is the parallel current energy sink in which the first term is parallel resistive dissipation and the second term is due to sheath

losses, $S_\perp = -\mu_\perp \langle \tilde{\phi} \nabla_\perp^2 \tilde{\Omega} \rangle / E_{tot} + D_n \langle \frac{T_{e_0}}{n_0} \tilde{n} \nabla_\perp^2 \tilde{n} \rangle / E_{tot} + D_{T_e} \langle \frac{3n_0}{2T_{e_0}} \tilde{T}_e \nabla_\perp^2 \tilde{T}_e \rangle / E_{tot}$ is the perpendicular energy dissipation rate, $S_{drag} = \langle \nu_{in} \tilde{\phi} \tilde{\Omega} \rangle / E_{tot}$ is the ion-neutral drag energy dissipation rate, $S_{\chi_\parallel^e} = \langle \frac{3n_0}{2T_{e_0}} \chi_\parallel^e \tilde{T}_e \nabla_\parallel^2 \tilde{T}_e \rangle / E_{tot}$ is the parallel conductivity energy dissipation rate, $S_{source} = \nu_s (\langle \frac{T_{e_0}}{n_0} \tilde{n}_Z^2 \rangle + \langle \frac{3n_0}{2T_{e_0}} \tilde{T}_{eZ}^2 \rangle) / E_{tot}$ is the ad-hoc source energy rate, and $S_{adv} = \langle \frac{T_{e_0}}{n_0} \tilde{n} \tilde{\mathbf{v}} \cdot \nabla_\perp \tilde{n} \rangle / E_{tot} + \langle -\tilde{\phi} \tilde{\mathbf{v}} \cdot \nabla_\perp \tilde{\Omega} \rangle / E_{tot} + \langle \frac{3n_0}{2T_{e_0}} \tilde{T}_e \tilde{\mathbf{v}} \cdot \nabla_\perp \tilde{T}_e \rangle / E_{tot}$ is the energy rate of nonlinear advection terms. The averaging operator $\langle f \rangle = \int dz \int r dr \sum_m f$ denotes a volume average operator, where m is the azimuthal mode number.

The extra factors n_0 and T_{e_0} are added to the energy terms in order to show energy conservation of adiabatic response in Eqn. 2.30. While the physical energy contains extra factors of n_0 and T_{e_0}, the physical energy does not preserve the property of conservative nonlinearities in Eqns. 2.27-2.29, and therefore produces a more complicated analysis[FCU+12]. Therefore, since we are using a nonlocal model and $\nabla_\perp \cdot \frac{T_{e_0}}{n_0}$ is nonzero, we have decided to show conservation of the adiabatic response in our formulation for better understanding of parallel energy conservation. We should also note that terms with $\langle f \partial_\theta f \rangle$ yield zero volume averaged energy due to azimuthal symmetry, hence they are not shown in our calculations.

Here, to verify the energy conservation of the simulation, the energy balance of linear runs with both insulating and conducting end plates, discussed in detail in Chapter 3, is shown in Fig. 2.3.

We observe the curves settle to steady values as the dominant modes establish themselves. The energy conservation error, which can is obtained by subtracting the right hand side of Eqn. 2.68 from the total energy rate of the system, is shown with the dashed line. The energy errors of the linear runs are less than 1% of other energy rates in the system, indicating a good conservation of energy in the system.

By turning on the nonlinear terms in the system (what we denote as the advection terms), the fluctuations will grow in a linear phase regime began to interact and exchange

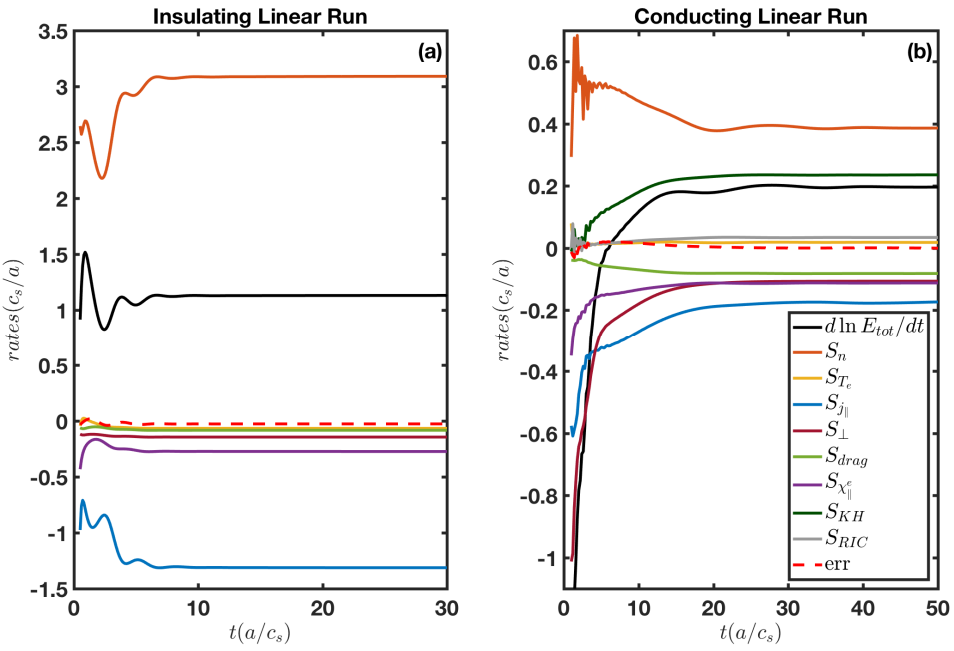

Figure 2.3: Energy balance time traces of (a) the insulating end plate linear run, and (b) the conducting end plate linear run. Dashed lines show time trace of energy balance error.

energy across spatiotemporal scales, eventually saturate where the time averaged total energy rate of the system becomes zero. The conservation of energy in the nonlinear simulations are also been investigated and the results are shown Fig. 2.4. Again, a good conservation of energy (about 1% of system energy rates) in the nonlinear runs are obtained.

Other verification tests on the simulation requires sensitivity scan on the free variables, such as domain resolution, or source damping rates, as discussed in the next two sections.

2.4.3 Domain Sensitivity Analysis

For any finite difference scheme, domain analysis is an essential part of code verification studies. Domain analysis consists of a series of simulation runs with different

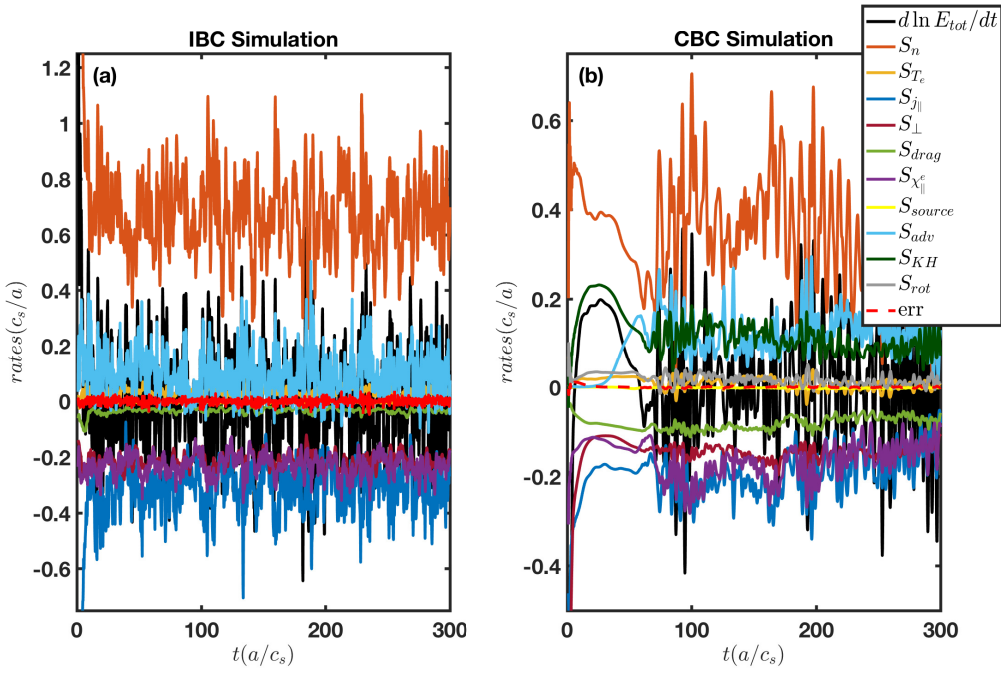

Figure 2.4: Energy balance time traces of (a) the insulating end plate nonlinear simulation, and (b) the conducting end plate nonlinear simulation. Dashed lines show time trace of energy balance error.

grid resolutions. When the results of a specific resolution is statistically similar to the higher resolution, one can claim that the simulation domain has enough grid points to resolve the simulations correctly.

Additional simulations were run to check the convergence of our results with respect to grid resolution. Figs. 2.5 - 2.6 show convergence of mean energy rates (time-averaged in the saturation regime), and diminishing energy error at higher grid resolution. One can observe that the finite difference based nonlinear advection terms are the most susceptible term to grid resolution, and the energy error becomes an order of magnitude smaller than the rest of energy rates for the medium and high resolution simulations. The nonlinear saturation results shown in this thesis are done with grid resolution of $100 \times 128 \times 36$ points. In both set of simulations, the time-averaging window of saturated turbulence ($\tau_{avg} \approx 3ms$) is chosen to be about two orders of magnitude larger than the

auto-correlation timescale ($\tau_c \approx 50\mu s$).

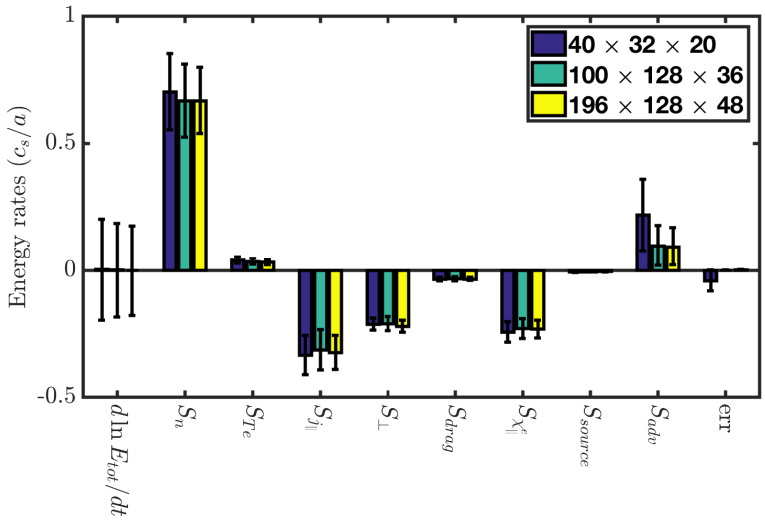

Figure 2.5: Temporal average (shown as bars) and standard deviation (shown as errorbars) of volume averaged energy rates in saturation regime with different grid resolutions ($n_r \times n_\theta \times n_z$) of the insulating end plate simulation.

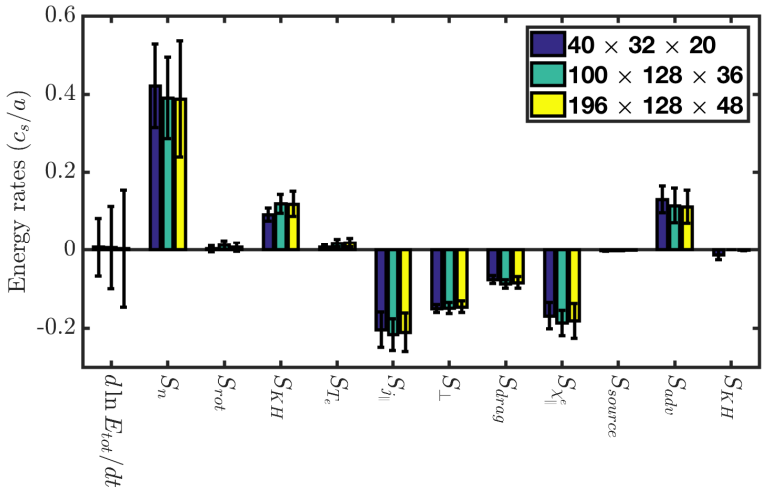

Figure 2.6: Temporal average (shown as bars) and standard deviation (shown as errorbars) of volume averaged energy rates in saturation regime with different grid resolutions ($n_r \times n_\theta \times n_z$) of the conducting end plate simulation.

2.4.4 Ad-hoc Source Sensitivity Analysis

Since detailed measurements or models of the particle and heat source profiles are not available, we apply the ad-hoc damping term to the zonal component of the density and electron temperature fluctuations, so that the total profiles stay close to the equilibrium profiles. Hence, the $S_n = -\nu_s \tilde{n}$ and $S_{T_e} = -\nu_s \tilde{T}_e$ terms effectively act as particle and heat sources to maintain equilibrium profiles and, as a result, the turbulent transport. Fig. 2.7 compares total profiles (sum of equilibrium profile and time averaged zonal component of fluctuations) of density and electron temperature against the input equilibrium profiles. The total profiles of density and electron temperature stay close to initial equilibrium profiles and vary no more than 1% of reference values in the simulations.

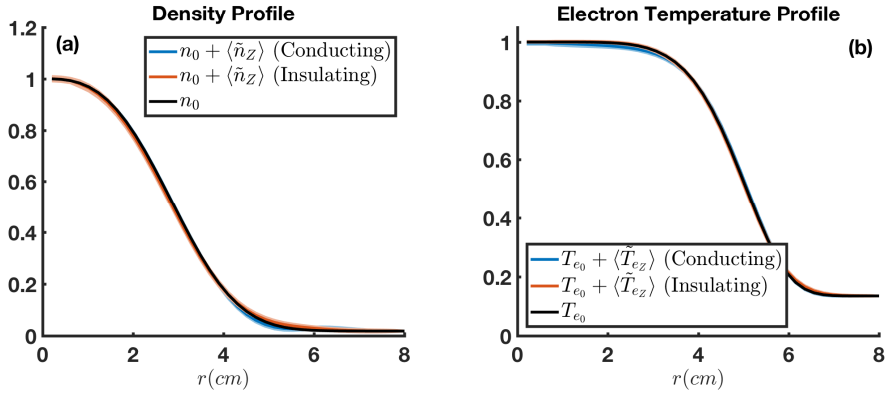

Figure 2.7: Time averaged total profile of (blue) conducting and (red) insulating simulation compared to (black) equilibrium profile for normalized (a) density and (b) electron temperature (case $\nu_s = 2c_s/a$ shown here)

Another way to represent the effect of the source, is to track the zonal density and zonal electron temperature energies (E_{nZ} and E_{T_eZ}). Strong enough damping keep the zonal density and electron temperature energies near zero throughout the saturation, keeping mean density and temperature profiles close to zero. The time evolution of zonal density energies with respect to ν_s is shown in Fig. 2.8, and we can observe that the amount of energy for quasi-flatting of equilibrium gradient is diminishing with stronger

ν_s value.

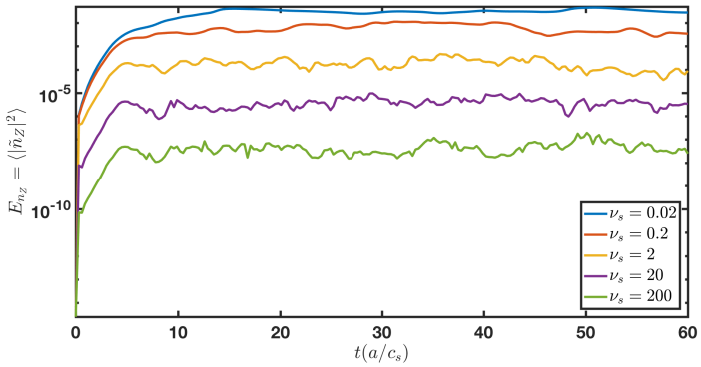

Figure 2.8: Time evolution of zonal density energies with respect to ν_s.

To show the convergence of turbulence properties with respect to this damping parameter, a sensitivity analysis for the ν_s damping coefficient was performed; the results of the scan are shown in Fig. 2.9. The scan shows that the transport properties are influenced by the choice of ν_s below a certain value, and the statistical volume-averaged density and kinetic energy, radial profile of total density, and turbulent particle flux profile converge for about $\nu_s \geqslant O(10^1)c_s/a$. The simulation results shown in this thesis use $\nu_s = 20c_s/a$.

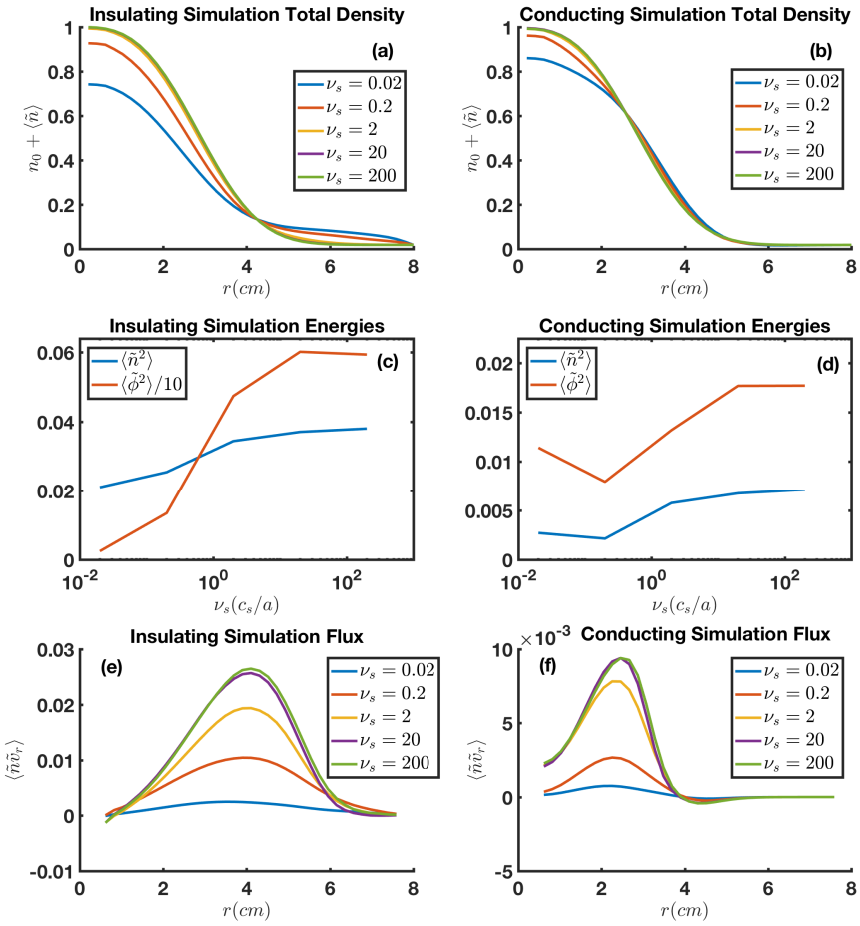

Figure 2.9: Time-averaged total density of (a) Insulating and (b) Conducting end plate simulations versus zonal damping rate. Temporally volume averaged density and kinetic energy of (c) insulating and (d) conducting end plate simulations versus zonal damping rate. (e) Insulating and (f) conducting end plate simulations radial profile of flux versus different zonal damping value.

Chapter 3

Impact of Endplate Boundary Conditions on Turbulence

Edge and Scrape-Off Layer (SOL) turbulence has been a subject of interest in magnetically confined fusion for many decades. It is well-understood that turbulent transport is a major constraint in determining the performance of tokamaks[TFM09]. Many experimental measurements, turbulence modeling, and simulations have tried to understand instabilities and transport in the SOL[ZBG$^+$07, LBC$^+$07, KDM08, RMD$^+$11]. Nevertheless, the complicated geometry of larger toroidal magnetically confined devices makes detailed code-experiment validation studies challenging. Linear plasma devices such as the Controlled Shear Decorrelation Experiment (CSDX) are useful in studying some of the basic underlying physics due to their simple geometry. CSDX inherently operates at low temperature with plasma densities such that collisions are important, similar to the tokamak SOL.

This section aims to build upon the previous CSDX simulations[HTJ$^+$07, DRM$^+$12] by adding new key elements. First, a 3D capability to describe the axial dynamics of turbulence is added, including proper sheath boundary conditions. The choice of proper

boundary conditions is known to be important in the edge simulations[NWG08]. For instance, [RMD09] showed that sheath dissipation can be a sink for momentum transport in the SOL and can thereby affect turbulence levels. Second, these simulations evolve electron temperature fluctuations to enable synthetic diagnostics studies of probes and camera. [MGR$^+$05] report experimental measurements from a low temperature plasma, in which the electron temperature fluctuations are small enough not to affect floating potential measurements significantly. However, simulations by [NRR$^+$12] showed that in higher temperature plasmas, electron temperature fluctuations are more significant and the synthetic floating potential is strongly distorted when compared to the actual plasma potential. Before the work presented here, there has not been much focused simulation study on the effect of T_e fluctuations in low temperature plasmas. Third, unlike previous simulations of CSDX, radially varying plasma profiles and parameters are retained, since micro-turbulence gradient length-scales are comparable to the device length-scale. In this Chapter, we will investigate the physics differences of insulating versus conducting endplate on the operative linear instability and its nonlinear saturation.

3.1 Experimental Condition

Motivated by a desire for a better understanding of magnetized plasma turbulence dynamics, this study of the CSDX linear plasma device aims to define a simple self-regulating description of drift-wave turbulence/zonal flow dynamics[DIIH05]. Previously, CSDX experimental results[BTA$^+$05] showed that the dominant instability in CSDX is the density gradient-driven collisional drift-wave instability. Experimental measurements[XTH$^+$09, XTH$^+$10, MXTT11] showed these modes saturated due to the nonlinear re-distribution of turbulent energy in CSDX via wave-wave coupling and energy transfer to large scale zonal flow without any apparent momentum source.

[CTXM$^+$13] experimentally investigated the effects of changing the endplates from insulating boundary condition (IBC) to the conducting boundary condition (CBC) on the turbulence induced zonal flow. The experiment was conducted by changing the type of endplates while keeping other input parameters such as input gas pressure, magnetic field and source power constant. Equilibrium density, equilibrium electron temperature, and mean plasma potential profiles were measured through RF compensated swept Langmuir probes. In both cases, similar equilibrium profiles of density and electron temperature profiles are measured within error bars (see Fig. 3.3 a-b). Moreover, the CBC case potential profile is dominated by electron temperature profile when the endplate is grounded. However, in the IBC case, the potential of the endplate floats to whatever value necessary to force the parallel current to vanish, resulting in much smaller mean plasma potential gradients (see Fig. 3.3 c). Ion temperature measured using Laser Induced Fluorescence (LIF) technique[CTML$^+$12, TML$^+$12] and neutral gas temperature estimated through high resolution ($10m$) ELIAS spectrometry. The typical values of plasma parameters in the core of CSDX for these experiment are shown in Table 3.1.

Table 3.1: Typical values of CSDX core plasma at $1kG$.

Parameter	Value
Plasma density (n)	$0.9-1\times10^{13}cm^{-3}$
Electron temperature (T_e)	$3.0-3.3eV$
Ion temperature (T_i)	$0.5-0.7eV$
Neutrals temperature (T_g)	$0.4-0.6eV$
Ion sound speed (c_s)	$2.8\times10^5cm/s$
Ion sound Gyroradius ($\rho_s=c_s/\Omega_{c_i}$)	$1.1cm$
Ion-ion viscosity ($\mu_\perp$)	$4.6\times10^3cm^2s^{-1}$
Ion-neutral collision frequency (ν_{in})	$6\times10^3s^{-1}$

Measurements on CSDX show that a change of endplate from CBC to IBC can

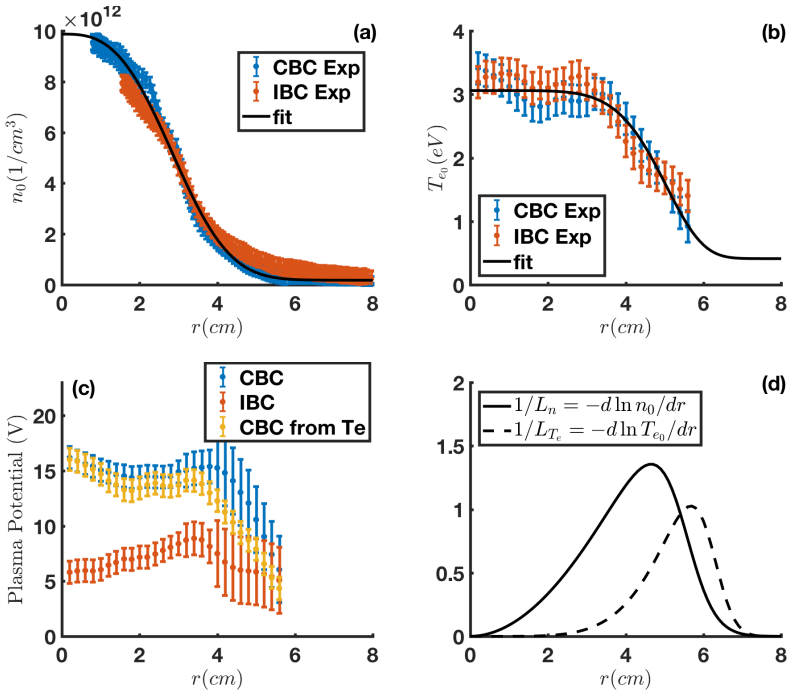

Figure 3.1: Experimentally measured (a) equilibrium density profile (b) equilibrium electron temperature profile, (c) mean plasma potential profile calculated with RF compensated swept probe (red and blue) and potential profile calculated from sheath theory (yellow). Data measured at $B = 1kG$, $P_{rf} = 1500W$, with argon gas pressure of $3.2mTorr$. Data taken from [CTXM$^+$13]. Black line is the fit to the profiles. (d) Radial profiles of inverse gradient lengthscale for the electron density and temperature fits.

affect the turbulence structure, resulting in broadband turbulence in the IBC case and coherent modes in the CBC case (Fig. 3.2). The parallel current induced through sheath driven instability influences the perpendicular momentum balance of conducting case. Fig. 3.3 shows the difference in density fluctuations, floating potential fluctuations and azimuthal flow between IBC and CBC experiments.

Simulations of insulating versus conducting case in this Chapter have been done with the same equilibrium fit (black lines in Fig. 3.3) to equilibrium profiles and plasma parameters (taken from CSDX 1kG CBC experiment) in order to focus our studies of change in the turbulence due to the changes of the boundary condition. In this Chapter, we use drift-reduced nonlocal cold-ion model to explore the sheath loss effects between

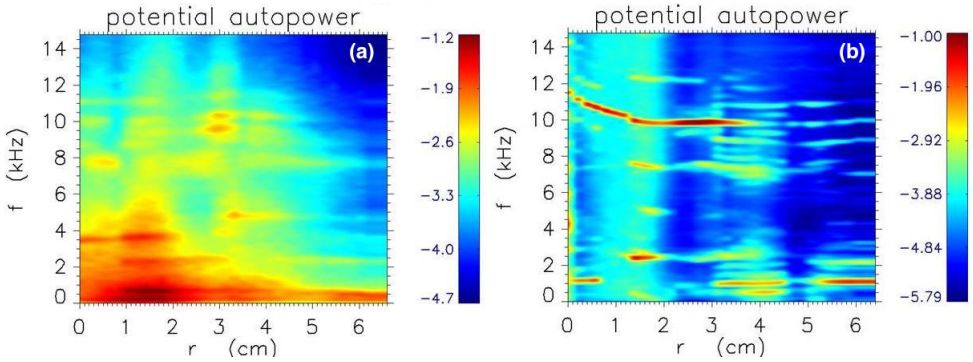

Figure 3.2: Experimental radial profiles of floating potential fluctuations power spectra obtained for $B = 1kG$, $P_{rf} = 1500W$, argon gas pressure of $3.2mTorr$ for (a) the insulating boundary condition and (b) the conducting boundary condition. Reprinted with permission from [CTXM$^+$13].

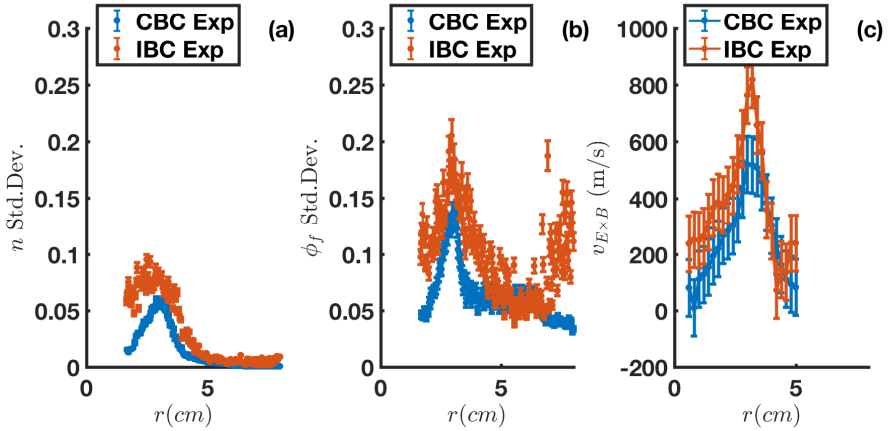

Figure 3.3: (a) Experimental density fluctuation amplitudes normalized to the core density measured with Langmuir probe, (b) experimental floating potential fluctuations normalized to the core electron temperature measured with Langmuir probe, (c) experimental $E \times B$ velocity calculated by subtracting ion diamagnetic velocity from LIF measured azimuthal velocity. Data taken from [CTXM$^+$13].

the two boundary conditions.

In the CSDX experiments, the perpendicular length scales are comparable to the gyroradius. Therefore, it is important to retain the radial variation of profiles. Equilibrium profiles were determined by fitting a general functional form $n_0 = (\bar{n} - n_{base})\exp(-(r/l_n)^{n\alpha}/n_\alpha) + n_{base}$ using the least square method to the measurements taken from experimental conditions[CTXM$^+$13]. The general function fits to the experimental equilibrium profiles are shown in Figs. 3.4(a-b). Plasma parameters, such as the

parallel electron heat conductivity and resistivity then vary radially in a self-consistent manner according to equilibrium density and temperature profile fits, shown in Figs. 3.4a-b. However, the ion-ion viscosity is taken to be radially constant for simplicity of numerical implementation (see red dashed line in Fig. 3.4c). Our calculations show that the radial standard deviation of viscosity away from the mean is less than 20%. To estimate ion-neutral drag in the experiment, by knowing the injected gas pressure at the wall and assuming ideal gas behavior, we can approximate the neutral gas density from neutral gas temperature. Although in general the ion-neutral drag can radially be varying, in this Chapter, we have assumed a radially constant drag $\nu_{in} = 0.17 c_s/a$ (neutral gas drag in the core), and the effects of a radially varying drag profile are deferred to future studies.

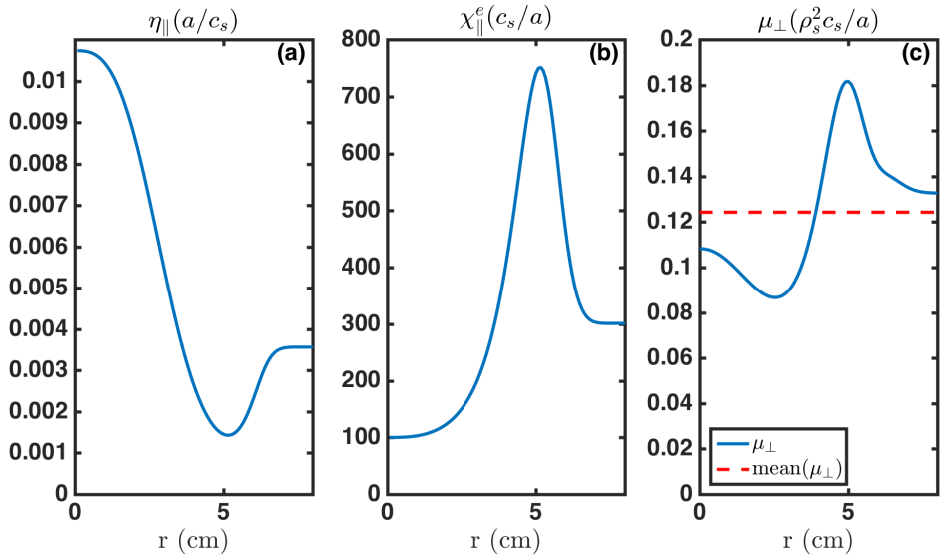

Figure 3.4: Radial profile of (a) resistivity $\eta_{\parallel}$ (b) radial profile of electron heat conductivity $\chi^e_{\parallel}$ (c) radial profile of ion-ion viscosity $\mu_{\perp}$ (radially averaged viscosity shown with red dashed line). Here, $a = 8cm$, $\rho_s = 1.13cm$ and $c_s = 2.8 \times 10^5 cm/s$ as shown in Table 3.1.

3.2 Linear Physics

In this section, we discuss the linear physics of conducting versus insulating endplate simulations. Linearly, the IBC case allows only drift-waves to grow and propagate within the plasma. The dominant instability in the IBC case is the density gradient-driven drift-waves[Yan09]. Electron temperature gradient-driven drift-waves (thermal drift-waves) are also present but is less prominent and usually suppressed via parallel conduction. However, in the CBC case, since the equilibrium plasma potential is locked to the equilibrium electron temperature by the endplate sheath physics, sheath-driven linear transverse Kelvin Helmholtz (KH) instability due to the $-\frac{a}{\rho_s}\frac{1}{r}\frac{\partial\Omega_0}{\partial r}\frac{\partial\tilde{\phi}}{\partial\theta}+\frac{a}{\rho_s}\frac{1}{r}\frac{\partial\phi_0}{\partial r}\frac{\partial\tilde{\Omega}}{\partial\theta}$ term, rotational (centrifugal) modes due to the $\frac{a}{\rho_s}\frac{1}{r}\frac{\partial\phi_0}{\partial r}\left(\frac{\partial n_0}{\partial r}\frac{\partial^2\tilde{\phi}}{\partial r\partial\theta}-\frac{\partial^2\phi_0}{\partial r^2}\frac{\partial\tilde{n}}{\partial\theta}\right)$ term, as well as the sheath-driven electron temperature gradient instability due to non-zero parallel current $\tilde{j}_{\parallel}=\pm(\tilde{\phi}-\Lambda\tilde{T}_e)$ at the sheath boundary, appear in addition to the drift-waves[RR10].

In Fig. 3.5, we show a comparison of the linear growth rate and real frequency versus azimuthal mode number for the local pure drift-wave in the IBC case, the nonlocal pure drift-wave in the IBC case, and nonlocal growth rates of the CBC case. For the nonlocal linear runs, we have solved the Eqns. 2.27-2.30 without nonlinear advection terms, and the equilibrium profiles are taken from Fig. 3.3. However, in the local limit, the equilibrium density and temperature are taken to be radially constant and equal to their on-axis values, and the equilibrium density and temperature gradients taken to be independent parameters which are also radially uniform, and solving for Eqns. 2.27-2.30 in the linear limit. The linear growth rates (frequencies) of the eigenmodes have been obtained by calculating imaginary (real) part of $\partial\ln\tilde{\phi}_m/\partial t$ after convergence in our initial value solver, where m denotes the azimuthal mode number. We observe that inclusion of the global radial profile effects decreases the growth rate, and shifts the linear frequencies,

showing that even in the linear limit retaining the radial profile of input parameters is important. In the CBC case, the various types of instabilities (density gradient-driven drift-waves, sheath-driven linear KH and centrifugal force, and sheath-driven electron temperature gradient instability) compete with each other. Consequently, the linear eigenmodes in the CBC have smaller growth rates as compared to the drift-wave growth rates found in the IBC case.

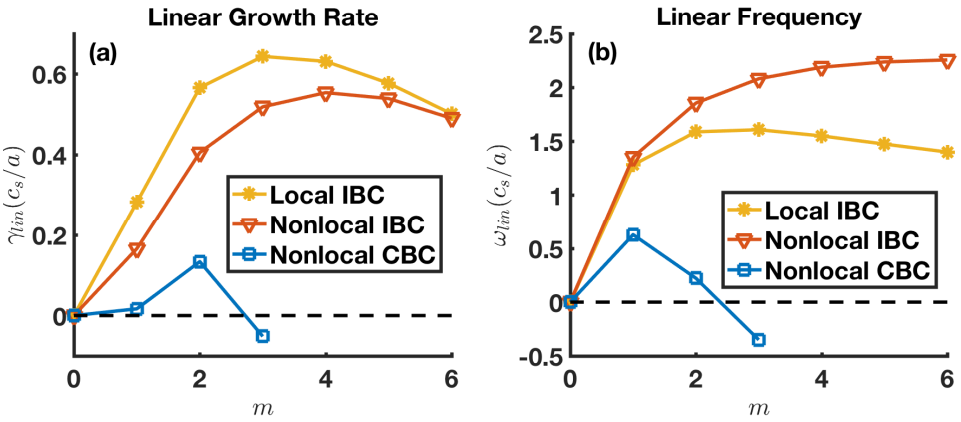

Figure 3.5: (a) linear growth rate and (b) real frequencies of fastest growing azimuthal modes for different physics cases.

To understand the physics of the instabilities, we performed a density profile scan below and above experimental condition by changing the exponential exponent parameter n_α in our functional form for $n_0(r)$, causing a decrease or increase in the density gradient ($1/L_n = -d\ln n_0/dr$). Afterward, the energy balance analysis introduced in Chapter 2, is used to analysis the energy components of this density scan. The results of these scans are shown in Fig. 3.6. We can observe that in the IBC case (Fig. 3.6 a), S_{T_e} is small because the maximum electron temperature gradient ($1/L_{T_e} = -d\ln T_{e_0}/dr$) is located in the region of low density, and also due to the presence of strong parallel damping of electron temperature fluctuations. The drift-waves are primarily driven by the density gradient as seen by the dominant S_n term. Therefore, we can deduce that the electron temperature gradient drift-wave is not a main contributor instability to the CSDX IBC

case, even with very small density gradients profiles.

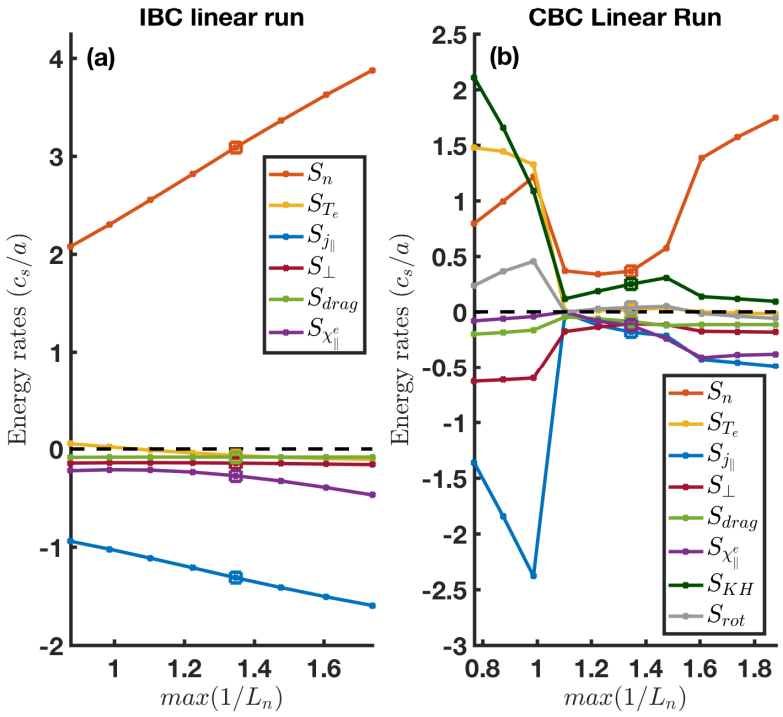

Figure 3.6: (a) IBC linear run, and (b) CBC linear run mode-established energy rates as a function of maximum density gradient. Square dots show linear energy rates of experimental density gradient.

In the CBC case (Fig. 3.6 b), we can observe some notable changes compared to the IBC case. First, the presence of conducting sheath allows additional linear instabilities such as sheath-driven electron temperature gradient instability, plus linear transverse KH and rotational (centrifugal) instability generated by the sheath-driven equilibrium $E \times B$ shear. Changes in the density profile then leads to different dominant linear instabilities regimes, due to variations in the electron diamagnetic frequency ($\omega_{*_e} = k_\theta \rho_s c_s \frac{1}{L_n}$) and parallel electrical conductivity ($\sigma_\parallel = 1/\eta_\parallel$). [Jas72] demonstrated different regimes of drift-waves and KH instability, depending on electron diamagnetic frequency and parallel electrical conductivity in $k_\perp \gg k_\parallel$ limit. In Fig. 3.7, we show contour plots of linear growth rates and the density-potential cross-phase $\zeta(\tilde{n}, \tilde{\phi}) = \arg(\tilde{n}_m^* \tilde{\phi}_m)$ for the CBC linear density gradient scan study. Through this plot, we can designate which mode is

unstable for a given set of parameters. We should note that due to the nonlocal nature of our model, the radial structure of the cross-phase is not radially uniform and different instabilities may be dominant locally at certain radii, however this simple analysis can gives us insight about the most dominant general instability regime via radially averaged cross-phase values.

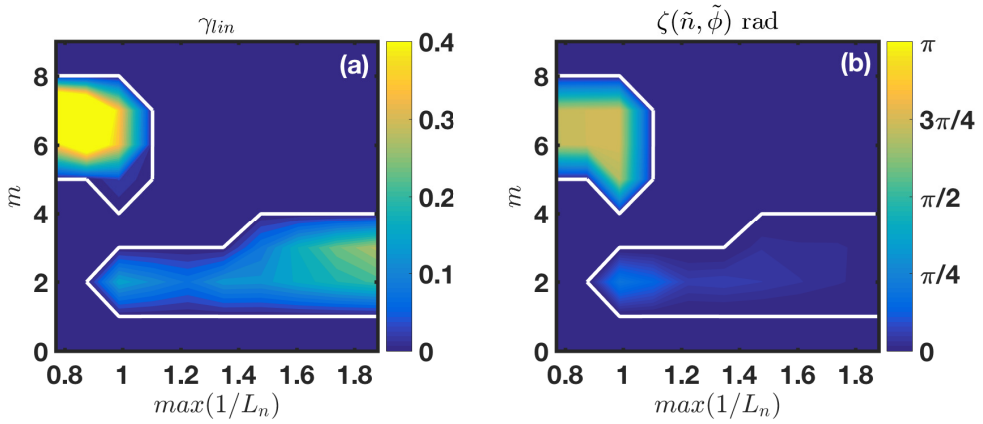

Figure 3.7: (a) contour of CBC linear run growth rate γ_{lin} for different maximum density gradients and azimuthal modes. (b) contour of CBC linear run density and potential cross-phase $\zeta(\tilde{n},\tilde{\phi})$ for density maximum density gradients and azimuthal modes. The growth rates and cross-phase values have been averaged radially, axially and temporally. Growth rate and cross-phase values of stable modes have been filtered out in the plots, due to limitation of initial value solver in capturing noisy highly damped modes. White lines show boundary between unstable and stable modes.

For the CBC case, at low density gradient, where $\max(1/L_{T_e}) > \max(1/L_n)$, we can observe in Figs. 3.6b-3.7 that sheath imposed linear KH (S_{KH}) and sheath driven electron temperature gradient modes (S_{T_e}) act as main driving sources of instability, while density-gradient drift-waves and centrifugal instabilities are present but less prominent. The presence of S_{T_e} at low density gradients is mainly because of sheath driven electron temperature modes, and smaller parallel conduction of electron temperature fluctuations (smaller $\chi_{\parallel}^{e}$). Here, most of density-gradient driven drift-waves are strongly damped through parallel current dissipation $S_{j_{\parallel}}$. From Fig. 3.7 when $1/L_n$ is small, we can observe $5 < m < 8$ modes are unstable and have average density-potential cross-phase

$\pi/2 < \zeta(\tilde{n}, \tilde{\phi}) < \pi$ which is indicator of dominant linear KH instability[Jas72].

As $1/L_n$ is increased to approach the experimental value we observe that the S_n becomes the most dominant instability, while S_{KH} is still present and contributing to the linear drive of system. The sheath-driven electron temperature gradient modes (S_{T_e}) become smaller and eventually become damped due the nonlinear dependence of the parallel heat conductivity $X_{\|}^{e}$ on density. In Fig. 3.7, we can see formation of a new set of modes ($1 < m < 4$) as $1/L_n$ increased which have $\zeta(\tilde{n}, \tilde{\phi}) < \pi/4$ density-potential cross-phase, indicating the dominance of drift-waves. The CSDX CBC experimental condition lies within a hybrid resistive drift-wave/KH regime, where the flow driven modes are opposed to drift-wave, and may be expected to have different turbulence characteristics compared to IBC case. At even higher density gradients, S_n becomes the main drive of instabilities and S_{KH} contribution becomes smaller, and the system becomes dominated by drift-waves. The CBC density profile scan within different regimes of instabilities is in qualitative agreement with the picture depicted by [Jas72].

3.3 Nonlinear Simulations

Building upon the linear analysis of Chapter 3.2, nonlinear simulations of the IBC and CBC cases were performed. The simulations include a growing linear phase followed by the development of a saturated turbulence regime. Fig. 3.8 shows the time trace of the volume averaged total energy for both insulating and conducting simulation. Both simulations were run with the same fit to equilibrium profiles shown in Fig. 3.3 (a-b). We observe that the average total energy of the system in the CBC simulation is smaller than in the IBC case and saturates more slowly, consistent with expectations from linear analysis which gave a smaller γ_{lin} in the CBC case, while the IBC exhibits a more pronounced time-variation in the total energy $E_{tot}(t)$.

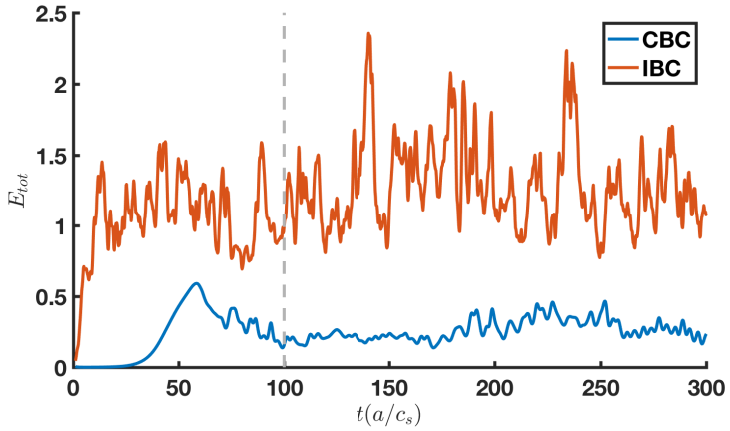

Figure 3.8: Time trace of volume averaged total energy for the CBC and IBC case. All nonlinear results in this Chapter are averaged over $100-300a/c_s$ unless otherwise noted.

Snapshots of the $r-\theta$ distribution of density fluctuations filtered for finite wave numbers in the two cases are shown in Fig. 3.9. We can observe statistically $m \approx 2$ modes dominate both simulations. In the IBC case, density blobs are mostly being formed in the region of maximum density gradient, propagate in electron diamagnetic direction, and they exhibit a radial extension that becomes tilted azimuthally as the structure approaches the shear layer. Similar qualitative behavior has been reported experimentally[CTXM$^+$13], as well.

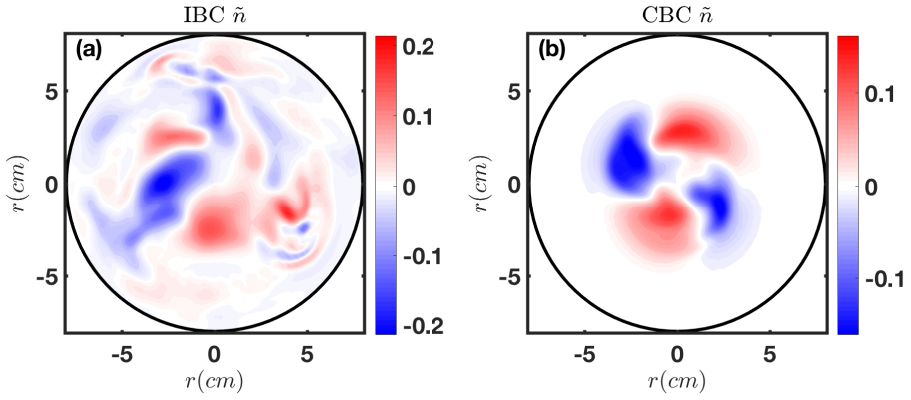

Figure 3.9: $r-\theta$ snapshot of density fluctuations filtered for finite wave numbers of (a) IBC saturation (b) CBC saturation at $z = L_z/4, t = 100(c_s/a)$.

Moreover, in Fig. 3.10, we have shown the snapshots of of the $r-z$ distribution of density fluctuations filtered for finite wave numbers for the IBC and CBC simulation. We observe the dominant axial mode is $n \approx 1$ for both cases, indicating the dominance of drift-waves instability. However, the shape of eigenfunctions is changing from IBC to CBC case, due to effects of axial boundary change. We should note that axial equilibrium gradients are not included in the current model and its effects may change the shape of eigenfunctions. Currently, there is no axial measurements of fluctuations in the experiment, and further study on this subject is needed.

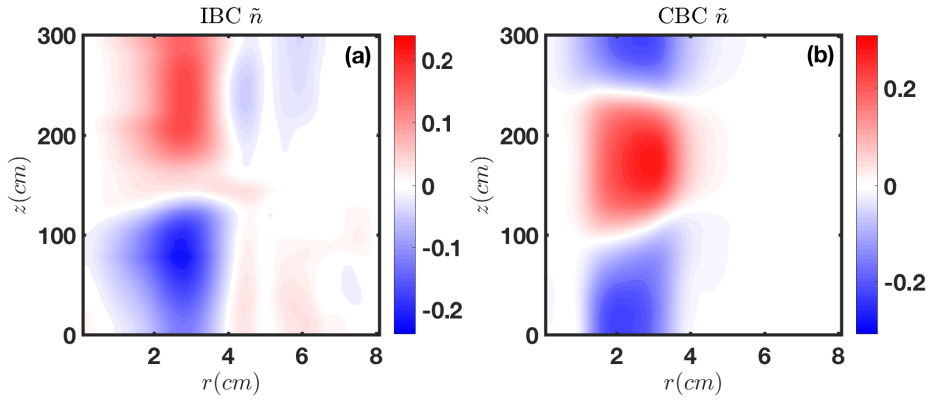

Figure 3.10: $r-z$ snapshot of density fluctuations filtered for finite wave numbers of (a) IBC saturation (b) CBC saturation at $\theta = \pi/2, t = 100(c_s/a)$.

Fig. 3.11 shows the mean averaged values of energy rates in the saturated turbulent regime. We observe a smaller value of the density-gradient drive (S_n) in the CBC case than the IBC case. Moreover, as shown in Sec. 3.2, S_{KH} and S_{RIC} are present as other mechanisms of turbulence drive in the CBC simulation, however they are smaller compared to S_n similar to the linear energy analysis consistent with the drift-turbulence dominated system. One notable difference we observe between the linear energy rates and the nonlinear saturation energy rates is the larger dissipation energy dissipation rates in the nonlinear simulation, mainly due to the damping of turbulence-generated $m = 0$ plasma potential energy by ion-ion viscosity and ion-neutral drag.

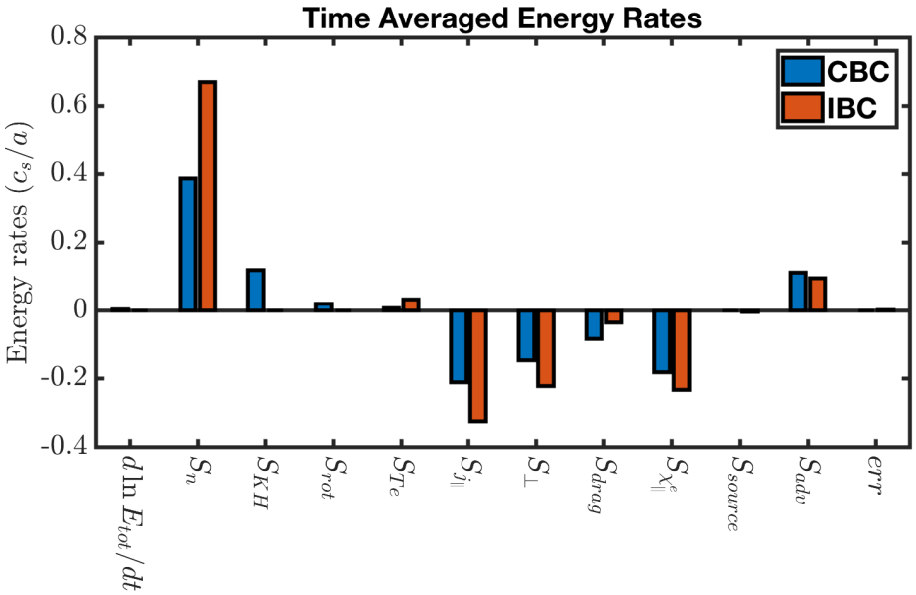

Figure 3.11: Saturated mean energy rates comparison of CBC and IBC simulation.

To further understand saturation mechanism and drift-wave/zonal flow paradigm in the nonlinear simulations, we investigate spectral energy balance of the vorticity equation. The spectral energy balance of the vorticity equation (Eqn. 2.28) for azimuthal mode m reads as

$$\frac{\partial}{\partial t}\langle E_{kinm}\rangle = \langle\tilde{\phi}_m^*\nabla_\parallel\tilde{j}_{\parallel_m}\rangle + \frac{a}{\rho_s}\langle\frac{1}{r}\partial_r\phi_0\tilde{\phi}_m^*\partial_\theta\tilde{\Omega}_m\rangle + \frac{a}{\rho_s}\langle\frac{1}{r}\partial_r\phi_0\tilde{\phi}_m^*(\partial_r n_0\partial_{r\theta}^2\tilde{\phi} - \partial_{rr}^2\phi_0\partial_\theta\tilde{n})_m\rangle + \langle\nu_{in}\tilde{\phi}_m^*\tilde{\Omega}_m\rangle - \mu_\perp\langle\tilde{\phi}_m^*\nabla_\perp^2\tilde{\Omega}_m\rangle - \frac{a}{\rho_s}\langle\tilde{\phi}_m^*\{\tilde{\phi},\tilde{\Omega}\}_m\rangle \quad (3.1)$$

where the star superscript denotes the complex conjugate, and the averaging operator is defined as $\langle f\rangle = \Re(\overline{\int dz\int rdrf})_t$, and time averaged variation of kinetic energy $\partial_t\langle E_{kinm}\rangle$ in the saturation regime goes to zero. In addition, the $\langle\tilde{\phi}_m^*\nabla_\parallel\tilde{j}_{\parallel_m}\rangle$ term can be rewritten as a sum of the injected energy into potential fluctuations from the adiabatic response $\langle\tilde{j}_{\parallel_m}^*\nabla_\parallel\tilde{\phi}_m\rangle$; plus the potential sheath boundary loss term $-\langle\nabla_\parallel(\tilde{\phi}_m\tilde{j}_{\parallel_m}^*)\rangle$. Thus, we can

rewrite the generalized spectral kinetic energy balance as

$$\frac{\partial}{\partial t}\langle E_{kinm}\rangle = \langle \tilde{j}^*_{\parallel_m} \nabla_\parallel \tilde{\phi}_m\rangle - \langle \nabla_\parallel (\tilde{\phi}_m \tilde{j}^*_{\parallel_m})\rangle + \frac{a}{\rho_s}\langle \frac{1}{r}\partial_r \phi_0 \tilde{\phi}^*_m (\partial_r n_0 \partial^2_{r\theta}\tilde{\phi} - \partial^2_{rr}\phi_0 \partial_\theta \tilde{n})_m\rangle$$
$$+\frac{a}{\rho_s}\langle \frac{1}{r}\partial_r \phi_0 \tilde{\phi}^*_m \partial_\theta \tilde{\Omega}_m\rangle + \langle \nu_{in}\tilde{\phi}^*_m \tilde{\Omega}_m\rangle - \mu_\perp \langle \tilde{\phi}^*_m \nabla^2_\perp \tilde{\Omega}_m\rangle - \frac{a}{\rho_s}\langle \tilde{\phi}^*_m \{\tilde{\phi}, \tilde{\Omega}\}_m\rangle. \quad (3.2)$$

In Fig. 3.12, we plot the time the averaged spectral energy rates of the IBC and CBC simulation in the saturated regime, normalized to the total kinetic energy. We observe the IBC simulation has more active modes ($2 \leq m \leq 8$) contributing to the energy transfer into the $m = 0$ zonal flow. Although in the CBC simulation the energy injection from the adiabatic response is smaller than in the IBC case, the CBC simulation exhibits additional KH and centrifugal energy injection into finite m fluctuations. In addition, the potential sheath boundary loss term is an important energy sink in the CBC simulation, resulting in significant damping of kinetic energy. Consequently, due to the larger sheath boundary loss of vorticity energy balance in the CBC case, the nonlinear kinetic energy advection term $T_u = -\frac{a}{\rho_s}\langle \tilde{\phi}^*_m \{\tilde{\phi}, \tilde{\Omega}\}_m\rangle$ is weaker in transferring energy from finite m modes to the $m = 0$ zonal potential, resulting in weaker inverse cascade dynamics for the CBC case. Thus, we observe the zonal potential energy to be smaller in the conducting case. As a result, the IBC simulation exhibits more prominent 2D turbulence dynamics, in which the most linearly unstable modes have a negative T_u and thus losing kinetic energy, while the higher order modes ($m > 6$) and the zonal mode ($m = 0$) have $T_u > 0$ and are receiving kinetic energy from the intermediate fluctuations. These observations of the inverse energy transfer dynamics are also qualitatively consistent with previous experimental measurement of frequency space kinetic energy transfer in various CSDX experiments[XTH$^+$10, MXF$^+$12, CTXM$^+$13].

The saturated amplitude profiles of the fluctuations are shown in Figs. 3.13 for the both cases. We observe that the plasma potential and density fluctuations have the largest

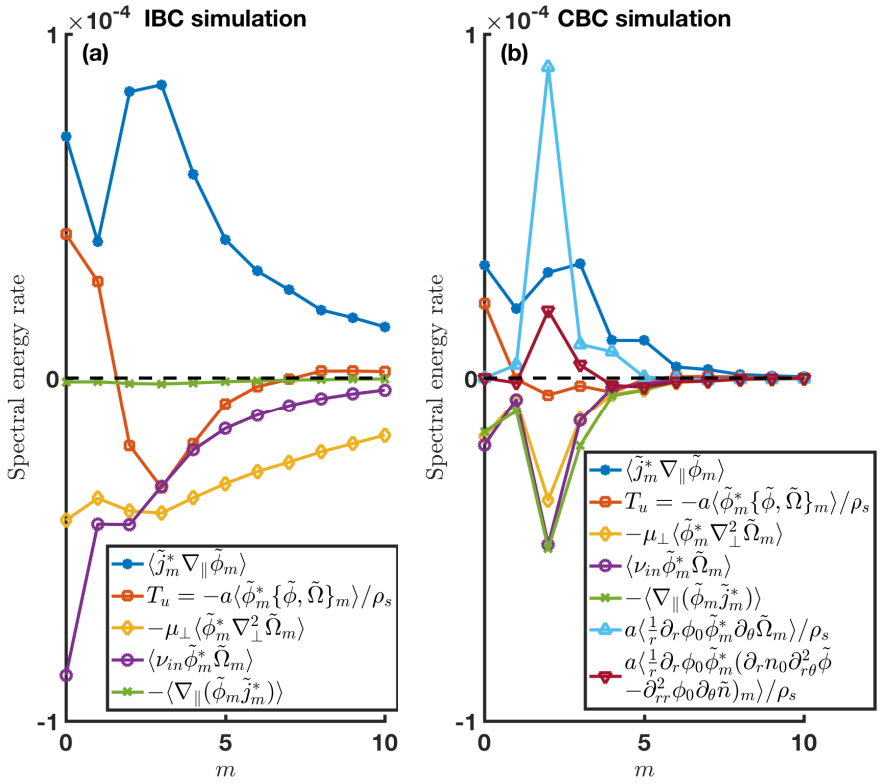

Figure 3.12: Spectral energy balance of vorticity equation in nonlinear (a) IBC simulation, and (b) CBC simulation.

fluctuations amplitudes, and the electron temperature fluctuations is small compared to $\tilde{n}$ and $\tilde{\phi}$ (see Fig. 3.13 a-c). The RMS density peaks near $r \approx 2.5cm$, consistent with experimental measurement of density (see Fig. 3.3 a). However, the plasma potential RMS amplitudes peak more toward the edge ($r \approx 4cm$ for CBC simulation and $r \approx 6cm$ for IBC simulation), while the experimental floating potential measurements peak at $r \approx 3cm$ (see Fig. 3.3 b). Additional simulations not shown here indicate that the location of the peak RMS plasma potential fluctuation is sensitive to the details of the equilibrium profile as well as to the radial profile of ion-neutral drag.

Fig. 3.13 (d) shows total mean plasma potential profile (the sum of equilibrium potential ϕ_0 and zonal potential $\tilde{\phi}_Z$). We observe that the IBC case exhibits a completely different behavior compared to CBC case. The generated zonal electric field in IBC

simulation is radially inward, causing an $E \times B$ drift in electron diamagnetic direction. However in the CBC simulation, the mean potential profile is mostly dominated by sheath-driven equilibrium electron temperature with an outward electric field, while the CBC turbulent-driven component of the zonal potential gives a radially outward electric field in the core and radially inward electric field near edge, qualitatively consistent with the experimental observations (see Fig. 3.3 c).

Fig. 3.13 (e-f) shows smaller Reynolds stress and zonal flow in the CBC case, indicating that the conducting endplate partially short-circuits the Reynolds stress. This phenomena can be explained with the charge conservation equation, $\nabla \cdot \tilde{j} = \nabla_\perp \cdot \tilde{j}_\perp + \nabla_\parallel \tilde{j}_\parallel = 0$. Surface integrating current conservation over a flux tube in the plasma, we can write for radial current at radius r as

$$\oiint d\theta dz(\hat{r} \cdot \tilde{j}_r(r)) = \oiint r dr d\theta(-\hat{z} \cdot \tilde{j}_\parallel(z=0)) + \oiint r dr d\theta(\hat{z} \cdot \tilde{j}_\parallel(z=L_z)) = 2 \oiint r dr d\theta(\hat{z} \cdot \tilde{j}_\parallel(z=L_z)). \quad (3.3)$$

Since in the CBC simulation, the parallel current is non-zero at the sheath boundary, $\tilde{j}_\parallel(z=L_z) = \tilde{\phi} - \Lambda \tilde{T}_e$, there is finite radial current opposing the polarization drift. However, in the IBC simulation, this radial current vanishes due to zero parallel current at the sheath boundary. As a result, the turbulence inverse energy cascade is weaker in the case of CBC simulation. This simple explanation is also consistent with our spectral kinetic energy balance analysis shown in Fig. 3.12. Experimental measurements[CTXM$^+$13] also observe similar qualitative reduction in Reynolds stress and zonal flow for conducting endplate case.

Unlike [DRM$^+$12] simulation which had a dipolar azimuthal velocity with zero net azimuthal momentum, our IBC simulation (Fig. 3.13 f) shows non-symmetric lobes of $v_{E\times B}$ due to the presence of ion-neutral drag and nonlocality of vorticity fluctuations

in the cylindrical geometry. The CBC simulation shows two weaker lobes of $v_{E\times B}$ which is also non-symmetric. [YXD+10] discusses the experimental evidence of net plasma rotation in the absence of momentum input due to the ion-neutral damping in the outer region of plasma. Here, in the simulations, even a radially uniform ion-neutral drag profile creates a residual stress acting on the net plasma rotation. However, the radial location of shear is different from the experimental measurements. The generation of the zonal flow is a highly nonlinear process, and many factors and input profile uncertainties can affect its amplitude and radial structure.

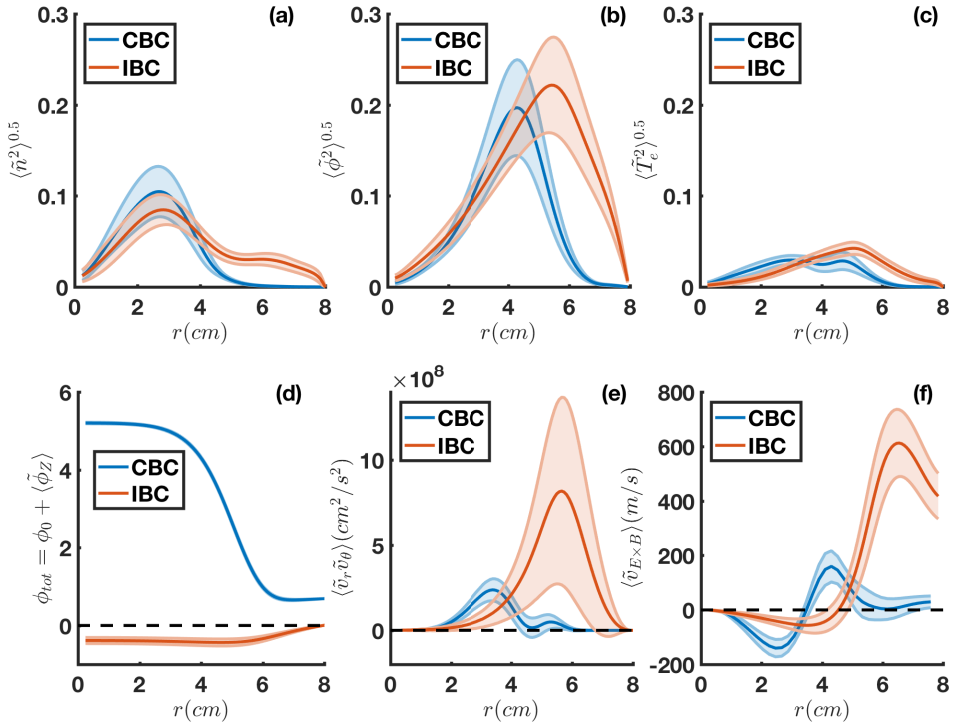

Figure 3.13: Fluctuation amplitudes in the CBC and IBC case. Finite azimuthal ($m > 0$) fluctuations RMS of (a) density, (b) plasma potential, (c) electron temperature, (d) sum of mean and zonal plasma potential profile (e) Reynolds stress, and (f) turbulence driven zonal flow. Shaded bars are temporal standard deviations of simulation values.

Fig. 3.14 shows the potential fluctuations autopower spectra in frequency and azimuthal wavenumber space. The IBC case shows more broadband turbulence, where the energy is mostly accumulated in low frequencies consistent with the spectral transfer

results, while the CBC case exhibits a more quasi-coherent narrow band spectra. In both cases, the power spectra peak not far from the Doppler shifted linear frequencies (shown as the white curve in Fig. 3.14 c-d) calculated from nonlocal linear frequencies (Fig. 3.5 b), which shows that the linear instabilities continue to play an important role for setting the turbulence dispersion relation. We can clearly observe coherent features in the $m-f$ contour of the CBC simulation. One of the main differences observed in qualitative comparison with experiment is that the potential fluctuation amplitude is peaked more radially outward near the edge of the simulations. Simulation plasma potential power spectral density contours (Fig. 3.14 a-b) qualitatively look like the experimental floating potential autopower contours (Fig. 3.2). A direct quantitative simulation-experiment comparison requires a detailed validation study and use of synthetic diagnostics, and will be reported in a separate publication.

3.4 Summary

In this Chapter, we have illuminated how changing the parallel boundary conditions have effect on the development of electrostatic drift turbulence and sheared $E \times B$ flows in a linear plasma column. Linearly, our analysis showed that with insulating endplates, the dominant instability is the density gradient-driven collisional drift-wave. With conducting endplates, the plasma lies in a hybrid drift-wave/KH regime, where the density gradient-driven drift-wave is still the dominant instability, but KH instability generated by the sheath-driven equilibrium $E \times B$ shear is also an important player and integral to the model. Both sheath-driven electron temperature gradient and rotational (centrifugal) force are feeble and compete against density gradient drift-waves. Presumably, in CBC case, by decreasing the density gradient, the system would go to KH dominated regime.

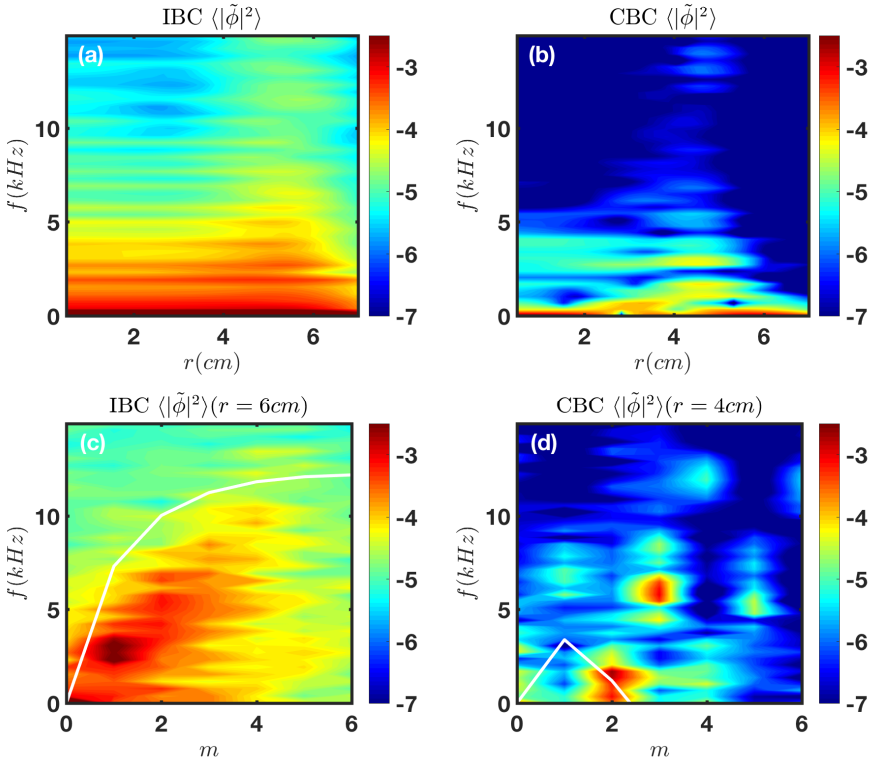

Figure 3.14: Radial frequency distribution of potential fluctuations autopower in (a) IBC simulation, and (b) CBC simulation. Local spectrum of azimuthal mode number versus frequency in (c) IBC simulation at $r = 6cm$, and (d) CBC simulation at $r = 4cm$. White lines are Doppler shifted real frequencies calculated from $\omega = \omega_{lin} + m\partial_r\tilde{\phi}_Z/r$ where $\tilde{\phi}_Z$ is the turbulence driven zonal potential. Values of ω_{lin} are taken from Fig. 3.5 (b).

Moreover, we can conclude that endplates can have significant effect on vorticity equation balance. Conducting endplate allows the current and the heat flux to escape the device. These sheath losses dissipate energy from the system and weakens the Reynolds stress. In general, the endplate change affects the momentum equation, polarization current, vorticity flux, and shear layer generation. These results are qualitatively consistent with experimental report of [CTXM$^+$13] and previous 2D slab simulations of [DRM$^+$12]. In addition, we have shown that in the CSDX insulating case the electron temperature does not significantly alter the nature of instabilities, while in the CSDX conducting case electron temperature can be an essential part of the physics by imposing an

equilibrium potential profile on the plasma that can counteract the turbulent driven zonal flow. However, in both cases electron temperature fluctuations may become important in validation studies, and should be neglected only with considerable deliberation.

These simulations provide a basis for validation studies of turbulence and transport in CSDX linear device. Experimental studies on CSDX have used saturation current and floating potential measured by Langmuir probes, and light intensity fluctuations measured by fast imaging camera, to interpret the turbulent transport. Many of these measurement techniques are also being used in larger magnetically confined devices, where these measurements might differ from real density and the plasma potential values because of the effects of electron temperature fluctuations. These effects have been neglected in CSDX experimental studies, due to diagnostic limitations. The model derived in this thesis allows one to translate back the real physical quantities into synthetically measured quantities and compare them to experimental measurements. Next Chapter will provide a detailed validation study on the IBC simulation case, and will discuss the effects of profile uncertainty on the degree of agreement between simulation and experiment.

3.5 Acknowledgement

The text and data in Chapter 3, is a reprint of the material as it appears in Vaezi, P., Holland, C., Thakur, S. C., & Tynan, G. R. (2017). *Understanding the impact of insulating and conducting endplate boundary conditions on turbulence in CSDX through nonlocal simulations*. Physics of Plasmas, 24(4), 042306. Copyright 2017 American Institute of Physics. The dissertation author was the primary investigator and author of this paper.

Chapter 4

Validation Study of a CSDX Experiment

Validation studies, which systematically explore the relationship between a computational model and the real world, have been carried out in many physics areas[OTH04]. The systematic verification and validation (V&V) of turbulence models in magnetically confined plasma is beginning to play an integral role in the understanding of plasma turbulence and transport. Through such studies, we can gain a better understanding of how a given model approximates an experimental condition, and what additional physics needs to be added to the model in order to capture the essential elements of real-world behavior. [TGL$^+$08] were among the first to describe how to apply V&V concepts such as validation metrics to plasma studies. Other examples include [RTF$^+$09, RHJ$^+$12, RRT$^+$15], who studied the influence of synthetic diagnostics on Langmuir probe observations, and [RMD$^+$11], who studied synthetic gas puff imaging diagnostics in the srape-off-layer turbulence setting. More recently, [Hol16] discussed the importance of uncertainty quantification and its inclusion within validation metrics, and the need for utilizing synthetic diagnostics for code-experiment comparisons.

Systematic validation studies can lead to a better understanding of the fidelity and limitations of experimental measurement techniques, as many experimental measurements are directly being used to interpret the transport physics. The uncertainty in gradient-driven instabilities as well as difficult diagnostics access to the plasma in toroidal devices makes the quantification of turbulence and the code-experiment validations challenging in those conditions. In contrast, linear plasma devices such as the Controlled Shear Decorrelation Experiment (CSDX) due to their simple geometry provide a platform to study basic underlying instability physics in more detail than possible in hot confinement devices. CSDX operates at low electron temperatures and is highly collisional similar to the scrape-off layer (SOL) of confinement devices, while excluding some of the toroidal-specific complexities such as tearing or ballooning instabilities. Moreover, various experimental techniques such as multi-tip Langmuir probe and fast imaging camera which are also being used in larger fusion devices, can be used to measure plasma profiles and parameters in CSDX [BTA$^+$05, YHT$^+$07, XTH$^+$09, YTH$^+$10, CTML$^+$12, TML$^+$12, LTB$^+$13]; thus making CSDX a useful testbed for detailed validation studies.

In this Chapter, we will pursue a synthetic validation study of a nonlinear collisional drift-wave model against the experimental results of CSDX linear device. This work follows up on an earlier verification and physics study of CSDX simulations under different boundary conditions of insulating and conducting end plates at a fixed magnetic field in the previous chapter. The simulations in this Chapter used experimental profiles and parameters of CSDX experimental with insulating endplates from [CTXM$^+$13] as the inputs to the model. The first key point that is addressed in this Chapter is the classification and linear sensitivity analysis of input parameter uncertainties to reduce the number of uncertainties needed for simulation runs (also known as uncertainty dimensionality reduction). Second, the role of synthetic Langmuir diagnostics has been

explored, and the synthetic simulated fluctuations quantities have been compared against the experimental measurements. Finally, independent experimental measurements of azimuthally symmetric low-frequency $E \times B$ flow are compared with the predicted $E \times B$ flow obtained from the simulations.

The rest of the Chapter is organized as follow. In Sec. 4.1, we will introduce experimental uncertainties in the measurements, and their translation into input parameter uncertainty. In Sec. 4.2, we will discuss the response of the linearized growth rates to these input uncertainties. In Sec. 4.3, we will introduce the synthetic diagnostics techniques for creating a set of qouantity of interest (QoI). In Sec. 4.4, we will use these QoIs to test the performance of the model in predicting the experimental measurements. In Sec. 4.5, we will conclude the results of this validation case study.

4.1 Experimental Uncertainties

The V&V process begins by constructing a model based on the assumptions taken from a specific experimental condition. The experimental profiles in this Chapter are taken from [CTXM$^+$13] for CSDX experimental condition at $1kG$ with insulating boundary endplates where the plasma terminates. In this experiment, the Argon plasma is created by an $m = 0$ helicon source operating at $1.5kW$.

Based on the experimental timescales and length scale ratios, we can make assumptions to reduce the generalized Braginskii fluid equations into a simpler model following the approach of Hasegawa and Wakatani[HW83]. Simplicity of the model is needed to make the computational requirements tractable, however an overly simplified model may not capture the essential elements of the experiment. We have introduced a nonlocal cold ions fluid set of equations to describe the physics of drift-wave turbulence in CSDX in Chapter 2. The model evolves fluctuations of density $\tilde{n}$, vorticity $\tilde{\Omega} = \nabla_\perp \cdot$

$(n_0\nabla_\perp\tilde{\phi})$ and electron temperature $\tilde{T}_e$, in the presence of an axially uniform background density profile, $n_0(r)$, and electron temperature profile, $T_{e_0}(r)$, where the tilde superscript denotes the fluctuation part and 0 subscript denotes the equilibrium part of the quantities.

Due to the strong nonlinear dependence of plasma turbulence on drive and dissipation mechanisms, uncertainties in experimental inputs may have surprisingly large effect on the turbulence. Thus, it is important to understand the types of uncertainties in the system and the measurement errors, and the effective response of the model to these uncertainties. Different types of uncertainties such as statistical uncertainties, systematic uncertainties, reduced model uncertainties, etc. may affect the validation studies of a computational model. In this Chapter, we will perform a detailed study of statistical and systematic uncertainties for the CSDX experimental condition. These uncertainties could propagate into instability driving forces such as equilibrium gradients, as well as damping mechanisms such as the ion viscosity and dragt from ion-neutral collisions.

Since we have no measurement of the source heat deposition and resulting ionization source in CSDX, in the model we have used ad-hoc particle and heat sources to damp the zonal (i.e. azimuthally and axially uniform) density and electron temperature profile variations that arise from turbulent transport, and thereby maintain the total equilibrium profiles as the turbulence saturation develops. These profiles were measured through RF compensated swept Langmuir probes[CTXM$^+$13], and their uncertainties can influence the drift-wave instability drive, as well as the vorticity, resistivity, and heat conductivity profiles. Thus, the uncertainties of the equilibrium profiles must be considered, where they inherently arise from experimental measurement uncertainties.

We should note that in CSDX experimental measurements, we have measurements of mean density at two different axial locations of $z = L_z/4$ and $z = L_z/2$ downstream from the source, where $z = 0$ denotes the location of helicon source, and $L_z = 300(cm)$ is the axial extent of the plasma column. In Fig. 4.1 we have shown the measurements of

mean density profile at two different axial locations. We observe a slight difference in the equilibrium density measured at two different axial ports, and in particular note that $\nabla_r n$ is larger at $L_z/4$. However, our current collisional drift-wave model do not account for such axial variation of equilibriums. Hence, we need to include this systematic uncertainty in the simulation scans. In this validation study, we have performed a detailed statistical uncertainty scans using the experimental density equilibrium and other plasma parameters of $z = L_z/2$ downstream from the source, and also included an additional scan using experimental density of $z = L_z/4$ downstream from the source to include the systematic uncertainty of different experimentally measured profiles.

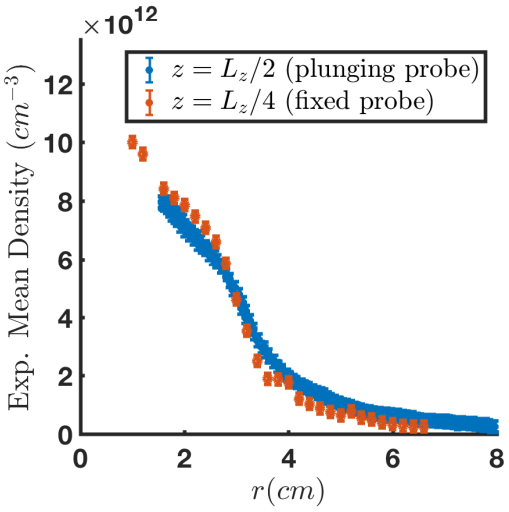

Figure 4.1: Comparison of experimentally measured mean density profiles at two different axial locations $z = L_z/2$ and $z = L_z/4$ from the source. Experimental data is taken from [CTXM$^+$13] with permission.

Fitting a smooth temperature and density profiles to the discrete measurements requires us to define a mathematical functional form. We have used a generalized double Gaussian functional form

$$n_0(r) = (\bar{n}_1 - n_{base}) \exp(-(r/l_{n_1})^{n_{\alpha_1}}/n_{\alpha_1}) + (\bar{n}_2 - n_{base}) \exp(-(r/l_{n_2})^{n_{\alpha_2}}/n_{\alpha_2}) + n_{base} \tag{4.1}$$

for the density equilibrium profiles, and a generalized single Gaussian functional form

$$T_{e_0}(r) = (\bar{T}_e - T_{e_{base}}) \exp(-(r/l_{T_e})^{T_{e\alpha}}/T_{e_\alpha}) + T_{e_{base}} \tag{4.2}$$

for the electron temperature equilibrium profiles. In the simulations, we have normalized the equilibrium density and electron temperature profiles to the on-axis density and electron temperature of $z = L_z/2$, respectively. To estimate statistical uncertainty of the equilibrium fits, a procedure like that of [WPR$^+$10] has been implemented, where experimental equilibriums are varied within the experimental uncertainty in a Monte Carlo approach to produce a set of 100 realizations for each profile. Each realization is obtained through a regression fit to the functional form via a least square method. Fig. 4.2 shows the resulting fits to the experimental measurements of density and electron temperature equilibrium profile measurements of $z = L_z/2$.

We should note that there is no reliable experimental measurement for electron temperature equilibrium at $r > 6cm$, therefore an artificial value of temperature with larger estimated error is chosen at the edge ($r = 8cm$) to obtain a plausible fit over the entire simulation domain. Then, three different fits with low, median and high values of radially integrated equilibrium density gradient ($1/L_n = -d\ln n_0/dr$), and equilibrium electron temperature gradient ($1/L_{T_e} = -d\ln T_{e_0}/dr$) are chosen as input fit uncertainty into the code. The goodness of fits have been tested through chi-squared parameter[Tay97] $\chi^2 = \frac{1}{N}\sum(f_{fit} - f_{exp})^2/\sigma^2$, where the sum is over all experimental measurement points (f_{exp}). f_{fit} is the fit value, σ quantifies the uncertainty of the experimental measurement, and N is the number of experimental data points minus the number of free parameters in the functional form. In table 4.1, we show $\chi^2 < 1$ for all the equilibrium fits, indicating reasonable goodness of the fits. We should note that we also tested single Gaussian profile for density profiles, however the resulting χ^2 value was

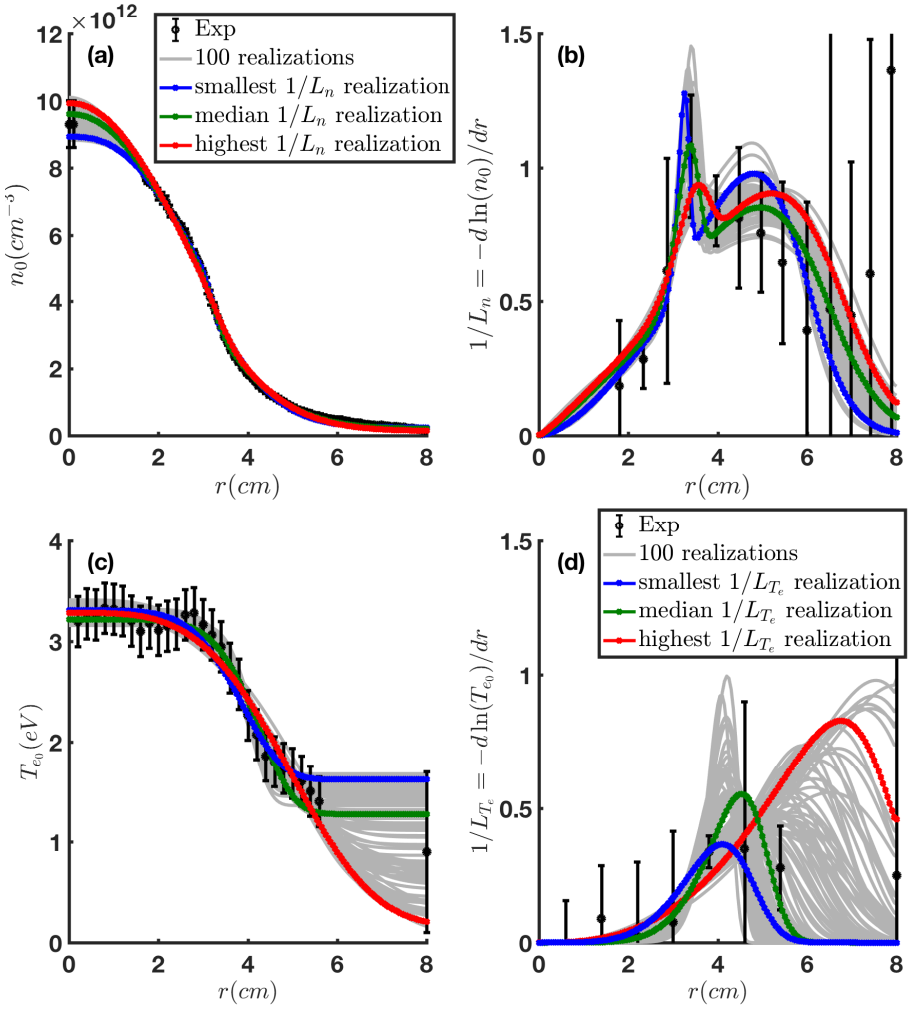

Figure 4.2: Fit realization in a Monte Carlo analysis for experimentally measured (a) density equilibrium and (c) electron temperature equilibrium at $z = L_z/2$. (b) Density gradient lenghtscale ($1/L_n$) of fits compared with experimentally calculated gradient. (d) electron temperature gradient ($1/L_{T_e}$) of fits compared with experimentally calculated gradient. Gray lines show the 100 realization generated in the Monte Carlo approach.

large and the functional form regression could not fully capture the underlaying trend of the experimental data, especially in the maximum density gradient region. As a result, double Gaussian functional form is chosen for the density fits.

The same procedure is repeated for fitting the functional form to the equilibrium density measurements of $z = L_z/4$, and results are shown in Fig. 4.3. We note that

Table 4.1: Characteristics of equilibrium fits.

Fit	parameter	low	median	high
n_0	$\int dr(1/L_n)/a$	0.45	0.46	0.48
n_0	χ^2	0.25	0.16	0.17
T_{e_0}	$\int dr(1/L_{T_e})/a$	0.09	0.11	0.34
T_{e_0}	χ^2	0.28	0.23	0.38

maximum $1/L_n$ at $z = L_z/4$ is almost twice the value found at $z = L_z/2$. In general, we observe that the experimental measurements of equilibrium density from both probe port measurements are well characterized, with a very small statistical uncertainty, while the systematic uncertainty is fairly large. Propagation of these uncertainties in the linearized model is discussed in more details in Sec. 4.2.

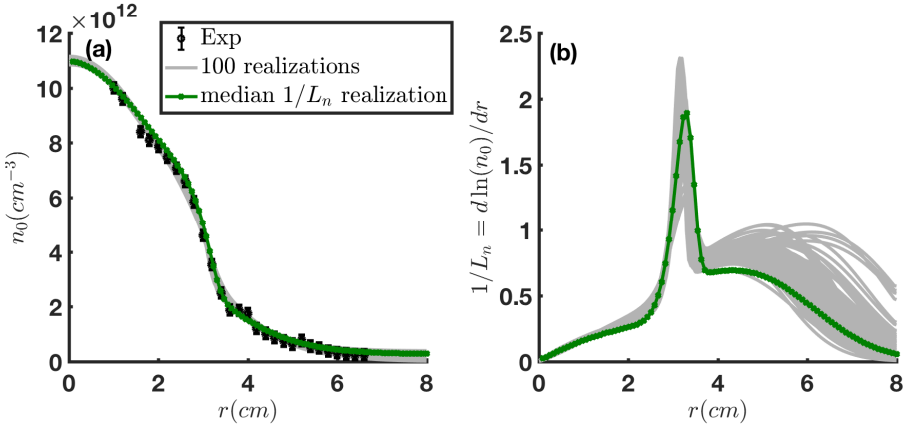

Figure 4.3: (a) Fit realization in a Monte Carlo analysis for experimentally measured density equilibrium of $z = L_z/4$. (b) Density gradient lengthscale $(1/L_n)$ of fits.

Within the damping mechanisms, uncertainties in the quantities such as ion and neutral temperature measurements can affect momentum balance and zonal flow generation through their effects on the ion-ion viscosity and ion-neutral drag. The ion-ion viscosity has a nonlinear dependence on the ion temperature and density. To simplify the code implementation, we have assumed a radially uniform ion-ion viscosity profile, where the core ion temperature determines the viscosity value. The ion temperature is measured between $0.5 < T_{i_0} < 0.7eV$ using Laser Induced Fluorescence (LIF)

technique[CTML$^+$12]. Moreover, the neutral gas temperature can influence ion-neutral collision frequency, but there are no previous radial profiles of neutral gas temperature in any of CSDX experiments. The neutral gas temperature measurement was performed over a central chord via high resolution ($10m$) emission spectroscopy, resulting in on-axis neutral gas temperature of $0.4 < T_{g_0} < 0.6eV$. Therefore, we need to treat the neutrals temperature at the edge and neutrals temperature steepness as *known unknowns*. We have assumed the neutral gas temperature to have functional form

$$T_g(r) = (\bar{T}_g - T_{g_{base}}) \exp(-(r/l_{T_g})^{T_{g\alpha}}/T_{g_\alpha}) + T_{g_{base}}, \tag{4.3}$$

in which the neutrals at the edge ($r = 8cm$) have temperature uncertainty between room temperature $0.03eV$ to $0.1eV$. Also, the steepness of neutral temperature is taken to be same as ion temperature steepness with $\pm 20\%$ variation ($l_{T_g} = 2.1cm; T_{g_\alpha} = 2.3 \pm 0.5$). Ion-neutral drag then can be calculated assuming ideal gas behavior with constant gas pressure of $3.2mTorr$. We have also assumed fixed profile of ion-neutral drag with respect to evolving plasma fluctuations in these simulations. Further experimental measurements are needed to confirm these assumptions.

4.2 Linear Sensitivity Analysis

In the previous section, we discussed the input uncertainties that could influence the turbulence. In this section, we will investigate the response of the linearized model to such uncertainties. This sensitivity scan of experimental parameters provides us with the information about the sensitivity of the linearized model, as well as insight into the input experimental parameters that need to be explored in the nonlinear simulations.

A rigorous approach in magnetically confined fusion validation study is the implementation of local sensitivity plots for presenting validation[Hol16]. In this approach,

one identifies a single input parameter (often the driving gradient of the dominant micro-instability, or a damping mechanism), and performs a discrete set of simulations in which this parameter is systematically varied about the experimental base value, holding all other inputs in the model fixed. Here, the base case is chosen as the statistical median in the range of uncertainties. The base $n_0(r)$ and $T_{e_0}(r)$ profiles are chosen from the median case shown in Fig. 4.2 and Table 4.1, and the density and electron temperature scans are done with the low and high labeled fits. In addition, we have included the median realization to the equilibrium density measurements at $z = L_z/4$, shown in Fig. 4.3, as an additional input in the linear sensitivity of the model, to explore the systematic uncertainty of the measurements. The base T_{g_0} is taken to be $0.5eV$, and the scan is done with low and high values of $0.4eV$ and $0.6eV$ respectively. The base edge neutral temperature estimated as $T_{g_b} = 0.065eV$, with the range from $0.03eV$ to $0.1eV$. We also have chosen three values $T_{i_0} = 0.5, 0.6, 0.7eV$ as ion temperature input uncertainty with base value of $T_{i_0} = 0.6eV$.

We then calculated the most unstable linear growth rate of the collisional drift-wave for each uncertainty linear scan, and compared them to the growth rate of the base case. The linear growth rates can be obtained by calculating imaginary part of $\partial \ln \tilde{\phi}_m / \partial t$ after convergence in the linearized initial value solver. The results of such scans are shown in Fig. 4.4, where we can observe the linear response of the system for the expected range of input parameter variations associated with the experimental uncertainties. A widen horizontal extent denotes larger measurement uncertainty, while steeper slope indicates a stiffer model response.

Examining these results, we can observe that while the electron temperature gradient input is very uncertain, it doesn't contribute much to the linear growth rates. The statistical uncertainty in density gradient is relatively small and equilibrium density measurements are very well characterized, hence the response range is small. However, the

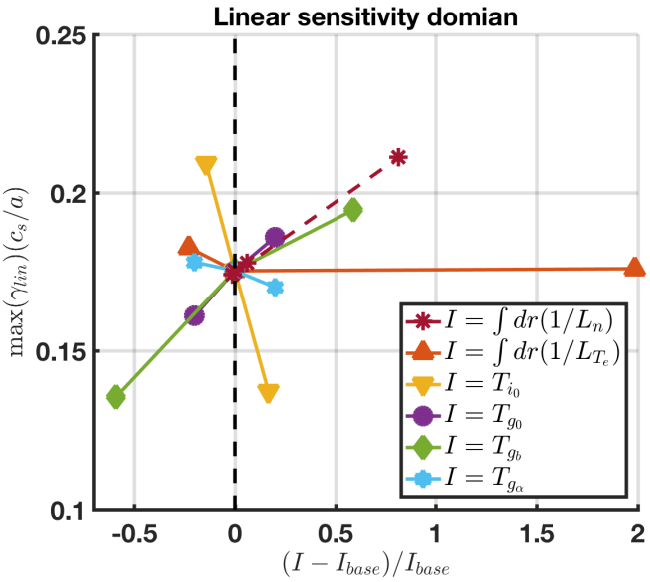

Figure 4.4: Maximum linear growth rate sensitivity analysis of uncertainty scans. I indicates the input parameter uncertainty normalized to the base case value (I_{base}). Solid colors lines show statistical uncertainties sensitivity as follow: radially integrated density equilibrium scan (red), radially integrated electron temperature equilibrium scan (orange), core ion temperature scan (yellow), core neutral temperature scan (purple), base neutral temperature scan (green), and neutral temperature profile steepness scan (light blue). Dashed red line shows the linear growth rate response due to the systematic uncertainty in equilibrium density measurements.

systematic uncertainty of equilibrium density fits of different axial location measurements is large, and linear growth of such uncertainty is very different from the base case growth rate. The other sensitive responses from input parameter uncertainty are associated with ion temperature and neutral gas temperature uncertainty at the edge which influence ion viscosity and neutral drag in the model. Motivated by these results, we ran the nonlinear simulations for the base case, plus five other simulations including statistical variations of ion temperature and edge neutrals temperature, as well as systematic uncertainty of equilibrium density fit due to equilibrium density measurements at $z = L_z/4$ and $z = L_z/2$. The results of these simulations are compared to the experimental measurements in Sec. 4.4.

4.3 Quantities of Interest

To quantify the fidelity of the turbulent model in describing the experimental measurements accurately, we need indentify the appropriate quantities to compare. In this section, we consider a number of physical quantities that are suitable for experiment-simulation comparison. Typically, the experimental diagnostics do not measure the identical quantities that the code computes, and thus the development of synthetic diagnostics is crucial[BN06]. Synthetic diagnostics are computational algorithms used to transform the simulation results into predicted experimentally observable quantities and enable meaningful quantitative comparisons[Hol16].

Three main types of diagnostics that have been used in the CSDX linear device: multi-tip Langmuir probes, visible light fast imaging camera[TBL$^+$14], and laser induced fluorescence[CTML$^+$12]. In this Chapter, we will discuss the construction of synthetic Langmuir probe diagnostics, which will be used in Sec. 4.4 for experiment-simulation comparisons. The benchmarking of synthetic camera imaging will be studied in a separate publication.

A synthetic Langmuir probe translates the electron density, temperature, and plasma potential fluctuations predicted by a simulation into the measured ion saturation current and floating potential fluctuations[RTF$^+$09]. The fluctuations of ion saturation current and floating potential can be obtained by linearizing the approximated sheath relations[Hut02],

$$\frac{\tilde{I}_{sat}}{\bar{I}_{sat}} = \frac{\tilde{n}}{\bar{n}} + 0.5\frac{\tilde{T}_e}{\bar{T}_e}, \tag{4.4}$$

$$\frac{e\tilde{\phi}_f}{\bar{T}_e} = \frac{e\tilde{\phi}}{\bar{T}_e} - \Lambda\frac{\tilde{T}_e}{\bar{T}_e}, \tag{4.5}$$

where $\tilde{I}_{sat}$ is the ion saturation current fluctuation, $\bar{I}_{sat} = 0.61e\bar{n}c_sA_{probe}$ is the on-axis reference value of the ion saturation current (we assumed $T_i \ll \bar{T}_e$), $\tilde{n}$ is the density

fluctuation, $\bar{n} = n_0(r = 0)$ is the on-axis reference value of the density, $\tilde{\phi}$ is the plasma potential, fluctuation $\tilde{\phi}_f$ is the floating potential fluctuation, $\bar{T}_e = T_{e_0}(r = 0)$ is the on-axis reference value of the electron temperature, and Λ is the sheath factor, where theoretically in the absence of secondary electron emissions can be obtained as $\Lambda_t = -\log\sqrt{m_e/(2\pi m_i)}$.

We should note that in the cold plasma experiments due to the diagnostic limitation in measuring small electron temperature fluctuations, this quantity is often neglected so that $\tilde{I}_{sat}$ and $\tilde{n}$, and $\tilde{\phi}_f$ and $\tilde{\phi}$ are often used interchangeably in analysis of experiments. In reality, this assumption may not be accurate. Here in the simulations, we are evolving electron temperature fluctuations, and through synthetic diagnostics, we can translate back real physical quantities into experimentally measured quantities. More complicated quantities such as time-averaged particle flux, Reynolds stress, time-delay-estimation (TDE), and nonlinear kinetic energy transfer of fluctuations can then be calculated in the simulation the same way they are being calculated from the experimental measurements.

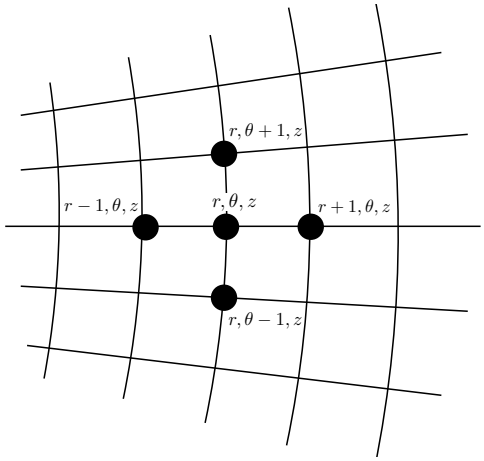

Figure 4.5: Simulation grid points in perpendicular plane.

For instance, by calculating the ion saturation current and floating potential fluctuations in the simulation grid (see Fig. 4.5), we can mimic experimentally measured quantities by calculating synthetic radial $E \times B$ velocity fluctuations ($\tilde{v}_r^f = -\partial_\theta \tilde{\phi}_f / B$)

and azimuthal $E \times B$ velocity fluctuations ($\tilde{v}_\theta^f = \partial_r \tilde{\phi}_f / B$) using numerical gradients of floating potential fluctuations, and obtain the normalized local synthetic particle flux (Γ^{syn}) and the normalized synthetic Reynolds stress (R_t^{syn}) at the grid point (r, θ, z) as

$$\Gamma^{syn}_{(r,\theta,z)} = \frac{\bar{n}\tilde{I}_{sat_{(r,\theta,z)}}}{\bar{I}_{sat}} \frac{(\tilde{\phi}_{f_{(r,\theta-1,z)}} - \tilde{\phi}_{f_{(r,\theta+1,z)}})}{2Br^2\Delta\theta}, \tag{4.6}$$

$$R^{syn}_{t_{(r,\theta,z)}} = \frac{(\tilde{\phi}_{f_{(r+1,\theta,z)}} - \tilde{\phi}_{f_{(r-1,\theta,z)}})(\tilde{\phi}_{f_{(r,\theta-1,z)}} - \tilde{\phi}_{f_{(r,\theta+1,z)}})}{4B^2r^2\Delta\theta\Delta r}. \tag{4.7}$$

In addition, the TDE technique can be applied to relate the peak time lag $\tau_p(\tilde{\phi}_1, \tilde{\phi}_2)$ of the fluctuations cross-power to estimate the local azimuthal phase velocity[HTMF04, YHT$^+$07]. Experimentally, two azimuthally separated Langmuir probe tips measuring floating potential at a specific radius, and axial location are used to estimated the phase velocity, while in the simulations, we can average the velocity over multiple azimuthally separated points at a certain radius, and axial location to obtain the azimuthal phase velocity,

$$V_{ph_{(r,\theta,z)}} = \frac{r\Delta\theta}{\tau_p(\tilde{\phi}_{f_{(r,\theta+1,z)}}, \tilde{\phi}_{f_{(r,\theta,z)}})}. \tag{4.8}$$

In addition, the nonlinear kinetic energy transfer is measured experimentally through a 3×3 array of Langmuir probes measuring floating potential[XTH$^+$09, XTH$^+$10, MXTT11]. Experimentally, vorticity fluctuations simply been calculated by taking Laplacian of floating potential fluctuations, hence we can compute the normalized synthetic nonlinear kinetic energy transfer at a fixed spatial location (r, θ, z) for frequency f as

$$T_u^{syn}(f) = -\frac{a}{\rho_s}\Re\left(\frac{e\tilde{\phi}_f^*(f)}{\bar{T}_e} P_\Omega^{syn}(f)\right), \tag{4.9}$$

in which the star superscript denotes the conjugate complex, and $P_\Omega^{syn} = \left\{\frac{e\tilde{\phi}_f}{\bar{T}_e}, \frac{n_0}{\bar{n}}\rho_s^2\nabla_\perp^2(\frac{e\tilde{\phi}_f}{\bar{T}_e})\right\}$ is the synthetic vorticity Poisson bracket.

4.4 Comparison of Simulation-Experiment

For comparison of simulations against the experimental results, we have conducted six simulation scans where the input parameters were varied over the expected range of uncertainties. By running the nonlinear simulations for this range of input parameters, we can compute the resulting time series of synthetic turbulence observables. In Fig. 4.6, we show the total fluctuation energy $E_{tot} = 0.5(\langle \tilde{n}^2 \rangle + \langle n_0 (\nabla_\perp \tilde{\phi})^2 \rangle + \langle \tilde{T}_e^2 \rangle)$ time trace of the base case simulation. We have calculated the mean quantities for each simulation by dividing the saturation regime into five (ten for spectra comparisons) sub-averaging windows, as shown by the red lines in Fig. 4.6. The mean of all of the sub-averaging windows is then taken as the mean turbulence quantity of that specific simulation, and the standard deviation as the uncertainty. The sub-averaging window length $\tau_{sub} = 150 a/c_s$ is chosen to be about two orders of magnitude larger than the auto-correlation timescale ($\tau_{corr} \approx 2a/c_s$) that are, in turn, about one order of magnitude larger than the simulation integration timestep ($\Delta t = 0.2a/c_s$). In this section, we compare the computed QoIs from the simulations against the experimental measurements.

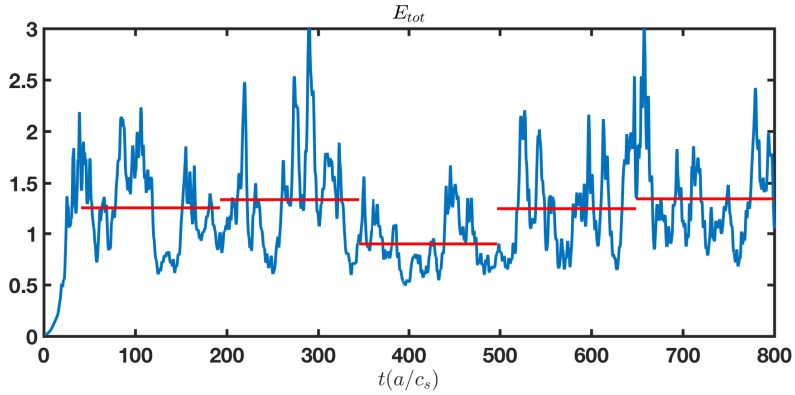

Figure 4.6: Time trace of the normalized total energy in base case simulation. Red lines indicate mean values of sequential $150a/c_s$ sub-averaging windows.

4.4.1 Ion saturation current $\tilde{I}_{sat}$

Basic fluctuations statistics such as I_{sat} and ϕ_f are the most fundamental quantities to examine in simulation-experiment comparisons. Fig. 4.7a illustrates the radial $\tilde{n}$ root mean squared (RMS) fluctuation amplitudes normalized to the reference density, $\bar{n} = n_0(r = 0)$, computed from the simulations, at an axial location $z = L_z/2$ downstream from the source. Fig. 4.7b shows the radial $\tilde{I}_{sat}$ RMS fluctuation amplitudes of the simulations, compared with the experimental measurements at the same axial location, both normalized to $\bar{I}_{sat}$. The experimental measurements are calculated by taking the standard deviation of ion saturation fluctuations after subtracting the mean I_{sat}, and normalizing to $\bar{I}_{sat} = I_{sat}(r = 0)$. The experimental measurements in this case are made with a plunging Langmuir probe for higher radial resolution. In the simulations, the RMS amplitude of ion saturation current fluctuations for finite perpendicular and parallel wavenumbers are calculated. In Fig. 4.7, the blue line shows the base case simulation results, while other colors dashed lines represent the simulation results carried out for input parameters that range over the experimental uncertainties as discussed earlier. The shaded band shows the sub-window averaging standard deviation of base case simulation.

We observe the simulations have good agreement with experimental $\tilde{I}_{sat}$ measurements for $r < 4cm$, while overestimating the fluctuations at $4cm < r < 6cm$. Moreover, we observe that the $\tilde{I}_{sat}$ and $\tilde{n}$ are not very different, and ion saturation current can fairly be used to describe the density.

A comparison of the power spectral density (PSD) of ion saturation current and the density fluctuations for finite wavenumbers at $z = L_z/2$ is shown in Figs. 4.8a-b, which shows the $r - f$ contour plots of power spectral density for the base case simulation. We observe that the simulation ion saturation current and density fluctuations have very similar spectra properties. The experimental autopower spectra of ion saturation current, obtained via fixed Langmuir probe measurements at $z = L_z/2$ location for high temporal

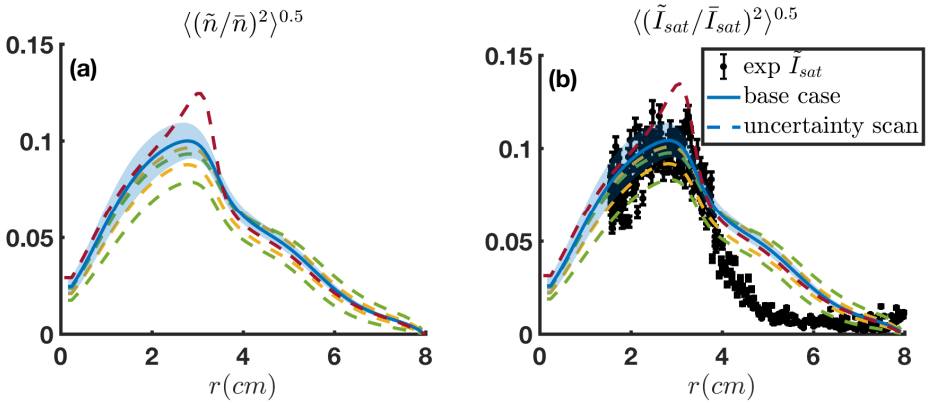

Figure 4.7: (a) Density fluctuations at $z = L_z/2$ of the simulations. (b) Comparison of the experimental and synthetic ion saturation current fluctuation measurements at $z = L_z/2$. The dashed lines correspond to nonlinear simulation of the cases shown in Fig. 4.4, and the shaded band indicates the standard deviation of sub-window averaging of the base case simulation.

resolution, is shown in Fig. 4.8c. Moreover, a comparison of the synthetic ion saturation current autopower spectra with the experimental measurements of I_{sat} spectra for $r = 3cm$ is shown Fig. 4.8d.

Comparing the experimental measurements and synthetic ion saturation current spectra, first we observe that the simulation spectra peaks at frequencies fairly similar to the experiment. Second, the simulations shows finite $\tilde{I}_{sat}$ power at $r > 5cm$, while the experimental $\tilde{I}_{sat}$ power is low at that radii. We can relate the extra autopower difference observed in the simulation spectra in $4cm < r < 6cm$ to the RMS fluctuation amplitudes difference between simulations and experiment observed in Fig. 4.7b. Nevertheless, at $2cm < r < 3cm$, the simulations produce the rate of power change with frequency similar to the experimental measurement, and the experimental spectral amplitudes is seen to be in agreement with the scatter expected from the uncertainty scan. Third, the simulation scan with the equilibrium density fit of experimental measurements of $z = L_z/4$ (red line in Fig. 4.8) contains larger autopower, and peaks at different frequencies compared to the experimental measurements and other simulation performed with equilibrium

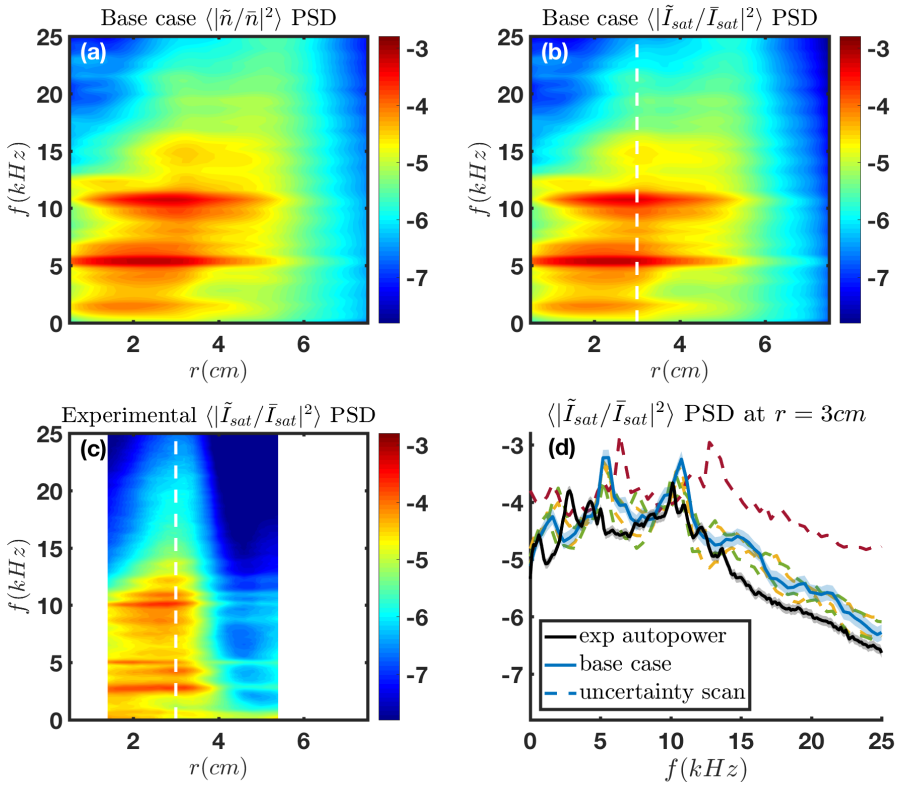

Figure 4.8: Autopower spectra of (a) density, and (b) ion saturation current fluctuations for the base case simulation. (c) Experimental measurement of ion saturation current autopower spectra. (d) Comparison of $\tilde{I}_{sat}$ autopower spectra of simulation scans against the experimental measurements at $r = 3cm, z = L_z/2$. The shaded band indicates the uncertainty due to the number of sub-windows of the base case simulation.

density fit to the measurements of $z = L_z/2$. One can deduce that local density profile of $z = L_z/2$ axial location is necessary for reproducing the experimental ion saturation current fluctuations autopower measurements at $z = L_z/2$.

4.4.2 Floating potential $\tilde{\phi}_f$

Another essential quantity in our validation study is the plasma potential fluctuations generated in the process of drift-wave/zonal-flow turbulence dynamics. In Fig. 4.9a, we show the radial profile of plasma potential $\tilde{\phi}$ RMS fluctuation amplitudes from the simulation, at the axial location $z = L_z/2$. Fig. 4.9b shows the radial synthetic floating

potential $\tilde{\phi}_f$ RMS fluctuation amplitudes of the simulations, compared with the experimental measurements. In the simulations, the $\tilde{\phi}_f$ amplitudes agree with experimental measurements in the core ($r < 3cm$) for the input parameter uncertainty scans, while they overestimate the amplitudes in the outer region.

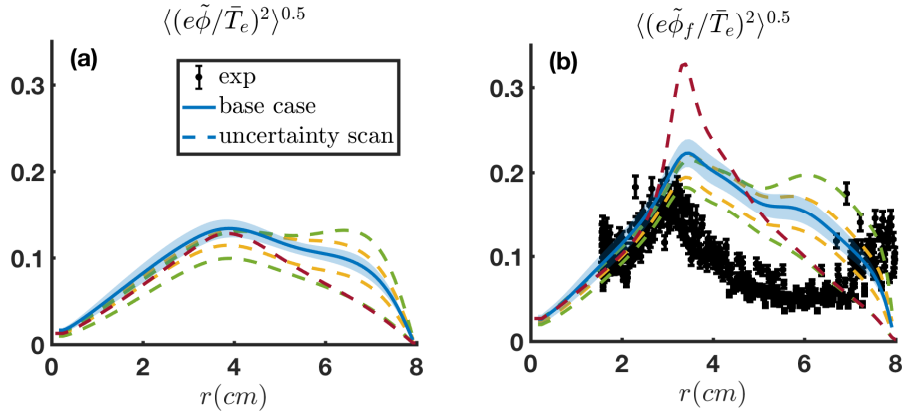

Figure 4.9: (a) Plasma potential fluctuation RMS amplitude of the simulations at $z = L_z/2$. (b) Comparison of the experimental and synthetic floating potential fluctuation measurements at $z = L_z/2$. The dashed lines correspond to nonlinear simulation of the cases shown in Fig. 4.4, and the shaded band indicates the standard deviation of sub-window averaging of the base case simulation.

Unlike the negligible difference between $\tilde{I}_{sat}$ and $\tilde{n}$ fluctuations, there is a noticeable difference between computed synthetic floating potential and the plasma potential fluctuation amplitudes. This difference is more obvious in the systematic uncertainty scan of the density profile. The simulations show the electron temperature fluctuation RMS amplitude is small compared to plasma potential fluctuations (see Fig. 4.10a for the normalized electron temperature fluctuations). However, the relatively large sheath factor $\Lambda = 5.1$ of Argon increases the weight of electron temperature fluctuations in setting the floating potential. We should note that magnitude of electron temperature fluctuations is larger in the systematic uncertainty scan of density profile, mainly due to increase of drift-wave instability with a more steepened profile and larger energy transfer from density fluctuations to electron temperature fluctuations through the adia-

batic response[VHTT17]. Furthermore, we find that the plasma potential and electron temperature fluctuations have non-zero phase shift. Fig. 4.10b show power-weighted plasma potential-electron temperature cross-phase $\zeta(\tilde{\phi},\tilde{T}_e)$. As a result, floating potential phase is different from the plasma potential phase. This different phase characteristics of floating potential can affect fluxes inferred from Langmuir probe floating potential. This cross-phase distortion also founded in studies of density-potential cross-phase by [MGR$^+$05], where they observed the floating potential RMS amplitudes can be distorted from the plasma potential.

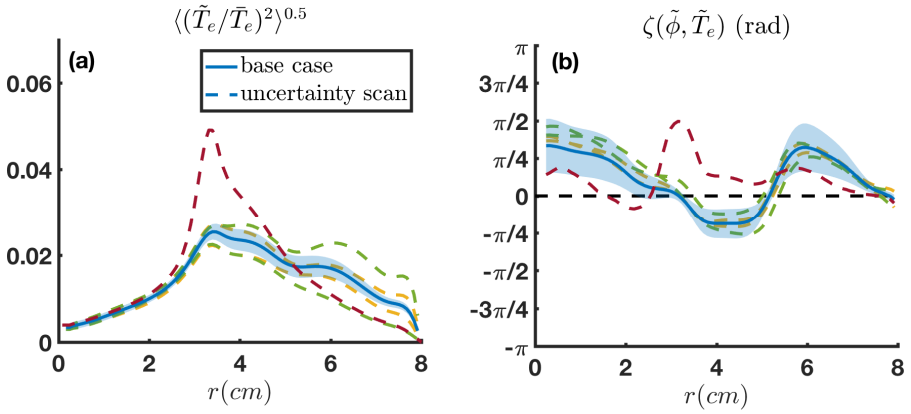

Figure 4.10: (a) Electron temperature fluctuations of the simulations, and (b) power-weighted plasma potential-electron temperature fluctuations cross-phase $\zeta(\tilde{\phi},\tilde{T}_e)$ at $z = L_z/2$. The dashed lines correspond to nonlinear simulation of the cases shown in Fig. 4.4, and the shaded band indicates the standard deviation of sub-window averaging of the base case simulation.

Similar to earlier $\tilde{I}_{sat}$ autopower spectra, we see similar simulation spectra from plasma potential and floating potential fluctuations, shown in Fig. 4.11a-b. In the comparison presented in Figs. 4.11a-b, we can observe that the difference between plasma potential and the floating potential is also visible in frequency domain, where the floating potential contains more power than the plasma potential, indicating the importance of the electron temperature fluctuations on the synthetic Langmuir probe diagnostics.

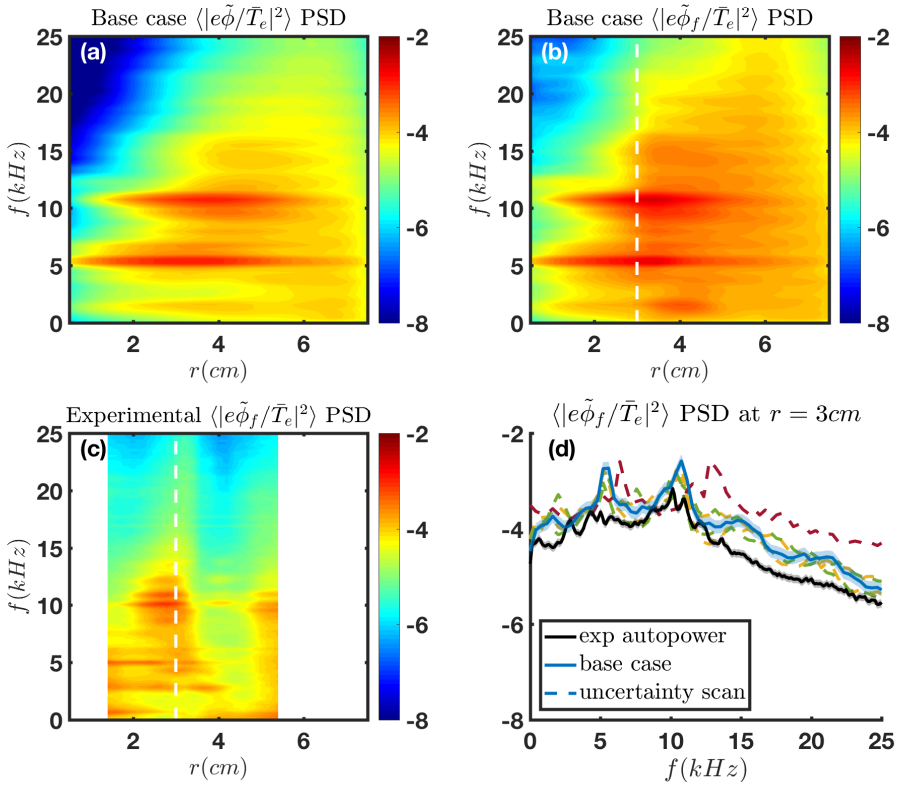

Figure 4.11: Autopower spectral density of (a) plasma potential and (b) synthetic floating potential fluctuations for the base case simulation. (c) Experimental measurement of floating potential autopower spectra. (d) Comparison of $\tilde{\phi}_f$ autopower spectral density of simulation scans against the experimental measurements at $r = 3cm, z = L_z/2$. The shaded band indicates the uncertainty due to the number of sub-windows of the base case simulation.

Moreover, in Fig. 4.11c, the experimental measurement of floating potential autopower via fixed Langmuir probe at $z = L_z/2$ is plotted. For a more quantitative comparison, we have plotted the synthetic floating potential power spectra of the simulations and the experimental floating potential spectra at $r = 3cm$, and the results are shown in Fig. 4.11d. Similar to the earlier ion saturation current spectra, the simulation floating potential autopower peaks at same frequencies as the experiment. The expectations to this results is the density equilibrium profile scan, which contains more autopower and peaks at different frequencies when the $z = L_z/4$ density profile is used. From floating potential comparisons, we can again deduce that the axially local density equilibrium profile of

$z = L_z/2$ gives better agreement with turbulence quantities measured at $z = L_z/2$.

4.4.3 Particle Flux Γ

The estimation of cross-field transport in plasma turbulence models has been a subject of interest in many magnetically fusion turbulence models. However, calculation of the quantities such as particle flux includes the uncertainties of the phase between fluctuations of density or heat fluctuations and velocity fluctuations[RTF$^+$09]. In Fig. 4.12a, we show the radial particle flux from the simulations, at axial location $z = L_z/2$. Fig. 4.12b compares the radial synthetic flux of simulations against the experimental measurements of particle flux. Experimentally, the flux has been calculated at $z = L_z/2$ and filtered from 5 to $30kHz$ to isolate the finite drift-wave-driving modes[CTXM$^+$13]. This frequency range corresponds to the dominant linearly unstable drift-wave modes[CTXM$^+$13]. From the simulation, we have also filtered the flux within the same frequency range. A similar trend between synthetic flux in the simulations and experimental measurements is obtained, where the simulations capture the highs and dips of experimental measurements within the uncertainties. Moreover, the peaks of synthetic particle flux and real particle flux qualitatively show relatively similar maximum transport. However, the simulation scan with the systematic uncertainty of equilibrium density shows larger particle flux, and significantly larger synthetic flux compared to other simulation scans. This again shows better agreement of simulation scans with the $z = L_z/2$ density profile to predict the experimental measurements of flux at $z = L_z/2$.

An interesting observation in the particle flux measurements is the difference between the synthetic and the physical flux. The electron temperature fluctuations influence the ion saturation current and floating potential cross-phase $\zeta(\tilde{I}_{sat}, \tilde{\phi}_f)$, setting it apart from the radial cross-phase profile of density-plasma potential cross-phase $\zeta(\tilde{n}, \tilde{\phi})$. In Fig. 4.13, we have compared the difference in the power-weighted $\zeta(\tilde{I}_{sat}, \tilde{\phi}_f)$

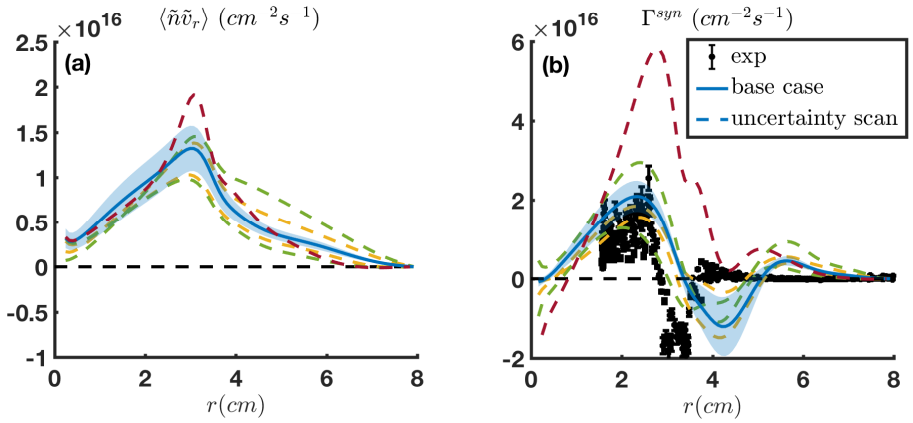

Figure 4.12: (a) Radial particle flux of the simulations at $z = L_z/2$. (b) Comparison of the experimental particle flux measurements and the synthetic particle flux at $z = L_z/2$. The dashed lines correspond to nonlinear simulation of the cases shown in Fig. 4.4, and the shaded band indicates the standard deviation of sub-window averaging of the base case simulation.

and $\zeta(\tilde{n}, \tilde{\phi})$ in the base case simulation. Both cross-phases show less than $\pi/4$ phase difference indicating dominant drift-wave dynamics, and are similar to the sign of synthetic and physical fluxes shown in Fig. 4.12, indicating that the density-potential cross-phase is important in determining the the direction of flux. The power weighted cross-phase of ion saturation current and floating potential is measured in the CSDX linear device at different experimental condition[BTA$^+$05], where the experimental and synthetic $\zeta(\tilde{I}_{sat}, \tilde{\phi}_f)$ profile qualitatively similar to our simulation conditions.

In drift-wave turbulence, the transport depends on the sign of density-potential cross-phase and k_θ[Hor99], and one would expect monotonically decreasing density to yield outward transport. Thus, the sign reversal of the experimental flux may be due to these phase distortion due to finite $\tilde{T}_e$ effects on the measurements. Nevertheless, in the experiments, the cross-field flux reversal is also observed in the other experimental condition of CSDX[CTD$^+$15], which has been found by direct time-resolved imaging of the inward motion of light intensity fluctuations. Further study and synthetic camera imaging diagnostics is needed to fully understand these experimental observations.

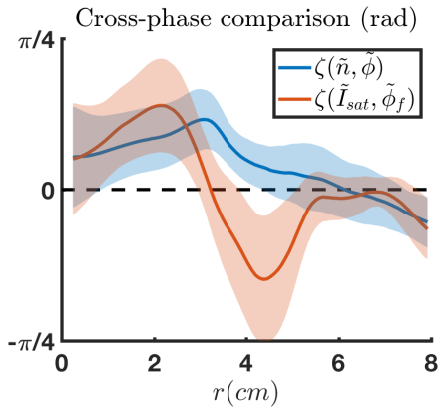

Figure 4.13: Comparison of power-weighted density-plasma potential cross-phase $\zeta(\tilde{n},\tilde{\phi})$ and ion saturation current-floating potential cross-phase $\zeta(\tilde{I}_{sat},\tilde{\phi}_f)$ in the base case simulation. The shaded bands indicate the standard deviation of sub-window averaging of the base case simulation.

It is important to note that the presence of secondary electron emissions in the Langmuir probe measurement at even very low temperatures can reduce the value of sheath factor[NXK$^+$16]. To further investigate the sensitivity of secondary electron emissions in the sheath factor on our simulation interpretation, we have performed an initial sensitivity analysis on the synthetic diagnostics setup using the modified sheath factor using half the theoretical value $\Lambda_m = 2.5$ (In reality, the sheath factor can have radial dependence, but the radial dependency is not explored in this thesis). In Fig. 4.14, we have plotted the synthetic floating potential and synthetic particle flux of the base case simulation, with both theoretical $\Lambda_t = 5.1$ and modified $\Lambda_m = 2.5$ values, and compared them against the experimental measurements. We can see for either finite sheath factor, the floating potential is affected and the $\zeta(\tilde{I}_{sat},\tilde{\phi}_f)$ cross-phase gets distorted from $\zeta(\tilde{n},\tilde{\phi})$. As observed, the magnitude of sheath factor intensifies the effects of cross-phase distortion in the interpretation of floating potential fluctuation amplitudes and the calculation of synthetic particle flux. Similar cross-phase distortion due to electron temperature fluctuations in synthetic Langmuir probe measurement also reported by [NRR$^+$12]. Nonetheless, for a more conclusive validation study, a rigorous study of

sheath factor radial profile is needed.

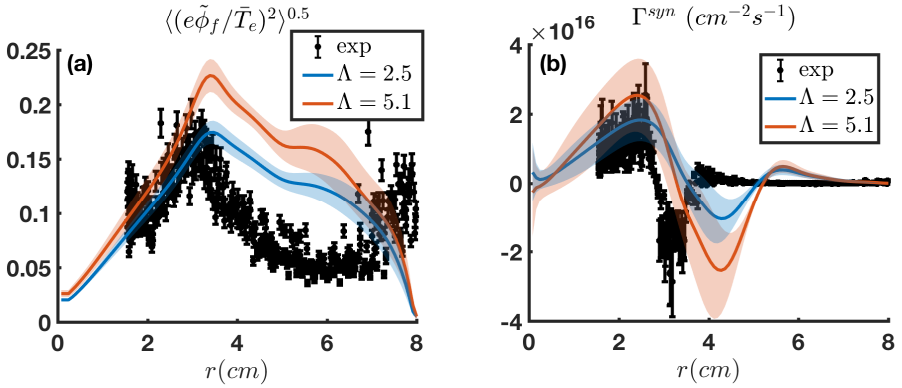

Figure 4.14: Comparison of experimental and synthetic (a) floating potential fluctuation RMS amplitudes and (b) particle flux measurements with different values of sheath factors $\Lambda_t = 5$ and $\Lambda_m = 2.5$ at $z = L_z/2$. Shaded error bars indicate standard deviation of sub-averaging window for the base case simulation. The shaded bands indicate the standard deviation of sub-window averaging of the base case simulation.

4.4.4 Reynolds Stress R_t

Another important turbulence quantity is the Reynolds stress or vorticity flux (R_t). Predicting this parameter is essential in studies of zonal flow generation. Experimentally, this value is calculated by multiplying turbulent radial velocity and azimuthal velocity calculated from spatial gradients in Langmuir probe floating potentials. Hence, similar to particle flux, a synthetic Reynolds stress measurement may differ from the actual Reynolds stress. In Fig. 4.15a, we have shown the Reynolds stress obtained from the simulation scans at $z = L_z/2$. In Fig. 4.15b, we have compared the synthetic Reynolds stress R_t^{syn} against the experimental measurements at $z = L_z/2$. We observe the Reynolds stress magnitude is significantly larger in simulation scan with $z = L_z/4$ density profile. This effect is even more pronounced in the synthetic Reynolds stress observations. The Reynolds stress shown in Fig. 4.15 has been filtered from 5 to 30kHz in both the synthetic and the experimental measurements.

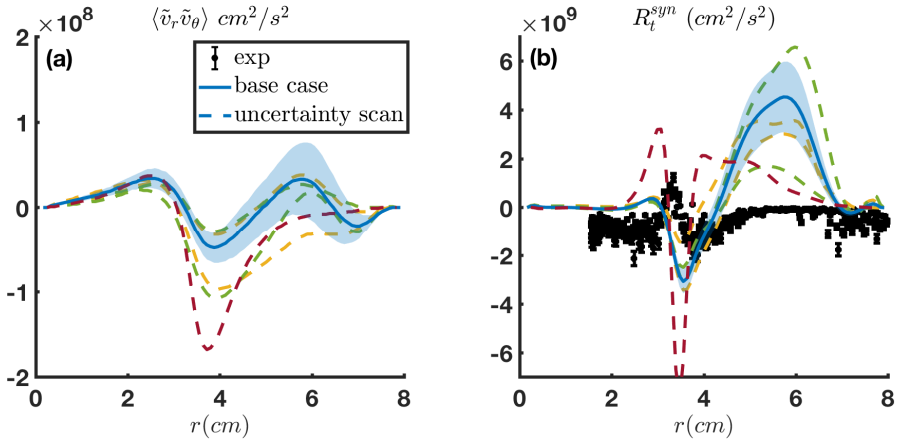

Figure 4.15: (a) Reynolds stress computed from the simulations at $z = L_z/2$. (b) Comparison of the experimental Reynolds stress measurements and the synthetic Reynolds stress at $z = L_z/2$. The dashed lines correspond to nonlinear simulation of the cases shown in Fig. 4.4, and the shaded band indicates the standard deviation of sub-window averaging of the base case simulation.

We can observe that the synthetic R_t^{syn} is about one order of magnitude larger than physical R_t. In the experimental measurements, Reynolds stress is vanishingly small at $5cm < r < 7cm$ in the experimental measurements, while the simulations are producing positive stress. This result is consistent with overprediction of fluctuation amplitudes at larger radii.

4.4.5 Azimuthal Velocities $\tilde{V}_{ph}, \tilde{V}_{E\times B}$

Zonal flows[DIIH05] are an important drift-wave regulation mechanism, and their formation dynamics have been subject of many studies. Experimentally, the measurement of zonal flows is a difficult task, since one has to average the velocity over both azimuthal and axial potential fluctuations. Usually a radial profile of the *low-frequency* portion of $E_r(r)$ is measured or inferred, the results of which is then taken to be the *zonal flow*. For example, in our work the low-frequency ($\leq kHz$) azimuthal velocity has been measured through different techniques such as time-delay-estimation (TDE)[YHT$^+$07], laser-induced fluorescence (LIF)[CTML$^+$12], and swept Langmuir probe[CTXM$^+$13]

techniques. In this section we will compare the azimuthal velocities with the results of these independent set of measurements.

In the experiments, the study of zonal flow generation and nonlinear energy transfer have been previously reported at $L_z/4$ downstream from the source[CTML$^+$12], at a different axial location from the measurements shown in the previous sections. Hence in this section, we compare the simulation prediction at $z = L_z/4$ against the experimental observation. In Figs. 4.16, we have compared the experimental TDE phase velocity of floating potential time series obtained from multi-tip probes against the TDE phase velocity of synthetically computed floating potential time series at two azimuthally separated grid points of the simulation domain at $z = L_z/4$. Both experimental measurements and simulation potentials are filtered for wavenumber $0.1cm^{-1} < k_\theta < 12cm^{-1}$, and low and high bandpass filters on frequency is used to filter for only frequencies of interest ($3kHz < f < 20kHz$) where the finite drift-wave modes are experimentally known to be active. The systematic uncertainty of TDE velocity in experiments is estimated by choosing different two-tips configuration of from 9-tip array, while in the simulation, the uncertainty is calculated by taking standard deviation of each two adjacent grid points in the azimuthal direction. We observe that the TDE velocity computed from synthetic floating potential is in reasonable agreement with experimental measurements in the inner core $r < 4cm$, while it largely overestimates the edge phase velocity and shearing rate.

To understand the phase velocity of the simulation results, we investigated the difference of the two-point spectrum $S(m, f)$ for synthetic floating potentials, computed at two different radii $r = 3.6cm$ and $r = 5cm$ for the base case simulation (see Fig. 4.17). Moreover, we have also over-plotted the linear plasma frequency ω_{lin} calculated from the linear dispersion relation, the $E \times B$ frequency $\omega_{E\times B} = k_\theta v_{E\times B}$, the electron diamagnetic frequency $\omega_{*_e} = k_\theta \rho_s c_s / L_n$, and the TDE phase velocity V_{ph} calculated from the floating

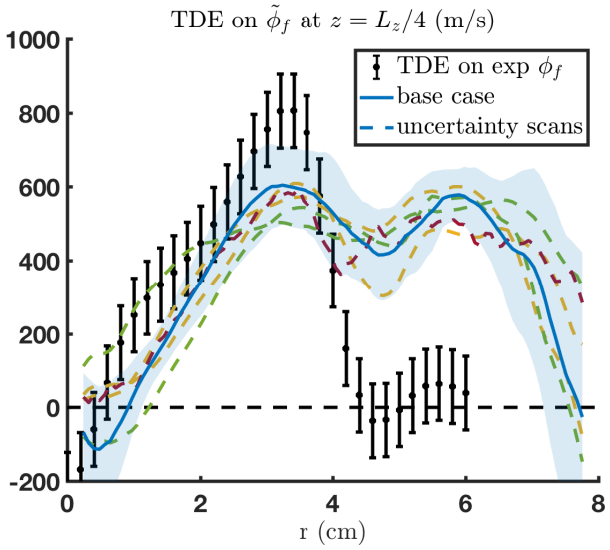

Figure 4.16: Comparison of experimental time-delay-estimation (TDE) phase velocity of floating potential measurements versus TDE velocity of synthetic floating potential of simulation scans at $z = L_z/4$. The dashed lines correspond to nonlinear simulation of the cases shown in Fig. 4.4, and the shaded band indicates the standard deviation of sub-window averaging of the base case simulation.

potential in the simulation. We observe that linear frequency is very dispersive with $\omega_{lin} > \omega_{*_e}$ for lower mode numbers due to nonlocality of the model. As discussed below, the self-generated $E \times B$ velocity in the simulation is fairly small and thus Doppler shift effects are minimal. However, we observe the nonlinearly saturated phase velocity is different than both diamagnetic frequency and $E \times B$ velocities.

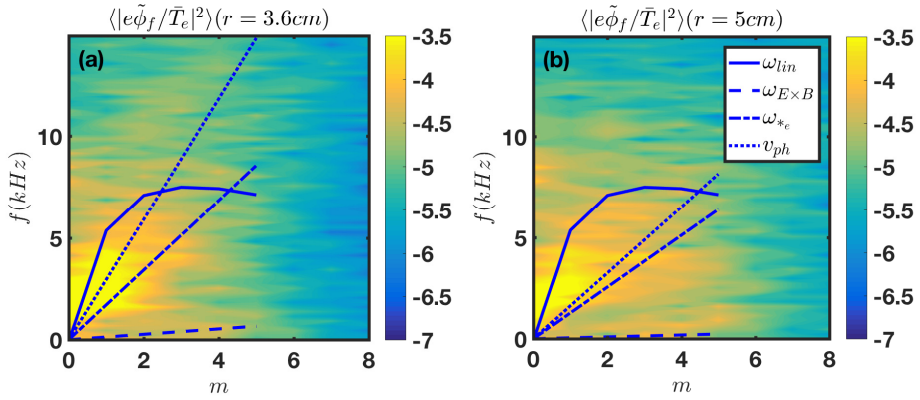

Figure 4.17: Comparison of frequencies and two-point spectrum at (a) $r = 3.6cm$ and (b) $r = 5cm$ of the base case simulation.

We also have compared the self-generated zonal $\tilde{v}_{E\times B}$ velocity against the $v_{E\times B}$ velocity calculated from LIF measurements. In the experiments, the $E\times B$ velocity can be obtained by subtracting the ion diamagnetic velocity (v_{*_i}), computed from the ion temperature and density profiles, from the bulk fluid velocity measured from the LIF diagnostics (v_{LIF}). A detailed discussion of this subject and comparison with other independent experimental diagnostics of $E\times B$ (e.g. swept Langmuir probe measurements of plasma potential) can be found in a previous publication[CTML$^+$12].

In Fig. 4.18, we compare the self-generated $E\times B$ velocity in the simulation against the experimentally inferred $E\times B$ profile from LIF measurements. We can observe that the simulations scans with equilibrium density profiles at $z=L_z/2$ largely underestimate the experimental $E\times B$ velocity measurements at $z=L_z/4$. However, the simulation scan with equilibrium density of $z=L_z/4$ fairly captures the shape and magnitude of experimentally measured $E\times B$ flow. These results show the importance of local steepening, and a detailed uncertainty scan for quantitive validation of self-generated zonal $E\times B$ flow.

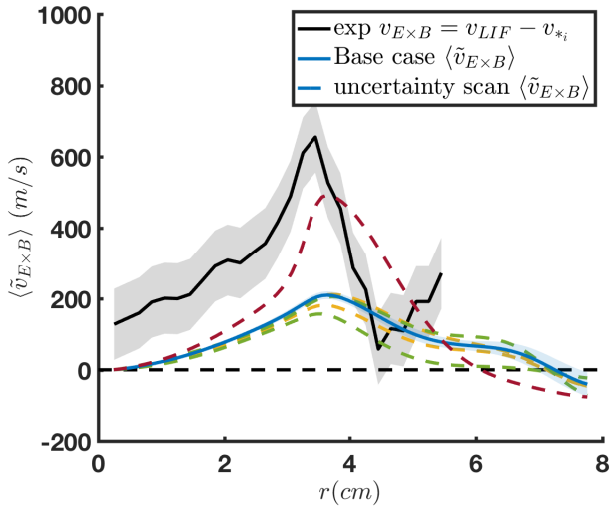

Figure 4.18: Comparison of $v_{E\times B}=v_{LIF}-v_{*_i}$, and $v_{E\times B}=\partial_r\tilde{\phi}_{pl}$ obtained from experimental measurements, against the simulations self-generated $\langle\tilde{v}_{E\times B}\rangle$.

4.4.6 Nonlinear kinetic energy transfer T_u

The most complicated turbulence observables in model-experiment comparisons are the nonlinear kinetic energy transfer T_u, and the internal energy transfer T_n. Experimentally, kinetic energy transfer in CSDX has been measured through floating potentials using a 3×3 Langmuir probe array installed at $z = L_z/4$ down the plasma source, calculating $T_u^{exp}(f) = -\sum_{f_1} \Re\langle(\hat{z} \times \nabla_\perp \phi_f^*(f))[(\hat{z} \times \nabla_\perp \phi_f(f - f_1) \cdot \nabla)(\hat{z} \times \nabla_\perp \phi_f(f_1))]\rangle$[XTH+10]. In our simulations, the normalized physical nonlinear kinetic energy transfer can be computed as $T_u(f) = -\frac{a}{\rho_s}\Re\langle(e\tilde{\phi}^*(f)/\bar{T}_e)P_\Omega(f)\rangle$ where $P_\Omega = \{e\tilde{\phi}/\bar{T}_e, e\rho_s^2\tilde{\Omega}/\bar{n}\bar{T}_e\}$ is the normalized vorticity Poisson bracket used in the model. We can also construct the synthetic kinetic energy transfer rate for the simulation results using floating potential instead of floating potential as $T_u^{syn}(f)$ as introduced in Sec. 4.3. We should note that radial variation of equilibrium density is not included in the experimental vorticity measurements, therefore has not been taken into account in our synthetic diagnostics setup as well.

The contour plots of $T_u(f)$ and $T_u^{syn}(f)$ in the region of maximum equilibrium gradients for the base case simulation are shown in Figs. 4.19a-b, respectively. We can observe transfer of energy in $T_u(f)$, where the energy in finite frequency $f \approx 8kHz$ transfers to low frequencies $f < 2kHz$. The same qualitative trend can also be observed in the synthetic diagnostic measurements. However, the effect of electron temperature fluctuations significantly amplifies the measured nonlinear energy transfer (about two orders of magnitude), and may influence the sign of the measured energy transfer (e.g. see the energy transfer of $f \approx 1kHz$ at $r \approx 3cm$ in the Fig.4.19b). In Fig. 4.19c we compare the kinetic nonlinear energy transfer T_u of the simulation scans. One notable observation is the difference between the simulation scans with the density equilibrium of $z = L_z/2$ versus the simulation scan of $z = L_z/4$ density equilibrium. We observe the simulation with the steeper equilibrium density of $z = L_z/4$, shows much larger nonlinear

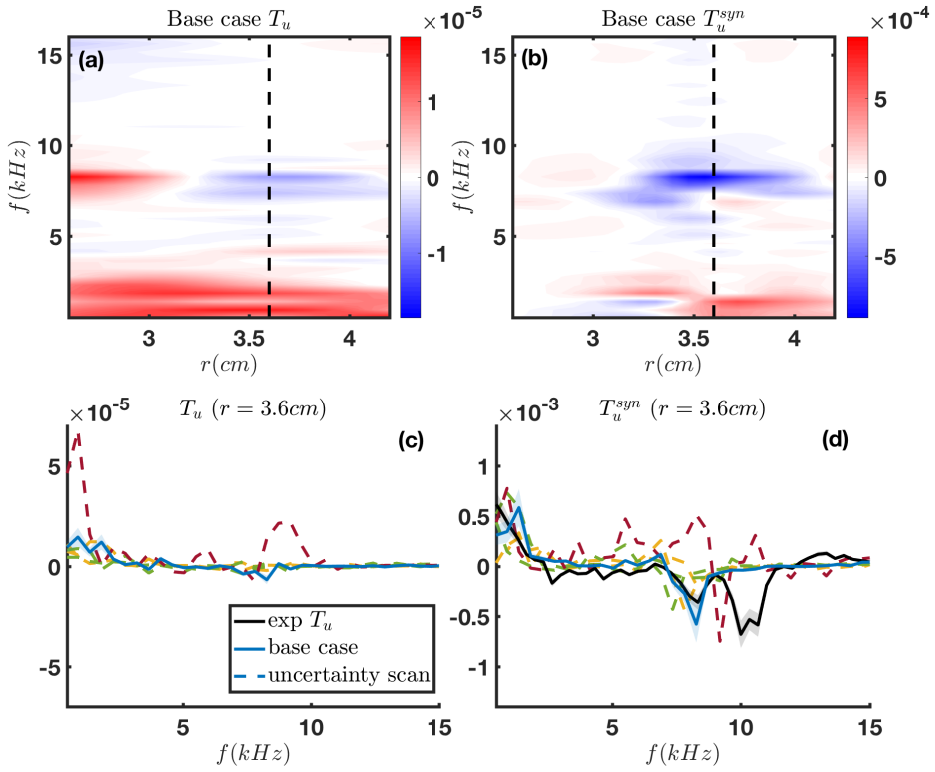

Figure 4.19: (a) Physical nonlinear kinetic energy transfer, and (b) synthetic nonlinear energy transfer for the base case simulation. (c) Comparison of T_u spectra of simulation scans at $r = 3.6cm$ and $z = L_z/4$. (d) Comparison of T_u^{syn} spectra of simulation scans against the experimental measurements at $r = 3.6cm$ and $z = L_z/4$. Shaded bands indicate the sub-window resolution error. Experimental data is taken from [XTH+10] with permission.

energy transfer to the lower frequencies, consistent with the larger generation of $E \times B$ flow, shown in Fig. 4.18.

In Fig. 4.19c, we have shown the comparison of normalized kinetic energy transfer between experimental measurements and synthetic diagnostics measurements of the simulation results at maximum density gradient region ($r = 3.6cm$). Although T_u^{syn} Qoi shows fairly good qualitative agreement with experiment, the magnitude of T_u^{syn} is about one order of magnitude larger than T_u, mainly due to the effects of finite fluctuations of electron temperature. Moreover, we observe nearly all the simulation scans

reproduce experimental measurements of nonlinear kinetic energy transfer within the uncertainties, and the major difference of physical nonlinear kinetic energy transfer due to the systematic uncertainty of density equilibrium is not seen in the synthetic diagnostic measurements. These results indicate that local kinetic energy transfer measured in both experiment and through synthetic diagnostics is a good qualitative representation of nonlinear advection of kinetic energy, however they do not quantitatively correspond to energy transfer needed for experimentally generated zonal flow. Further generalization of vorticity, including the density fluctuations in the perpendicular divergence is needed for capturing the quantitive physical nonlinear kinetic energy transfer.

4.5 Discussion

In this Chapter, we have performed validation of a collisional drift-wave/zonal-flow turbulence model against the experimental measurement of CSDX linear device with insulating end plates. We recognized the experimental measurement uncertainties, and performed linear scans and nonlinear simulations with various input profiles within the experimental uncertainties. The input profile uncertainties can lead to large variation in the linear growth rates. A statistical uncertainty study showed that the largest linear sensitivities in the system arise from the ion temperature and the edge gas temperature uncertainties. Moreover, variation in the density equilibrium profile at different axial locations, gives rise to a systematic uncertainty of equilibrium density input to the model. Since our current model does not account for the axial variation of equilibrium profiles, we ran additional simulations with different fits to equilibrium density measurements from different probe port. We ran a simulation with the median base case with the equilibrium density of the middle of device, plus additional set of five simulation scans over the sensitive input parameters T_{i_0}, T_{g_b}, and equilibrium density fit of measurements

at the other probe port to account for the input parameter uncertainties.

For the simulation comparison against the experimental measurements, we translated the typical simulation outputs ($\tilde{n}$, $\tilde{\phi}$, and $\tilde{T}_e$) into synthetically measured quantities such as $\tilde{I}_{sat}$ and $\tilde{\phi}_f$, and compared the radial profile and frequency domain of QoIs against the experimental observations. We observed a fairly good agreement between simulation and the CSDX experimental measurements in the core region ($r \lessapprox 4cm$). However, the simulations overestimate the fluctuations in the edge region ($r > 4cm$). We suspect since the density fluctuations become comparable to the density equilibrium (i.e. $\tilde{n}/\bar{n} \approx 1$) at the edge of plasma column ($r > 5cm$) the small flucutations assumption ($\tilde{n}/n_0 \ll 1$) breaks down. A source driven model that evolves full profiles of turbulence quantities (instead of evolving just fluctuations on a fixed background profile) might be needed for better quantitive validation of the experimental observations near the edge. In addition, the effects of parallel ion dynamics might be important in convecting the fluctuations in axial direction, which is neglected in the current model and needs to be studied as well.

Moreover, the effects of electron temperature fluctuations in the synthetic Langmuir probe interpretation for a cold plasma setting was investigated as well. We observed that the measurement of ion saturation current fluctuations through Langmuir probe is a good representation of density fluctuations in CSDX experimental condition. However, the floating potential fluctuations may be different from plasma potential fluctuations due to the finite electron temperature fluctuations. This distortion can have an effect on the interpretation of fluxes where the velocity fluctuations are obtained from spatially separated floating potential fluctuations instead of plasma potential fluctuations. The results motivate the electron temperature fluctuations measurement in the experiments. Moreover, the results shows the importance of synthetic diagnostics in the simulation-experiment comparisons.

Perhaps, the most important observation in our simulation scans, was the differ-

ence in turbulence characteristics due the systematic uncertainty of density equilibrium inputs. We observed that equilibrium density steepening influences the main source of instability drive, and stiffly affects the turbulence saturation levels. By comparing the simulation predictions against the experimental measurements, we realized that local equilibrium density input at a specific axial location is important in validating the experimental measurements of that specific axial location. Moreover, our simulation scans show that the generation of $E \times B$ is very sensitive to the steepening of density equilibrium.

The current experimental measurements and simulation benchmarks indicate a modest axial density equilibrium gradient is necessary for quantitive quantitative agreement with $E \times B$ zonal flow experimental measurements at different axial location. A source-driven model which evolves full parameters, and accounts for axial variations, with source being on one side and insulating sheath on the other side may be needed for further improvement of simulation results against the experimental measurements.

4.6 Acknowledgement

The text and data in Chapter 4, is a reprint of the material as it appears in Vaezi, P., Holland, C., Thakur, S. C., & Tynan, G. R. (2017). *Validation Study of a Drift-Wave Turbulence Model for CSDX Linear Plasma Device*. Physics of Plasmas 24 (9), 092310. The dissertation author was the primary investigator and author of this paper.

Chapter 5

Improved Uncertainty Quantification in a Plasma Turbulence Validation Study

One of the primary challenges for computational validation studies of magnetic fusion energy experiments such as International Thermonuclear Experiment Reactor (ITER) are the many uncertainties in experimentally derived input parameters[FBC+16]. Addressing this issue requires forward propagation of input uncertainties through a computational model, and performing statistical model-experiment comparison assessments on the resulting model responses[GEMC+06, Mah00]. A rigorous uncertainty quantification process moves beyond qualitative sensitivity analysis to enable quantitive validation studies[Hol16]. Classical sensitivity analysis, as often used by the plasma micro-turbulence community[RHS+11, Hol16], can give insight into the goodness or deficiency of a specific model. However, it does not quantify the input uncertainties with a rigorous confidence interval. [OTH04] identified a process by which qualitative comparisons, i.e. what where termed *viewgraph norms*, can be transformed into rigorous

quantitative metrics via inclusion of these uncertainties. Many past and current plasma turbulence validation studies using nonlinear simulations were limited to qualitative comparison. More recently, the plasma community has recognized the importance of uncertainty quantification (UQ) in validation and prediction of magnetically-confined plasma turbulence[Hol16]. Within the computational power of current clusters, the plasma community has explored the inclusion of UQ in analysis of reduced models, such as TGLF [SKW07], but UQ analysis in core-hour limited nonlinear simulations, e.g. gyrokinetic simulations, remains a challenging task[Hol16]. Some previous literature of UQ inclusion in reduced model assessments, and in the fitting of experimental measurements, includes but not limited to Refs. [PLD$^+$98, WPR$^+$10, CGM$^+$15].

To quantify the aggregate fractional error (the relative error between simulation and experimental measurement) of a non-deterministic validation study, we need to have knowledge of the quantity of interest (QoI) probability distributions. In this Chapter, we investigate the Probabilistic Collocation Method (PCM)[WTM96, TPPM97] for improved, fast and accurate uncertainty quantification. This method has been introduced and widely used for quantification of uncertainties in other fields e.g. fluid turbulence simulations. Here, we present the implementation and implications of using this UQ method in validation studies of magnetically confined plasma turbulence simulations.

The rest of this Chapter is organized as follows: In Section 5.1, we discuss the theory and logic behind the Probabilistic Collocation Method. In Section 5.2, we compare the forward propagation of uncertainties through the PCM against the analytical transformation of probability distributions. In Section 5.3, we study the forward propagation of uncertainties above and near the critical gradients, in a simple set of collisional drift-wave simulations. In Section 5.4, we apply the PCM uncertainty quantification method to a validation study of the CSDX linear plasma device, using the model from Sec. 5.3. In Section 5.5, we summarize the findings and discuss the future directions.

5.1 Uncertainty quantification via Probabilistic Collocation Method

Different sources of uncertainty all contribute to validation studies of an experimental case. Experimental uncertainties may originate from plasma reproducibility, diagnostic properties, or experimental fitting evaluations[RRT$^+$15]. Simulation uncertainties may arise from the use of a reduced models form[OM11] (e.g. errors originating from use of a reduced model rather than a full kinetic description of the plasma), due to numerics[ODR$^+$02] (e.g. due to the numerical integration scheme used or finite grid resolution), or uncertainties in input parameter measurements. In this Chapter, we will focus on quantifying the uncertainties from input parameter uncertainties arising due to experimental measurements, and defer the detailed analysis of other error sources to a future study. A probability distribution function (PDF) of uncertainties in the input parameters becomes a PDF of simulation outputs. The goal here is to quantify the uncertainty of the simulation response for quantities of interest (QoIs) via these PDFs, so that the direct statistical comparison of predicted quantities with experimental measurements can be made.

Assuming an initial value problem in space $\mathbf{x}$, and time t, the aim is to quantify the uncertainty in the response

$$r = f(\mathbf{x}, t, \mathbf{I}),$$

which depends on the uncertain parameters $\mathbf{I}$. The typical setting is that we know the joint probability distribution of input parameters $p_{\mathbf{I}}$ from experimental measurements e.g. temperature gradient, but nothing is known about probability distribution (p_r) of model response r e.g. turbulent flux. A goal of uncertainty quantification is to determine p_r for QoIs.

To quantify the uncertainties in QoIs, several methods exist. A straightforward

method is Monte Carlo simulation, where many random samples taken from the input parameter PDF are used to construct the p_r distribution[RK11]. However, Monte Carlo simulation for nonlinear turbulence models is often computationally very expensive due to the large numbers of degrees of freedom in the equations[LWB07]. Another approach as shown in Fig. 5.1 is to approximate $r(\mathbf{I})$ in high probability region of $p_\mathbf{I}$ to estimate response probability distribution p_r[WTM96], assuming that the transformation from the input parameters to the response is smooth. As a result, as also shown in Fig. 5.1, with the knowledge of inputs probability distribution, $p_\mathbf{I}$, an actual or approximated response-input relation, $r(\mathbf{I})$, one can find the response probability distribution p_r using the concept of the probability transformation, $\int p_r dr = \int p_\mathbf{I} d\mathbf{I}$, so that if $r(\mathbf{I})$ relation is smooth and one-to-one, we shall have $p_r = p_\mathbf{I}|dr/d\mathbf{I}|$.

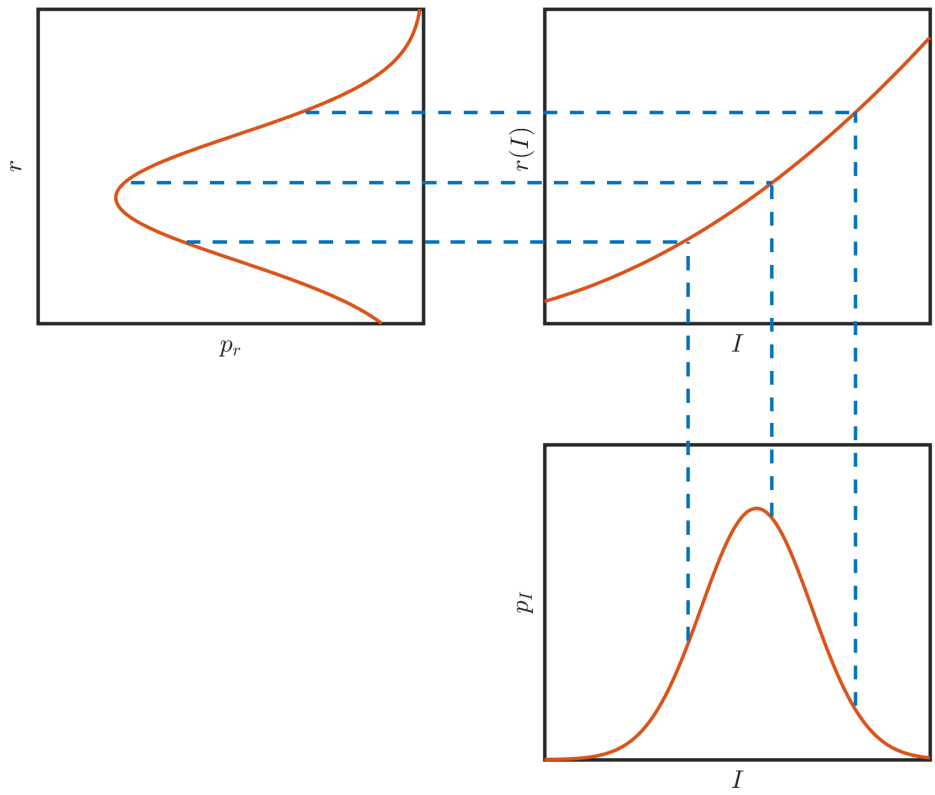

Figure 5.1: The schematic of constructing p_r by approximating $r(\mathbf{I})$. Samples (blue dashed lines) are used to estimate the $r(\mathbf{I})$ function.

The common methods that utilize such approximation includes the intrusive Galerkin polynomial chaos, non-intrusive pseudo-spectral method, and the non-intrusive probabilistic collocation method [LWB07]. Among these, the Galerkin method requires rewriting the model equations to account for the uncertainties when solving the equations. Non-intrusive methods have the advantage of needing only input parameters and simulation response values, while treating the model and simulation as a black box function. Thus, they make excellent choices for uncertainty quantification using established codes, since they can benefit from previous nonlinear simulation runs. In this Chapter, we have pursued the uncertainty quantification via probabilistic collocation method (PCM), due to its relative simplicity and easier implementation.

The PCM approach combines the idea of a chaos transformation like polynomial chaos[Bec73] and the collocation approach for Lagrange interpolation[FL15], to find the probability distribution of response quantities using a reduced number of simulations with a decoupled system of equations. Previous UQ studies in other fields have used the PCM approach[WTM96, TPPM97, LWB07, HL04]. Multiple numerical packages are publicly available for use in implementing these methods, such as DAKOTA Project[GEMC$^+$06], and open-source framework chaospy[FL15]. In this study, we have used chaospy for our uncertainty quantification analysis. In the rest of this section, we will explain the step-by-step implementation of PCM.

5.1.1 Specifying Input Uncertainty Distribution

The first step in obtaining the probability distribution of the response p_r via PCM is to determine the input parameters probability distributions $p_{\mathbf{I}}$. This first step is necessary for both generating the polynomial chaos expansion and for efficient sampling of the input uncertainty distributions when performing simulation runs.

Knowledge of the input PDF usually comes from either direct observation or

modeling of the experimental measurements. For instance, the input PDF of a stochastic quantity can be determined from sufficiently long temporal measurements in the experiment. Another approach is to perform a specific experiment multiple times and obtain the experimental probability distribution of input parameters. These uncertainties can correspond to plasma reproducibility, diagnostic properties, or experimental fitting evaluations. Thus, joint probability distribution of different experimental uncertainties should be considered as input parameter probability distribution into the simulation.

In general, the PDFs of multiple input parameters must be specified, and these inputs can be correlated. Understanding the joint distributions and their correlation can directly affect input sampling, as will be shown in following sections.

5.1.2 Generating Chaos Polynomials expansion

The polynomial chaos expansion[FL15] is a subset of polynomial expansions specifically designed for uncertainty quantification, where a sum of orthogonal polynomials is used to approximate the response parameter r, and can be written as

$$r = f(\mathbf{x}, t, \mathbf{I}) \approx \hat{f}(\mathbf{x}, t, \mathbf{I}) = \sum_{n=0}^{N} c_n \mathbf{P_n}(\mathbf{I}), \tag{5.1}$$

where the $\mathbf{P}_n$s denote the set of orthogonal polynomials, the c_ns denote the coefficients of the polynomial expansion, and n is the order of polynomials to be used. Unlike Lagrange polynomials, chaos polynomials are orthogonally generated according to the input probability distribution to avoid numerical oscillations. Assuming the transformation from $p_{\mathbf{I}}$ to p_r is smooth, we can draw samples and find an approximate $\hat{f}$ using chaos polynomials instead of the general function f, to enable the transformation of probabilities. The set of polynomials must satisfy the orthogonality property for an arbitrary vector in the input

probability distribution space **I**,

$$\langle \mathbf{P}_n, \mathbf{P}_m \rangle = \int P_n(\mathbf{I}) P_m(\mathbf{I}) p_I(\mathbf{I}) d\mathbf{I} = 0 \qquad n \neq m. \tag{5.2}$$

For constructing the orthogonal polynomials, the numerically stable three-term discretized Stieltjes recursion can be used[Gau82],

$$P_{n+1} = (\mathbf{I} - A_n) P_n - B_n P_{n-1}; \quad P_{-1} = 0; P_0 = 1, \tag{5.3}$$

with A_n and B_n are the recurrence coefficients defined as

$$A_n = \frac{\langle \mathbf{I} P_n, P_n \rangle}{\|P_n\|^2}; \qquad B_n = \begin{cases} \frac{\|P_n\|^2}{\|P_{n-1}\|^2} & n > 0 \\ \|P_n\|^2 & n = 0 \end{cases} \tag{5.4}$$

where $\|P_n\| = \sqrt{\sum_{i=1}^{n} |P_i|^2}$ denotes l^2 norm. One can fit different orders of chaos polynomials to the samples, and perform sensitivity analysis on the order of polynomials to obtain the optimal fit. Furthermore, the PCM approach can be extended to multiple dimensions, to accommodate multivariate input probability distributions, as discussed by [FL15].

5.1.3 Input sampling and generation of collocation points

Choosing a minimum set of input parameter samples within the range of uncertainties is another crucial step. Depending upon the details of the joint PDF of the uncertain input parameters, different sampling techniques such as Latin Hypercube, Hammersley sequence, Sobol sequence sampling, etc. can be utilized to draw a number of collocation points from input probability distribution[FL15]. Moreover, taking samples from multivariate input distributions is not an easy task. Nevertheless, effective sampling

from multivariate input probability distribution can be facilitated with the aid of Rosenblatt transformations[Ros52]. Rosenblatt transformation can transform any arbitrary distribution can be transformed to/from the uniform distribution[Bro07]. Then, relevant sampling method can be applied to the transformed distribution to draw samples. In the end, the samples can be transformed back to the original multivariate input distribution, using inverse Rosenblatt transformation.

5.1.4 Solving for Chaos Polynomial approximation and analyzing the uncertainties

After performing the simulations for a set of sample input parameters ($\mathbf{I}_k$), we obtain solutions for the model response $r \approx \hat{f}$ values, which yields in an over-determined set of linear equations ($k > N$) for the polynomials coefficients (c_n),

$$\begin{bmatrix} P_0(\mathbf{I}_0) & \cdots & P_N(\mathbf{I}_0) \\ \vdots & \ddots & \vdots \\ P_0(\mathbf{I}_{k-1}) & \cdots & P_N(\mathbf{I}_{k-1}) \end{bmatrix} \begin{bmatrix} c_0 \\ \vdots \\ c_N \end{bmatrix} = \begin{bmatrix} \hat{f}(\mathbf{I}_0) \\ \vdots \\ \hat{f}(\mathbf{I}_{k-1}) \end{bmatrix}. \tag{5.5}$$

One then directly can obtain the polynomial coefficients c_n, using conventional regression techniques such as the least squares method. With the polynomial coefficients c_n thus determined, the approximate response function $\hat{f}$ can now be used to calculate an approximate PDF of the response, using the concept of probability transformation. This approximated p_r can be used to calculate statistical quantities suitable for comparisons against the experiment. For instance, the mean model response,

$$\mu_{\hat{f}} = \left\langle \sum_{n=0}^{N} c_n P_n \right\rangle = \sum_{n=0}^{N} c_n \langle P_n, P_0 \rangle = c_0, \tag{5.6}$$

and variance,

$$\sigma_{\hat{f}} = \sum_{n=0,m=0}^{N} c_n c_m \left(\langle P_n, P_m\rangle - \langle P_n\rangle\langle P_m\rangle\right) = \sum_{n=0,m=0}^{N} c_n c_m \langle P_n, P_m\rangle - c_0^2$$
$$= \sum_{n=1}^{N} c_n^2 \|P_n\|^2, \tag{5.7}$$

are straightforward to calculate, using the orthogonal property of the chaos polynomals expansion.

5.2 Discussion on probability transformation

As discussed above, one can obtain an approximation to the response probability distribution for quantities of interest (QoIs) using the PCM uncertainty quantification scheme. To illustrate the utility of PCM in doing so, we first compare its output for a simple problem, to simple UQ approach (where it assumes the QoI distributions are normal, and mean and standard deviation of the QoI from samples correspond to the mean and standard deviation of the normal distribution) widely used in the microturbulence community[Hol16]. Consider case of a simple offset-linear flux-gradient relationship $Q(z) = Q_0 z + Q_1$. Here, the flux Q is the QoI or the response of model, and the normalized driving gradient length scale $z = -R\nabla T/T$ is the input. Thus, according to the previous definitions, in this case $p_{\mathbf{I}} = p_z$ and $p_r = p_Q$. Therefore, by knowing that z and $Q(z)$ functions are continuous, and one-to-one in the region of our interest, we can obtain the analytical QoI distribution $p_Q = p_z/|dQ/dz|$. For a specified normal input probability distribution p_z (Fig. 5.2a), and analytical relation between Q and z (Fig. 5.2b), and the analytical QoI probability distribution p_Q is shown in Fig. 5.2c as the dashed black line. Now, we draw five samples from the high probability region of z (the mean of the distribution, as well as $\pm 0.5\sigma$ and $\pm 1\sigma$ confidence intervals, where σ is the varience

of p_z), and calculate the $Q(z)$ for those sample points. A simple UQ approach used in the plasma microturbulence community would be to assume the QoI distribution, p_Q, is normal, and that the mean and standard deviation of the samples are the same as that of the QoI normal distribution. The resulting QoI distribution of this simple UQ method is shown in Fig. 5.2c as the red line. As we observe, the p_Q given by the simple method does not match analytic p_Q. The main reason behind this discrepancy is the lack of information due to too few number of samples drawn from the input probability distribution. By rearranging the samples points at different probabilities, e.g. the mean of distribution, plus $\pm 1\sigma$ and $\pm 2\sigma$ confidence intervals, using the simple approach, we still obtain a different normal distribution with approximately 40% larger than analytical standard deviation, which indicates that with simple UQ the type of sampling affects the QoI probability distribution with smaller number of samples.

One can overcome this limitation by increasing the number of samples to converge to analytical solution. However, the convergence of the simple method is relatively slow, and expensive computation of nonlinear turbulence simulations make UQ analysis with a large number of samples impractical. On the other hand, using chaos polynomials, one can approximate $Q(z)$ in the high probability region of z, and obtain the PCM QoI distribution also plotted in Fig. 5.2c. As shown, we can observe PCM is much closer to the analytical solution, and has much better accuracy with a small number of samples. We also observed that the PCM approach is less sensitive to the sampling details, compared to simple approach.

In a second example, we take the analytical relation between temperature gradient to be nonlinearly stiff $Q(z) = Q_0 \exp\left(Q_1 \exp\left(z+\beta\right)^{\alpha}\right)$ as plotted in Fig. 5.3b. Here, we have assumed $Q_0 = 5 \times 10^{-9}$, $Q_1 = 1.3$, $\beta = 0.6$, and $\alpha = 1.8$. If there is a relatively small uncertainty in z near the critical gradient, as shown in Fig. 5.3a, we obtain the QoI distribution shown in Fig. 5.3c. As shown, we again observe relatively close agreement

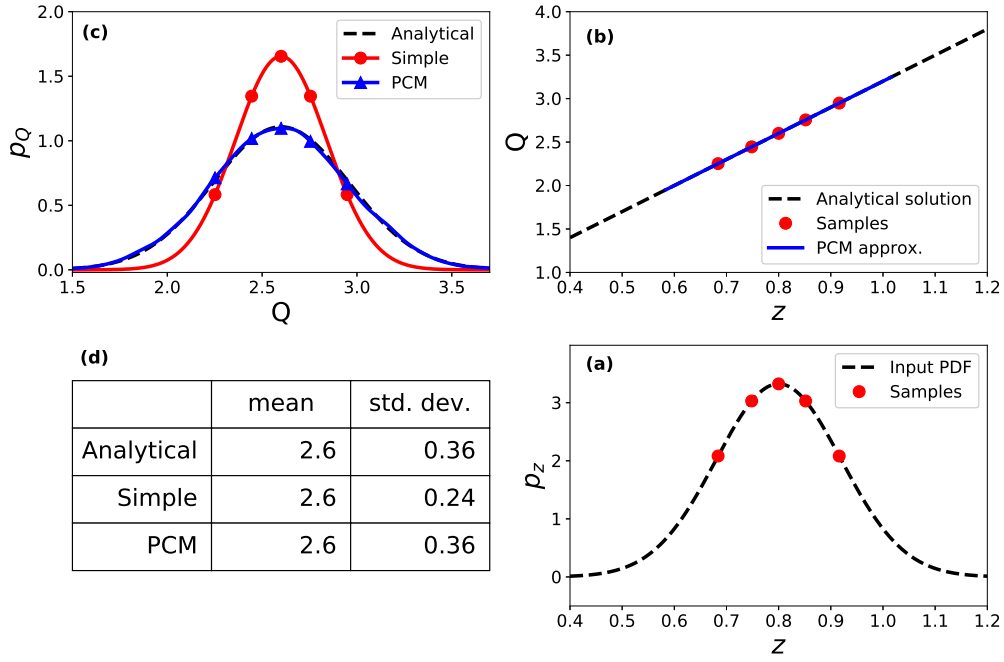

(d)

	mean	std. dev.
Analytical	2.6	0.36
Simple	2.6	0.24
PCM	2.6	0.36

Figure 5.2: (a) input probability distribution (black dashed line), and samplings (red dots). (b) Chaos polynomial approximation (blue solid line) compared with analytical relation between QoI and input (black dashed line). (c) Analytical probability distribution of QoI (dashed black line) is compared with PCM approximation of QoI distribution (solid blue line), and simple averaging UQ assuming normal distribution (solid red line). (d) Table of mean ($\sum Q/n$) and standard deviation ($\sqrt{\sum(Q-\bar{Q})^2/n}$) of QoI probability distribution with different methods.

between the analytical solution and the approximated distribution via PCM using only a few number of samples. More importantly, the PCM approach recovers the skewness of p_Q, while the simple approach does not, and will not regardless of sampling. Note that the agreement between the chaos polynomials approximation to $Q(z)$ and the analytical relation falls off for $z < 0.95$. However, in this region of small p_z, the effects of poor fidelity in the chaos polynomials approximation on p_Q approximation are minimal.

In above examples, we have included up to third order chaos polynomials to the sample points. For different problems, one needs to perform a sensitivity analysis on the best order of polynomials to use, assumed using statistical measures such as the *p-value* and R^2 of the fits.

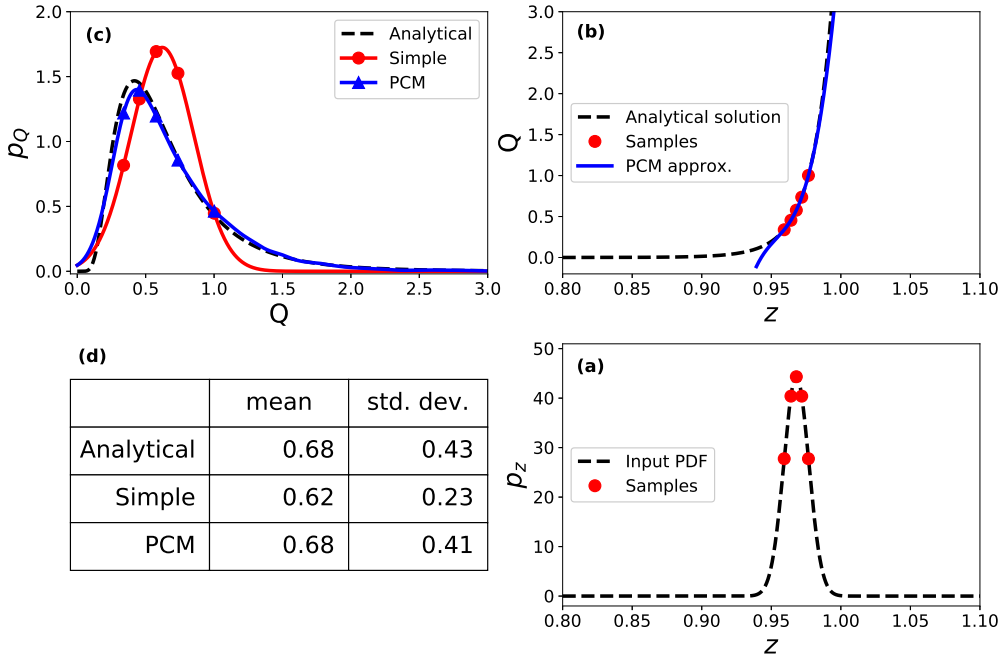

(d)

	mean	std. dev.
Analytical	0.68	0.43
Simple	0.62	0.23
PCM	0.68	0.41

Figure 5.3: (a) input probability distribution (black dashed line), and samplings (red dots). (b) Chaos polynomial approximation (blue solid line) compared with analytical relation between QoI and input (black dashed line). (c) Analytical probability distribution of QoI (dashed black line) is compared with PCM approximation of QoI distribution (solid blue line), and simple averaging UQ assuming normal distribution (solid red line). (d) Table of mean and standard deviations of QoI probability distribution with different methods.

5.3 Inclusion of probabilistic UQ above and near critical gradients

The topic of critical gradients in plasma turbulence has been intensively pursued in magnetically-confined fusion, as many times, confined fusion plasmas operate near this condition[MST$^+$09, HDP$^+$13]. In this section, we discuss the implications of correctly transforming probabilities above and near critical gradients. To illustrate the issue, we use the results from a simple collisional drift-wave model. The model has been introduced in Chapter 2, which evolves fluctuations of density $\tilde{n}$, vorticity $\tilde{\Omega} = \nabla_\perp \cdot (n_0 \nabla_\perp \tilde{\phi})$, and electron temperature $\tilde{T}_e$, in the presence of a background density profile, $n_0(r)$, and

electron temperature profile, $T_{e_0}(r)$ in a cylindrical geometry. The model equations are shown below,

$$\frac{\partial \tilde{n}}{\partial t} - \frac{a}{\rho_s}\frac{1}{r}\frac{\partial n_0}{\partial r}\frac{\partial \tilde{\phi}}{\partial \theta} = \nabla_{\parallel}\tilde{j}_{\parallel} + D_n\nabla_{\perp}^2\tilde{n} - \nu_s\langle\tilde{n}\rangle_{\theta,z} + \frac{a}{\rho_s}\{\tilde{\phi},\tilde{n}\}, \tag{5.8}$$

$$\frac{\partial \tilde{\Omega}}{\partial t} = \nabla_{\parallel}\tilde{j}_{\parallel} + \mu_{\perp}\nabla_{\perp}^2\tilde{\Omega} - \nabla_{\perp}\cdot\left(\nu_{in}n_0\nabla_{\perp}\tilde{\phi}\right) + \frac{a}{\rho_s}\{\tilde{\phi},\tilde{\Omega}\}, \tag{5.9}$$

$$\frac{\partial \tilde{T}_e}{\partial t} - \frac{a}{\rho_s}\frac{1}{r}\frac{\partial T_{e_0}}{\partial r}\frac{\partial \tilde{\phi}}{\partial \theta} = \chi_{\parallel}^e\nabla_{\parallel}^2\tilde{T}_e + \frac{2}{3}1.71\frac{T_{e_0}}{n_0}\nabla_{\parallel}\tilde{j}_{\parallel} + D_{T_e}\nabla_{\perp}^2\tilde{T}_e - \nu_s\langle\tilde{T}_e\rangle_{\theta,z} + \frac{a}{\rho_s}\{\tilde{\phi},\tilde{T}_e\} \tag{5.10}$$

$$\tilde{j}_{\parallel} = \frac{1}{\eta_{\parallel}}\left(1.71n_0\nabla_{\parallel}\tilde{T}_e + T_{e_0}\nabla_{\parallel}\tilde{n} - n_0\nabla_{\parallel}\tilde{\phi}\right). \tag{5.11}$$

For further the details and explanation of terms in the model, refer to Chapter 2.

In this discussion, we assume all input plasma parameters and profiles are known, except for the density profile, which is obtained by fitting a function of the form

$$n_0(r) = (\bar{n} - n_{base})\exp(-(r/l_n)^{n_\alpha}/n_\alpha) + n_{base}, \tag{5.12}$$

to a coarse set of hypothetical experimental measurement (shown with black error bars in Fig. 5.4a).

In Fig. 5.4a, we show multiple possible fits by changing the exponent factor n_α in the functional form, and holding all other parameters fixed, to study the effects of profile steepening only. In Fig. 5.4b, we show the corresponding variation of the most unstable linear growth rate ($m = 2$) as a function of maximum density gradient lengthscale ($1/L_n = -d\ln n_0/dr$), obtained via the n_α parameter variation. As seen from the figure, for $\max(1/L_n) \leq 1.05$, the drift-wave modes are stable. In Fig. 5.4c,

we show the density fluctuation RMS amplitudes $\langle \tilde{n}^2 \rangle^{0.5}$ at $r = 3cm$ as a function of maximum density gradient, predicted by a series of nonlinear simulations carried out for the profiles shown in Fig. 5.4a. We observe no fluctuations for stable cases, and for unstable cases a sudden increase in the nonlinearly saturated amplitude of fluctuations above the critical density gradient corresponding to $\max(1/L_n) = 1.05$. Moreover, in Figs. 5.4(d-f), we have shown the changes of particle flux at $r = 3cm$, maximum $E \times B$ velocity, and nonlinear kinetic energy transfer into zonal flow at a position corresponding to the radial location of $v_{E \times B_{max}}$ as a function of the density gradient lengthscale. We observe as density equilibrium steepens above a critical value, saturated fluctuations amplitude grows rapidly. However, as the fluctuations become larger with a steepened density gradient, the nonlinear energy transfer becomes significant and as a result the zonal $E \times B$ velocity grows, while the turbulence amplitude increase begins to flatten out and saturate, and even reduction of fluctuations and turbulent flux can occur with large enough density steepening.

Although the uncertainty quantification can be applied to each of the turbulence quantities discussed and shown above, here we consider density fluctuations RMS as the QoI to perform UQ analysis as an example. Using this model, we illustrate the results of using the PCM approach for uncertainty quantification. As shown in Figs. 5.5(a-c), we consider three different input distributions for $\max(1/L_n)$, ranging from a distribution that peaks well above the critical density gradient (Fig. 5.5a), to a case where the $\max(1/L_n)$ distribution is smaller but still above the critical gradient (Fig. 5.5b), to a case where the $\max(1/L_n)$ PDF peaks just above the critical gradient (Fig. 5.5c). In each range, we assume a normal distribution for the $\max(1/L_n)$ input parameter.

For each case, we fit second-order chaos polynomials to the $\langle \tilde{n}^2 \rangle^{0.5} - \max(1/L_n)$ relation needed for the probability transformation, as shown in Fig. 5.5(d-f). In this case, $\langle \tilde{n}^2 \rangle^{0.5}$ is the QoI, and $\max(1/L_n)$ is the input parameter. One notable observation in

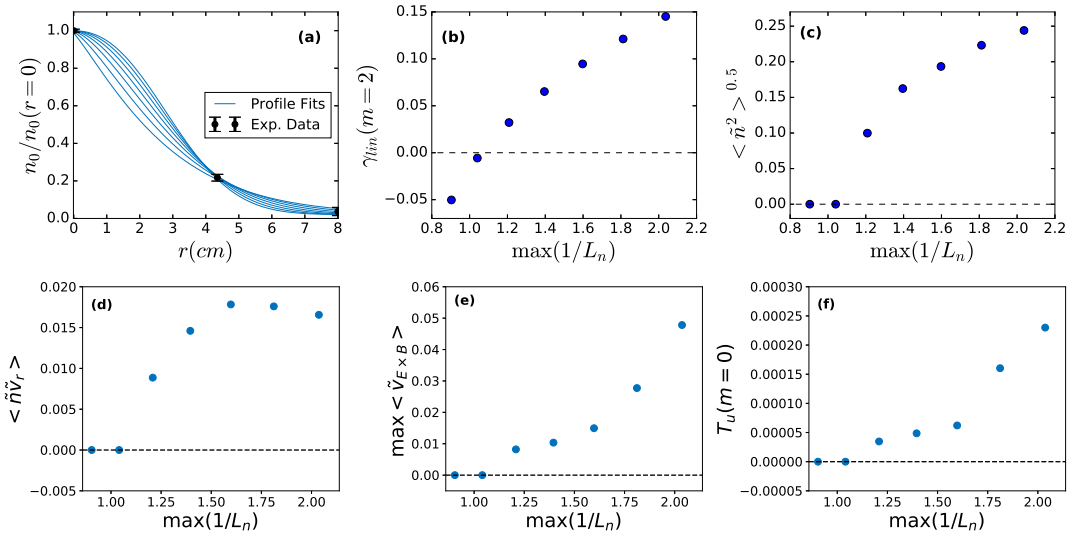

Figure 5.4: (a) Equilibrium density fits (blue lines) to experimental data points (black errorbars). (b) Scan of linear growth rate ($m = 2$) as a function of maximum density gradient lengthscale. (c) Scan of density fluctuation RMS amplitudes as a function of maximum density gradient lengthscale. (d) Scan of turbulence particle flux as a function of maximum density gradient lengthscale. (e) Scan of maximum $E \times B$ velocity as a function of maximum density gradient lengthscale. (f) Scan of nonlinear kinetic energy transfer to the maximum zonal $E \times B$ as a function of maximum density gradient lengthscale.

this simple practice is the concavity change of the chaos polynomial fits in the different cases. We can then directly obtain the density fluctuation RMS amplitude PDF, using the concept of the probability transformation. In Fig. 5.5(g-i), we plot the resulting QoI distributions. We can observe in the case with density gradient well above the critical gradient, where QoI-input relation is relatively linear, the QoI distribution remains fairly Gaussian (Fig. 5.5g). However, as we get closer to the critical gradient where the the QoI-input relation is nonlinear and has downward concavity, the QoI probability distribution has negative skewness (Fig. 5.5h). Furthermore, near the critical gradient where the QoI-input relation has upward concavity, resulting in QoI distribution with a positive skewness (Fig. 5.5i). From this simple practice, it can be easily deduced that near critical gradients (which is often the case in experiments) a careful statistical comparison of simulation and experiment is necessary for a truly rigorous validation study, instead of

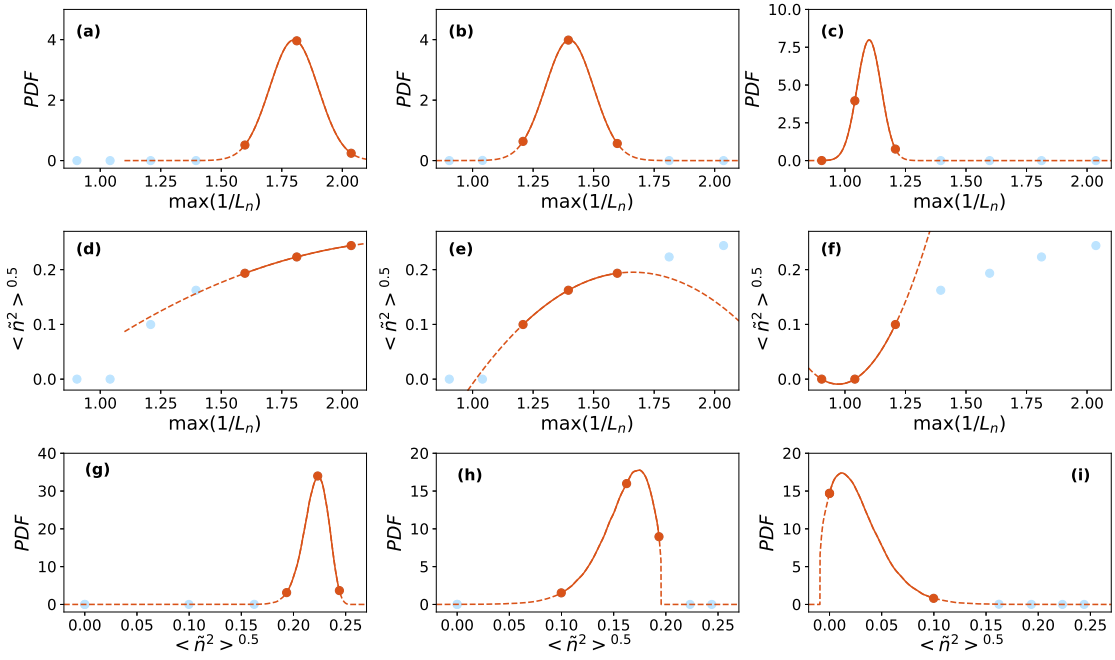

Figure 5.5: Probability density function of input (maximum density gradient lengthscale) in three case of (a) high, (b) medium, and (c) low density steepening. QoI (density fluctuation RMS amplitudes) and input (maximum density gradient lengthscale) relation fitted with Chaos Polynomials in three case of (d) high, (e) medium, and (f) low density steepening. Forward propagated QoI (density fluctuation RMS amplitudes) probability density function in three case of (g) high, (h) medium, and (i) low density steepening. Solid lines indicate the probability within the range of samples, while dashed lines show the probability outside the range of samples.

merely comparing the mean and standard deviation of the QoIs obtained from simple sampling or parametric variations.

We should note that the choice of samplings can result in significant improvement as measured by faster convergence of the QoI distribution function, as we will discuss in the next Section.

5.4 Application of PCM uncertainty quantification in validation study of drift-turbulence in linear plasma device

In this section, we discuss the results of using the PCM approach uncertainty quantification in a validation study of drift-turbulence in the CSDX linear plasma device experiment. The experimental condition is taken from [CTXM$^+$13] for CSDX experimental condition at 1kG with insulating boundary endplate. In this experiment, the Argon plasma is created by an $m = 0$ helicon source operating at $1.5kW$. The model[VHTT17] that was previously introduced and used in the previous section, is used for this study. The CSDX experimental uncertainties that can affect input parameters and profiles in the computational model have been identified and discussed in detail in Chapter 4. The findings can be summarized in forms of a vector of nominal input parameter uncertainties affecting both driving forces and damping mechanisms of in the model, $\mathbf{I} = \{\int dr(1/L_n), \int dr(1/L_{T_e}), T_{i_0}, T_{g_0}, T_{g_b}, T_{g_\alpha}\}$, where $\int dr(1/L_n)$ is the radially integrated equilibrium density gradient lengthscale, $\int dr(1/L_{T_e})$ is the radially integrated equilibrium electron temperature gradient lengthscale, T_{i_0} is the on-axis ion temperature, T_{g_0} is the on-axis neutral gas temperature, T_{g_b} is neutral gas temperature at the edge, and T_{g_α} is the steepness of neutral gas temperature profile.

We should note that like other UQ methods, the PCM algorithm suffers from the curse of dimensionality. Although more advanced versions of PCM utilize sparse grids to improve the computational feasibility for much higher numbers of uncertain parameters[FWK08], it is still recommended to reduce the uncertainty dimensionality as much as possible when using nonlinear simulations. Toward this end, we performed a linear growth sensitivity analysis on the uncertain parameters, varying only one input

parameter at a time while holding all other inputs fixed. The results of this linear sensitivity analysis are shown in Fig. 5.6.

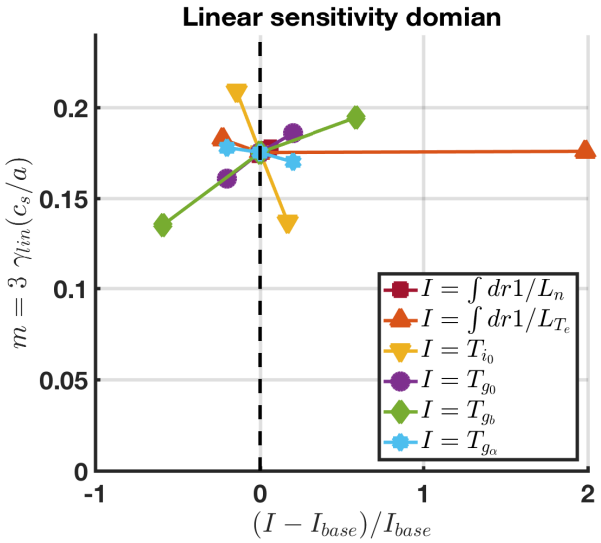

Figure 5.6: Maximum linear growth rate sensitivity analysis of uncertainty scans. I indicates the input parameter uncertainty normalized to the mean of uncertainty (I_{base}).

We see that the growth rate is most sensitive to T_{i_0}, and T_{g_b}, and therefore we expect these parameters to have the most influence on the turbulence simulations. To use the PCM approach, we first need to define the probability distributions of these input parameters. For ion temperature, we use the experimental measurements obtained via Laser-Induced Fluorescence (LIF)[CTML$^+$12] to determine the $p_{T_{i_0}}$. However, for neutral gas temperature, there is no experimental measurement, and we have assumed a relatively large range of feasible values for gas temperature at the edge, with a uniform distribution. Specifically, the probability distribution of ion temperature is taken to be normal with mean value of $0.6eV$ and standard deviation of $0.1eV$, while the neutral gas edge temperature is assumed to have uniform distribution between $0.03eV$ to $0.1eV$ (shown in Fig. 5.7).

Assuming no correlation between T_{i_0} and T_{g_b}, their joint PDF can be directly specified (Fig. 5.8). Once specified, we can obtain the chaos polynomial expansion on

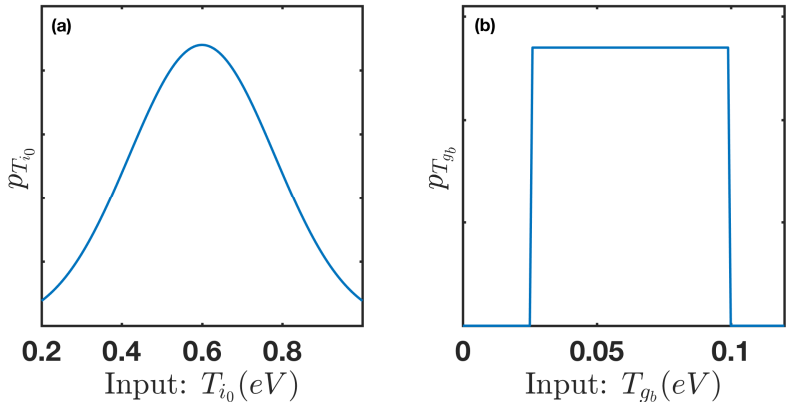

Figure 5.7: Probability distribution of input parameters: (a) ion temperature (T_{i_0}), (b) neutral gas temperature at the edge (T_{g_b}).

this bivariate input probability distribution.

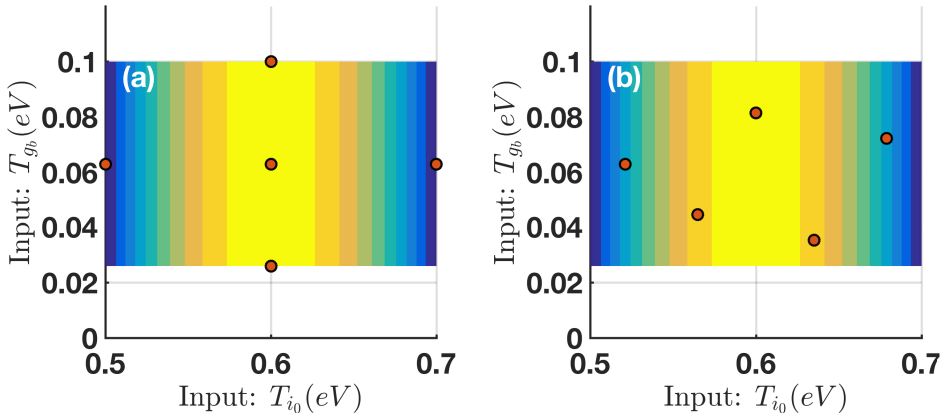

Figure 5.8: Choices of input parameters collocation points in $T_{i_0} - T_{g_b}$ input distribution space. Red dot indicate the samplings using (a) simple sampling, (b) Space-filling Hammersley sequence sampling in a normal-uniform input probability distribution. Color contour in the shows probability distribution of input parameters, where lighter colors denote higher probability.

In Fig. 5.8, we also show two different ways of drawing samples from the input distribution. In the simple approach often taken by the plasma micro-turbulence community, a mean base case is chosen, and simulation scans are performed by changing individual parameters within these uncertainties[Hol16]. In Fig. 5.8a, we have shown the *simple* samplings taken from input distribution. As one can observe, the samples

are not filling the distribution space evenly, and samplings from the low probability region may have very small contribution to the mean of the QoI uncertainty. Better space filling sampling can be applied by minimizing the integrated mean squared error over the probability distribution.

Many different sampling techniques have been developed and adopted in UQ studies, such as Latin hypercube sampling, or low-discrepancy sampling methods such as Hammersley sequence sampling[FL15]. Here, we have used the Hammersley sequence sampling method due to its accurate sampling spread in multivariate probability distributions[SLC01]. To briefly mention, Hammersley sequence sampling is a low discrepancy sequence method that can be used to describe a uniform space by minimize the integrated error in the uniform space given the number of samples. We refer the reader to Refs. [FL15, SLC01] for further reading in this matter. Moreover, [HWB07] showed that the solution using Hammersley samples resulted in more stable results than using conventional pseudo-random samples. In Fig. 5.8b, we have shown the sample indentified using Hammersley sampling method.

We performed five nonlinear simulations using input parameters corresponding to the points identified by the Hammersley sequence samplings, and compare the simulation results with experimental observations. In Fig. 5.9, we have compared experimental measurements with the individual simulation results, and the expected value and 1σ confidence interval uncertainty of forward propagated input probability distribution via PCM (using first order polynomials). As shown in Fig. 5.9(a-b), now we can claim confidently that the model captures the experimental fluctuations within the 1σ confidence interval at $r \approx 2-3cm$, while it overestimates the experimental fluctuations at $r \approx 5cm$. Moreover, we can observe in Fig. 5.9(c-d) that within the 1σ confidence interval the synthetic particle flux get distorted from the physical particle flux.

We should note that using PCM approximation, we found the expected value and

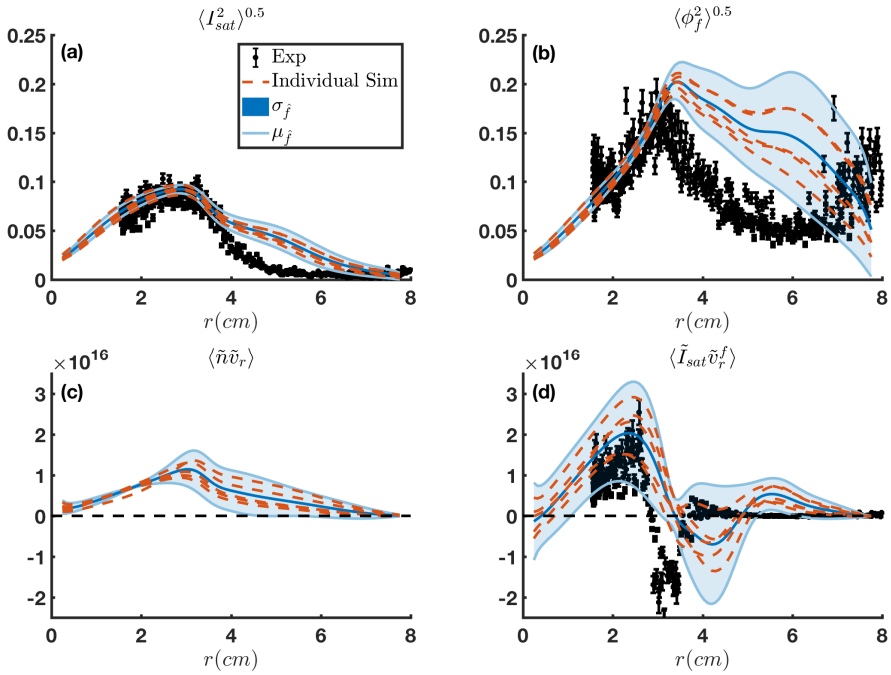

Figure 5.9: Comparison of experimental measurement (black), with individual simulations (red dashed lines), and the uncertainty obtained from the model within 1σ confidence interval (blue shaded band), for (a) radial profile ion saturation current fluctuation RMS amplitudes, (b) radial profile of floating potential fluctuation RMS amplitudes, (c) fluctuations particle flux, and (d) synthetic particle flux.

confidence interval of quantified uncertainty remain approximately the same with the choice of sampling mainly influencing faster convergence of uncertainties only. However, with simple averaging, the choice of sampling can have noticeable effect on determining confidence interval bounds.

A QoI comparison of experimental measurement histogram against the normalized probability distribution obtained via PCM and through simple averaging approaches at $r = 3cm$ is shown in Fig. 5.10. The experimental measurements are done with a fixed multi-tip Langmuir probe, and the histogram of experimental QoI is obtained via sub-window averaging. We observe good agreement between experimental-simulation distributions, however the experimental measurements show larger standard deviations compared to the simulation's quantified uncertainties. Moreover, we observe relatively

similar quantified uncertainty with both PCM and simple averaging approaches in this validation study. This is mainly because this experimental condition of CSDX is well above the critical density gradient, where the QoIs-inputs relation is relatively linear (similar to the case discussed in Fig. 5.2). We should note that here we have not included uncertainties of temporal variation (turbulence burstiness) of simulation QoIs, nor quantified the systematic errors from using a reduced model. Such uncertainties can in principle be included in the QoIs PDF using Bayesian methods.

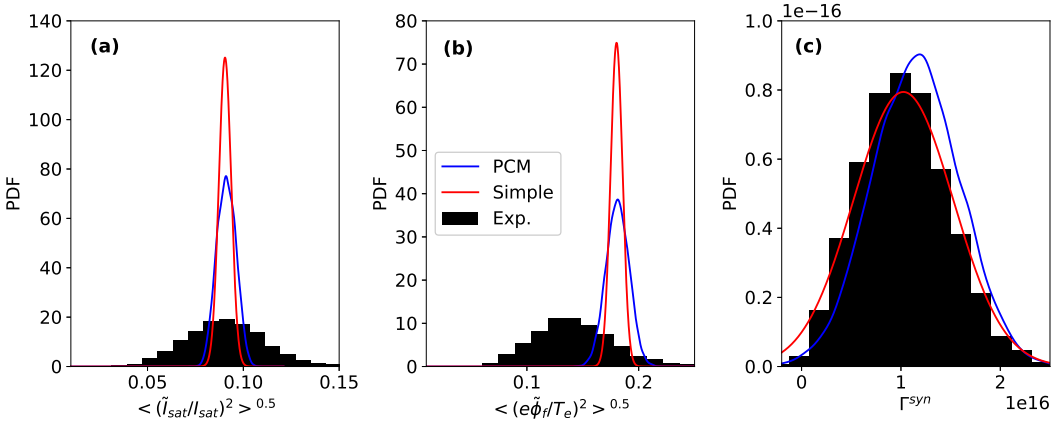

Figure 5.10: Comparison of the QoI PDFs of experimental measurement (black), and quantified uncertainty from the model using PCM (blue), and through simple averaging (red) at $r = 3cm$. All probabilities have been normalized.

5.5 Conclusion

In this Chapter, we have investigated the use of the PCM approach to UQ for a fluid-based plasma turbulence simulation. We believe the results show that the PCM approach can increase the quality of the validation studies, by enabling statistically improved comparisons between simulation and experiment, such as comparison of higher statistical moments of QoIs, and measuring the statistical distance between simulation and experiment.

The advantages of PCM were illustrated by applying to a simple critical gradient model. We found that with simple mean and standard deviation of only few samples can not adequately describe the response probability distribution accurately. However, PCM uncertainty quantification approach was shown to be an efficient method for quantification of parametric uncertainties with arbitrary distributions in the input quantity. In particular, the PCM approach is well-suited to cases with non-normal model input and output PDFs.

Nevertheless, the non-intrusiveness of the PCM enables the use of a computationally expensive model in the process of uncertainty quantification. As an example, we have applied the PCM uncertainty quantification to obtain the stochastic properties of turbulence quantities in validation studies of CSDX linear plasma device. The method rigorously quantified the model response within the known input uncertainties.

Future work includes applying this uncertainty quantification method in a real world validation study of the critical gradient behavior in gyrokinetic simulations, along with inclusion of temporal variations (turbulence burstiness) of QoI statistics.

5.6 Acknowledgement

The text and data in Chapter 5, in full, is accepted for publication at Journal of Fusion Science and Technology under Vaezi, P. & Holland, C. (2017). *An Improved Approach to Uncertainty Quantification for Plasma Turbulence Validation Studies*. The dissertation author was the primary investigator and author of this paper.

Chapter 6

Conclusion and Possible Future Directions

In this thesis, a series numerical simulation studies of the plasma turbulence in the CSDX linear plasma device were performed. The high level goal of this work was to see how well a minimal collisional drift-wave model can describe the observed turbulence in CSDX. The study included both qualitative physics studies, more quantitative validation studies, and to assess the utility of novel UQ approaches to validation studies of plasma turbulence models.

6.1 Summary of this thesis

There have been a few theoretical and experimental studies on the effects of end plate boundary conditions on the turbulence in the scrape-off layer turbulence found in tokamaks. These effects have also been studied in simpler linear plasma devices with different end plate configurations. In Chapter 2, a fluid-based model with the rigorous boundary conditions was derived to describe the different end plate experiments. In

Chapter 3, a set of linear runs and nonlinear simulations were performed with both insulating and conducting end plate boundary conditions at a fixed magnetic field, to understand the differences between two different conditions. The effects of additional sheath-imposed instabilities due to the presence of conducting end plate was studied and shown to be important for parameters close to those of CSDX. These effect can also be present in the tokamak SOLs, and the current work provides a better understanding of transport and energy transfer analysis in these experimental conditions.

In Chapter 4, a quantitative validation study of simulation results for insulating end plate boundary conditions was is performed. The goal was to quantify how well the reduced drift-wave model can reproduce the experimental results. The procedure included extensive linear sensitivity analysis of experimental input uncertainties into the code, followed by a nonlinear scan and implementation of synthetic Langmuir probe diagnostics to translate the simulation results into synthetically measured quantities for direct comparison of simulation results and experimental measurements. A fairly good quantitative agreement for most plasma saturation characteristics between insulating simulation and experimental results, in the plasma core, are obtained. However at this level, the minimal model can only produce qualitative results for conducting end plate simulation case. The comparison of conducting end plate simulations against the experimental measurements are shown in Appendix A, as a reference for future work.

In Chapter 5, a technique to provide more through validation studies using forward propagation input parameter uncertainties in the computational model is introduced and discussed. The novel Probabilistic Collocation Method, and more advanced sampling techniques are performed for the first time in the validation studies of plasma turbulence. The importance of uncertainty quantification in the simulations near critical gradient was then studied using both a simple analytic model, and also using the minimal turbulence model of CSDX experiments. The methods introduced here provide more utility

and quality for validation metrics by moving from non-deterministic comparisons to measuring the statistical mismatch between simulation and experiment. The uncertainty quantification proposed in this Chapter, can be applied to more complex gyrokinetic simulations of confinement devices with currently available computational clusters.

6.2 Recommended future work

The current work provides a guide for the numerical study of more exciting physics questions, and extending the validation techniques for simulation-experiment comparisons. There are several topics that seem particularly suited for further study and extension of the work contained in this thesis. Some these interesting areas are briefly mentioned in this section.

6.2.1 Moving toward source-driven simulations

Validation studies in Chapter 4, indicate that a source-driven simulation is necessary for both better qualitative and quantitative studies of drift-turbulence. By looking at the measurements of mean density and floating potential measurements at different axial locations ($z = L_z/2$ and $z = L_z/4$), we observe that the profiles are steeper near the source (shown in Fig. 4.1). Our minimal model collisional drift-wave model does not include the axial profile variations and assumed dominant 2D turbulence. Experimentally, these weak axial gradients can be reduced by decreasing the gas pressure, and increasing the helicon source input power. Moreover, in the validation studies, we observed that the simulation performs well in reproducing the experimental fluctuations in the core, while overestimating the experimental fluctuation amplitude in the edge. We suspected the main reason behind subpar performance of simulations at the edge is that the density fluctuations amplitude and equilibrium density are within the same order of magnitude,

resulting in the break-down of small flucutations assumption of our current model. Thus, for more realistic simulations of turbulence in CSDX linear device, we suggest that the model should be modified to avoid the small flucutations assumption, with particle and heat sources included. The profiles would then evolve until they became self-consistent with the sources and turbulent-driven fluxes. Such a flux-driven simulation would be well-suited for numerical studies of the transition to turbulence, formation of steepened density profiles and reduced turbulent transport, and zonal flow formation and transport regulation. experimental measurements of source characteristics, or turbulence characteristics of plasma near the source may be necessary for an accurate source input to the model. On this subject, a recent source-driven simulation attempt of LAPD linear plasma device done by [FRR$^+$15] can be insightful as an starting point for a source-driven simulation of drift-turbulence in CSDX.

6.2.2 Adding mild 3D equilibrium effects

The current validation studies provided in this thesis showed that the saturated turbulence level and turbulent-driven sheared $E \times B$ zonal flow is very sensitive to the equilibrium density gradient. In particular, the slight variation in density gradient observed from ports at $z = L_z/4$ and $z = L_z/2$ gave a very significant increase in the estimated zonal flow amplitude. It would therefore seem useful to extend the minimal drift turbulence model to include the possibility of weak axial equilibrium plasma gradients as observed in the experiment. A systematic exploration of how these weak axial gradient affect and influence the development of drift turbulence and zonal flows could then be carried out. Such work would have relevance not only for small linear devices, but also for turbulence in edge/SOL plasmas of confinement devices, where similar axial equilibrium gradients can also exist.

6.2.3 Adding parallel ion momentum physics

The current model neglects the parallel ion momentum physics. In the derivation of boundary conditions (especially conducting sheath boundary condition), we have neglected parallel ion physics. Our validation studies using this model showed that the simulation with insulating boundary condition could not recover experimental fluctuations in the edge. Recent experimental studies in CSDX suggest that sheared parallel flows may develop in the edge plasma region, which has been neglected in these set of simulations. Moreover, in the derivation of conducting boundary conditions, the parallel ion velocity has an explicit contribution for defining the boundary conditions at the sheath entrance. It is suspected that the overestimation of fluctuations and fluxes observed in the validation studies (discussed in Appendix A), might be due to the absence of parallel ion dynamics and axial variation of equilibrium profiles. Recent simulations done by [PUCF10b] included the effects of ion parallel momentum in simulation of cylindrical plasma, and showed results that support the supposition that parallel flow dynamics may be important.

6.2.4 Experimental measurements of electron temperature fluctuations

The initial validation studies of CSDX experimental condition using synthetic Langmuir probe diagnostics, suggest that ion saturation current fluctuations is a good representation of density fluctuations. However, the synthetic floating potential fluctuations is not quite equivalent to the plasma potential fluctuations. The reasoning behind such difference is found to be because of relatively large sheath factor of Argon plasma, and small but finite fluctuations of electron temperatures. We observed that plasma potential and electron temperature fluctuations cross-phase is negative in a range of radii, distorting the synthetic floating potential fluctuations phase from the plasma potential phase.

Experimentally, due to diagnostic limitations electron temperature fluctuations have not been measured. Previous experimental measurements of ion saturation current-floating potential fluctuations cross-phase by [BTA$^+$05], indicated a negative cross-phase across a range of radii, different from analytical expectations of drift-wave theory. However, in order to correctly infer the turbulent particle flux from Langmuir probes, one must be aware of the finite density-plasma potential cross-phase in the experimental measurements. Thus, accurate measurements of electron temperature fluctuations are necessary to quantify this phase.

6.2.5 Experimental measurements of profiles in both radial and axial directions

Experimental measurements of turbulence characteristics in CSDX at different axial ports indicated that the equilibrium plasma profiles have variations along axial direction (see Fig. 4.1), that can impact the validation studies. Although our simulations underestimate the self-generated $E \times B$ profile with the axially uniform input experimental profiles, our benchmarking shows that $E \times B$ shearing rate is very sensitive to the steepness of density equilibrium profiles. Thus, for a better validation studies, as well as better understanding of physics from the experimental measurements, it is high recommended to perform experimental measurements of mean profiles as well as fluctuations at multiple axial locations. This set of measurements can also be useful in understanding of plasma detachment studies which has been observed at certain magnetic fields in CSDX experiments.

Moreover, spatial variation of some plasma parameters are not considered in the current model for the sake of simplicity. Among such, ion-ion viscosity profile is the most spatially varying one. Our calculations of generalized ion-ion viscosity based on radial variations of density and ion temperature profile, shows a decrease of viscosity at

larger radii. Accounting for such spatial variation introduces the challenges of solving for the viscosity tensor, which is numerically non-trivial.

6.2.6 Synthetic camera imaging diagnostic studies

Last but not least, in the validation studies of CSDX experiment diagnostics, we have only looked at the Langmuir probe measurements. However, a fast imaging camera is also used to measure the light intensity of plasma with a fairly high 2D resolution. The light intensity is related to both density and electron temperature, with some exponent factors $I = An^{\alpha_n} T_e^{\alpha_{T_e}}$. One-to-one comparison of simulation data against the experimental light intensity fluctuations can be obtained via synthetic light intensity construction from the simulation data. [Czi11] showed that for Helium and Deuterium plasma the changes of α_n and α_{T_e} as a function mean density and electron temperature. However, no such calibration data for Argon gas exists at the moment. As future work, it is suggested to repeat the experimental measurements with lighter gases where the calibration data exists, and/or perform calibration studies to obtain the Argon plasma intensity coefficients. In this way, a synthetic visible light fluctuation diagnostic could be constructed, and then used with simulation results to compare against imaging data from experiment.

Appendix A

Validation Study of Conducting Boundary Condition Simulation

Similar to the validation study of insulating boundary condition (IBC) simulation of CSDX, the validation study of conducting boundary condition (CBC) can be performed, and the initial results of such code-experiment comparison is shown in this Appendix. Note that the results obtained for validation study of CBC case at this stage still yields qualitative agreement. However, the procedure and the results of such comparison is shown here for future endeavors.

Similar to the procedure explained in Chapter 4, we have classified the types of uncertainties in the experimental measurements, obtained linear sensitivity of these input uncertainties in the linear response of the model, ran nonlinear simulations for stiff input cases, and compared the simulation results with the experimental measurements using synthetic diagnostics.

The experimental data is taken from [CTXM$^+$13] for the conducting case, that is also studied in Chapter 3. For the equilibrium density and electron temperature profiles are fitted via functional forms of Eqns. 4.1-4.2. Experimental profiles varied within

the uncertainties of experimental measurements in a Monte Carlo analysis and 100 realizations of each profile is produced. The lowest, median and highest $\int dr(1/L_n)$ and $\int dr(1/L_{T_e})$ profiles are chosen to perform the simulations with. The fits and experimental data are shown in Figs. A.1 and Table A.1.

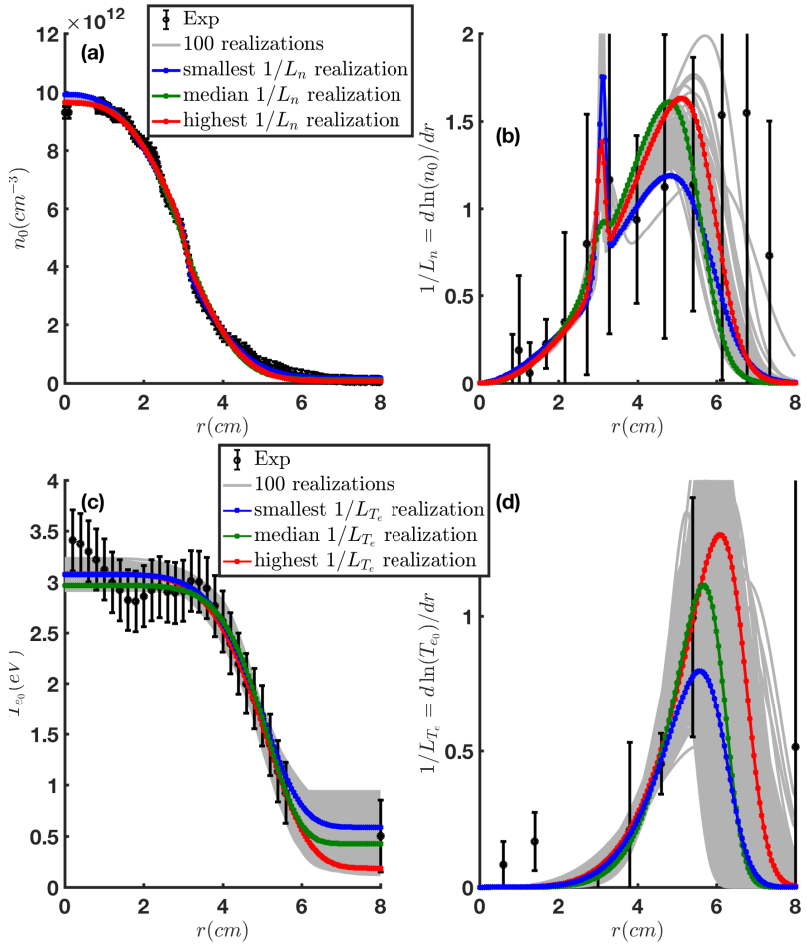

Figure A.1: Fit realization in a Monte Carlo analysis for experimentally measured CBC (a) density equilibrium and (c) electron temperature equilibrium at $z = L_z/2$. (b) Density gradient lenghtscale $(1/L_n)$ of fits compared with experimentally calculated gradient. (d) electron temperature gradient $(1/L_{T_e})$ of fits compared with experimentally calculated gradient. Gray lines show the 100 realization generated in the Monte Carlo approach.

The ion temperature, and neutral gas temperature is chosen to be similar to the IBC case inputs discussed in Chapter 4. A linear sensitivity analysis is then performed

Table A.1: Characteristics of CBC equilibrium fits.

Profile	Parameter	low	median	high
n_0	$\int dr(1/L_n)/a$	0.5	0.55	0.6
n_0	χ^2	0.18	0.21	0.26
T_{e_0}	$\int dr(1/L_{T_e})/a$	0.19	0.24	0.28
T_{e_0}	χ^2	0.30	0.34	0.33

using profiles and parameters uncertainties, and the maximum linear growth rate of these scan are shown in Fig. A.2. The coefficient of variation of response versus input uncertainty is then obtained and shown in Table A.2. We can observe that the conducting case is very sensitive to both equilibrium profile uncertainties and damping mechanisms. This is typical case of multiple instability linear growth response which is similar to near critical gradient behavior in tokamaks. The smallest uncertainty in each of the input parameters can translate to large difference in the outputs. Hence, a median case simulation along with a set of 10 uncertainty simulation scans are performed over parameters $\mathbf{I} = \{\int dr(1/L_n)/a, \int dr(1/L_{T_e})/a, T_{i_0}, T_{g_0}, T_{g_b}\}$, where the $CoV > 0.15$.

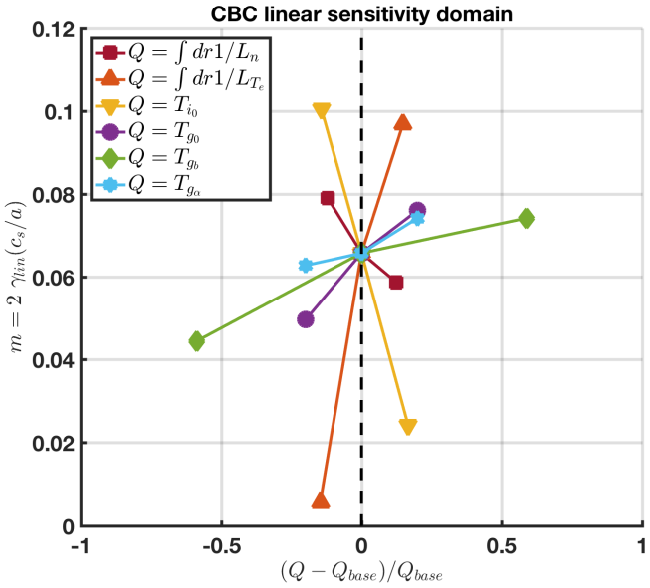

Figure A.2: (a) Maximum linear growth rate sensitivity analysis of uncertainty scans. Q indicates the input parameter uncertainty normalized to the base case value (Q_{base}).

Table A.2: Sensitivity analysis of CBC linear growth rate response.

Profile	CoV_{input}	$CoV_{response}$
$\int dr(1/L_n)/a$	0.12	0.15
$\int dr(1/L_{T_e})/a$	0.14	0.83
T_{i_0}	0.15	0.60
T_{g_0}	0.20	0.21
T_{g_b}	0.59	0.25
T_{g_α}	0.20	0.09

Quantities of interest similar to the procedure for the IBC validation study shown in Chapter 4 are considered for simulation-experiment comparison. The comparisons of ion saturation current, floating potential, synthetic particle flux, and Reynolds stress are shown in Figs. A.3-A.6.

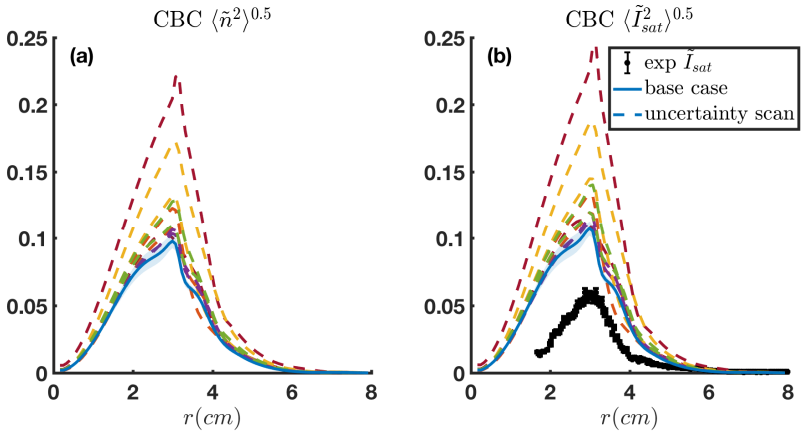

Figure A.3: (a) Density fluctuations at $z = L_z/2$ of the simulations. (b) Comparison of the experimental ion saturation current fluctuation measurements and the synthetic $\tilde{I}_{sat}$ at $z = L_z/2$. Colors correspond to nonlinear simulation of the cases shown in Fig. A.2. Shaded error bars indicate standard deviation of sub-averaging window for the base case simulation.

We observe that the simulation estimates the fluctuations about two times larger than the experimental measurements. One possible reason behind this discrepancy could be the absence of axial equilibrium gradients. Since the model neglects these axial gradients, we are adding the sheath-imposed $E \times B$ shear throughout the whole domain to keep consistency of the model that does not include axial equilibrium gradients, while

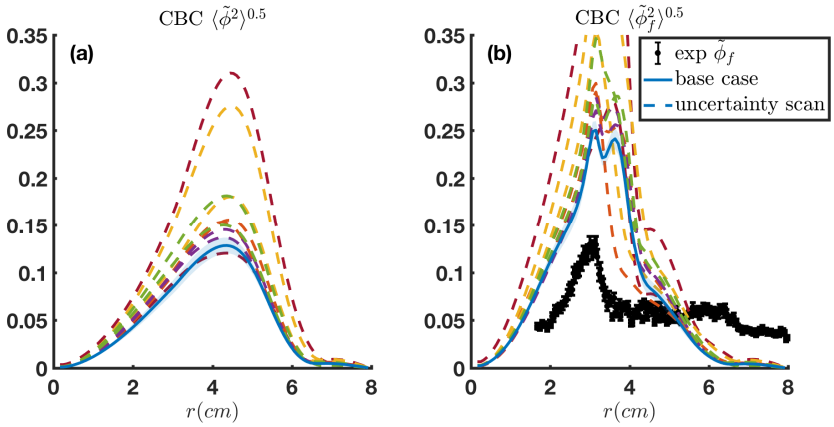

Figure A.4: (a) Plasma potential fluctuations at $z = L_z/2$ of the simulations. (b) Comparison of the experimental floating potential measurements and the synthetic $\tilde{\phi}_f$ at $z = L_z/2$. Colors correspond to nonlinear simulation of the cases shown in Fig. A.2. Shaded error bars indicate standard deviation of sub-averaging window for the base case simulation.

these effect should only locally be added at the sheath entrance. Moreover, we have neglected the parallel ion velocity and its fluctuations in our studies, and the presence of axial parallel ion velocity can be non-negligible in the derivation of boundary conditions. Nevertheless, the conducting endplate physics and validation are immensely important with direct application in limiter and SOL physics. Further studies on validation of conducting endplate simulation with a more advanced model is needed.

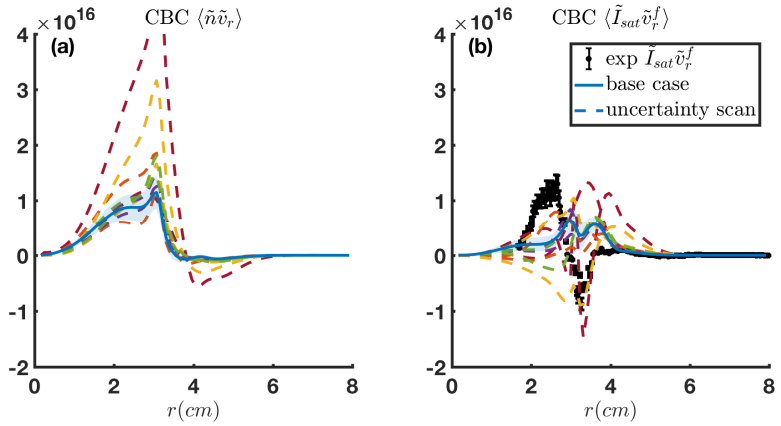

Figure A.5: (a) Physical particle flux at $z = L_z/2$ of the simulations. (b) Comparison of the experimental flux measurements and the synthetic flux at $z = L_z/2$. Colors correspond to nonlinear simulation of the cases shown in Fig. A.2. Shaded error bars indicate standard deviation of sub-averaging window for the base case simulation.

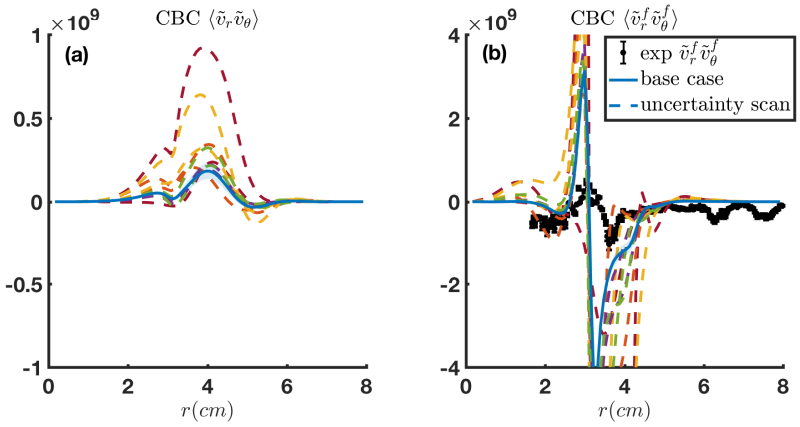

Figure A.6: (a) Physical Reynolds stress at $z = L_z/2$ of the simulations. (b) Comparison of the experimental Reynolds stress measurements and the synthetic Reynolds stress at $z = L_z/2$. Colors correspond to nonlinear simulation of the cases shown in Fig. A.2. Shaded error bars indicate standard deviation of sub-averaging window for the base case simulation.

Appendix B

Preliminary Magnetic Field Scan Studies

It is known that the low frequency ($\omega/\Omega_{c_i} \ll 1$) and large magnitude fluctuations ($\tilde{n}/\bar{n} \approx 0.1 - 1$) near the edge of large-scale magnetically confined plasma devices are associated with the high cross-field transport[End99]. Thus, in order to predict the confinement, understanding of the mechanisms behind these low frequency fluctuations are essential. It has been experimentally observed that the transport rate of these low frequency fluctuations can be mitigated through the formation of large scale electrostatic structures such as turbulent driven $E \times B$ zonal flows[BDT90, Ter00, DIIH05]. In addition, at a threshold power, a bifurcation into an enhanced confinement can occur due to nonlinear interaction between turbulence and zonal flow[MXW$^+$12], and reduces both fluctuations and cross-field transport. Furthermore, destabilization of zonal flow can break up the coherent structure of zonal flows via Kelvin-Helmholtz instabilities[NBD07].

These low frequency fluctuations are usually triggered by the presence of pressure gradient driven drift-wave (DW) instability at the edge of magnetically confined devices. There has been numerous studies on the drift-turbulence in both labora-

tory plasma devices[KLP$^+$97, BTA$^+$05, YTH$^+$10] and large-scale tokamaks[Sco97, LHM$^+$05, TFM09]. Various theoretical[BK85] and experimental studies[BTA$^+$05, YTH$^+$10, ZHB$^+$12, TBL$^+$14] have tried to understand the development of the drift-turbulence regime from coherent drift-waves. Different experimental approaches that have explored this transition include but are not limited to electric grid biasing[ZHB$^+$12], variable neutral gas pressure[YTH$^+$10], and magnetic field strength scans[BTA$^+$05, TBL$^+$14]. However, while simulations of fully developed drift-turbulence have been published, to our knowledge nonlinear simulation studies of the transition to the drift-turbulence have not been pursued in great detail. Numerical simulation of transition to the drift-turbulence can provide us a deeper understanding of the full spatial and temporal behavior of evolving fluctuations, which experimental diagnostic limitations may not allow. Furthermore, a validated numerical simulation of the turbulence dynamics, might then provide predictive capabilities of the turbulence and transport in magnetically fusion devices.

The Controlled Shear Decorrelation Experiment (CSDX) linear plasma device has been one of the experimental laboratory devices that is used to study this transition to the drift-turbulence regime[BTA$^+$05, TBL$^+$14]. Previous experiments on CSDX showed that by increasing the magnetic fields (and hence reducing ρ_s/L_n and ion viscosity) DW fluctuations evolve from narrow-band coherent wavelike perturbations to a state of broadband spectra turbulence[BTA$^+$05]. On the route to the fully developed turbulence it has also been reported that, at a certain magnetic field, the plasma goes through global transition resulting in steepening of pressure gradient, reduction of turbulence, onset of strong transverse $E \times B$ shear, and reduced cross-field transport[CAT$^+$16]. By increasing the magnetic field even further after the global transition, particle transport becomes very intermittent[TBL$^+$14].

In this Chapter, we use the collisional drift-wave model introduce in Chapter

2 and respective experimental measurements of CSDX at different magnetic fields to investigate the turbulence characteristics. Although in our fixed gradient model, we can not observe this transition behavior in a self-consistent manner, the changes of turbulence characteristics at different magnetic fields can provide useful insight of the transition mechanism, which will be useful for a future flux-driven simulation. In this chapter, first we discuss the experimental setup in Sec. B.1, second we study the linear physics of the magnetic field scan in Sec. B.2, finally we investigate the turbulence characteristics of such scan in Sec. B.3, followed by a brief discussion in Sec. B.4.

B.1 Experimental Setup

The experimental magnetic field scan was performed in the CSDX cylindrical magnetized helicon plasma device. The length of the device is about $3m$ with radius about $10cm$. The plasma operates at $0.43Pa$ gas pressure, and magnetic field can be varied from $0.4kG$ to $2.4kG$ when using insulating endplates[TBL$^+$14]. Unlike the $m = 0$ helicon experiments that have been discussed in the previous chapters, in the published reference, the plasma is generated and heated via upgraded $m = 1$ helicon source at antenna radius of $8cm$. In these settings, the equilibrium density and electron temperature is measured by an RF compensated single tip swept Langmuir probe[CTML$^+$12]. The changes in the equilibrium density (n_0) profile, and density gradient lengthscale ($1/L_n = -d\ln n_0/dr$) is plotted in Fig. B.1. We can observe that as the magnetic field increases, first the density profile steepens gradually, at around $\sim 1.4kG$, a sudden transition to localized steepened gradients happens. At higher magnetic field, the density gradients relaxes and

the maximum density gradient shifts toward the core of plasma. A functional form,

$$n_0(r) = (\bar{n}_1 - n_{base})\exp(-(r/l_{n_1})^{n\alpha_1}/n_{\alpha_1}) + (\bar{n}_2 - n_{base})\exp(-(r/l_{n_2})^{n\alpha_2}/n_{\alpha_2}) \quad \text{(B.1)}$$
$$+(\bar{n}_3 - n_{base})\exp(-(r/l_{n_3})^{n\alpha_3}/n_{\alpha_3}) + n_{base}$$

fitted to the profiles. Then based on the minimum goodness of fit (χ^2) of random generated profiles within the experimental uncertainty, the best fit is chosen as the simulation input. Note that, this study only focused on the trends changes across magnetic field scan, and uncertainty quantification of such studies is deferred to another publication. Thus, the results presented here in this chapter represent only a preliminary investigation that pave the way for future, more in depth investigation.

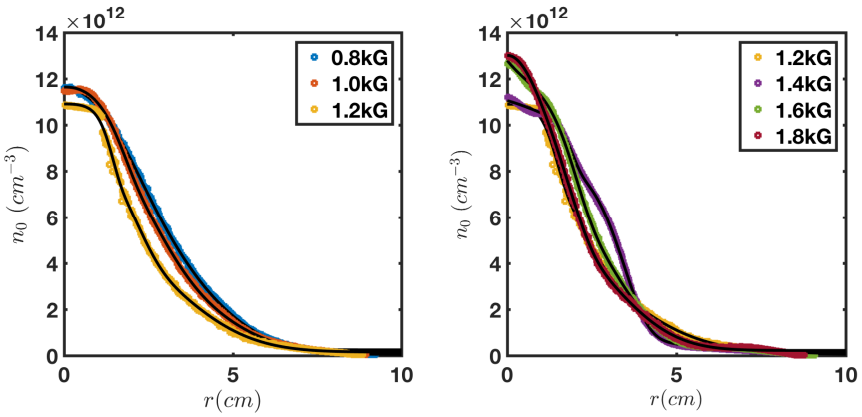

Figure B.1: Radial equilibrium density profile versus magnetic field taken from [TBL+14] with permission. Black line shows the best fit to the experimental data.

The electron temperature equilibrium is observed to remain constant within experimental uncertainties throughout the magnetic field scan. The electron temperature peak observed in the experimental measurements at the edge of plasma ($r > 5cm$) is neglected due to the probe measurement limitations in less dense plasma (e.g. RF-induced distortion of the probe data can be stronger). Hence, the same fit is chosen as the fit to all

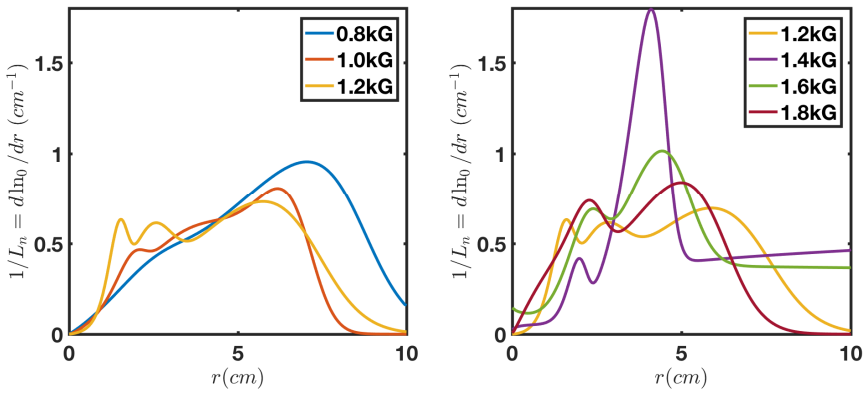

Figure B.2: Equilibrium density gradient length-scale ($1/L_n = -d\ln n_0/dr$) of fits versus magnetic field.

the magnetic field simulations,

$$T_{e_0}(r) = 3.2\exp(-(r/15.2)^{2.7}/2.7)eV.$$

Another significant change that the plasma goes through is the effect of decreasing gyroradius with the increase of the magnetic field. The ion sound radius (ρ_s) versus magnetic field is plotted in Fig. B.3a. In addition, the ion temperature is measured using Laser Induced Fluorescence (LIF) technique[CTML$^+$12]. As shown in Fig. B.3b, below $1.4kG$ an increasing trend in the on-axis ion temperature is observed, while after $1.4kG$ the ox-axis ion temperature decreases. Although, our model assumes negligible fluctuations of ion temperature, the ion temperature can significantly affect the ion-ion viscosity. The neutral gas temperature $T_g(r)$ is assumed to be 75% of ion temperature at the axis, and is equal to room temperature at the plasma edge, profile of the form,

$$T_g(r) = (\bar{T}_g - 0.03)\exp(-(r/2.11)^{2.27}/2.27) + 0.03(eV).$$

is used to describe its variations, by analogy to the T_i profile. The magnetization factors $\Omega_{c_i}\tau_i$ for ions and $\Omega_{c_e}\tau_e$ for electrons versus magnetic field are shown in Figs.

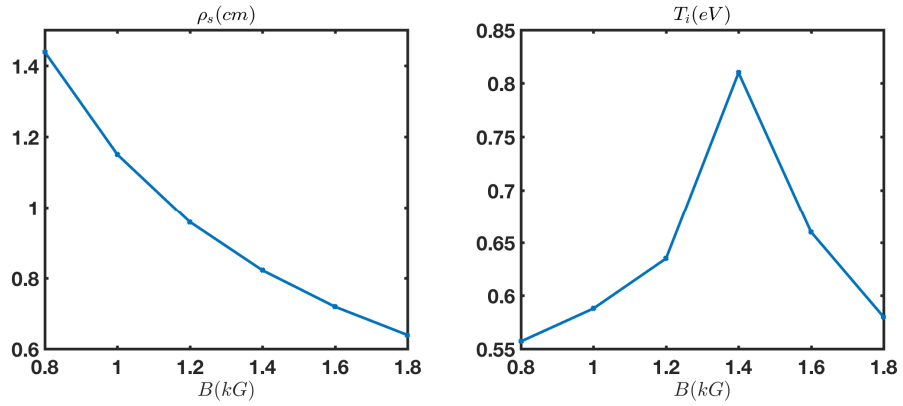

Figure B.3: (a) Changes in gyroradius versus magnetic field. (b) Changes in on-axis ion temperature value versus magnetic field. Data is taken from [TBL+14] with permission.

B.4-B.5. We observe that $\Omega_{c_e}\tau_e$ is much larger across the domain, indicating the electrons are well-magnetized. However, the magnetization factor for the Argon ions $\Omega_{c_i}\tau_i$ is about four orders of magnitude smaller, indicating a weakly magnetized ions in the core, and fairly well-magnetized ions in the less dense edge region. By increasing the magnetic field, the ions become more magnetized but still have $\Omega_{c_i}\tau_i < 1$ at $r < 3cm$.

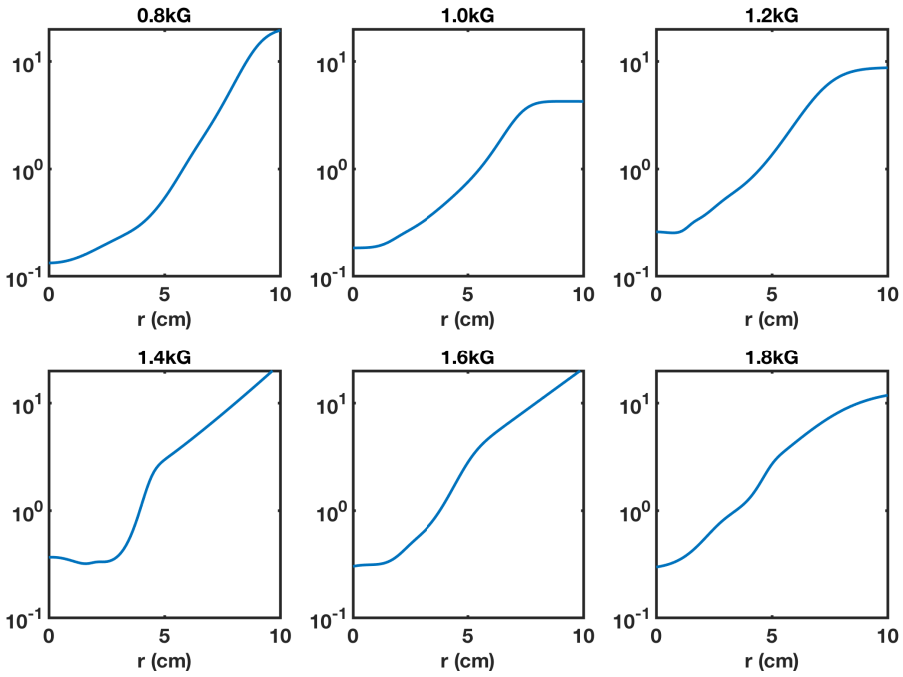

Figure B.4: Radial profiles of $\Omega_{c_i}\tau_i$ for different magnetic fields.

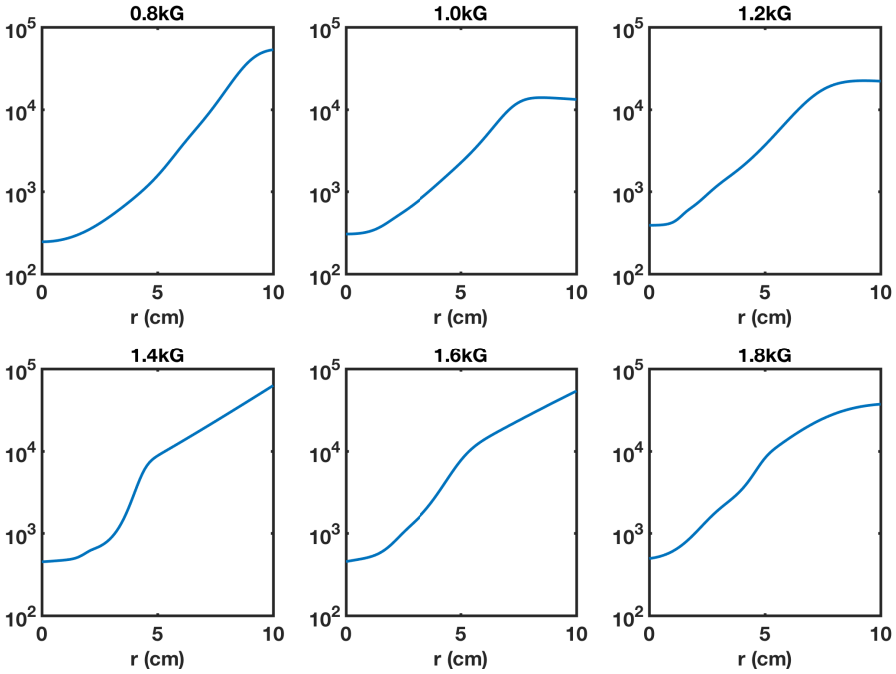

Figure B.5: Radial profiles of $\Omega_{c_e}\tau_e$ for different magnetic fields.

From above argument, we treat the core of plasma ions to be weakly magnetized ($\Omega_{c_i}\tau_i < 1$), while electrons to be very well magnetized ($\Omega_{c_e}\tau_e \gg 1$). This results in using generalized Braginskii formula for ion-ion viscosity[Bra65]

$$\mu_\perp = \frac{a v_{th_i}^2 \tau_i}{\rho_s^2 c_s} \frac{2.23 + 1.2X^2}{2.33 + 4.03X^2 + X^4},$$

and electron-electron collisions in the fully magnetized limit for the density and electron temperature collisional diffusion

$$D_n = D_{T_e} \approx 0.51 \rho_e^2 / \tau_e.$$

In Fig. B.6, we have shown the experimental radial profiles ion-ion viscosity, calculated from the generalized Braginskii formula. We can observe qualitative decreasing trend of radially averaged viscosity, with the increase of magnetic field. For numerical

simplicity of the code, we have chosen the radially average viscosity value at each magnetic field as the inputs to the model. Our preliminary studies shown that simulations with $\mu(r)\nabla^2\tilde{\Omega}$ and $\nabla\cdot\left(\mu(r)\nabla\tilde{\Omega}\right)$ do not differ in term of turbulence amplitudes. However, we defer the full inclusion of a radially varying viscosity effects of the viscosity stress tensor to another study.

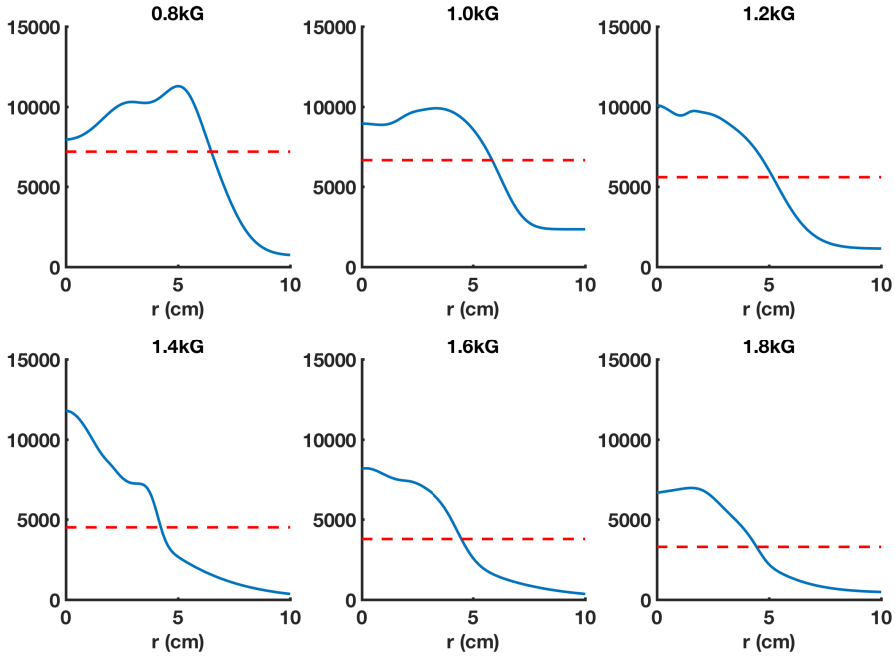

Figure B.6: Radial profiles of ion-ion viscosity for different magnetic fields. The dashed lines indicate the radially averaged values of viscosity.

In Fig. B.7, we have shown the radial average of the generalized ion-ion viscosity as a function of magnetic field. Two set of calculations for ion-ion viscosity were performed; one with a respective density equilibrium profile of each magnetic field (blue triangles), and the other time with a fixed density equilibrium profile taken from $1.2kG$ case and varying the gyroradius and ion temperature values (purple squares). We observe that the trend of the viscosity changes is fairly independent from the changes in equilibrium density profile as a function of magnetic field. Moreover, we observe that the decrease in the generalized viscosity does not scale with $1/B^2$, since the ions in the

central region are not fully magnetized.

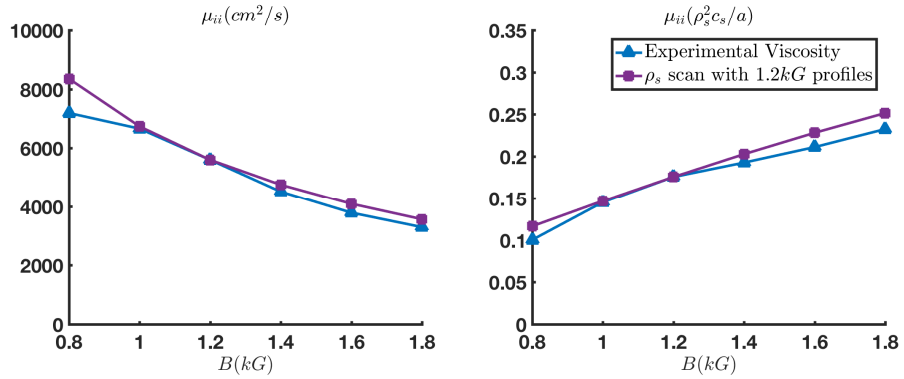

Figure B.7: Viscosity scan versus magnetic field.

In the experiment[TBL$^+$14], as the magnetic field is varied from $0.6kG$ to $1.4kG$, the fluctuations amplitude increases. However, around $1.4kG$ the fluctuation levels and cross-field particle transport reduce significantly. By increasing the magnetic field further, the fluctuations in the turbulence then recover. The experimental trend of ion saturation current fluctuation RMS amplitudes, and experimental measurement of particle flux (filtered for $3-25kHz$) plotted in Figs. B.8 - B.9, respectively.

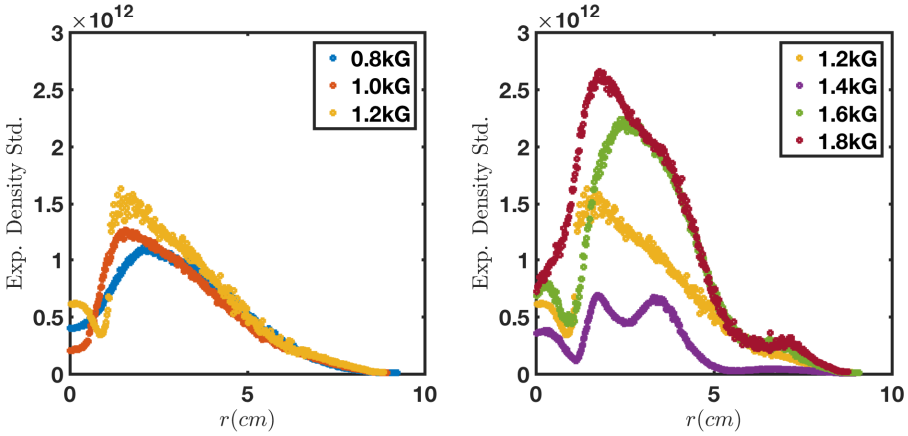

Figure B.8: Radial experimental measurement of ion saturation current fluctuation RMS amplitudes versus magnetic field. Data is taken from [TBL$^+$14] with permission.

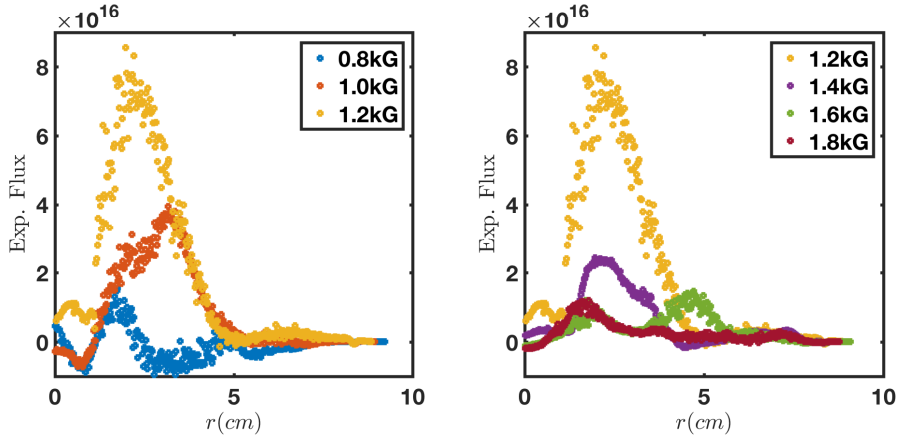

Figure B.9: Radial experimental measurement of particle flux versus magnetic field filtered for $3-25kHz$. Data is taken from [TBL+14] with permission.

B.2 Linear Analysis

In this Section, we will take two different approaches in our magnetic field scan studies. In the first approach, we use density, ion temperature, and neutral gas temperature of each magnetic field to best represent the experimental condition at each magnetic field. In the second approach, we have used a fixed density profile corresponding to the $1.2kG$ case for all the magnetic fields and only varied ρ_s to isolate and explore this effects. In these two approaches, we analyze the results of the linearized version of our model to obtain linear growth rate and frequencies in a magnetic field scan. The linear runs are preformed with both the experimental profiles setting, and with the ρ_s scan with fixed equilibrium profiles taken from the $1.2kG$ experimental case.

The linear growth rates (frequencies) of the eigenmodes have been obtained by calculating imaginary (real) part of $\partial \ln \tilde{\phi}_m / \partial t$ after the modes establish themselves in our initial value solver, where m denotes the azimuthal mode number. In the experimental conditions, the results of linear growth rate and frequencies at different magnetic fields are shown in Fig. B.10.

We can observe that at $B = 0.8kG$ only two modes ($m = 0$ and $m = 1$) are linearly

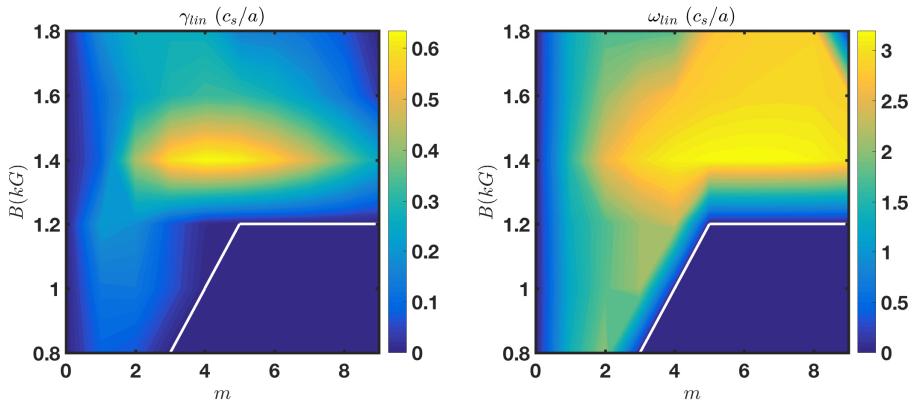

Figure B.10: Contour plots of linear (a) growth rates and (b) frequency of each azimuthal mode m in experimental condition for various magnetic fields. Growth rate and linear frequencies of stable modes have been filtered out in the plots, due to limitation of initial value solver in capturing noisy highly damped modes. White lines show boundary between unstable and stable modes.

unstable. As we increase the magnetic field, more modes ($m = 1$ to $m = 8$) become unstable, and growth rates and real frequencies increase. When reaching $B = 1.4kG$, the growth rates and linear frequencies go through a sudden change, and many higher modes also become linearly unstable. This phenomena happens simultaneously with the local steepening of the density gradient (See Fig. B.2) at $B = 1.4kG$, indicating the sudden increase in the linear drift-wave driving force. By further increasing the magnetic field, the linear growth rates and frequencies start to decrease, where the localized density steepening becomes less prominent.

In the second set of linear scan, the effects of gyroradius tightening with a fixed equilibrium profile is explored. The linear growth rate and frequencies of this linear scan is shown in Fig. B.11.

We can observe unlike the experimental scan there is a smooth linear increase in both linear growths rate and frequencies in gyroradius scan. For $B < 1.2kG$ the maximum growth rate is for $m = 1$, and for higher magnetic fields, the maximum mode number shifts to $m = 2$ as more modes become unstable due to gyroradius tightening. However, no sudden change between linear properties of $1.2kG$ and $1.4kG$ occurs when we only

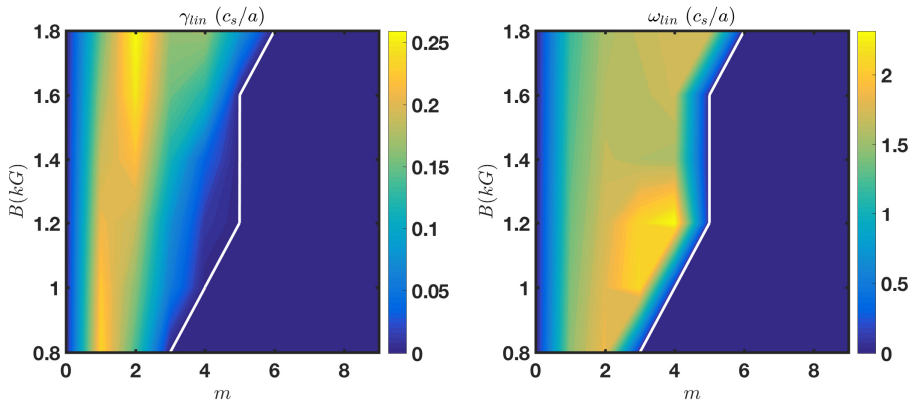

Figure B.11: Contour plots of linear (a) growth rates and (b) frequency of each azimuthal mode m for ρ_s scan with experimental profiles of $1.2kG$ case. Growth rate and linear frequencies of stable modes have been filtered out in the plots, due to limitation of initial value solver in capturing noisy highly damped modes. White lines show boundary between unstable and stable modes.

change ρ_s value, which indicates that the equilibrium profile steepening is the main linear contributor to the transition between $1.2kG < B < 1.4kG$. Thus, a complete numerical simulation of this transition would need to include self-consistent profile evolution.

B.3 Turbulence Saturation Studies

As discussed in the previous section, we have identified the equilibrium density steepening as a main contributor to the linear changes across magnetic field scan. Although the causality of equilibrium steepening can not be simulated with the fixed gradient model that is developed in this thesis, by looking at the trend of turbulence saturation properties at different magnetic field, we can obtain insights into the density steepening process. To investigate this issue, we have ran the nonlinear simulations of the linear cases with the experimental profiles shown in the previous section. The simulations are run after initial saturation for about 100 times of typical autocorrelation timescales. The $r-\theta$ snapshots of density fluctuations at $t = 80a/c_s$ for magnetic field scan simulations are shown in Fig. B.12.

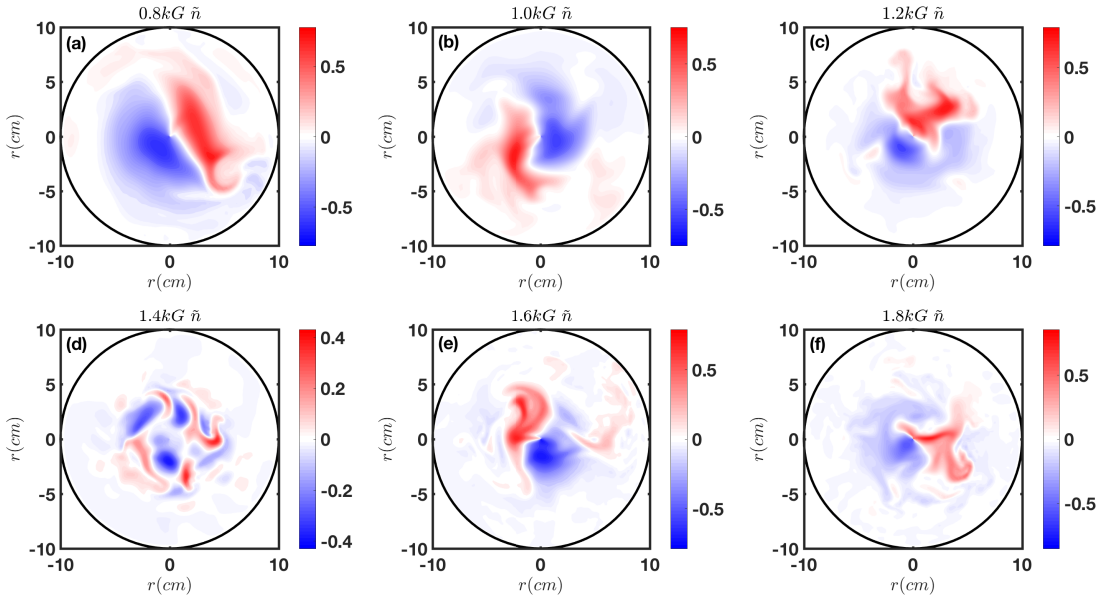

Figure B.12: $r-\theta$ snapshots of density fluctuations in a magnetic field scan simulations.

We observe that at lower magnetic fields the $m=1$ azimuthal mode is dominant. As we increase the magnetic field from $0.8kG$ to $1.2kG$, the size of blobs reduces. However, at $B=1.4kG$, the $m=5-6$ modes are more dominant, as we expected from the linear growth rate analysis from Fig. B.10. Moreover, the density fluctuation blobs at $1.4kG$ are much more tilted than other magnetic fields, indicating larger shearing rate of zonal flows at the transition magnetic field. Furthermore, at higher magnetic fields, the lower modes seems to be dominant again.

Furthermore, we have computed the two point spectra of density fluctuations as a function of magnetic, and results are shown in Fig. B.13.

To better discuss the statistical properties of the turbulence, the results of magnetic field simulations of density, plasma potential, and electron temperature fluctuation RMS amplitudes, along with particle flux, and $E\times B$ profile are shown in Figs. B.14-B.18.

We observe that the computed density fluctuation RMS amplitudes increase with the increase of magnetic field from $0.8kG$ to $1.2kG$ (see Fig. B.14). This is expected

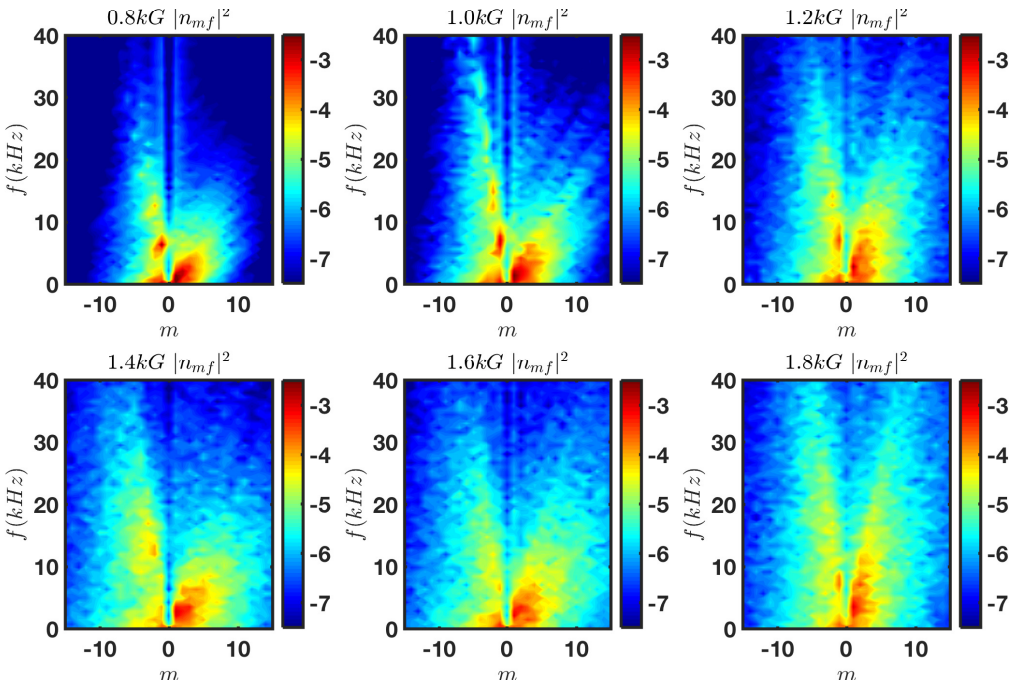

Figure B.13: Two point spectra of density autopower as a function of magnetic field at $r = 3.6cm$, and $z = L_z/2$.

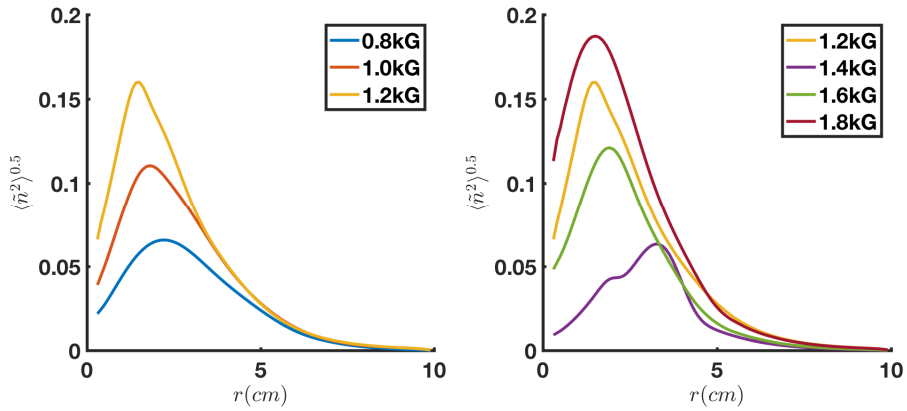

Figure B.14: Radial profile of density fluctuation RMS amplitudes versus magnetic field from the simulations.

due to gyroradius tightening with the increase of magnetic field. However, in the more steepened equilibrium density case of $1.4kG$, the fluctuations are significantly reduced. A similar trend is also observed in the scan of plasma potential fluctuation RMS amplitudes, shown in Fig. B.15. However, the electron temperature fluctuation RMS amplitudes do

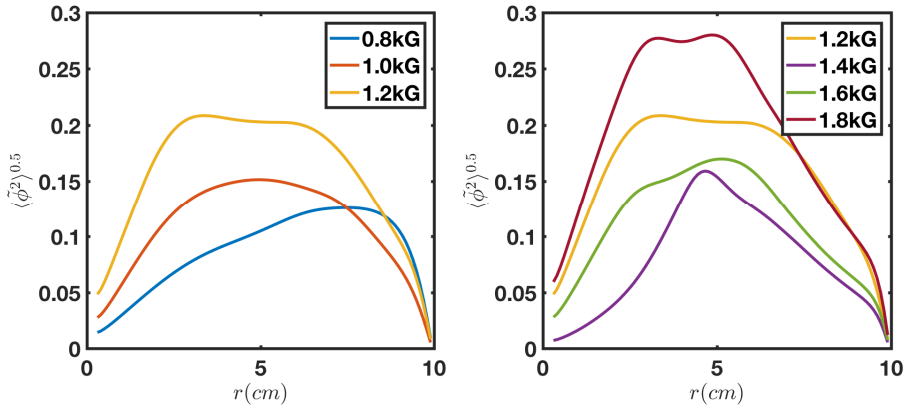

Figure B.15: Radial profile of potential fluctuation RMS amplitudes versus magnetic field from the simulations.

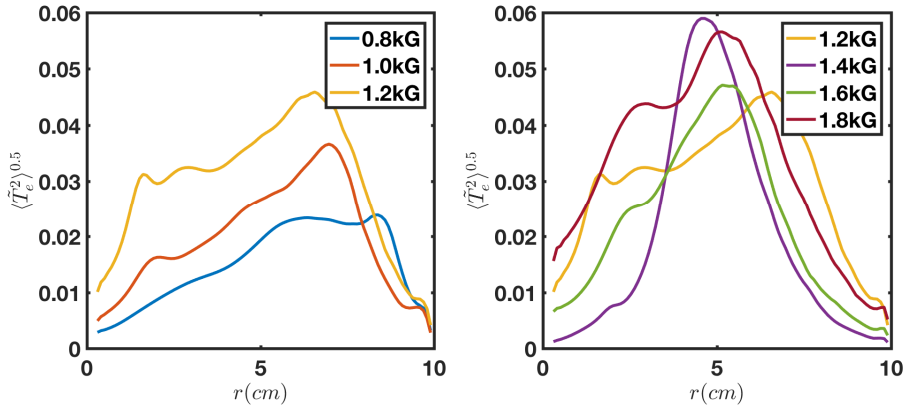

Figure B.16: Radial profile of electron temperature fluctuation RMS amplitudes versus magnetic field from the simulations.

not change much with the increase of magnetic field, shown in Fig. B.16. Note that the electron temperature fluctuations are relatively small compare to the other fluctuations; in the case of the $1.4kG$ simulation where there is sharp reduction in both density and plasma potential fluctuations, the electron temperature fluctuations becomes comparable to the other fluctuations in the system.

The computed particle flux behavior (see Fig. B.17) is also consistent with reported experimental changes in turbulent particle flux at magnetic fields below $1.4kG$. Moreover, the computed particle flux reduction in the $1.4kG$ case is also similar to

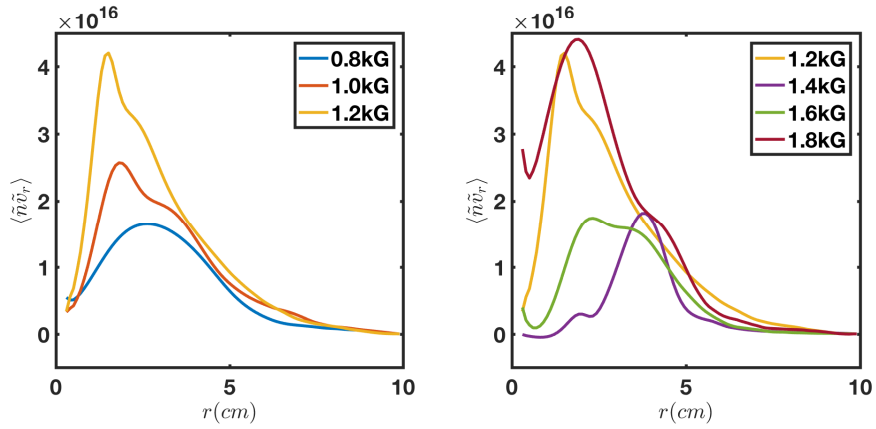

Figure B.17: Radial profile particle flux versus magnetic field from the simulations.

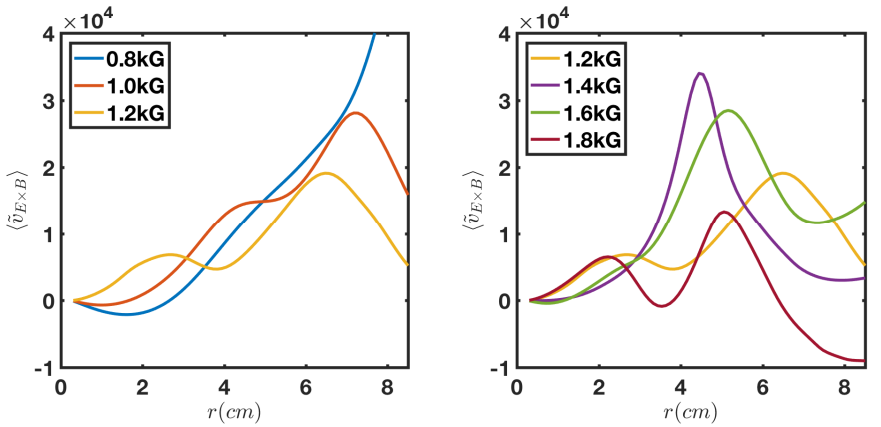

Figure B.18: Radial $E \times B$ velocity profile versus magnetic field from the simulations.

the experimental observations. However, the simulations show particle flux recovery for $B > 1.4kG$, while the experimentally measured particle flux remain small. A more rigorous validation study using synthetic diagnostic is required to study the difference between simulation and experiment, but has to be deferred to future work. We also observe an increase in the azimuthally averaged $E \times B$ profile (i.e. zonal flow) at the critical magnetic field $1.4kG$, where the shear layer peaks at the region of maximum equilibrium density gradient lengthscale (see Fig. B.18).

To understand the changes in density equilibrium, have also looked at the evolution of equilibrium density. If we neglect the parallel diffusion and parallel flux (which

can essentially be an important contributors, but we have neglected them in our fairly simple model), we can write as

$$\frac{\partial n_0}{\partial t} + \nabla_\perp \cdot (\tilde{n}\tilde{v}_r) = D_n \nabla_\perp^2 n_0 + S_n, \tag{B.2}$$

where S_n is the particle source term that maintains the balance of turbulence saturation level and equilibrium profiles. Note that, although in our model we do not evolve the equilibrium profiles, we still can calculate the divergence of turbulent flux of the fluctuations obtained from the simulations, and calculate the classical diffusion of fixed density equilibrium. Furthermore, because the equilibrium profiles are in steady state at each magnetic field, we can approximate the radial profile of particle source term. The results of the analysis of each term in Eqn. B.2 terms is shown in Fig. B.19.

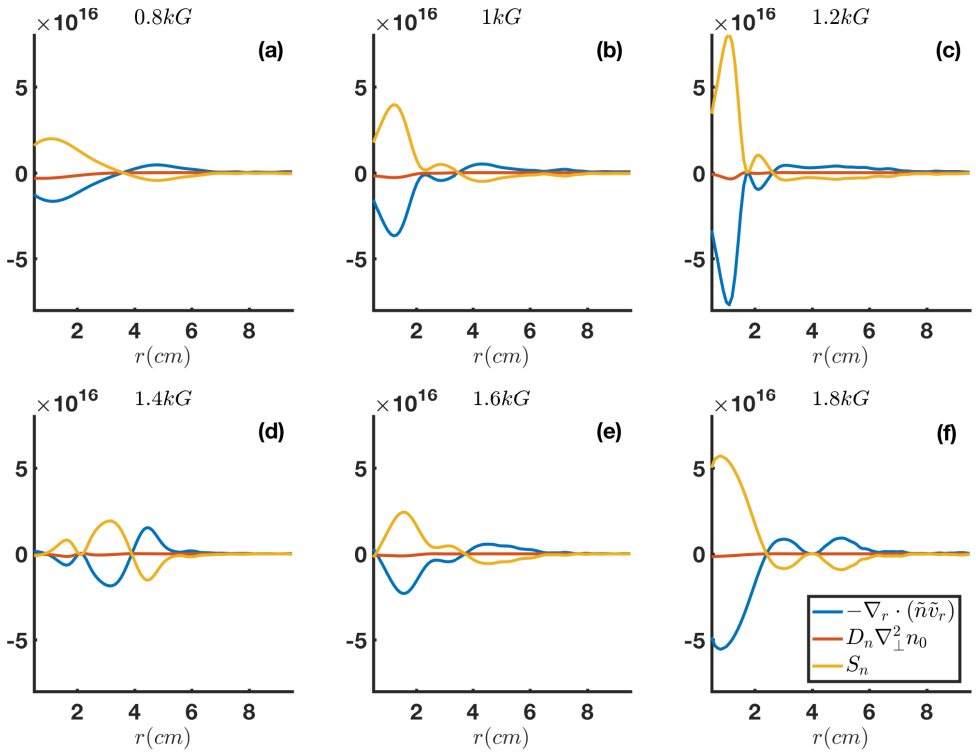

Figure B.19: The comparison of turbulent diffusion and classical diffusion of density as a function magnetic field.

We can observe that the classical diffusion of electrons are relatively small compared to the turbulent flux, and decreases with $\propto B^{-2}$ scaling as function of magnetic field. However, from low magnetic fields, the turbulent flux increases with increase of magnetic field. This increase is mainly due to the increase of drift-wave linear growth rates as a result of gyro-orbit tightening. Through Eqn. B.2, we can deduce that for $B < 1.4kG$, the source term must increase to explain the density profile evolution. However, at $B = 1.4kG$ there is sudden decrease in turbulent particle flux, and the inferred particle source term must also decrease. We suspect at $B = 1.4kG$ that either the source power deposition to the plasma changes as function of magnetic field, or parallel turbulent transport - which has been neglected in our model - must become significant. However, our current computational model can not test these theories, and further expansion of model is necessary investing them.

B.4 Discussion

In this Chapter, we have performed an initial set of simulations to study the turbulence changes in magnetic field scan of CSDX linear plasma device. Although the simulations shown here were performed with the fixed gradient approach developed in this thesis, we were still able to obtain some qualitative trend similar to the experiments.

We observed two major parameters control the transition to the fully developed turbulence. First, is the effects of gyroradius tightening with the increase of magnetic fields. The gyro-orbit tightening reduces the particle collisions, allowing for more broadband turbulence development. Second, the changes in the density steepening of equilibrium profiles is another important factor in setting the turbulence level. CSDX simulations suggest that the gyroradius tightening can drive more fluctuations, while the changes in the density equilibrium gradient can drastically influence the turbulence.

Nevertheless, our current simulations use the equilibrium profiles as an input to the computational model, hence do not simulate the steepening of density equilibriums. These results motivates a source driven simulations of CSDX which evolve total density and temperature fields, instead of only fluctuations about fixed, specified equilibrium.

Appendix C

Code Details

The turbulence model code discussed in this thesis was written in the open-source BOundary Turbulence (BOUT++) framework[DUX$^+$09]. The framework was written in C++ programming language, and is highly modular with parallel capability. The uncertainty quantification analysis in Chapter 5 was performed via python based ChaosPy framework[FL15]. In this Appendix, details of the frameworks installation and code setup is discussed, to enable reproducibility of simulations.

The latest developer edition of BOUT++ framework can be downloaded from GitHub repository, `git@github.com:boutproject/BOUT-dev.git`. The current version of BOUT++ framework used for the turbulence study in this thesis is version 3.0. The user manual inside the repository explains the details of installation and usage of the framework. To successfully install the framework, couple of libraries must be pre-installed. If installing on a local computer parallel enabling libraries such as `mpich`, or `open-mpi` must be installed. If installing the framework on a supercomputer cluster, these packages are usually pre-installed. To read/write simulation data, either `NetCDF` or `PDB` packages must be installed. The framework also uses `fftw` framework for Fast-Fourier transform calculations. By default, the framework uses `PVODE` solver as the

time integration scheme. Furthermore, as an optional package, one can also pre-install PETSC solver to enable more advanced bundled solvers such as `CVODE`, `IMEX`, etc. The current developer version of BOUT++ is not compatible with newer version of NetCDF and PETSC at the time of writing this thesis. The library versions tested to work is `mpich-3.2`, `netcdf-4.1.3`, `fftw-3.3.4`, `petsc-3.4.5` which needs to be manually installed in locally accessible folder.

The manually configuration and installation instruction of the packages is provided below. If installing the framework on a supercomputer cluster, check available modules, if not available, the libraries should be installed manually.

1. Installing MPICH:

```
$ ./configure --disable-fortran
$ make
$ make install
```

2. Installing FFTW:

```
$ ./configure --prefix=~/local
$ make
$ make install
```

3. Installing NetCDF:

```
$ ./configure --prefix=~/local --disable-fortran --disable-netcdf-4
$ make
$ make install
```

4. Installing PETSC (optional):

```
$ ./configure --with-fortran=0 --with-c++-support=1 --with-mpi=1
 --download-superlu_dist --download-metis --download-parmetis
 PETSC_DIR=~/local/petsc-3.4.5 PETSC_ARCH=linux-gnu-c-debug
$ make PETSC_DIR=~/local/petsc-3.4.5 PETSC_ARCH=linux-gnu-c-debug
all
```

5. Adding these paths in the bash profile and restarting the shell:

```
export PYTHONPATH=~/BOUT-dev/tools/pylib/:$PYTHONPATH
export IDL_PATH=~/BOUT-dev/tools/idllib/:$IDL_PATH
export PETSC_DIR=~/local/petsc-3.4.5
export PETSC_ARCH=linux-gnu-c-debug
```

5. Finally, configuring and installing BOUT-dev:

```
$ ./configure --with-fftw=~/local --with-netcdf=~/local
--prefix=~/local --with-petsc=~/local/petsc-3.4.5
PETSC_DIR=~/local/petsc-3.4.5
$ make
$ make install
```

The code is written as a `.cxx` file, calling necessary libraries for simulations and reads the `data/BOUT.inp` file for simulation inputs. In directory `BOUT-dev/examples` plenty of sample cases are available to explore and setup. In this Appendix, the details of a sample CSDX simulation `.cxx` file and `BOUT.inp` file is explained.

In the header of C++ file, the necessary libraries must be loaded:

```
#include <bout/physicsmodel.hxx>
#include <derivs.hxx>
#include <interpolation.hxx>
#include <initialprofiles.hxx>
#include <invert_laplace.hxx>
```

Then the variables need to be defined. The variables be in form of integer `int`, real double precision `BoutReal`, 2-D radially and axially variables `Field2D`, or evolving 3-D variables `Field3D`.

```
Field2D n0, Ti0, Te0, Tg0, nuin, Rxy, Zxy, dn0dr, dTe0dr, dnuindr;
Field3D n, vor, Te, phi, jpar, Vx, Vy;

BoutReal a, Bz, Lz;
BoutReal nbar, nbase, nalpha, Ln, Lambda;
BoutReal Tebar, Tebase, Tealpha, LTe;
BoutReal Tibar, Tibase, Tialpha, LTi;
BoutReal Tgbar, Tgbase, Tgalpha, LTg;
BoutReal nuin_hat, Dn_hat, nu_source, AA;
bool nonlinear, local;
int axial_sheath;
BoutReal low_pass_z;
```

```
int MXG, MYG;

BoutReal dx, dy, m_i, omega_ci, c_s, rho_s, rho_i, rho_e, mu_ii,
mui_hat, mui_par_hat;
Field2D loglam_ei, tau_e, eta, chi_e_par;
BoutReal loglam_ii, tau_i;
BoutReal Gamma_minus_1;
double PI, m_e, m_p, e0;
```

The BOUT++ framework uses two different protected functions to setup or restart the physics of simulation in function `physics_init(bool restarting)` and run the simulations in function `physics_run(BoutReal t)`. The physics setup, parameters options needs to be read from the input file `BOUT.inp`. The get section refers to the parameters defined below bracket in the input file. If they are not defined in the input file, the function `OPTION` uses the default value, defined in the third argument.

```
Options *options = Options::getRoot()->getSection("CSDX");
OPTION(options, AA, 40.);          /* m_i/m_p, atomic mass */
OPTION(options, Lambda, 5.1);      /* sheath factor */
OPTION(options, a, 8.);          /* cm */
OPTION(options, Bz, 1.);          /* kG */
OPTION(options, Lz, 200.0);    /* cm */
OPTION(options, nbar, 5.0e12);   /* cm^-3 */
OPTION(options, nbase, 0.0e12);   /* cm^-3 */
OPTION(options, nalpha, 2.);    /* n0 profile exponent */
OPTION(options, Ln, 2.);        /* cm */
OPTION(options, Tebar, 3.);       /* eV */
OPTION(options, Tebase, 0.);       /* eV */
OPTION(options, Tealpha, 2.);    /* Te0 profile exponent */
OPTION(options, LTe, 2.);        /* cm */
OPTION(options, Tibar, 0.5);       /* eV */
OPTION(options, Tibase, 0.5);       /* eV, defaults Ti0 flat */
OPTION(options, LTi, 2.);        /* cm */
OPTION(options, Tialpha, 2.);    /* Ti0 profile exponent */
OPTION(options, Tgbar, 3711.5);  /* K, core neutral gas temp */
OPTION(options, Tgbase, 300);  /* K, wall neutral gas temp */
OPTION(options, LTg, 2.5);        /* cm */
OPTION(options, Tgalpha, 2.);    /* Tg0 profile exponent */
OPTION(options, nuin_hat, 0.0);   /* c_s/a */
OPTION(options, Dn_hat, 0.0);   /* rho_s^2 c_s/a */
```

```
OPTION(options, nu_source, 0.);   /* c_s/Ln */
OPTION(options, axial_sheath, 0); /* options: 0=periodic;
1=conducting; 2=insulating */
OPTION(options, nonlinear, false);  /* nonlinear terms */
OPTION(options, local, false); /* local approximation */
OPTION(options, low_pass_z, -1); /* de-aliasing filtering */
```

Later, constant values and reference values are defined,

```
Gamma_minus_1 = 2./3;
PI = 2*asin(1.);
m_e = 9.10938261697e-31;  //electron mass
m_p = 1.66053892173e-27;  //proton mass
e0 = 1.602176487e-19;  //eV -> J
m_i = AA*m_p; //ion mass
omega_ci = e0*(Bz/10)/m_i;  //1/s, Bz from kG -> T
c_s = sqrt(e0*Tebar/m_i)*100;  //m/s -> cm/s
rho_s = c_s/omega_ci;   //cm
rho_i = sqrt(Tibar/Tebar)*rho_s;
rho_e = sqrt(m_e/m_i)*rho_s;
```

BOUT++ has the option to load any arbitrary form of grids using variety of mesh generators. However, in this study a simple cylinderical grid is generated within the physics setup. The framework default coordinates in the cartesian coordinate. However, one can translate the coordinates using metric tensors. The cylindrical geometry of CSDX is defined as,

```
/* rescale mesh dx, dy with MXG, MYG guard cells, x starts at dx */
dx = (a/rho_s)/(mesh->getNXPE()*(mesh->ngx - 2*MXG) + 2*MXG - 1);
mesh->dx = dx;
dy = (Lz/a)/(mesh->getNYPE()*(mesh->ngy - 2*MYG));
mesh->dy = dy;
Rxy = 0.;
Zxy = 0.;
/* g11 = g22 = g_11 = g_22 = 1. by default */
for(i=0;i<mesh->ngx;i++)
    for(j=0;j<mesh->ngy;j++)
    {
        Rxy[i][j] = mesh->XGLOBAL(i+1)*dx;
        Zxy[i][j] = mesh->YGLOBAL(j)*dy;
    }
mesh->g_33 = Rxy*Rxy; //metric tensor for cylinderical geometry
```

```
mesh->g33 = 1./mesh->g_33;
mesh->jacobian();
mesh->geometry();
```

Thus, equilibrium profiles and plasma parameters are defined in the physics setup section using manually defined function and according to the plasma formulary.

```
n0 = 1.;
Ti0 = 1.;
Te0 = 1.;
dn0dr = 0.;
dTe0dr = 0.;
n0 = nbase
+ (nbar-nbase)*exp(-(((rho_s/Ln)*Rxy)^nalpha)/nalpha);
Te0 = Tebase
+ (Tebar-Tebase)*exp(-(((rho_s/LTe)*Rxy)^Tealpha)/Tealpha);
Ti0 = Tibase
+ (Tibar-Tibase)*exp(-(((rho_s/LTi)*Rxy)^Tialpha)/Tialpha);
Tg0 = Tgbase
+ (Tgbar-Tgbase)*exp(-(((rho_s/LTg)*Rxy)^Tgalpha)/Tgalpha);
n0 /= nbar;
Te0 /= Tebar;
Ti0 /= Tibar;
dn0dr = DDX(n0);
dTe0dr = DDX(Te0);
if (local)
{
   dn0dr /= n0;
   dTe0dr /= Te0;
   n0 = 1.;
   Te0 = 1.;
   Ti0 = 1.;
}
dn0dr.applyBoundary("dirichlet");
mesh->communicate(dn0dr);
dTe0dr.applyBoundary("dirichlet");
mesh->communicate(dTe0dr);

/* from NRL formulary */
/* NRL, Te < 10 eV, = loglam_ee */
loglam_ei = 23. - 0.5*log(nbar*n0) + 1.5*log(Tebar*Te0);
tau_e = 3.44e5*((Tebar*Te0)^1.5)/(nbar*n0*loglam_ei);
/* norm. "eta" = 0.51*a/(c_s*tau_e) */
```

```
eta = (m_e/m_i)*(a/c_s)*(0.51/tau_e);
/* chi_e_par = (2./3)*3.16*v_te^2*tau_e
= (2*3.16/3)*(v_te/c_s)^2*(c_s/a*tau_e) in norm units */
chi_e_par = (2.*3.16/3)*(m_i/m_e)*(c_s/a)*tau_e;
/* 0D for now; can updated to 2D later */
/* NRL, "mixed" ion-ion */
loglam_ii = 23. - 0.5*log(2*nbar) + 1.5*log(Tibar);
tau_i = 2.09e7*pow(Tibar,1.5)*sqrt(AA)/(nbar*loglam_ii);
/* mu_ii = V_ti^2*tau_i*((2.33 + 1.2*X^2)/(2.33 + 4.03X^2 + X^4))
X= omega_ci*tau_ii goes to 0.3*rho_i^2/tau_i as X = 2*omega_ci*tau_i
-> inf formula from Braginskii review article */
mu_ii=(Tibar/Tebar)*c_s*c_s*tau_i*(2.23+1.2*pow(2*omega_ci*tau_i,2))
/(2.33 + 4.03*pow(2*omega_ci*tau_i,2)
+ pow(2*omega_ci*tau_i,4));
mui_hat = mu_ii / (rho_s*rho_s*c_s/a);
/* nuin = n_g * 6e-19 * sqrt(T_i*e0/mi) (1/s) formula from
n_g = P_g / (k_B * Tg0) assuming ideal nuetral gas */
nuin = 5.8975e-16*(0.39996711/1.3806e-23/Tg0);
nuin /= c_s/a;
dnuindr = DDX(nuin);
```

At the end of physics setup, the evolving variables must be added to the solver class, and we need to define the parameters we need to save once or at each iteration. `SAVE_ONCE` saves the variable only time before the beginning of the simulation, while `SAVE_REPEAT` and `solver->add` functions save the variables at each time-step, adding additional temporal dimension to the variable.

```
// Specify evolving variables
solver->add(vor, "vor"); // Vorticity
solver->add(n, "n");     // Electron density
solver->add(Te, "Te");   // Electron Temperature

SAVE_REPEAT(phi);
SAVE_REPEAT(jpar);
SAVE_REPEAT(Vx);
SAVE_REPEAT(Vy);

SAVE_ONCE2(Rxy, Zxy);
SAVE_ONCE4(n0, Ti0, Te0, Tg0);
SAVE_ONCE2(dn0dr, dTe0dr);
SAVE_ONCE5(a, Bz, Ln, LTe, Lz);
```

```
SAVE_ONCE6(nbar, Tebar, c_s,rho_s,rho_i,rho_e);
SAVE_ONCE6(mu_ii, mui_hat, nuin, Dn_hat, eta, chi_e_par);
SAVE_ONCE(nu_source);
```

In the `physics_run(BoutReal t)` section, we set the time derivative of evolving variables based on the right-hand-side of the evolving equations in the model. The 2-D invert Laplace operator is used to obtain plasma potential. Moreover, custom axial boundary conditions are applied at each timestep. The code in the current form is can only be parallelized in azimuthal direction and not in axial direction, Details of the functions used here can be found in BOUT++ user manual.

```
// Solve for potential
if (local) {
    phi  = invert_laplace(vor, 1+2, NULL, NULL);
} else {
    phi = invert_laplace(vor/n0, 1+2, NULL, &n0);
}
mesh->communicate(phi, vor, n, Te);

// Calculate jpar
jpar = -Grad_par_LtoC(n0*phi - Te0*n - 1.71*n0*Te)/eta;
mesh->communicate(jpar);

// conducting boundary condition
// requires setting ixsep1=0 in input file
// currently doesnt work with multi processors in axial direction
if(axial_sheath == 1) {
      //Upper axial BC
      for (int ir=0; ir<mesh->ngx; ir++)
        for (int y=mesh->ngy-3; y<mesh->ngy; y++)
          for (int z=0; z<mesh->ngz; z++) {
            n[ir][y][z] = n[ir][y-1][z];
            Te[ir][y][z] = Te[ir][y-1][z];
            phi[ir][y][z] = phi[ir][y-1][z];
            jpar[ir][y][z]=phi[ir][y-1][z]-Lambda*Te[ir][y-1][z];
            vor[ir][y][z] = 0.;
          }
      //Lower Axial BC
      for (int ir=0; ir<mesh->ngx; ir++)
        for (int y=2; y>=0; y--)
          for (int z=0; z<mesh->ngz; z++) {
```

```
            n[ir][y][z] = n[ir][y+1][z];
            Te[ir][y][z] = Te[ir][y+1][z];
            phi[ir][y][z] = phi[ir][y+1][z];
           jpar[ir][y][z]=-(phi[ir][y+1][z]-Lambda*Te[ir][y+1][z]);
            vor[ir][y][z] = 0.;
          }
} else if(axial_sheath == 2) { //insulating boundary condition
      //Upper axial BC
      for (int ir=0; ir<mesh->ngx; ir++)
        for (int y=mesh->ngy-3; y<mesh->ngy; y++)
          for (int z=0; z<mesh->ngz; z++) {
            n[ir][y][z] = n[ir][y-1][z];
            Te[ir][y][z] = 0.;
            phi[ir][y][z] = 0.;
            jpar[ir][y][z] = 0.;
            vor[ir][y][z] = 0.;
          }
      //Lower Axial BC
      for (int ir=0; ir<mesh->ngx; ir++)
        for (int y=2; y>=0; y--)
          for (int z=0; z<mesh->ngz; z++) {
            n[ir][y][z] = n[ir][y+1][z];
            Te[ir][y][z] = 0.;
            phi[ir][y][z] = 0.;
            jpar[ir][y][z] = 0.;
            vor[ir][y][z] = 0.;
          }
}

/* evolving density */
ddt(n) = 0.;
ddt(n) += (a/rho_s)*(dn0dr/Rxy)*DDZ(phi);
ddt(n) += Grad_par_CtoL(jpar);
ddt(n) += Dn_hat*Delp2(n);
ddt(n) -= nu_source*averageY(n.DC());
if (nonlinear)
  ddt(n) += (a/rho_s)*bracket(phi, n, BRACKET_ARAKAWA)/Rxy;

/* evolving vorticity */
ddt(vor) = 0.;
ddt(vor) += Grad_par_CtoL(jpar);
ddt(vor) -= nuin_hat*vor;
ddt(vor) += mui_hat*Delp2(vor);
```

```
if (nonlinear)
  ddt(vor) += (a/rho_s)*bracket(phi, vor, BRACKET_ARAKAWA)/Rxy;

/* evolving Te */
ddt(Te) = 0.;
ddt(Te) += (a/rho_s)*(dTe0dr/Rxy)*DDZ(phi);
ddt(Te) += Gamma_minus_1*Te0*Grad_par_CtoL(1.71*jpar/n0);
ddt(Te) += Dn_hat*Delp2(Te);
ddt(Te) += chi_e_par*D2DY2(Te);
ddt(Te) -= nu_source*averageY(Te.DC());
if (nonlinear)
    ddt(Te) += (a/rho_s)*bracket(phi, Te, BRACKET_ARAKAWA)/Rxy;

Vx = -DDZ(phi)/Rxy;
Vx.applyBoundary("Dirichlet");
Vy = DDX(phi);
Vy.applyBoundary("Dirichlet");
mesh->communicate(Vx, Vy);

if(low_pass_z > 0) {
    // Low-pass filter, keeping n up to low_pass_z
    // -1 mean keep zonal harmonic
    ddt(n) = lowPass(ddt(n), low_pass_z, -1);
    ddt(vor) = lowPass(ddt(vor), low_pass_z, -1);
    ddt(Te) = lowPass(ddt(Te), low_pass_z, -1);
}
```

In the `BOUT.inp` file, the parameters for each simulation, initial perturbation form, and boundary conditions can be set. A sample input file for nominal CSDX simulation is shown below,

```
timestep = 0.2 # normalized time step
nout = 2000 # number of time steps
MZ = 129 # azimuthal grid points
ZPERIOD=1
MXG = 2 # number of ghost cells in radial direction
NXPE = 24 # number of processors in radial direction
NYPE = 1 # only one processor in the axial direction

[mesh]
nx = 100 # number of radial grid points
ny = 36 # number of axial grid points
```

```
dx = 1.
dy = 1.
ixseps1 = 0 # means ALL points in SOL (needed for boundary
conditions in axial direction, comment this for periodic runs)

[ddx] #setting radial derivative types
first = C4   # C4 = 4th order central, C2 = 2nd order central
second = C4
upwind = W3   # U1 = 1st order upwind, W3 = 3rd order WENO

[ddy] # setting axial derivative types
first = C4
second = C4

[ddz] # setting azimuthal derivative types
first = FFT
second = FFT
upwind = W3

[laplace] # 2D invert Laplace operator
flags = 0   # flags for Laplacian inversion
all_terms = true
nonuniform = true # needed for cylindrical geometry

[CSDX] # CSDX parameters
a = 8.   # cm
Bz = 1.0  # kG
Lz = 300. # cm
nbar = 9.87295e+12 # cm^-3
nbase = 1.81096e+11  # cm^3
nalpha = 2.9395  # n0 profile exponent
Ln = 2.2696 # cm
Tebar = 3.0597  # eV
Tebase = 0.41243 # eV
Tealpha = 6.3166  # Te0 profile exponent
LTe = 3.875 # cm
Tibar = 0.4 # eV
Tibase = 0.4 # eV
Tialpha = 2.0 # Ti0 profile exponent
LTi = 2. # cm
Dn_hat = 0.0198 # rho_s^2 c_s/a
nu_source = 20.0 # c_s/a
axial_sheath = 2 # 0=periodic; 1=conducting; 2=insulating
```

```
nonlinear = true
local = false
low_pass_z = 41  # <= MZ/3

[solver] # setting time integration scheme
type = PVODE
timestep = 0.1
mxstep = 100000

[All] # initializing options
scale =0.07  # default size of initial perturbations
# form of initial profile
xs_opt = 1 # setting Gaussian initial fluctuation profile
ys_opt = 2 # setting sinusoidal initial fluctuation profile
zs_opt = 3 # setting mix of modes initial fluctuation profile
xs_mode = 1 # initial radial mode number
ys_mode = 1 # initial parallel mode number
zs_mode = 1 # initial azimuthal mode number
bndry_all = dirichlet # setting boundary conditions
bndry_yin = none # manually overriding axial boundary condition
bndry_yout = none # manually overriding axial boundary condition

[n]
bndry_core = neumann # overriding BC in the inner core

[Te]
bndry_core = neumann # overriding BC in the inner core
```

A sample `.cxx` file and `BOUT.inp` of the CSDX simulation setup is available on GitHub repository,

`github.com/pvaezi/BOUT-dev/tree/master/examples/csdx-3f`.

For uncertainty quantification analysis, open-source ChaosPy python based framework is used. It a very easy to use framework, with most of the probability distributions and quantification scheme written and ready-to-use. To install `chaospy`, a source of the code can be downloaded from the GitHub repository and installed,

```
git clone git@github.com:jonathf/chaospy.git
cd chaospy
pip install -r requirements.txt
python setupy.py install
```

The details of all the functions used in the framework is explained in the manual enclosed in the framework. For a sample probability collocation method uncertainty quantification in the IBC case, a simple script can be written in python syntax. The fluctuation properties are then imported into the script in array format. The following libraries are loaded into python for uncertainty quantification analysis.

```
import chaospy as cp
import numpy as np
```

Then the UQ analysis can be done in couple of easy steps. First, the types of input probability distributions and their normalized distributions ($\int_{-\infty}^{\infty} p_q dq = 1$) should be defined,

```
#actual distribution space
rv = cp.J(
cp.Normal(mu=0.6, sigma=0.1816), #Ti0
cp.Uniform(0., 1160.-300.)  #Tgb (K - 300) Rosenblatt transformation
gives wrong answer in uniform distribution with offset. Subtracting
the lower bound offset.
)
#mapping to normalized multivariate distribution space
#normalized distributions require int(df*dist,x=min..max) = 1
rv_proxy = cp.J(
cp.Normal(0, 1),
cp.Uniform(0, 1)
)
```

Then, the number of collocation nodes drawn from the multivariate probability distribution of input parameters. The second argument in `sample` function, determines the type of sampling. For instance, `"M"` designates the Hammersley sequence sampling method. The nodes are then mapped into normalized distribution space.

```
nosamples = 5
samples = rv.sample(nosamples, "M")
nodes = rv_proxy.inv(rv.fwd(samples))
```

The set of chaos polynomials orthogonal to each other in the normalized proxy distribution space are furthermore generated.

```
order = 1 #order of the polynomials
P = cp.orth_ttr(order, rv_proxy, normed=False)
```

Finally, after solving for the simulations, the coefficients of polynomials are fitted via regression according to the response quantities obtained from the simulations. Then, mean and standard deviation of probability distribution can be obtained from the chaos polynomials expansion.

```
u_hat = cp.fit_regression(P, nodes, flux)
pcmmean = cp.E(u_hat, rv_proxy) # mean of response probability
pcmstd = cp.Std(u_hat, rv_proxy) # std.dev. of response probability
```

Bibliography

[AL81] Akio Arakawa and Vivian R. Lamb. A potential enstrophy and energy conserving scheme for the shallow water equations. *Monthly Weather Review*, 109(1):18–36, 1981.

[BCR+93] H.-L. Berk, R.H. Cohen, D.D. Ryutov, Yu.A. Tsidulko, and X.Q. Xu. Electron temperature gradient induced instability in tokamak scrape-off layers. *Nuclear Fusion*, 33(2):263, 1993.

[BDT90] H. Biglari, P. H. Diamond, and P. W. Terry. Influence of sheared poloidal rotation on edge turbulence. *Physics of Fluids B: Plasma Physics*, 2(1):1–4, 1990.

[Bec73] Petr Beckmann. *Orthogonal polynomials for engineers and physicists*. Golem Pr, 1973.

[Bew08] Thomas R Bewley. Numerical renaissance: Simulation, optimization, and control, 2008.

[BH99] George D. Byrne and Alan C. Hindmarsh. Pvode, an ode solver for parallel computers. *The International Journal of High Performance Computing Applications*, 13(4):354–365, 1999.

[BK85] Dieter Biskamp and He Kaifen. Three ĂŘdrift ĂŘwave interaction at finite parallel wavelength: Bifurcations and transition to turbulence. *The Physics of Fluids*, 28(7):2172–2180, 1985.

[BN06] R. V. Bravenec and W. M. Nevins. System for simulating fluctuation diagnostics for application to turbulence computations. *Review of Scientific Instruments*, 77(1), 2006.

[Bra65] S. I. Braginskii. Transport Processes in a Plasma. *Reviews of Plasma Physics*, 1:205, 1965.

[Bro07] AE Brockwell. Universal residuals: A multivariate transformation. *Statistics & probability letters*, 77(14):1473–1478, 08 2007.

[BTA+05] M. J. Burin, G. R. Tynan, G. Y. Antar, N. A. Crocker, and C. Holland. On the transition to drift turbulence in a magnetized plasma column. *Physics of Plasmas*, 12(5), 2005.

[Bur97] K. H. Burrell. Effects of exb velocity shear and magnetic shear on turbulence and transport in magnetic confinement devices. *Physics of Plasmas*, 4(5):1499–1518, 1997.

[CAT+16] L. Cui, A. Ashourvan, S. C. Thakur, R. Hong, P. H. Diamond, and G. R. Tynan. Spontaneous profile self-organization in a simple realization of drift-wave turbulence. *Physics of Plasmas*, 23(5):055704, 2016.

[CGM+15] M.A. Chilenski, M. Greenwald, Y. Marzouk, N.T. Howard, A.E. White, J.E. Rice, and J.R. Walk. Improved profile fitting and quantification of uncertainty in experimental measurements of impurity transport coefficients using gaussian process regression. *Nuclear Fusion*, 55(2):023012, 2015.

[CS84] Francis F Chen and Mark D Smith. *Plasma*. Wiley Online Library, 1984.

[CTD+15] L. Cui, G. R. Tynan, P. H. Diamond, S. C. Thakur, and C. Brandt. Up-gradient particle flux in a drift wave-zonal flow system. *Physics of Plasmas*, 22(5):050704, 2015.

[CTML+12] S. Chakraborty Thakur, D. McCarren, T. Lee, N. Fedorczak, P. Manz, E. E. Scime, G. R. Tynan, and M. Xu. Laser induced fluorescence measurements of ion velocity and temperature of drift turbulence driven sheared plasma flow in a linear helicon plasma device. *Physics of Plasmas*, 19(8), 2012.

[CTXM+13] Saikat Chakraborty Thakur, Min Xu, Peter Manz, Nicolas Fedorczak, Chris Holland, and George R. Tynan. Suppression of drift wave turbulence and zonal flow formation by changing axial boundary conditions in a cylindrical magnetized plasma device. *Physics of Plasmas*, 20(1), 2013.

[CW03] J. Candy and R.E. Waltz. An eulerian gyrokinetic-maxwell solver. *Journal of Computational Physics*, 186(2):545 – 581, 2003.

[Czi11] Istvan Cziegler. *Turbulence and transport phenomena in edge and scrape-off-layer plasmas*. PhD thesis, Massachusetts Institute of Technology, 2011.

[DBB+00] A. M. Dimits, G. Bateman, M. A. Beer, B. I. Cohen, W. Dorland, G. W. Hammett, C. Kim, J. E. Kinsey, M. Kotschenreuther, A. H. Kritz, L. L. Lao, J. Mandrekas, W. M. Nevins, S. E. Parker, A. J. Redd, D. E. Shumaker, R. Sydora, and J. Weiland. Comparisons and physics basis of tokamak transport models and turbulence simulations. *Physics of Plasmas*, 7(3):969–983, 2000.

[DII10] Patrick H Diamond, Sanae-I Itoh, and Kimitaka Itoh. *Modern Plasma Physics: Volume 1, Physical Kinetics of Turbulent Plasmas*. Cambridge University Press, 2010.

[DIIH05] P H Diamond, S-I Itoh, K Itoh, and T S Hahm. Zonal flows in plasmaâĂŤa review. *Plasma Physics and Controlled Fusion*, 47(5):R35, 2005.

[DMO+16] Ben Dudson, Jens Madsen, John Omotani, Peter Hill, Luke Easy, and Michael Løiten. Verification of bout++ by the method of manufactured solutions. *arXiv preprint arXiv:1602.06747*, 2016.

[DRM+12] D. A. DIppolito, D. A. Russell, J. R. Myra, S. C. Thakur, G. R. Tynan, and C. Holland. Effect of parallel currents on drift-interchange turbulence: Comparison of simulation and experiment. *Physics of Plasmas*, 19(10), 2012.

[DUX+09] B.D. Dudson, M.V. Umansky, X.Q. Xu, P.B. Snyder, and H.R. Wilson. Bout++: A framework for parallel plasma fluid simulations. *Computer Physics Communications*, 180(9):1467 – 1480, 2009.

[End99] M. Endler. Turbulent sol transport in stellarators and tokamaks. *Journal of Nuclear Materials*, 266:84 – 90, 1999.

[FBC+16] A. Fasoli, S. Brunner, W. A. Cooper, J. P. Graves, P. Ricci, O. Sauter, and L. Villard. Computational challenges in magnetic-confinement fusion physics. *Nat Phys*, 12(5):411–423, 05 2016.

[FCU+12] B. Friedman, T. A. Carter, M. V. Umansky, D. Schaffner, and B. Dudson. Energy dynamics in a simulation of lapd turbulence. *Physics of Plasmas*, 19(10), 2012.

[FL15] Jonathan Feinberg and Hans Petter Langtangen. Chaospy: An open source tool for designing methods of uncertainty quantification. *Journal of Computational Science*, 11:46 – 57, 2015.

[Fre08] Jeffrey P Freidberg. *Plasma physics and fusion energy*. Cambridge university press, 2008.

[Fri13] Brett Friedman. Simulation analysis of zero mean flow edge turbulence in lapd, 2013.

[FRR+15] Dustin M. Fisher, Barrett N. Rogers, Giovanni D. Rossi, Daniel S. Guice, and Troy A. Carter. Three-dimensional two-fluid braginskii simulations of the large plasma device. *Physics of Plasmas*, 22(9), 2015.

[FWK08] Jasmine Foo, Xiaoliang Wan, and George Em Karniadakis. The multi-element probabilistic collocation method (me-pcm): Error analysis and applications. *Journal of Computational Physics*, 227(22):9572 – 9595, 2008.

[Gau82] Walter Gautschi. On generating orthogonal polynomials. *SIAM Journal on Scientific and Statistical Computing*, 3(3):289–317, 1982.

[GEMC+06] Joshua D. Griffin, Michael Scott Eldred, Monica L. Martinez-Canales, Jean-Paul Watson, Tamara Gibson Kolda, Anthony Andrew Giunta, Brian M. Adams, Laura Painton Swiler, Pamela J. Williams, and Patricia Diane Hough. *DAKOTA, a multilevel parellel object-oriented framework for design optimization, parameter estimation, uncertainty quantification, and sensitivity analysis:version 4.0 users's manual.* Oct 2006.

[GIVW10] X Garbet, Y Idomura, L Villard, and TH Watanabe. Gyrokinetic simulations of turbulent transport. *Nuclear Fusion*, 50(4):043002, 2010.

[HBB+98] R. J. Hawryluk, S. Batha, W. Blanchard, M. Beer, M. G. Bell, R. E. Bell, H. Berk, S. Bernabei, M. Bitter, B. Breizman, N. L. Bretz, R. Budny, C. E. Bush, J. Callen, R. Camp, S. Cauffman, Z. Chang, C. Z. Cheng, D. S. Darrow, R. O. Dendy, W. Dorland, H. Duong, P. C. Efthimion, D. Ernst, N. J. Fisch, R. Fisher, R. J. Fonck, E. D. Fredrickson, G. Y. Fu, H. P. Furth, N. N. Gorelenkov, B. Grek, L. R. Grisham, G. W. Hammett, G. R. Hanson, H. W. Herrmann, M. C. Herrmann, K. W. Hill, J. Hogan, J. C. Hosea, W. A. Houlberg, M. Hughes, R. A. Hulse, D. L. Jassby, F. C. Jobes, D. W. Johnson, R. Kaita, S. Kaye, J. S. Kim, M. Kissick, A. V. Krasilnikov, H. Kugel, A. Kumar, B. Leblanc, F. M. Levinton, C. Ludescher, R. P. Majeski, J. Manickam, D. K. Mansfield, E. Mazzucato, J. McChesney, D. C. McCune, K. M. McGuire, D. M. Meade, S. S. Medley, R. Mika, D. R. Mikkelsen, S. V. Mirnov, D. Mueller, A. Nagy, G. A. Navratil, R. Nazikian, M. Okabayashi, H. K. Park, W. Park, S. F. Paul, G. Pearson, M. P. Petrov, C. K. Phillips, M. Phillips, A. T. Ramsey, M. H. Redi, G. Rewoldt, S. Reznik, A. L. Roquemore, J. Rogers, E. Ruskov, S. A. Sabbagh, M. Sasao, G. Schilling, J. Schivell, G. L. Schmidt, S. D. Scott, I. Semenov, C. H. Skinner, T. Stevenson, B. C. Stratton, J. D. Strachan, W. Stodiek, E. Synakowski, H. Takahashi, W. Tang, G. Taylor, M. E. Thompson, S. Von Goeler, A. Von Halle, R. T. Walters, R. White, R. M. Wieland, M. Williams, J. R. Wilson, K. L. Wong, G. A. Wurden, M. Yamada, V. Yavorski, K. M. Young, L. Zakharov, M. C. Zarnstorff, and S. J. Zweben. Fusion plasma experiments on tftr: A 20 year retrospective. *Physics of Plasmas*, 5(5):1577–1589, 1998.

[HDP+13] J. C. Hillesheim, J. C. DeBoo, W. A. Peebles, T. A. Carter, G. Wang, T. L. Rhodes, L. Schmitz, G. R. McKee, Z. Yan, G. M. Staebler, K. H. Burrell,

E. J. Doyle, C. Holland, C. C. Petty, S. P. Smith, A. E. White, and L. Zeng. Experimental characterization of multiscale and multifield turbulence as a critical gradient threshold is surpassed in the diii-d tokamak. *Physics of Plasmas*, 20(5):056115, 2013.

[HH12] Claude Wendell Horton and Wendell Horton. *Turbulent transport in magnetized plasmas*. World Scientific, 2012.

[HL04] J. R. Hockenberry and B. C. Lesieutre. Evaluation of uncertainty in dynamic simulations of power system models: The probabilistic collocation method. *IEEE Transactions on Power Systems*, 19(3):1483–1491, Aug 2004.

[HM78] Akira Hasegawa and Kunioki Mima. Pseudo?three?dimensional turbulence in magnetized nonuniform plasma. *The Physics of Fluids*, 21(1):87–92, 1978.

[Hol16] C. Holland. Validation metrics for turbulent plasma transport. *Physics of Plasmas*, 23(6), 2016.

[Hor99] W. Horton. Drift waves and transport. *Rev. Mod. Phys.*, 71:735–778, Apr 1999.

[HTJ$^+$07] C Holland, G R Tynan, J H Yu A James, D Nishijima, M Shimada, and N Taheri. Numerical simulations of collisional drift-wave turbulence in a magnetized plasma column. *Plasma Physics and Controlled Fusion*, 49(5A):A109, 2007.

[HTK87] W. Horton, T. Tajima, and T. Kamimura. Kelvin helmholtz instability and vortices in magnetized plasma. *The Physics of Fluids*, 30(11):3485–3495, 1987.

[HTMF04] C. Holland, G. R. Tynan, G. R. McKee, and R. J. Fonck. Investigation of the time-delay estimation method for turbulent velocity inference. *Review of Scientific Instruments*, 75(10):4278–4280, 2004.

[Hut02] Ian H Hutchinson. Principles of plasma diagnostics. *Plasma Physics and Controlled Fusion*, 44(12):2603, 2002.

[HW83] Akira Hasegawa and Masahiro Wakatani. Plasma edge turbulence. *Phys. Rev. Lett.*, 50:682–686, Feb 1983.

[HWB07] Serhat Hosder, Robert Walters, and Michael Balch. Efficient sampling for non-intrusive polynomial chaos applications with multiple uncertain input variables. In *48th AIAA/ASME/ASCE/AHS/ASC Structures, Structural Dynamics, and Materials Conference*, page 1939, 2007.

[Jas72] D. L. Jassby. Transverse velocity shear instabilities within a magnetically confined plasma. *Physics of Fluids*, 15(9):1590–1604, 1972.

[KDM08] S. I. Krasheninnikov, D. A. D'Ippolito, and J. R. Myra. Recent theoretical progress in understanding coherent structures in edge and sol turbulence. *Journal of Plasma Physics*, 74:679–717, 10 2008.

[KLP+97] T. Klinger, A. Latten, A. Piel, G. Bonhomme, T. Pierre, and T. Dudok de Wit. Route to drift wave chaos and turbulence in a bounded low- β plasma experiment. *Phys. Rev. Lett.*, 79:3913–3916, Nov 1997.

[Kol62] A. N. Kolmogorov. A refinement of previous hypotheses concerning the local structure of turbulence in a viscous incompressible fluid at high reynolds number. 13(1):82–85, 1962.

[Lan44] Lev D Landau. On the problem of turbulence. In *Dokl. Akad. Nauk SSSR*, volume 44, pages 339–349, 1944.

[Law57] J D Lawson. Some criteria for a power producing thermonuclear reactor. *Proceedings of the Physical Society. Section B*, 70(1):6, 1957.

[LBC+07] B. Lipschultz, X. Bonnin, G. Counsell, A. Kallenbach, A. Kukushkin, K. Krieger, A. Leonard, A. Loarte, R. Neu, R.A. Pitts, T. Rognlien, J. Roth, C. Skinner, J.L. Terry, E. Tsitrone, D. Whyte, S. Zweben, N. Asakura, D. Coster, R. Doerner, R. Dux, G. Federici, M. Fenstermacher, W. Fundamenski, P. Ghendrih, A. Herrmann, J. Hu, S. Krasheninnikov, G. Kirnev, A. Kreter, V. Kurnaev, B. LaBombard, S. Lisgo, T. Nakano, N. Ohno, H.D. Pacher, J. Paley, Y. Pan, G. Pautasso, V. Philipps, V. Rohde, D. Rudakov, P. Stangeby, S. Takamura, T. Tanabe, Y. Yang, and S. Zhu. PlasmaâĂŞsurface interaction, scrape-off layer and divertor physics: implications for iter. *Nuclear Fusion*, 47(9):1189, 2007.

[LHM+05] B. LaBombard, J.W. Hughes, D. Mossessian, M. Greenwald, B. Lipschultz, J.L. Terry, and the Alcator C-Mod Team. Evidence for electromagnetic fluid drift turbulence controlling the edge plasma state in the alcator c-mod tokamak. *Nuclear Fusion*, 45(12):1658, 2005.

[Loi13] Joaquim Loizu. *The role of the sheath in magnetized plasma turbulence and flows*. PhD dissertation, EPFL, 2013.

[Lor63] Edward N. Lorenz. Deterministic nonperiodic flow. *Journal of the Atmospheric Sciences*, 20(2):130–141, 1963.

[LRHJ12] J. Loizu, P. Ricci, F. D. Halpern, and S. Jolliet. Boundary conditions for plasma fluid models at the magnetic presheath entrance. *Physics of Plasmas*, 19(12), 2012.

[LRT11] Joaquim Loizu, Paolo Ricci, and Christian Theiler. Existence of subsonic plasma sheaths. *Phys. Rev. E*, 83:016406, Jan 2011.

[LTB+13] A. D. Light, S. C. Thakur, C. Brandt, Y. Sechrest, G. R. Tynan, and T. Munsat. Direct extraction of coherent mode properties from imaging measurements in a linear plasma column. *Physics of Plasmas*, 20(8):082120, 2013.

[LWB07] G. J. A. Loeven, J. A. S. Witteveen, and H. Bijl. *Probabilistic Collocation: An Efficient Non-Intrusive Approach for Arbitrarily Distributed Parametric Uncertainties*. American Institute of Aeronautics and Astronautics, 2017/06/11 2007.

[Mah00] Sankaran Mahadevan. *Probability, reliability, and statistical methods in engineering design*. Wiley, 2000.

[MGR+05] N Mahdizadeh, F Greiner, M Ramisch, U Stroth, W Guttenfelder, C Lechte, and K Rahbarnia. Comparison of langmuir and emissive probes as diagnostics for turbulence studies in the low-temperature plasma of the torsatron tj-k. *Plasma Physics and Controlled Fusion*, 47(4):569, 2005.

[MST+09] P. Mantica, D. Strintzi, T. Tala, C. Giroud, T. Johnson, H. Leggate, E. Lerche, T. Loarer, A. G. Peeters, A. Salmi, S. Sharapov, D. Van Eester, P. C. de Vries, L. Zabeo, and K.-D. Zastrow. Experimental study of the ion critical-gradient length and stiffness level and the impact of rotation in the jet tokamak. *Phys. Rev. Lett.*, 102:175002, Apr 2009.

[MXF+12] P. Manz, M. Xu, N. Fedorczak, S. C. Thakur, and G. R. Tynan. Spatial redistribution of turbulent and mean kinetic energy. *Physics of Plasmas*, 19(1), 2012.

[MXTT11] P Manz, M Xu, S C Thakur, and G R Tynan. Nonlinear energy transfer during the transition to drift-interchange turbulence. *Plasma Physics and Controlled Fusion*, 53(9):095001, 2011.

[MXW+12] P. Manz, G. S. Xu, B. N. Wan, H. Q. Wang, H. Y. Guo, I. Cziegler, N. Fedorczak, C. Holland, S. H. Müller, S. C. Thakur, M. Xu, K. Miki, P. H. Diamond, and G. R. Tynan. Zonal flow triggers the l-h transition in the experimental advanced superconducting tokamak. *Physics of Plasmas*, 19(7):072311, 2012.

[NBD07] Ryusuke Numata, Rowena Ball, and Robert L. Dewar. Bifurcation in electrostatic resistive drift wave turbulence. *Physics of Plasmas*, 14(10):102312, 2007.

[NRR+12] B Nold, T T Ribeiro, M Ramisch, Z Huang, H W Müller, B D Scott, U Stroth, and the ASDEX Upgrade Team. Influence of temperature fluctuations on plasma turbulence investigations with langmuir probes. *New Journal of Physics*, 14(6):063022, 2012.

[NWG08] V. Naulin, T. Windisch, and O. Grulke. Three-dimensional global fluid simulations of cylindrical magnetized plasmas. *Physics of Plasmas*, 15(1), 2008.

[NXK+16] Lin Nie, Min Xu, Rui Ke, Boda Yuan, Jun Cheng, Yi Yu, Tao Lan, Huagang Shen, Rongjie Hong, Yunbo Dong, Dong Guo, and Yifan Wu. Experimental evaluation of langmuir probe sheath potential coefficient. 2016.

[ODR+02] William L. Oberkampf, Sharon M. DeLand, Brian M. Rutherford, Kathleen V. Diegert, and Kenneth F. Alvin. Error and uncertainty in modeling and simulation. *Reliability Engineering and System Safety*, 75(3):333 – 357, 2002.

[OKWZ16] J. Ongena, R. Koch, R. Wolf, and H. Zohm. Magnetic-confinement fusion. *Nat Phys*, 12(5):398–410, 05 2016.

[OM11] Todd A Oliver and Robert D Moser. Bayesian uncertainty quantification applied to rans turbulence models. *Journal of Physics: Conference Series*, 318(4):042032, 2011.

[OTH04] William L Oberkampf, Timothy G Trucano, and Charles Hirsch. Verification, validation, and predictive capability in computational engineering and physics. *Applied Mechanics Reviews*, 57(5):345–384, 2004.

[PH13] J. L. Peterson and G. W. Hammett. Positivity preservation and advection algorithms with applications to edge plasma turbulence. *SIAM Journal on Scientific Computing*, 35(3):B576–B605, 2013.

[PLD+98] C.C. Petty, T.C. Luce, J.C. DeBoo, R.E. Waltz, D.R. Baker, and M.R. Wade. Scaling of heat transport with beta in the diii-d tokamak. *Nuclear Fusion*, 38(8):1183, 1998.

[Pop01] Stephen B Pope. Turbulent flows. *Measurement Science and Technology*, 12(11):2020, 2001.

[PUCF10a] P. Popovich, M. V. Umansky, T. A. Carter, and B. Friedman. Modeling of plasma turbulence and transport in the large plasma device. *Physics of Plasmas*, 17(12), 2010.

[PUCF10b] P. Popovich, M. V. Umansky, T. A. Carter, and B. Friedman. Modeling of plasma turbulence and transport in the large plasma device. *Physics of Plasmas*, 17(12):122312, 2010.

[RHJ+12] P Ricci, F D Halpern, S Jolliet, J Loizu, A Mosetto, A Fasoli, I Furno, and C Theiler. Simulation of plasma turbulence in scrape-off layer conditions: the gbs code, simulation results and code validation. *Plasma Physics and Controlled Fusion*, 54(12):124047, 2012.

[RHS+11] T.L. Rhodes, C. Holland, S.P. Smith, A.E. White, K.H. Burrell, J. Candy, J.C. DeBoo, E.J. Doyle, J.C. Hillesheim, J.E. Kinsey, G.R. McKee, D. Mikkelsen, W.A. Peebles, C.C. Petty, R. Prater, S. Parker, Y. Chen, L. Schmitz, G.M. Staebler, R.E. Waltz, G. Wang, Z. Yan, and L. Zeng. L-mode validation studies of gyrokinetic turbulence simulations via multiscale and multifield turbulence measurements on the diii-d tokamak. *Nuclear Fusion*, 51(6):063022, 2011.

[RK11] Reuven Y Rubinstein and Dirk P Kroese. *Simulation and the Monte Carlo method*, volume 707. John Wiley & Sons, 2011.

[RMD09] D. A. Russell, J. R. Myra, and D. A. D'Ippolito. Saturation mechanisms for edge turbulence. *Physics of Plasmas*, 16(12), 2009.

[RMD+11] D. A. Russell, J. R. Myra, D. A. DĂŹIppolito, T. L. Munsat, Y. Sechrest, R. J. Maqueda, D. P. Stotler, S. J. Zweben, and The NSTX Team. Comparison of scrape-off layer turbulence simulations with experiments using a synthetic gas puff imaging diagnostic. *Physics of Plasmas*, 18(2), 2011.

[Ros52] Murray Rosenblatt. Remarks on a multivariate transformation. *The Annals of Mathematical Statistics*, 23(3):470–472, 1952.

[RR10] B. N. Rogers and Paolo Ricci. Low-frequency turbulence in a linear magnetized plasma. *Phys. Rev. Lett.*, 104:225002, Jun 2010.

[RRT+15] P. Ricci, F. Riva, C. Theiler, A. Fasoli, I. Furno, F. D. Halpern, and J. Loizu. Approaching the investigation of plasma turbulence through a rigorous verification and validation procedure: A practical example. *Physics of Plasmas*, 22(5), 2015.

[RT71] David Ruelle and Floris Takens. On the nature of turbulence. *Communications in Mathematical Physics*, 20(3):167–192, 1971.

[RTF+09] Paolo Ricci, C. Theiler, A. Fasoli, I. Furno, B. Labit, S. H. Muller, M. Podesta, and F. M. Poli. Langmuir probe-based observables for plasma-turbulence code validation and application to the torpex basic plasma physics experimenta). *Physics of Plasmas*, 16(5), 2009.

[Sco97] B Scott. Three-dimensional computation of collisional drift wave turbulence and transport in tokamak geometry. *Plasma Physics and Controlled Fusion*, 39(3):471, 1997.

[SKW07] G. M. Staebler, J. E. Kinsey, and R. E. Waltz. A theory-based transport model with comprehensive physics. *Physics of Plasmas*, 14(5):055909, 2007.

[SLC01] Timothy W Simpson, Dennis KJ Lin, and Wei Chen. Sampling strategies for computer experiments: design and analysis. *International Journal of Reliability and Applications*, 2(3):209–240, 2001.

[Sta00] P.C. Stangeby. *The Plasma Boundary of Magnetic Fusion Devices*. Series in Plasma Physics and Fluid Dynamics. Taylor & Francis, 2000.

[Tay97] John Taylor. *Introduction to error analysis, the study of uncertainties in physical measurements*, volume 1. 1997.

[TBL+14] S. C. Thakur, C. Brandt, A. Light, L. Cui, J. J. Gosselin, and G. R. Tynan. Simultaneous use of camera and probe diagnostics to unambiguously identify and study the dynamics of multiple underlying instabilities during the route to plasma turbulence. *Review of Scientific Instruments*, 85(11), 2014.

[Ter00] P. W. Terry. Suppression of turbulence and transport by sheared flow. *Rev. Mod. Phys.*, 72:109–165, Jan 2000.

[TFM09] G R Tynan, A Fujisawa, and G McKee. A review of experimental drift turbulence studies. *Plasma Physics and Controlled Fusion*, 51(11):113001, 2009.

[TGL+08] P. W. Terry, M. Greenwald, J.-N. Leboeuf, G. R. McKee, D. R. Mikkelsen, W. M. Nevins, D. E. Newman, D. P. Stotler, Task Group on Verification, Validation, U.S. Burning Plasma Organization, and U.S. Transport Task Force. Validation in fusion research: Towards guidelines and best practices. *Physics of Plasmas*, 15(6), 2008.

[TML+12] S. Chakraborty Thakur, D. McCarren, T. Lee, N. Fedorczak, P. Manz, E. E. Scime, G. R. Tynan, M. Xu, and J. Yu. Comparison of azimuthal ion velocity profiles using mach probes, time delay estimation, and laser induced fluorescence in a linear plasma devicea). *Review of Scientific Instruments*, 83(10), 2012.

[TPPM97] Menner A. Tatang, Wenwei Pan, Ronald G. Prinn, and Gregory J. McRae. An efficient method for parametric uncertainty analysis of numerical geophysical models. *Journal of Geophysical Research: Atmospheres*, 102(D18):21925–21932, 1997.

[VHTT17] P. Vaezi, C. Holland, S. C. Thakur, and G. R. Tynan. Understanding the impact of insulating and conducting endplate boundary conditions

on turbulence in csdx through nonlocal simulations. *Physics of Plasmas*, 24(4):042306, 2017.

[WPR+10] A. E. White, W. A. Peebles, T. L. Rhodes, C. H. Holland, G. Wang, L. Schmitz, T. A. Carter, J. C. Hillesheim, E. J. Doyle, L. Zeng, G. R. McKee, G. M. Staebler, R. E. Waltz, J. C. DeBoo, C. C. Petty, and K. H. Burrell. Measurements of the cross-phase angle between density and electron temperature fluctuations and comparison with gyrokinetic simulationsa). *Physics of Plasmas*, 17(5), 2010.

[WTM96] Mort David Webster, Menner A Tatang, and Gregory J McRae. Application of the probabilistic collocation method for an uncertainty analysis of a simple ocean model. 1996.

[XRD93] X. Q. Xu, M. N. Rosenbluth, and P. H. Diamond. Electron temperature gradient driven instability in tokamak boundary plasma. *Physics of Fluids B*, 5(7):2206–2214, 1993.

[XTH+09] M. Xu, G. R. Tynan, C. Holland, Z. Yan, S. H. Muller, and J. H. Yu. Study of nonlinear spectral energy transfer in frequency domain. *Physics of Plasmas*, 16(4), 2009.

[XTH+10] M. Xu, G. R. Tynan, C. Holland, Z. Yan, S. H. Muller, and J. H. Yu. Fourier-domain study of drift turbulence driven sheared flow in a laboratory plasma. *Physics of Plasmas*, 17(3), 2010.

[Yan09] Zheng Yan. Turbulence-driven shear flow and self-regulating drift wave turbulence in a cylindrical plasma device, 2009.

[YHT+07] J.H. Yu, C. Holland, G.R. Tynan, G. Antar, and Z. Yan. Examination of the velocity time-delay-estimation technique. *Journal of Nuclear Materials*, 363-365:728 – 732, 2007. Plasma-Surface Interactions-17.

[YTH+10] Z. Yan, G. R. Tynan, C. Holland, M. Xu, S. H. Muller, and J. H. Yu. Scaling properties of turbulence driven shear flow. *Physics of Plasmas*, 17(1), 2010.

[YXD+10] Z. Yan, M. Xu, P. H. Diamond, C. Holland, S. H. Müller, G. R. Tynan, and J. H. Yu. Intrinsic rotation from a residual stress at the boundary of a cylindrical laboratory plasma. *Phys. Rev. Lett.*, 104:065002, Feb 2010.

[ZBG+07] S J Zweben, J A Boedo, O Grulke, C Hidalgo, B LaBombard, R J Maqueda, P Scarin, and J L Terry. Edge turbulence measurements in toroidal fusion devices. *Plasma Physics and Controlled Fusion*, 49(7):S1, 2007.

[ZHB+12] S. Zhou, W. W. Heidbrink, H. Boehmer, R. McWilliams, T. A. Carter, S. Vincena, B. Friedman, and D. Schaffner. Sheared-flow induced confinement transition in a linear magnetized plasma. *Physics of Plasmas*, 19(1):012116, 2012.